PLPPR3 facilitates cytoskeleton-membrane interactions by condensate formation

Inaugural-Dissertation

To obtain the academic degree

Doctor rerum naturalium (Dr. rer. nat.)

Submitted to the Department of Biology, Chemistry, Pharmacy

of the Freie Universität Berlin

by

Shannon Francis Udo Bareesel

Berlin, 2024

For my grandparents – of whom none were able to witness this day.

The work presented in this thesis was performed from October 2019 until January 2024 under the supervision of Prof. Dr. Britta Johanna Eickholt at the Institute of Molecular Biology and Biochemistry of the Charité – Universitätsmedizin Berlin.

1st reviewer: Prof. Dr. Britta Johanna Eickholt

2nd reviewer: Prof. Dr. Oliver Daumke

Date of disputation: 30th April 2024

Declaration of Independence

I, *Shannon Francis Udo Bareesel*, hereby declare that I have written my thesis "PLPPR3 facilitates cytoskeleton-membrane interactions by condensate formation" independently and only with the aids and sources indicated.

The passages, taken from other works, were identified by stating the source. This also applies to diagrams, tables and pictorial representations.

This thesis has not been submitted to any other examination board and has not been published. The printed and electronic versions are identical.

Berlin, 25th January 2024 _____

Shannon Francis Udo Bareesel

Acknowledgements

The work presented here, was the result of a collaborative effort of many people, which I am deeply thankful for. Foremost, I would like to say thank you to my supervisor Britta Eickholt to entrust this part of the project to me and to Oliver Daumke for being my second reviewer and reading this work.

Dear Britta, I would like to express my deepest gratitude for the opportunity to work in your lab. Although the project was tough and there were many drawbacks, you never failed to encourage me and to provide optimism. You gave me the opportunity to explore science on an advanced level and find my own path. I have personally developed a lot these past years, for which I would like to thank you. It has been a privilege to experience scientific exchange in conferences and interact with lots of great minds. Looking back, I enjoyed this journey a lot. I will always remember to bring swimming trunks and have fun!

I would like to acknowledge and thank the entire Eickholt lab, for constant help, feedback, and teamwork. A huge thank you to our technicians, Kerstin Schlawe, Kristin Lehmann and Stephanie Bandura for providing me with buffers, material, cloning and prepping help.

My dearest thank you goes to our technician Katrin Büttner, which helped me clone countless constructs, re-iterating cloning strategies, providing help and being good company on the journey.

A very deep and special thank you to the "PLPPR3 Gang" including our former colleague Joachim Fuchs for providing me with the know-how to clone and all the great talks, coffee breaks and help!! Thank you to Fatih Ipek for handing over the project to me, introducing me to his protocols and purification strategies. Thank you to our newest Gang member Domonkos Nagy-Herzceg for help, data analysis and providing us with funny stories about theoretical ball stacking. Special thanks to the X-linker Willem Bintig, which sees the best in us, and wants to X-link everything. Thank you to Vasiliki Syropoulou, for help, feedback and optimism. Thank you to my student Laura Sandner for help with purifications and westerns. Thank you to the Greek PLPPR3 Gang members Alexandra

Acknowledgments

Acknowledgments

Table of Contents

Table of Contents

List of Abbreviations

°C	degrees Celsius
1,6-HD	1,6-Hexanediole
3C protease	3-chymotrypsin protease
6x His-Tag	Six Histidine residues (HHHHHH)
aa	Amino acid
ABP	Actin binding protein
AD	Alzheimer's disease
ADP	adenosine 5'-diphosphate
ATP	adenosine 5'-triphosphate
BASP1	Brain Acidic Soluble Protein 1
BS^3	Bis(sulfosuccinimidyl)suberat
CaM	Calmodulin
CAP23	Cortical cytoskeletal associated protein
CD	Circular dichroism
CHS	Cholesteryl Hemisuccinate
CL-MS	Crosslinking mass spectrometry
co-ip	Co-immnunoprecipation
CRY2	cryptochrome 2 oligomerization domain
Cryo-EM	Cryogenic electron microscopy
CTD	c-terminal domain
Da	Dalton
DDM	n-dodecyl-β-D-maltoside
Dil$_{C18}$	1,1'-Dioctadecyl-3,3,3',3'-Tetramethylindocarbocyanine Perchlorate
DIV	Day *in vitro*
DSS	Disuccinimidyl suberate
DTT	Dithiothreitol
$_{Ec}$PgpB	*Escherichia coli* phosphatidylglycerol phosphate phosphatase B
ER	Endoplasmic reticulum
Expi293F	Human embryonic kidney cell derived suspension cell line
F-actin	Filamentous actin

List of Abbreviation

FRAP	Fluorescence recovery after photo bleaching
FTD	Frontotemporal lobar degeneration
FUS	Fused in Sarcoma/Translocated in Liposarcoma
G-actin	Globular actin (monomers)
GPCR	G-protein coupled receptor
GUV	Giant unilamellar vesicle
$G_{\alpha i}$	Inhibitory alpha G-protein
$G_{\alpha s}$	Stimulatory alpha G-protein
h	hours
HA	Hemagglutinin signaling peptide
HEK293	Human embryonic kidney cells
High five	Insect cell line for protein over expression
HT	High tension voltage
ICD	intracellular domain of PLPPR3
IDP	Intrinsically disordered protein
IDR	Intrinsically disordered
in vitro	In the test tube
kDa	kilo Dalton
KO	knockout of specific gene
LCD	Low complexity domain
LC-MS/MS	Liquid chromatography /tandem mass spectrometry
LLPS	Liquid-liquid phase separation
LPA	Lysophosphatidic acid
LPAR	LPA-specific receptors
M1 Flag	N-terminal Flag tag (DYKDDDDA)
min	minutes
MLO	Membrane less organelle
MS	Mass spectrometry
MSA	Multiple sequence alignment
MT	microtubule
$N_{2\,(l.)}$	Liquid nitrogen
NAP22	Neuronal axonal membrane protein
NCID	Nephrin intracellular domain
NG311	Octyl Glucose Neopentyl Glycol

List of Abbreviation

NHS	N-hydroxysuccinimide
Ni-NTA	Nickel-NTA
NMR	Nuclear magnetic resonance
NTA	nitrilotriacetic acid
o.n.	over night
p	probability
PD	Parkinson's disease
PEG	Polyethylene glycol 8000
pH	*Potentia hydrogenii*
P_i	inorganic phosphate
PI(3,4,5)P$_3$	Phosphoinositol (3,4,5) triphosphate
PI(4,5)P$_2$	Phosphoinositol (4,5) bisphosphate
PI3K	Phosphatidylinositol 3-kinase
PKA	Protein Kinase A
PKC	Protein kinase C
PL	Poly-lysine
PLPP	Phospholipid phosphate protein
PLPPR	Phospholipid phosphatase-related protein
PLPPR3	Phospholipid phosphatase-related protein 3
PolyE box	Stretch of 20 glutamic acid residues
POPC	1-palmitoyl-2-oleoyl-sn-glycero-3-phosphocholine
POPS	1-palmitoyl-2-oleoyl-sn-glycero-3-phospho-L-serine
PrLD	Prion-like domain
PRM	Proline-rich motif
PSD	Post synaptic density
PTEN	Phosphatase and Tensin homolog
PTM	Posttranslational modification
PVA	Polyvinyl alcohol
RBP	RNA binding protein
RDF	Radial distribution function
roi	Region of interest
RT	Room temperature
s	second
S1P	Sphingosine-1-phosphate

List of Abbreviation

SDS-PAGE	Sodium dodecyl sulfate polyacrylamide gel electrophoresis
SEC	Size exclusion chromatography
*Sf*9	Insect cell line for protein over expression
SH3	SRC homology 3
SLB	Supported lipid-bilayers
SLC	Solute carrier protein
TDP-43	Transactive response in DNA binding protein of 43 kDa
TEV protease	Tabacco etch virus protease
TM	transmembrane domain
TMD	Transmembrane domain
TRP	Transient Receptor Potential
v/v	volume/volume
VASP	Vasodilator-stimulated phosphoprotein
w/v	weight/volume
x g	times g-force

List of Figures

List of Tables

I Summary

Neuronal branching is a developmental program, by which neurons acquire their complex morphologies. This highly dynamic process relies on various signaling molecules, cues and proteins such as the phospholipid-phosphatase related protein (PLPPR) family. PLPPR3, a family member of PLPPRs, is a transmembrane protein with a long intracellular domain (ICD) that primarily localizes to the axonal plasma membrane. Previous work demonstrated that PLPPR3 is highly expressed during neuronal development and can induce axonal filopodia. Prior to my project, no work had described a conclusive model of PLPPR3 ICD-facilitated filopodia formation.

The work presented here, establishes the purification of intracellular domain of PLPPR3 (Chapter 1). I gathered evidence that PLPPR3 ICD is a highly disordered protein domain utilizing circular dichroism spectroscopy and limited proteolysis (Chapter 2). Using *in vitro* assays, I showed that PLPPR3 ICD undergoes liquid-liquid phase separation (LLPS) (Chapter 3). LLPS is an interaction-driven process that orchestrates intrinsically disordered regions to form condensates, which serve as membrane less reaction compartments. PLPPR3 ICD condensates, follow liquid-like properties of phase separating proteins such as coalescence, fusion and circularity. With help of a blue-light inducible optogenetic PLPPR3 ICD CRY2 fusion construct, I was able to validated these properties in cells. To identify driving regions of PLPPR3 ICD LLPS, I utilized various deletion constructs and narrowed down the region to the membrane distal part of the protein. I further conceptualize a model of PLPPR3 ICD-facilitated filopodia formation *in vitro* (Chapter 4). I provide evidence that PLPPR3 ICD condensates can reshape giant unilamellar vesicle (GUV) membranes, by attracting PLPPR3 ICD condensates to the GUV interface. Using fluorescence microscopy, I demonstrate that PLPPR3 ICD condensates co-partion actin monomers and serve as actin nucleating compartments. Hence, I exhibit ring-shaped F-actin structures that polymerize out of PLPPR3 ICD condensates. I revealed that the formation of ring-shaped F-actin structures depends on the formation of PLPPR3 ICD condensate, while the polymerization from the condensates depend on the local actin concentration.

In summary, the presented work showed that PLPPR3 ICD forms liquid-like condensates, which nucleate actin. Considering PLPPR3s proven function to induce filopodia, this thesis provides a compelling model mechanism of PLPPR3 ICD condensates facilitating filopodia formation.

I Zusammenfassung

Die Verzweigung von Neuronen ist ein Entwicklungsprogramm, durch das Neuronen ihre komplexe Morphologie erhalten. Dieser hochdynamische Prozess hängt von verschiedenen Signalmolekülen, Stimuli und Proteinen wie der Familie der Phospholipid-Phosphatase-verwandten Proteine (PLPPR) ab. PLPPR3, ein Mitglied der PLPPR-Familie, ist ein Transmembranprotein mit einer langen intrazellulären Domäne (ICD), das hauptsächlich an der axonalen Plasmamembran lokalisiert ist. Die durchgeführten Arbeiten haben gezeigt, dass PLPPR3 während der neuronalen Entwicklung stark exprimiert wird und axonale Filopodien ausbilden kann. Vor meinem Projekt gab es keine Arbeit, die ein schlüssiges Modell für die Filopodienbildung durch PLPPR3 ICD beschrieben hat.

In dieser Arbeit wurde die Reinigung der intrazellulären Domäne von PLPPR3 etabliert (Kapitel 1). Mit Hilfe von Zirkulardichroismus-Spektroskopie und limitierter Proteolyse konnte ich nachweisen, dass PLPPR3 ICD eine hochgradig ungeordnete Proteindomäne ist (Kapitel 2). Mithilfe von *in-vitro* Experimenten, habe ich gezeigt, dass PLPPR3 ICD eine Flüssig-Flüssig-Phasentrennung (LLPS) durchläuft (Kapitel 3). LLPS ist ein interaktionsgesteuerter Prozess, der intrinsisch ungeordnete Regionen zur Bildung von Kondensaten bildet, die als membranlose Reaktionskompartimente dienen. Die PLPPR3 ICD Kondensate besitzen flüssigkeitsähnliche Eigenschaften von phasentrennenden Proteinen, wie Koaleszenz, Fusion und Zirkularität. Mit Hilfe eines durch blaues Licht induzierbaren, optogenetischen PLPPR3 ICD CRY2 Fusionskonstruktes, konnte ich diese Eigenschaften zusätzlich in Zellen validieren. Durch diverse Deletionskonstrukte, konnte ich die verantwortlichen LLPS Regionen von PLPPR3 ICD auf den membranfernen Teil des Proteins eingrenzen. Darüber hinaus habe ich ein Modell, der PLPPR3 ICD unterstützten Filopodienbildung *in vitro*, konzipiert (Kapitel 4). Ich konnte zeigen, dass PLPPR3 ICD Kondensate die Membranen von riesigen unilamellaren Vesikeln (GUV) umgestalten können, indem PLPPR3 ICD Kondensate an die GUV-Grenzfläche binden. Mit Hilfe der Fluoreszenzmikroskopie zeige ich, dass PLPPR3 ICD Kondensate Aktinmonomere ko-partionieren und als Aktin-Nukleierungskompartimente dienen. Dadurch bilden sich ringförmige F-Aktin-Strukturen, die aus PLPPR3 ICD Kondensaten polymerisieren. Ich konnte feststellen, dass die Bildung ringförmiger F-Aktin-Strukturen von der Bildung von PLPPR3 ICD Kondensaten abhängt, während die Polymerisation aus den Kondensaten von der lokalen Aktinkonzentration abhängt.

I Zusammenfassung

Zusammenfassend zeigt die vorliegende Arbeit, dass PLPPR3 ICD flüssigkeitsähnliche Kondensate bildet, die Aktin nukleieren können. In Anbetracht der nachgewiesenen Funktion von PLPPR3 bei der Induktion von Filopodien, liefert diese Arbeit einen neuen Modellmechanismus für die Rolle von PLPPR3 ICD Kondensaten bei der Bildung von Filopodien

1 Introduction

1.1 Discovery of highly organized units

During the late Renaissance, the invention of the microscope led to several scientific discoveries. Among those, in 1665, the British scientist Robert Hooke investigated cork under a microscope. He observed box-like structures, which he termed "cells" (Hooke et al., 1665). Although he didn't understand the complicated setup of cells, he discovered the basic unit of all living organisms that share common features[1]. Basic features in eukaryotic cells include a plasma membrane (lipid-bilayer) separating the inner environment from the outside, as well as numerous compartmentalized organelles in the cytoplasm that maintain specialized functions within the cell, including energy generation, gene expression, protein synthesizes and trafficking, degradation, recycling[2].

Organelles are membrane-bound and create unique environments by a lipid-bilayer "inner membrane" system (Cohen et al., 2018). However, cells exploit a further way of spatiotemporal control of biochemical reaction using membraneless compartments coined biomolecular condensates (Taniue & Akimitsu, 2022). Both, membrane separated and membraneless compartments permit cells to function as highly organized unit (Mitrea & Kriwacki, 2016), by allowing different biochemical reactions to take place simultaneously. Multicellular organisms have a strategy of specializing cells like muscles cells, epithelial cells or neuronal cells. Cells that have a similar function and structure are grouped into communities called tissue. Each tissue comprised of these communal cells have a specific function. Neuronal cells for example are signal integrators and transducer (Lovinger, 2008). Roughly, 100 billion neuronal cells make up ~10% of the human brain (Allen & Barres, 2009; Herculano-Houzel, 2009; Noctor et al., 2007).

1.2 Neuronal cells are highly polarized

Neurons are highly specialized cells that enable efficient communication of stimuli such as sensory, environmental and mechanical information via electric signals to various effectors including muscles and brain (Gaub et al., 2020; Horton & Ehlers, 2003; Krüppel

---

[1]Alberts B, Johnson A, Lewis J, et al. New York: Garland Science; 2002.

[2]Kent, M. (2000). Advanced Biology. In *Oxford University Press*.

& Tetzlaff, 2020; Terenzio et al., 2017). Their high polarization into an axon and soma-dendritic domains (Craig & Banker, 1994), lets them transfer electric input signals from dendrites, over soma, along the axon to other neurons (Cajal, 1989). Studying neurons *in vivo* is challenging, primarily caused by complexity of the nervous system itself, however dissociated neurons develop *in vitro* similarly, making them an ideal model system (Azari & Reynolds, 2016). As a hallmark of *in vitro* studies, Harrison, 1910 observed that 'nerve cells can be cultured and studied outside of the body'. Therefore, methods for culturing neurons *in vitro* emerged, ranging from culture flasks and roller tubes for better gas exchange, over microfluidic chambers for single or co-cultures (Millet & Gillette, 2012) to simple glass cover slips (Harrison, 1910). In general, surfaces are coated with substrates such as poly-lysine (PL) to adhere neurons via electrostatic interactions (Yavin & Yavin, 1974). Development *in vitro* can be characterized into 5 stages (Dotti et al., 1988). In stage one neurons, protrusions such as lamellipodia and filopodia form, which support the progression to stage two neurons with immature neurites. In stage three neurons, one neurite elongates rapidly and breaks the symmetry of immature neurites, to become the axon. In contrast, all remaining neurites will develop into dendrites. During stage 4, both axons and dendrites develop further by initiating complex growth. Finally, the final stage of this in vitro neuronal development program, stage 5, is characterized by the development and maturation of synapses including postsynaptic specializations called dendritic spines (Figure 1) (Polleux & Snider, 2010). Throughout the different stages in neuronal development, local actin network instability in specific neuronal compartments is necessary for initiation of mechanisms that transform the developing neuron (Bradke & Dotti, 1999). For example, slender, actin enriched membrane protrusions called filopodia, are essential precursors for the generation of neurites (progression from stage 1 to stage 2 neurons), for generation of axon branches (progression from stages 3 to stages 4 neurons), as well as for generation of dendritic spines (stage 5 neurons) (Joachim Fuchs & Eickholt, 2021b; Leondaritis & Eickholt, 2015; Mattila & Lappalainen, 2008; Medalia et al., 2007; Wit & Hiesinger, 2023; Ziv & Smith, 1996).

Stage 1 E14 + 0div — Lamellipodial and filopodial protrusion

Stage 2 E14 + 1−2div — Multiple immature neurite extension

Stage 3 E14 + 2−4div — Breaking of symmetry: axon specification

Stage 4 E14 + 4−15div — Axon and dendrite outgrowth, branching

Stage 5 E14 + 15−25div — Spine morphogenesis synapse formation

2
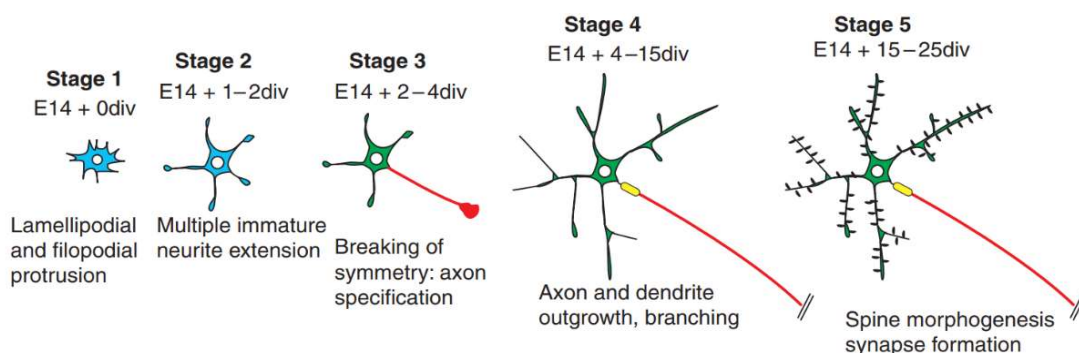
Figure 1. Polarization of neurons *in vitro*
Polarization of neurons in vitro can be divided into 5 stages, where stage one and two (DIV0 - DIV2), deal with protrusion formation like filopodia and lamellipodia. In stage three (DIV2 – DIV 4), one neurite breaks the symmetry to become the axon, while all others become dendrites. This axon is further elongated during stage four (DIV4 – DIV15) and matures along with dendrites and dendritic spines at stage five (DIV15 – DIV25)(Modified after Polleux & Snider, 2010).

1.3 Filopodia serve as precursors during neuronal morphogenesis

Filopodia are thin, dynamic and actin-enriched protrusions that emerge from cell membranes (Gallo, 2013). They play an important role in development, growth and function of neurons, being particularly important for axon guidance, migration and neurite outgrowth (Gallop, 2020; Wit & Hiesinger, 2023). Actin is one of the most abundant proteins in neurons (Dominguez & Holmes, 2011). In solution, actin is a monomeric protein (G-actin) that under physiological conditions self-assembles under tight regulation into filaments (F-actin) (Pollard, 2007). F-actin is a major protein interactor and can polymerize/depolymerize in a process called dynamic treadmilling (Wegner & Isenbergt, 1983). Filamentous actin provides the cell with stability, locomotion and contributes to neuronal development (Pollard & Cooper, 2009).

One key feature of filopodia is their rapid extension and retraction, which is crucial for exploration and sensing (Heckman & Plummer, 2013). Filopodia extend from the leading edge of neuronal growth cones, responding to guidance cues such as netrins and semaphorins (Lowery & Vactor, 2009). Enduring filopodia may lead to processes such as neurites (Dent et al., 2007; Smith, 1994), axonal branches (Brosig et al., 2019a; Katherine & Dent W., 2014), dendritic branches (Georges et al., 2008; Heiman & Shaham, 2010) and dendritic spines (Dailey & Smith, 1996; Ziv & Smith, 1996).

The formation of filopodia is a remarkably intricate and tightly regulated process, orchestrated by numerous pathways and mediators. Actin-binding proteins play a pivotal role in this process, as highlighted by Dobramysl et al., 2021. These proteins work in concert to coordinate the organization of actin filaments into bundles, not only preventing membrane pushback, but also furnishing mechanical stability, a concept discussed by Khurana & George, 2011.

Initiating this dynamic process are various extracellular cues, exemplified by netrins (Bashaw & Goodman, 1999). Furthermore, membrane receptors such as Robo1/2, which have been investigated by Hivert et al., 2002, can trigger intricate signalling pathways to set the filopodia formation in motion. The activation of Rho GTPase, particularly Cdc42,

plays a pivotal role in instigating actin polymerization at the prospective tip of filopodia, a phenomenon explored in depth by Govek et al., 2005 and previously noted by Nobes & Hall, 1995.

Notably, Cdc42 engages with WASP/N-WASP in a on phosphoinositol-(4,5)-bisphosphate (PI(4,5)P2) dependent manner. The interaction subsequently recruits and activates the actin nucleation factor ARP2/3 complex (Miki et al., 1998; Prehoda et al., 2000; Rohatgi et al., 1999). This complex, as detailed by Ideses et al., 2008, binds to actin filaments and orchestrates the formation of dense and highly branched actin networks. These intricate actin networks, are reorganized into actin bundles, ultimately giving rise to the formation of filopodia (Svitkina et al., 2003).

Alternative Cdc42-dependent pathways involve the overexpression of scaffolding protein IRSp53 binding to Cdc42, the effector protein WAVE2 and the Bar domain protein MENA to induce filopodia formation (Krugmann et al., 2001; Scita et al., 2008). IRSp53 alone can perform F-actin bundling and is involved in F-actin rearrangement (Yamagishi et al., 2004). Cd42-independent pathways include the small GTPase Rif, which recruits mDIA2 to induce filopodia (Ellis & Mellor, 2000; Pellegrin & Mellor, 2005).

Once a filopodia does not retract and "matures" into a neurite, it can be invaded by microtubules (MTs) and progresses to more stable neurites or branches (Higgs & Das, 2022). This invasion occurs by polymerizing microtubules into the filopodium (Dent & Kalil, 2001; Okabe & Hirokawa, 1988; Schaefer et al., 2002; Smith, 1994). Microtubules are stabilized by microtubules-associated proteins (MAPs), particular MAP2C, MAP1B and tau, by crosslinking MTs into bundles (Dehmelt & Halpain, 2004; Matenia & Mandelkow, 2009). Neurite outgrowth is mediated by many factors, such as the protein EB3 in complex with the actin binding protein Drebin (Flynn, 2013; Geraldo et al., 2008).

1.4 Transmembrane proteins control neuronal morphogenesis by conveying information from cell exterior to interior

Transmembrane (TM) proteins constitute a class of proteins anchored into the membrane by stretches of hydrophobic amino acid residues (Alberts et al., 2002). Initially, membrane proteins are co-translational inserted into the endoplasmic reticulum (ER) membrane (Guna & Hegde, 2018), and trafficked via the Golgi to the plasma membrane (Stalder & Gershlick, 2020). Their membrane spanning domains exhibit different

functions like signal transduction, ion transport or membrane trafficking, depending on the number of transmembrane domains and other factors (Müller et al., 2008). While an odd number of transmembrane spanning domains will likely result in an extracellular C-terminal domain (CTD), even number will result in an intracellular. The best studied class of transmembrane proteins are G-protein coupled receptors (GPCRs) with seven membrane spanning domains (Schiöth & Lagerström, 2008), followed by Transient Receptor Potential (TRP) channels with six (Cosens & Manning, 1969). GPCRs are agonist-coupled receptors that modulate downstream effects by activation of heterotrimeric G proteins (Rosenbaum et al., 2009). Extracellular ligands include hormones, neurotransmitters and chemokines (D. Yang et al., 2021), which trigger conformational changes in the GPCR membrane spanning domains and facilitate interaction with heterotrimeric G-proteins (Hanlon & Andrew, 2015). Downstream effects of GPCR signalling include regulation of second messenger Calcium, adenylyl cyclase, protein kinases and potassium channels (Tuteja, 2009).

TRP channels on the other hand, are a conserved superfamily of cation ion channels that convey sensory information in primary sensory neurons upon ligand binding e.g. capsaicin for TRPV1 channel and noxious heat > 42°C (Kwon et al., 2021; Lishko et al., 2007; Samanta et al., 2018). TRP channels function as multimers, where the p-loop between the 5th and 6th transmembrane (TM) domain forms the pore with selectivity filter that lets cations pass (Nilius & Owsianik, 2011). Downstream effects for TRPV1 include different modes of sensation like pain or itching, triggered by varying signalling cascades (Koivisto et al., 2022). Other examples of transmembrane proteins include the class of tweety proteins with five membrane-spanning domains, which serve as chloride ion channels (Attwood & Schiöth, 2021). Claudins have four transmembrane domains and are components of tight junctions (Morita et al., 1999), while solute carrier proteins (SLCs), with up to 14 transmembrane domains (Pizzagalli et al., 2021), shuttle larger or charged molecules across the membrane (Schlessinger et al., 2013).

1.4.1 Phospholipid phosphatases as signal transducers and lipid phosphate regulators

Phospholipid phosphates (PLPPs) are a class of transmembrane proteins consisting of PLPP1, PLPP2 and PLPP3 that each have six alpha-helical transmembrane domains (Brindley & Pilquil, 2009). All three PLPPs hydrolyze bioactive lipid phosphates such as

lysophosphatidic acid (LPA) and sphingosine-1-phosphate (S1P) (Brindley & Waggoner, 1996; Tang & Brindley, 2020). In addition, lipid phosphates can bind and signal through their specialized GPCRs, triggering intracellular cascades involved in cell proliferation (Tabata et al., 2007; Tang et al., 2019). PLPPs located in the membrane, however, attenuate all downstream effects by dephosphorylation of extracellular lipid phosphates, thereby antagonizing their cellular functions (Jasinska et al., 1999; Waggoner et al., 1996). The conserved lipid-binding motifs C1, C2 and C3 in the extracellular loops of PLPP1-PLPP3 seem not to have any lipid phosphate preference (Busnelli et al., 2018). Downregulation of PLPPs has been observed in many types of cancers, which in return leads to an increase in extracellular LPA and S1P (Tang et al., 2019). This downstream, may contribute to enhanced tumour growth and metastasis (reviewed in Tang & Brindley, 2020).

1.4.2 Phospholipid phosphatase-related proteins: an orphaned class of transmembrane receptors

Two decades ago, the identification of a new class of proteins antagonizing growth cone collapse (Bräuer et al., 2003), paved the way for the identification of the class of phospholipid phosphatase-related proteins (PLPPRs), recently reviewed in Fuchs et al., 2022. Derived from PLPPs (Sigal et al., 2005), PLPPRs share a conserved folding topology with six membrane spanning domains, where both N- and C-terminal domains are both located in the intracellular space (Brindley & Waggoner, 1998; Sigal et al., 2005). Noteably, PLPPRs differ from PLPPs in their extracellular catalytic domains C1, C2 and C3 (Figure 2), which appear to be incapable of catalysis due to several mutations of critical residues (Sigal et al., 2005; Waggoner et al., 1999).
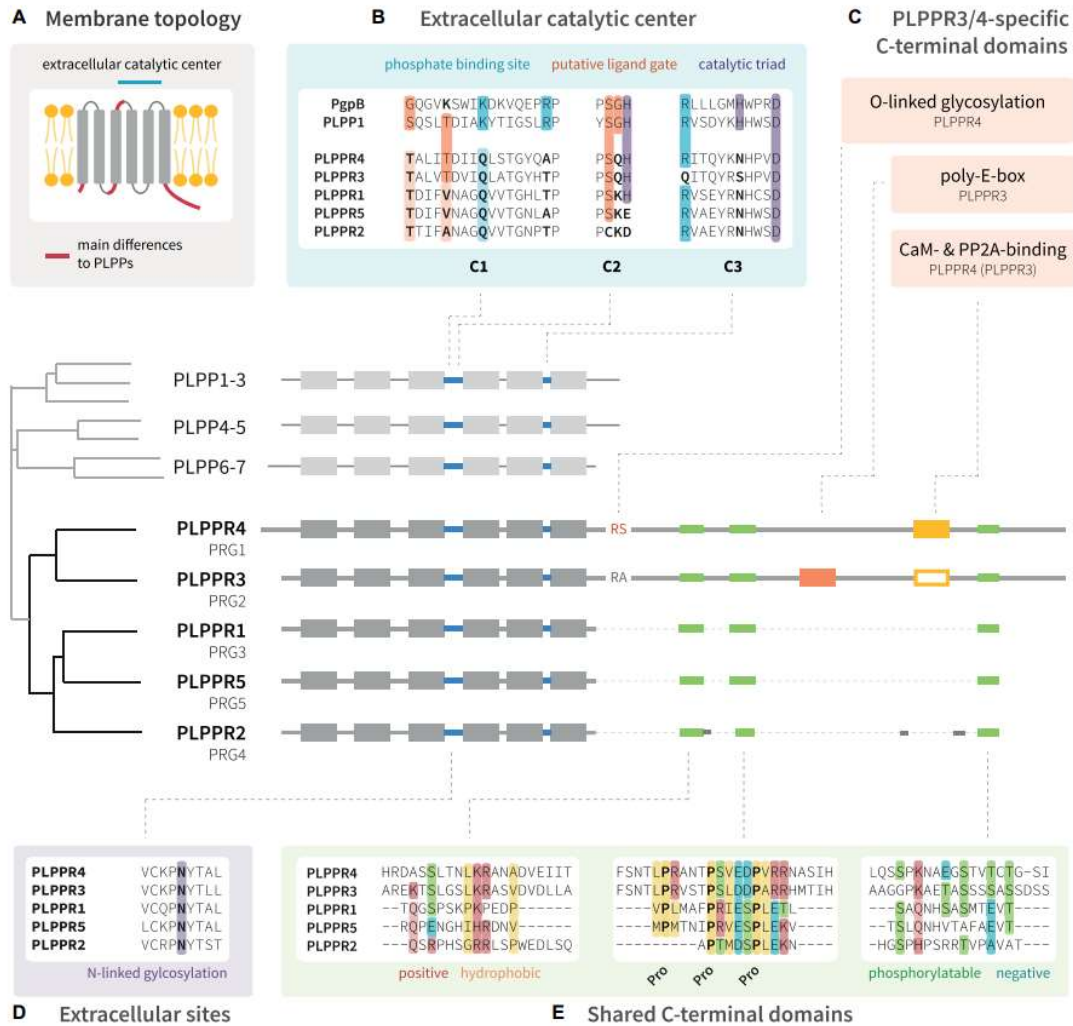
Figure 2. Topology comparison of the PLPPR family
A Conserved topology for all PLPPRs and PLPPs. B Comparison of the catalytic centre comprising the regions C1, C2 and C2 in the extracellular loops. C PLPPR specific modifications compared to PLPPs. D Conserved extracellular N-glycosylation site of PLPPRs. E Shared ICD stretches of positive and negative charges, hydrophobic and proline rich regions in all PLPPRs (Joachim Fuchs et al., 2022).

PLPPRs have diverged also among themselves, evolving a unique set of intracellular domains (ICDs) of various length (Bräuer & Nitsch, 2008). While PLPPR1 and PLPPR3 display ICDs of ~ 400 amino acid residues, the ICDs of PLPPR2, PLPPR4 and PLPPR5 have ~ 50 amino acid residues. Despite these differences, conserved regions exist among all PLPPRs (Figure 2B, D and E.).

In terms of expression patterns, PLPPRs are a class of brain enriched (Bräuer & Nitsch, 2008) and tight temporal regulated (Panpan Yu et al., 2015) proteins (Figure 3). Two distinct expression patterns emerge in neurons, where PLPPR1 and PLPPR3 mainly localize in the axon (Brosig et al., 2019; Cheng et al., 2016), while PLPPR4 and PLPPR5

are found in dendritic compartments (Figure 3 A) (Thomas Broggini et al., 2016b; Coiro et al., 2014a; Gross et al., 2022; Velmans et al., 2013b; Panpan Yu et al., 2015a).

Several PLPPRs have been observed to induce membrane protrusions, like filopodia (section 1.3). This was observed especially for PLPPR1 (Thomas Broggini et al., 2016a; Sigal et al., 2007; Velmans et al., 2013b; Panpan Yu et al., 2015a), PLPPR5 (Thomas Broggini et al., 2010; Coiro et al., 2014a), PLPPR4 (X. Liu et al., 2016a) and PLPPR3 (Brosig et al., 2019). Fewer filopodia were observed in hippocampal neurons generated from PLPPR3 Knockout (KO) mice (Brosig et al., 2019; Fuchs et al., 2020; Fuchs & Eickholt, 2021).
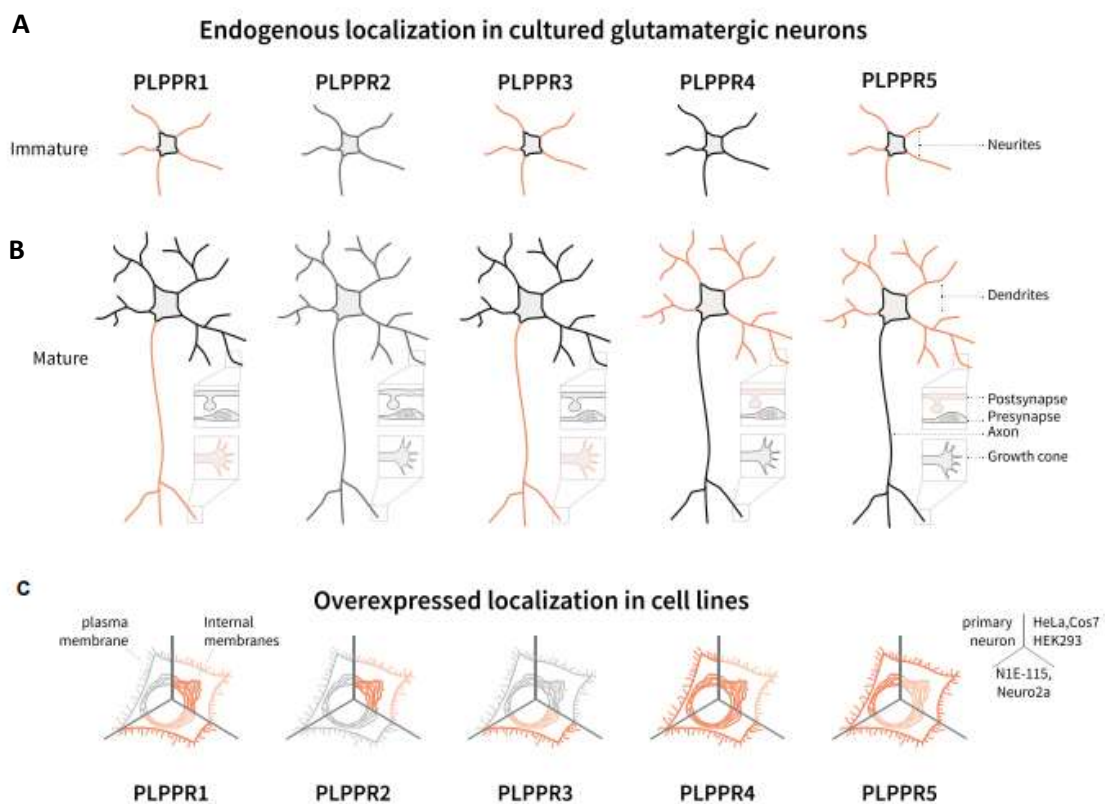
Figure 3. Localization pattern of PLPPR in neurons
*A. Localization of PLPPRs during different developmental stages. Formally, PLPPRs can be divided into two groups, the axonal group comprising PLPPR1 and PLPPR3 and the dendritic group with PLPPR4 and PLPPR5. For PLPPR2 not much information is available. **B**. Localization of overexpressed PLPPRs in cell lines. (Modified after Fuchs et al., 2022).*

1.4.3 Phospholipid phosphatase-related protein 3 (PLPPR3) locally inhibits PTEN at the axonal plasma membrane

Filopodia formation is one of the best studied functions of PLPPRs. A particular family member that carries a long ICD, is PLPPR3. The intracellular domain of PLPPR3 plays

an important role during the filopodia formation process (see section 1.4). We previously identified that PLPPR3 binds and locally inhibits phosphatase and tensin homolog deleted on chromosome 10 (PTEN) at the axonal plasma membrane (Figure 4). PTEN belongs to a growth inhibiting signalling pathway, which involves Phosphoinositide-3-kinase (PI3K) (Hemmings & Restuccia, 2012). PI3K promotes phosphorylation of phosphatidylinositol-4,5-bisphosphate (PI(4,5)P2) to phosphoinositol-3,4,5-trisphosphate (PI(3,4,5)P3) (Carnero & Paramio, 2014; Tariq & Luikart, 2021). PTEN antagonizes this pathway and reduces PI(3,4,5)P3 at the plasma membrane (Brazil & Hemmings, 2001). PI(3,4,5)P3 has been associated in neurons with morphogenic processes such as neurite formation, extension and polarity (Horiguchi et al., 2006; Ketschek & Gallo, 2010; Ménager et al., 2004). The interaction of PLPPR3 ICD with PTEN inhibits PTEN's phosphatase activity (Brosig et al., 2019); however, the exact mechanism requires further clarification.
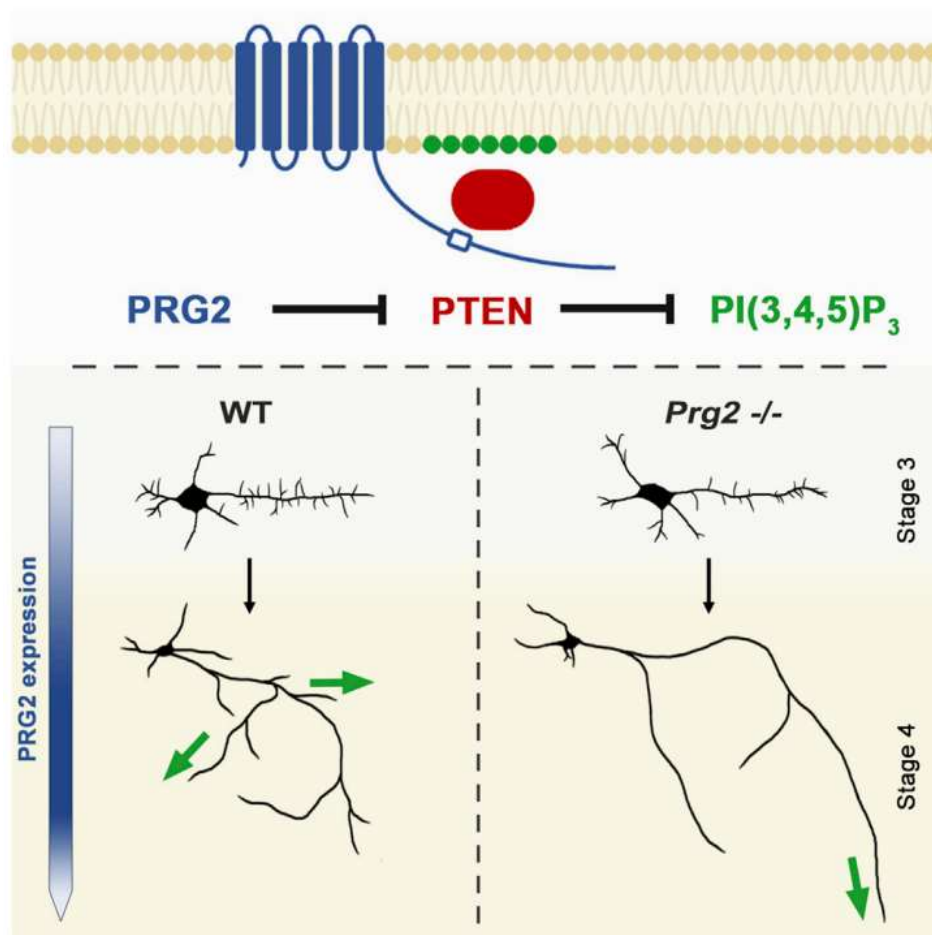
Figure 4. PLPPR3 locally inhibits PTEN at the axonal plasma membrane
PI3K/PTEN signalling pathway regulates axon branching in neuronal cells. PTEN, a tumour suppressor protein, can supress growth, thus maintaining a balance of PI(4,5)P2 and PI(3,4,5)P3. PLPPR3 was found to locally inhibit PTEN, thereby leading to an accumulation of PI(3,4,5)P3, which in return leads to

filopodia formation by recruiting F-actin into patches. Loss of PLPPR3 leads to less filopodia and branching events, not effecting overall branch length. (Modified after Brosig et al., 2019).

1.4.4 Special topology of PLPPR3 raises many unanswered questions

PLPPR3 exhibits a distinct predicted structure, with the intracellular N-terminus encompassing residues 1-17 (Figure 5). All six domains are predicted alpha helical, which resembles the solved crystal structure of its distant relative *Escherichia coli* phosphatidylglycerol phosphate phosphatase B ($_{Ec}$PgpB) (Fan et al., 2014). The extracellular loops three and five, contain the inactive, former catalytic motif that has been well characterized in PLPPs (Joachim Fuchs et al., 2022; Sigal et al., 2005). The function of the other loops remains to be elucidated. The intracellular domain (ICD) begins at residue Q284 and ends at D716 (Figure 5). Interestingly, ICD contains a "PolyE Box", a stretch of 20 glutamic acid residues that lead to a high negative charge of the intracellular C-terminus (Brosig et al., 2019). Although the function of the PolyE Box is currently unknown, unpublished data from our laboratory suggest an interactive function of the PolyE box with PTEN (see section 1.4.3)

In a mass-spectrometry approach to characterize posttranslational modifications (PTMs), many serine and threonine residues of ICD have been identified as phosphorylated (Kroon, 2023). In total, over 26 phosphorylation sites have been validated, which organize in clusters, comparable to the hyperphosphorylated clusters, present in the microtubule associated protein tau (Gong & Iqbal, 2008). Although not many phosphorylation sites have been characterized to date, Ser351 has been validated as a Protein Kinase A (PKA) substrate (Kroon et al., 2024, *in preparation*). As well as highly phosphorylated, PLPPR3 ICD is predicted of high flexible nature (PONDR - http://www.pondr.com/), suggesting its potential as a signaling hub with a non-limiting binding cavity. Hereby, phosphorylation may play an important role in recruiting interaction partners or triggering a change in topology for binding of extracellular lipid phosphates. The structure of PLPPR3 remains unknown, yet would provide valuable information concerning functionality, interaction partners and binding of extracellular signals.
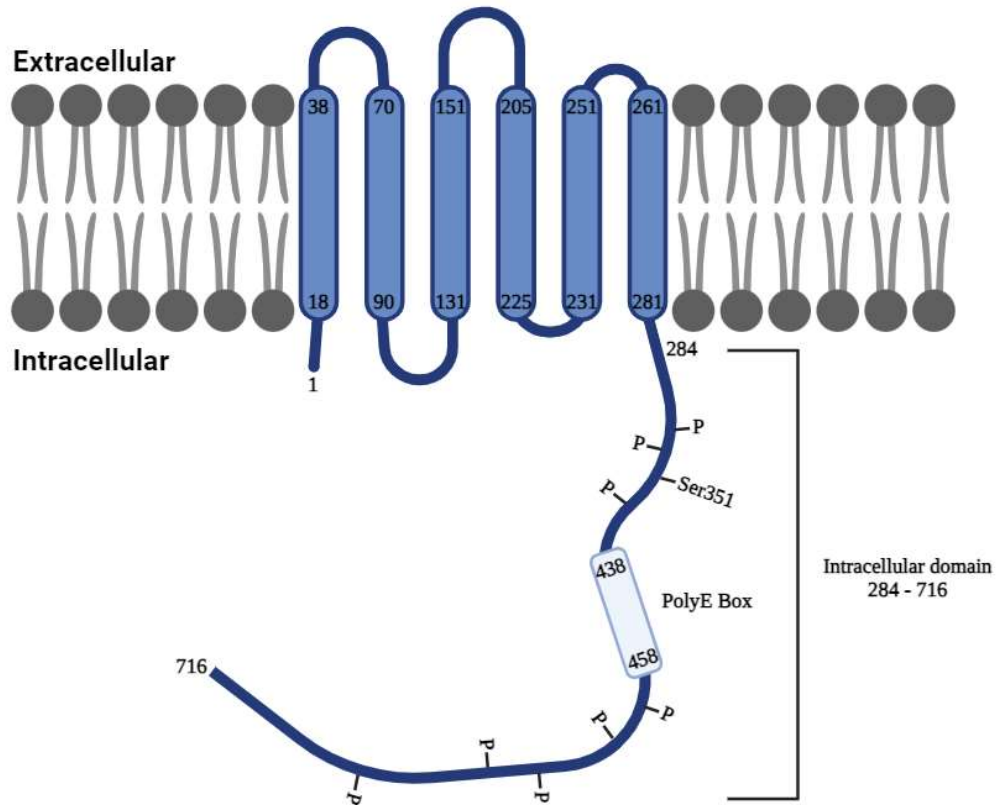
Figure 5. Topology of PLPPR3
PLPPR3 has six alpha-helical transmembrane domains with three extracellular and two intracellular loops. Loops three and five (extracellular) contain the inactive lipid binding motif C1, C2 and C3. While the entire transmembrane domain (TMD) makes up roughly one-third of the protein, the other two-thirds are intracellular domain (ICD). The ICD is made of several stretches of low complexity residues, containing a large amount of alanine, glycine, glutamine and serine residues. Serine makes up close to 10% of the ICD residues (calculated for Q7TPB0 with https://web.expasy.org/protparam/) and is modified by phosphorylation (Kroon, 2023). *Created with Biorender.com*

1.5. Liquid-liquid phase separation forms membraneless compartments

To sustain life and execute precise cellular responses, cells face a number of complex challenges. One of the imminent problems is the arrangement of a vast number of biochemical reactions simultaneously and within confined space. How can a cell accomplish such a vast task? In recent years, research has unveiled the existence of membraneless compartments. Although compartments like nuclei, mitochondria, endoplasmic reticulum, Golgi apparatus etc. have been extensively studied before (Alberts et al., 2002), research underlines the importance of membraneless compartments as mechanism to organize biochemical reaction in space and time. A compartment has two main functions: separation from the exterior and freely diffusible components in the interior. Membrane-separated compartments are surrounded by a physical boundary, a

lipid bilayer. In contrast, the 'membraneless' organization of biomolecules has been identified in recent years as important biophysical principle in cells. Conceptually, like a drop of oil in water, one can perceive a spontaneous formation of a distinct liquid-like compartment. Such distinct liquid-like compartment can be a protein-rich phase, which grants cells the ability to execute biochemical reactions in a confined space without the need of a physical barrier (Shin & Brangwynne, 2017; Weber & Brangwynne, 2012).

1.5.1 Molecular interactions oppose entropy-driven mixing

What drives biomolecules to form liquid-like condensates? The second law of thermodynamics states that a system e.g., the cytoplasm, will always favour a fully protein mixed state as a result of an increased Entropy S (Webb, 1885). However, for proteins to form a liquid-like compartment, a separation from the cytoplasm occurs in a process termed liquid-liquid demixing. By this process, the entropy-driven mixing of liquids is energetically unfavoured (Hyman et al., 2014a). Microscopic interactions play a vital role in the process (section 1.5.2), which considered the interaction energy E as contribution to the free energy F (equation 1).

$$F = E \cdot TS^{mix} \qquad (1)$$

This principal can be explained by blue (b) and red (r) molecules each representing a liquid e.g., a protein and the cytoplasm (Figure 6). In a system, where (b) and (r) molecules are mixed, entropy will be high as a result. How can interaction between the one molecule (b) and the other (r) result in a lower entropy state and therefore a demixed system? In this simplified model, the energies of neighbouring molecules in a lattice can be noted as ε_{bb} (two blue molecules interacting), ε_{rr} (two red molecules interacting) or ε_{br} (two different molecules interacting). If the interaction energy between red and blue molecules is large, then the system would not favour them next to each other. Therefore, the overall interaction energy of all hetero interactions (e.g., blue to red) can be described as $E_{unfavourable}$ and the interaction energy of all homo interactions (e.g., blue to blue, red to red) as $E_{favourable}$.
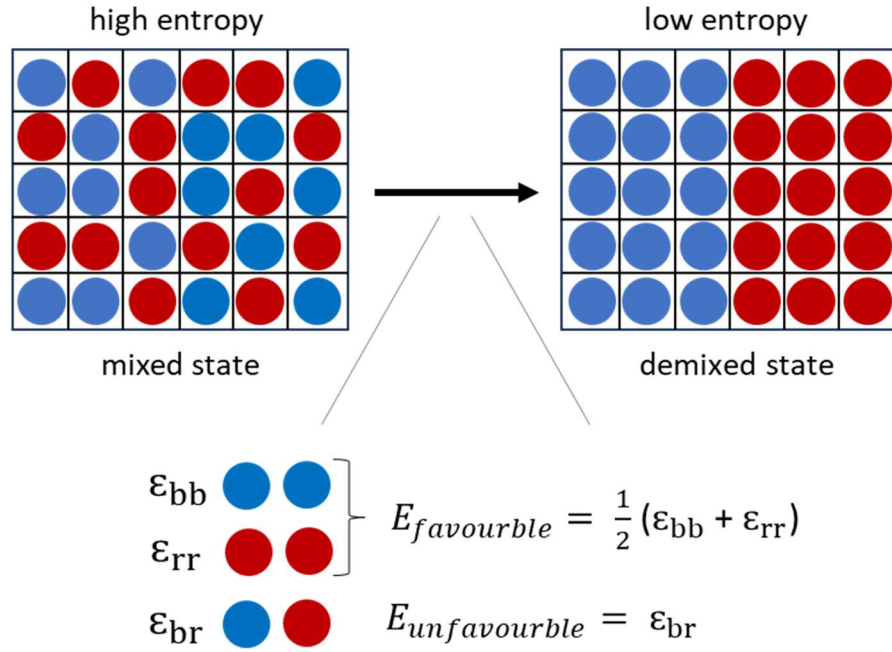
Figure 6. Simplified model of demixing
A high entropy state (mixed) is only favoured if the interaction energy $E_{unfavourable}$ between red molecules (r) and blue molecules (b) is lower, than the interaction energy $E_{favourable}$. If the interaction energy is higher, the system will favour a demixed state of two liquids that oppose the entropy S. However, within the demixed area, entropy leads to a mixed state again (Modified after Brangwynne et al., 2015).

To understand if a system can demix, it is essential to consider a simplified Flory-Huggins theory (Flory, 1942; Huggins, 1942) (equation 2), which involves the parameter χ, which describes the difference in the interaction energy between $E_{unfavourable}$ compared to $E_{favourable}$, divided by $k_B T$. If the term above the fraction line is larger than the term $k_B T$, which is the thermal energy (entropic force), then the system will favour demixing towards mixing (Brangwynne et al., 2015; Dill & Bromberg, 2003; Rubinstein & Colby, 2003).

$$\chi \approx \frac{E_{unfavourable} - E_{favourable}}{k_B T} \gg 1 \tag{2}$$

However, within the demixed biomolecular condensate the distribution of molecules is either entropy driven and mixed or organized to allow for dynamic exchange of water or reaction products with the surrounding (Handwerger et al., 2005; Molliex et al., 2015;

Patel et al., 2015). Either way, interactions between the molecules themselves contribute and drive biomolecular condensate formation.

1.5.2 Residue interactions between proteins are the main driving forces of demixing

Several molecular interactions between protein residues contribute to $E_{favourable}$ and thereby oppose $E_{unfavourable}$. One key concept is multivalency of proteins, which describes the effect of protein interacting with several binding sites (valency) (Zumbro & Alexander-Katz, 2020). With increasing valency, more interactions between proteins are possible (Mohanty et al., 2022). Li et al., 2022 examined the interaction of different engineered valency repeats of SRC homology 3 (SH3) with its ligand proline-rich motif (PRM) and observed liquid-liquid phase separation (LLPS) *in vitro* and cells. Additionally, multivalency is achieved by intrinsically disordered regions (IDRs) with repetitive motifs. This was discovered during precipitation of RNP granules (Kato et al., 2012), during which it became evident that low complexity domains like prion-like domains (PrLDs) are sufficient to phase separate biomolecules (Molliex et al., 2015; Xue et al., 2019). Low complexity domains (LCD), a type of IDR, are unstructured regions composed of polar, charged amino acids such as serine, tyrosine, glutamine and asparagine and glycine (Boija et al., 2018; Dunker et al., 2001; Vodnala et al., 2021). Other IDRs contain low amount of aromatic and stretches of positively or negatively charged residues (Figure 7) (Uversky et al., 2000). This distribution leads to a lack in classic tertiary structure in the IDR and to dynamic protein states, which increases protein-protein interaction (Dyson & Wright, 2005; Forman-Kay & Mittag, 2013).
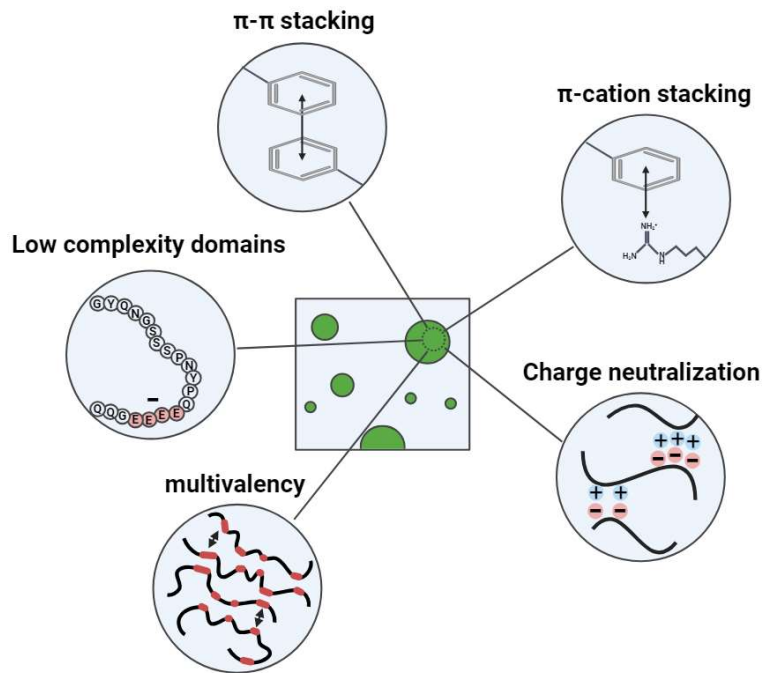
Figure 7. Driving forces of biomolecular condensate formation

Biomolecular condensates form by opposing entropy through several interactions between amino acid residues of same proteins. Some common interactions include π-π stacking between two aromatic residues or π-cation stacking between an aromatic residue and a charged residue, such as arginine. Additional interactions include charge neutralization between positive and negative stretches of amino acid residues that can be part of low complexity domains. Low complexity domains are stretches of polar, charged amino acids that are unstructured. Some biomolecular condensates, forming proteins are multivalent, meaning they have several stretches of low complexity within the sequence that can interact with other low complexity domains and form multivalent structures (Modified after Feng et al., 2019; Gomes & Shorter, 2019; Sherrill, 2013). Created with Biorender.com

Other important driving forces of biomolecular condensates will be mentioned in the following. Biomolecular condensate formation heavily depends on multivalent π-π stacking of aromatic residues such as tyrosine, phenylalanine and tryptophan (Sherrill, 2013), as well as more charged residues arginine, lysine, glutamic acid, glutamine and asparagine that are associated with delocalized π electrons (Figure 7) (McCoy Vernon et al., 2018). Condensate formation of Nephrin intracellular domain (NICD), for example, highly depends on positively charged interaction and aromatic residues. Truncation or mutagenesis resulted in reduced condensate formation, indicating the importance of π-π stacking (Pak et al., 2016). Moreover, cation-π interactions between aromatic residues and charged lysine and arginine have been shown to contribute to biomolecular condensate formation. For example, Qamar et al., 2018 as well as Bogaert et al., 2018 showed significant contribution of tyrosine in LCD with arginine residues in the structured region for FUS condensate formation.

Another critical concept leading to the formation of several biomolecular condensates is charge neutralization (Figure 7). Opposite charged residues can interact and thereby coacervate like observed for Nephrin (Pak et al., 2016) or the RNA helicase Ddx4 (Nott et al., 2015). Residues are thereby found often in patches or clusters, rather than spread throughout the sequence. This concept has been termed "sticker-spacer model" (Ginell and Holehouse, 2023). Sticker regions in intrinsically disordered proteins (IDPs) may be repetitive domains, linear motifs and LCDs, while in folded proteins and multivalent proteins, stickers can be folded domains (Choi et al., 2020). Spacers connect "sticky regions" and prevent overly dense packing, allowing for dynamic processes (Harmon et al., 2017; Hyman et al., 2014b; Mehta & Zhang, 2022).

1.5.3 Molecular-, Meso- and cellular-scale functions of biomolecular condensates

Biomolecular condensates exhibit diverse functions across different scales (Lyon et al., 2021). One fundamental function of a membraneless compartment is their impact on biochemical reaction rates of educts to increase (Woodruff et al., 2017) or decrease (Powers et al., 2019) a reaction kinetic, to promote a specific reaction towards another (Case et al., 2019) and to exclude molecules to keep a reaction running (Su et al., 2016). Different biomolecular condensates can form sub compartments within one condensate and undergo vectoral organisation, a purpose by which unfavoured reaction partners are excluded from the sub compartment (Feric et al., 2016). The reaction product can diffuse to the next sub compartment, where it serves as educt for the following reaction. One level up in scale, biomolecular condensates have been implied to establish architecture i.e., in the presynaptic active zone (Wu et al., 2019) or postsynaptic densities (PSD) (Zeng et al., 2016, 2018), where several scaffolding proteins assemble and condensate to organize e.g. formation of PSD or cluster receptors (NMDA and VGCC). Other mesoscale functions include DNA damage repair by compartmentalizing of DNA within the condensate (Singatulina et al., 2019). Finally, on a cellular scale, long-distance trafficking of RNA granules on Lysosomes as transport mechanism in neurons has been observed (Liao et al., 2019). In general, Klosin et al., 2020 provide evidence that membraneless compartments can effectively counter noise-dependent variability in protein expression in cells, by buffering and changing condensate size. Furthermore, sensing environmental changes like pH shift by pH sensor domains in yeast protein Sup35 and forming condensates as a result (Franzmann et al., 2018) or temperature stress sensing

by LCDs of yeast protein Pab1 by switching from mixed to demixed state (Riback et al., 2017), promote cellular fitness.

1.5.4 Aggregation of biomolecular condensates in neurodegenerative diseases

Many researchers have described the biological significance of condensates. Clifford P. Brangwynne et al., 2009 studied the importance of membraneless structures in *C. elegans*, providing first evidence was gathered that p granules in oocytes can transit between a condensed protein-rich phase and a soluble form. Observation of p granule fusion with each other, proved liquid-like behaviour of these structures and paved the path for the idea of phase transition of biomolecular condensates and downstream explanations of disease relevant mechanism. Biomolecular condensates have been associated with various diseases, including neurodegeneration and cancer (Boeynaems et al., 2023).

Due to the highly polarized morphology of neurons (section 1.2), trafficking proteins and other cargo to the synapses can be challenging. Biomolecular condensates have been implicated to play an important function in this process (Wu et al., 2020). In patients suffering from neurodegenerative disorders, such as Alzheimer's disease (AD), Parkinson disease (PD), Amyotrophic Lateral Sclerosis (ALS), Frontotemporal lobar degeneration (FTD) and others, axonal trafficking proteins that form biomolecular condensates were found aggregated (Figure 8). For instance, in ALS, two condensate forming RNA-binding proteins Fused in Sarcoma/Translocated in Liposarcoma (FUS) and Transactive response DNA binding protein of 43 kDa (TDP-43), aggregate via their PrLDs and form large aggregates during self-association (Li et al., 2013). While self-association serves a functional purpose, an imbalance, possibly induced by factors such as oxidative stress, can lead to increased aggregation (Zuo et al., 2021). In addition, irreversible liquid to solid transition was observed for tau, a microtubule-associated neuronal protein involved in AD. Biomolecular condensate formation of tau was shown to play a role in tau aggregation (Kanaan et al., 2020; Wegmann et al., 2018). Several other condensate-forming proteins were described to be involved in neurodegenerative disorder including α-synuclein (Calabresi et al., 2023; Mamais et al., 2013; Ray et al., 2020) for PD.
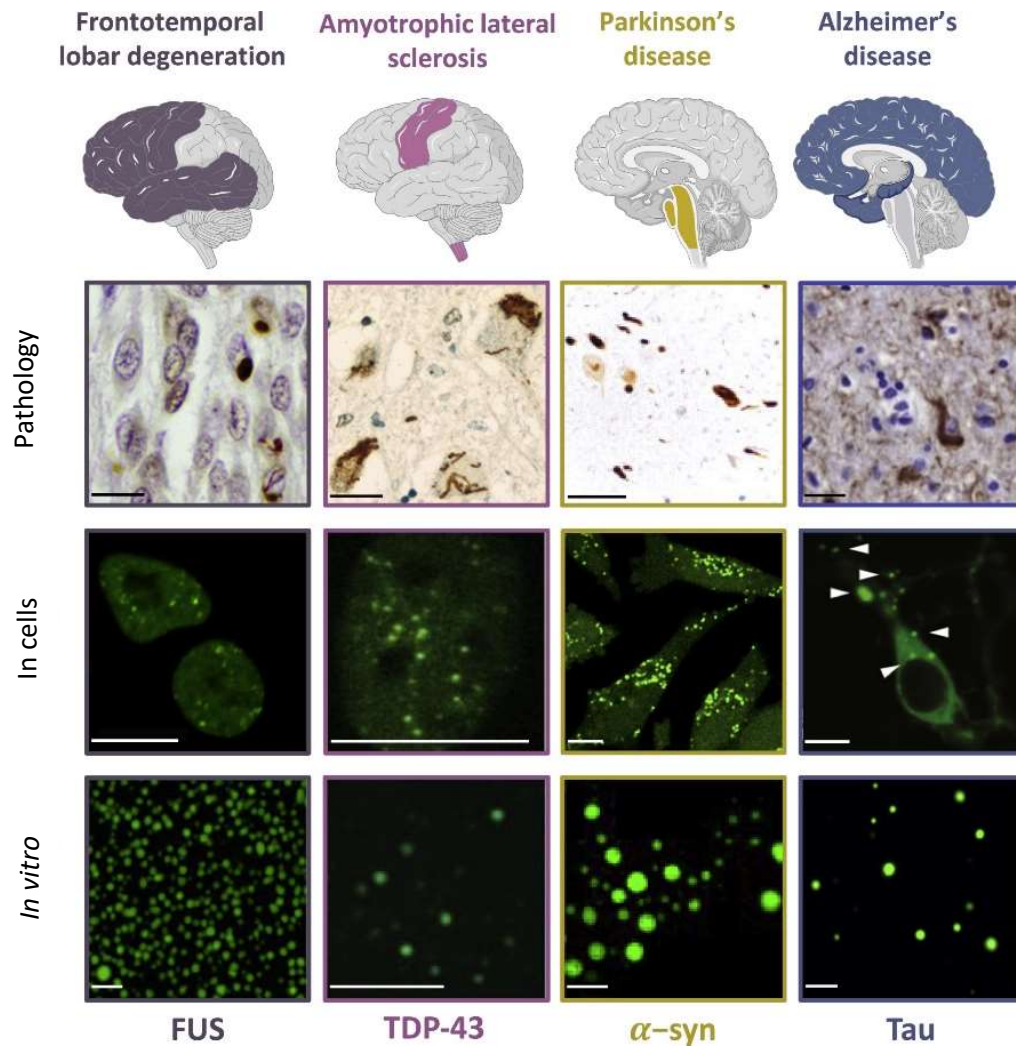
Figure 8. FUS, TDP-43, α-synuclein and tau biomolecular condensates
Representative images of FUS (grey), TDP-43 (magenta), α-synuclein (yellow) and tau (blue) condensates in vitro, in cells and their respective pathologies and affected brain areas, represented by schematic color-coded brain areas (Modified after Zbinden et al., 2020).

One additional example of a protein involved in cancer is protein Kinase A (PKA), which is activated by cyclic adenosine monophosphate (cAMP) (Ahmed et al., 2022; Zaccolo et al., 2021), a second messenger mostly involved in controlling gene expression, growth, proliferation, migration (Zaccolo, 2011). PKA is a tetrameric holoenzyme that is composed of two regulatory and two catalytic subunits and has been linked to mammary tumorigenesis (Beristain et al., 2015). PKA phosphorylates a wide range of substrates, including Ser351 of PLPPR3 (Kroon, 2023). In a recent study, (J. Z. Zhang et al., 2020) described condensate formation of the regulatory PKA subunit, which is promoted by cAMP binding and acts as a cAMP buffering system. The loss of regulatory PKA

condensate formation results in an increased cell proliferation, which highlights the importance of this process.

The novel field of condensate biology highlights the significance of membraneless reaction compartments and their implication in trafficking, regulation or as simple reaction chambers. Mis-regulation can result in fatal consequences, including cancer and neurodegenerative disorders. Our perception of how cells thread several processes simultaneously, although limited by reaction space, has opened a new interpretation of protein function.

2. Objectives of this thesis

PLPPR3 plays an important role during branch formation in neurons. To better understand this process, we aim for the structural characterization of PLPPR3, as structure can provide valuable information for biological function, for example possible binding partners, by identifying binding cavities and mechanistic insight like ion channel function.

My initial objective was to establish a purification pipeline of diverse PLPPR3 fusion constructs by overexpression in cell lines (Chapter 1 and Appendix). To determine the three-dimensional structure, I utilized Cryo-EM as best fitting approach considering PLPPR3 size and flexibility. Unfortunately, I was unable to gain structure information due to the intracellular domain's (ICDs) high flexibility. Therefore, my first objective was to establish a purification pipeline of PLPPR3 ICD (Chapter 1). In my second objective, I utilized my purification pipeline and characterized the intracellular domain for structural disorder (Chapter 2). I implemented biophysical and biochemical methods including circular dichroism, thermostability assay and limited proteolysis to test for secondary structure elements and stabilization of structure. This led to Chapter 3, in which I investigated biomolecular condensate formation of PLPPR3 ICD in cells and *in vitro*. I established a fusion protein with light-inducible CRY2 oligomerization domain, which I used to create clusters in cells "on-demand". By activation with blue light, I observed condensate behaviour in cells including condensate fusion (coalescing) and gained insight into possible functions like actin co-partitioning in cells. In addition, I implemented my purification pipeline (Chapter 1) to use purified PLPPR3 ICD for *in vitro* condensate characterization. I used FRAP and studied condensate coalescence to monitor highly liquid-like behaviour of condensates.

Finally, in Chapter 4, I pursued addressing the question, how membrane localized PLPPR3 can facilitate filopodia formation. By condensate formation of ICD, force is generated on a membrane. As a model, I used giant unilamellar vesicles (GUVs) and studied membrane shaping by *in vitro* condensates. Filopodia formation also depends on the polymerization of actin filaments. Therefore, to broaden my *in vitro* model, I characterized co-partitioning of actin into PLPPR3 ICD condensates and the resulting actin filamentous structures. By crosslinking actin in condensates to PLPPR3 ICD, I gathered proximity information about possible binding sites. This enabled the generation of structure prediction models based on crosslinker restrictions.

3 Material and Methods

3.1 Material

Table 1. *Materials*

Materials	Manufacturer	Reference number	Lot number
15 ml Falcon Tube	Corning	352096	20122070
50 ml Falcon Tube	Corning	352070	05522099
125 ml PETG flask	ThermoScientific	4115-0125	1335736
250 ml PETG flask	ThermoScientific	4115-0250	1326300
500 ml PETG flask	ThermoScientific	4115-0500	1342554
75 cm^3 flask	Corning	4307204	19722067
150 cm^3 flask	Corning	3291	35220008
Bacterial culture tube	VWR	60818-725	21601-227CB-225
Steritop® 45 mm	Millipore	17402	MP22140962
Serological pipette 5ml	Corning	357543	2260005
Serological pipette 10 ml	Corning	35755	2191007
Serological pipette 25 ml	Greiner Bio-one	760180	F221036P
Safe-lock tube 2 ml	Eppendorf	2423	L202179l
Safe-lock tube 0.5 ml	Eppendorf	1221	L203898K
Safe-lock tube 1.5 ml	Eppendorf	2212	K198392M
Serological pipette 2 ml	Sarstedt	86.1252.011	2172E 2025-06
Amicon Ultra-4	Merck	UFC 803096	R9KA78060
Amicon Ultra-15	Merck	UFC 903096	R9MA78053
Filterpur S 0.2	Sarstedt	83.1826.001	220591103
Imaging dish CG15	Miltenyi Biotec	6160-168	232101
Cell scraper 25 cm	Corning	353086	13319076Y
Cell scraper 18 cm	Corning	353085	03222057
Hamilton syringe	Carl Roth	X047.1	052103589
CryoPure 1.6 ml tube	Sarstedt	72.380	0080421
50 ml syringe	BD Platipak™	300865	1503271
Coverslips 24 x 40 mm	epreda	BB02400400A 113MNZ0	1181
Coverslips 24 x 32 mm	Roth	H877	
1 ml syringe Omnifix-F	Braun	9161406v	20F08C8
12-well plate	TPP	92012	20200158
Dish			F150238K
6-well plate	TPP	92006	20210260
24-well plate	TPP	92024	20180225
15 µ-slide 4 well (glass)	Ibidi	804426	210921/6
15 µ-slide 4 well (plastic)	Ibidi	80427	221013/1
0.22 µm MGE membrane	MF Millipore	GSWP04700	R1KB49246
Amicon Ultra-0.5 ml	Merck	UFC503096	R9BA90239
Amicon Ultra-4	Merck	UFC810096	R9SA27578
Amicon Ultra-0.5 ml	Merck	UFC510096	0000189931
Pierce centrifuge column 2 ml	ThermoScientific	89896	XA331375
Pierce centrifuge column 5 ml	ThermoScientific	89897	XB333320
0.22 µm Ultrafree-MC-GV centrifugal filters; PVDF	Merck	UFC30GV00	0000183549
Safe-lock tube 5 ml	Eppendorf	0030119401	L203590K
Blotting Pad, 703	VWR		15757070
Glass coverslips (Ø 18 mm, Ø 30 mm)			
Glass plate with 1.5 mm spacer	Biostep		20-30-118
Mini Trans-Blot Foam pads	BioRad	1703933	-

Mini Trans-Blot Gel holder cassette	BioRad	1703931	-
Mini-Protean 3 Systems Glass plates	BioRad	1653312	-
Mini-Protean Comb, 15 well	BioRad	1653366	-
Mini-Protean Gaskets	BioRad	1653305	-
Mini-Protean Gel releasers	BioRad	1653320	-
Mini-Protean Short plates	BioRad	1653308	-
Mini Trans-Blot Cell	BioRad	1703930	-
Parafilm	Bemis	PM-996	-
Rotilabo -Aluminiumfoil 15 µm	Roth	AA76.1	-
Dual-Chamber cell counting slides	BioRad	1450011	64472592
Roti-NC, Transfer-membrane, nitrocellulose	Roth	HP40.1	160894998
PVDF Transfer membrane	ThermoScientific	88520	WF3135833
Supported Nitrocellulose membrane	BioRad	16200097	A30311334
500 ml Erlenmeyer flask	thelabwarehouse	FK216-35	-
250 ml Erlenmeyer flask	thelabwarehouse	FK216-13	-
200 ml Erlenmeyer flask	thelabwarehouse	FK216-26	-
D-Tube™ Dialyzer Maxi, MWCO 12-14 kDa	Merck	71510-3	3679559

Table 2. *Inhibitors*

Inhibitor	Manufacturer	Mw [g/mol]	Reference number	Lot number
Cantharidin	Roth	196.20	3322.1	420233971
Complete tablets mini	Roche	-	04693159001	57084200
PMSF				
AEBSF-hydrochloride	Sigma	-	A8456-100MG	-
Protease inhibitor cocktail set III	Merck	-	539134	3884336

Table 3. *Chemicals*

Chemical	Manufacturer	Mw [g/mol]	Reference number	Lot number
Hepes	Roth	238.31	9105.3	301310928
Glycerol	J-T. Baker	92.10	7044.2500	2232805861
Sodiumchlorid	Roth	54.88	3957.1	202321891
TRIS	Roth	121.14	4855.2	281297206
TRIS-HCl	Merck	157.60	1.08219.1000	V020044019037

Magnesiumchlorid hexahydrate	Sigma-Aldrich	203.30	63064-500G	BCCD2692
Caliciumchlorid dehydrate	Merck	147.02	2382	TA552282
Imidazole	Sigma-Aldrich	68.08	56750-500G	STBK1250
EDTA	Roth	374.24	X986.1	361312585
2-Mercaptoethanol	Sigma-Aldrich	78.13	M7154	02896DK
DTT	Biomol	154.25	04010.100	4002
Agarose standard	Roth	-	3810.3	222320073
EGTA	AppliChem	380.35	A0878,0100	9P013094
APS	Roth	228.20	9595.3	501317338
EDTA	AppliChem	372.24	A1104,0250	1S006103
Glycine	Roth	75.07	3908.2	092317090
D-(+)-Glucose	Sigma	180.16	G7021-100G	SLBL4878V
PBS	Oxoid	-	BR0014G	-
Sodium deoxycholate	AppliChem	414.57	A1531,0100	3Z008424
Hanahan's Broth	Sigma	-	H8032-500G	MXBX5762V
Rubidium chloride	Sigma	120.92	R223-50G	WXBC7526V
D-(+)-Saccharose	Roth	342.30	4621.1	418274855
Magnesium sulfate	Sigma	120.37	M7506-500G	SLBD1731V
LB Broth	Sigma	-	L3022-1Kg	BCCH6853
Paraformaldehyde	Merck	-	1.04005.1000	K48966105724
Nonidet P40	AppliChem	-	A1694,0250	5V012788
Tween 20	Merck	-	655204-100ml	3088374
Triton X-100	Merck	-	1.12298.0101	K32674298502
Sodium proprionate	Sigma	96.06	P1880-1Kg	SLCF2446
Rotophorese 10x TAE	Roth	-	T845.2	192324255
Sodium azide	Sigma	-	S2002-25G	STBK3909
SDS-Solution 20%	AppliChem	-	A0675,1000	7P012262
Polyethylenimine, branched	Sigma	25.000	408727-1000ml	MKBN3988V
Sodium fluorid	Roth	41.99	P756.1	101169277
β-Glycerophosphate disodium pentahydrate	Roth	306.12	6847.2	027248205
Sodium orthovanadate	Sigma	183.91	S6508-50G	0000013743
Sodiummolybdate dehydrate	Roth	241.95	0274.1	324216606
Sodium butyrate	Sigma	110.09	303410-100G	MKCK9580
Valproic acid sodium salt	Sigma	166.19	P4543-10G	MKCJ7640
Virkon	LanXess	-	EE33/B4	2008BA0036
Paraffin wax	Sigma	-	76242-1Kg	BCCH6571
EtOH 70% (vergaellt)	Roth	46.07	T913.3	372328578
QuickCoomassieStain	ProteinArk (Serva)	-	35081.01	210952
EtOH 96.4%	Berkel AHK	46.07	1411U	220721/296
2-Propanol	Roth	60.10	9866.6	111307721
HCl	Roth	-	K025.1	19010131
Tryptanblue (C.I.23850)	Roth	960.82	CN76.2	330295347
MeOH	Roth	32.04	CP43.3	132318554
NaOH	Roth	40.0	9356.1	067253054
Ponceau-S solution	AppliChem	-	A2935,0500	20011495
Sodiumhydroxid 1M	Roth	-	K021.1	502194963
Rotiphorese gel 30 (37.5:1)	Roth	-	3029.1	262326205
Rotiphorese 10x SDS-PAGE	Roth	-	3060.2	372328940
Rotiphorese NF acrylamide/Bis solution 30% (29:1)	Roth	-	A124.1	040292384

Milk powder	Roth	-	T145.2	31235218
BSA	Sigma	66.000	A2153-50G	SLCJ9586
Prolong Glass Anti-fade Mountant	Invitrogen	-	P36984	2342116
TEMED	Roth	116.21	2367.1	359285051
10% DDM/CHS (10:1)	Anatrace	-	D310-CH210	4218466
5% LMNG/CHS (10:1)	Anatrace	-	NG310-CH210	4218445
Digitonin				
NG311				
NG310				
Fos-choline 14	Anatrace			
PIP3 Di8	Echelon	-	P3908	E00282-039-13
PageRuler plus prestained protein ladder	ThermoScientific	-	26619	01269486
ECL western blotting	Promega	-	W1001	0000491759
ECL select western blotting	Cytivia	-	RPN2235	17611883
PhosTag acrylamide	Nard institute, LTD.	-	AAL-107	-
Zincchloride				
Chloroform	Sigma	119.38	C2432-25ml	SHBD5858V
Polyethylenimine MAX, linear	Polysciences Inc.	40.000	24765-100	A815741
Dimethylsulfoxid	AppliChem		A3672,0100	4M017303
Fetal calf serum				
Goat serum	Gibco			
HOECHST	Sigma	-	14530	-
Penicillin/Streptavidin 100x	Gibco		14140122	15070
Poly-L-ornithine 100x	Sigma		P8638	
Mowiol	Sigma		81381-1Kg	BCBL1789V
GeneRuler 1 kb Plus DNA Ladder	ThermoScientific	-	SM1331	01333494
100 bp DNA ladder	Promega	-	G2101	0000380846
6x DNA Loading Dye	ThermoScientific	-	R0611	01309200
RedSafe	Intron	-	21141	0008-090501.54
1,6-Hexanediol	Sigma		240117-50G	

Table 4. *Constructs and Primers*

Construct	Primer	Sequence 5' – 3'
pCA_HA-M1-PLPPR3 ICD-His	-	Gene synthesis from Eurogentec which was subcloned into a pCA vector with 5' NheI and 3' PstI
pOET3_His_TEV_PTEN	Gene synthesis from Eurogentec, which was subcloned into a pOET3 vector with 5' EcoRI and 3' NotI by Brian Lally and Anja Koch (Lee et al., 2015)	
pMT4_PLPPR3 ICD-His	construct cloned by Fatih Ipek (PhD Thesis, 2022)	
pCA_HA-M1-PLPPR3 ICD-3C-His	PLPPR3 ICD_HindIII_PreSc_FW	GATGATGCAAAGCTTATGCAGGCACCACC
	PLPPR3_ICD_NotI_PreSc_Rev	CGAGCGGCCGCTCAGTGGTGGTGATGGTGATGGGGGCCCCTGGAACAGAACCTCGAGGGGCCGGCCGTCGACGTC
pCA_HA-M1-PLPPR3 ICD 284-463-3C-His	PLPPR3 ICD_HindIII_PreSc_FW	GATGATGCAAAGCTTATGCAGGCACCACC
	PRG2_1-156_Rev	CGAGCGGCCGCTCAGTGGTGGTGATGGTGATGGGGGCCCCTGGAACAGAACCTCGAGGGGCCGGCCGTCGACTGCTACCTGCTCTGCTGGGGCCCTC

pCA_HA-M1-PLPPR3 ICD 284-463-3C-His	PLPPR3 ICD_HindIII_PreSc_FW	GATGATGCAAAGCTTATGCAGGCACCACC
	PRG2_1-179_Rev	CGAGCGGCCGCTCAGTGGTGGTGATGGTGATGGGGGCCCCTGGAACAGAACCTCGAGGGGCCGGCCGTCGACAACAGGCCCTTCCTCTTCCTCCTCT
pCA_HA-M1-PLPPR3 ICD 438-716-3C-His	PRG2_154-434_FW	AGCGCAAAGCTTCAGGTAGCAGAGGAG
	PRG2ICDNotPreRev	CGAGCGGCCGCTCAGTGGTGGTGATGGTGATGGGGGCCCCTGGAACAGAACCTCGAGGGGCCGGCCGTCGACGTC
pCA_HA-M1-PLPPR3 ICD 460-716-3C-His	PRG2_258 -434_FW	CGGAAGGATAAGCTTGGGCCTGTTCCACCCTCACTC
	PRG2ICDNotPreRev	CGAGCGGCCGCTCAGTGGTGGTGATGGTGATGGGGGCCCCTGGAACAGAACCTCGAGGGGCCGGCCGTCGACGTC
pCA_HA-M1-PRG2 ICD 460-581-3C-His	176-297_HindIII_fw	GCATTGAAGCTTGGGCCTGTTC
	176-297_BamHI_rev	CCGATGGATCCACGGTCTGACG
pCA_HA-M1-PRG2 ICD 582-637-3C-His	298-353_HindIII_fw	CATTGAAGCTTGACTCTGCCAG
	298-353_BamHI_rev	CCGATGGATCCCTGTTTACAGC
pCA_HA-M1-PRG2 ICD 368-716-3C-His	354-434_HindIII_fw	GCATTGAAGCTTCCTGGAATG
	354-434_BamHI_rev	CCGATGGATCCGTCCTGGTACCTC
pMT4_PLPPR3 ICD - mscarlet-CRY2	PRG2ICD_BSRGI_Cry2FW	GACGAGCTGTACAAGGCGGCCACGCGTATGAAGATGG
	PRG2ICD_NotI_Cry2Rev	CCGCGGCCGCTTAGGTGGCGACCGGTGGATCC
pMT4_mscarlet-CRY2	mscarlet_NheI_FW	GGCAAGCTAGCGCCACCATGGTGAGCAAGGGCG
	CRY2_NotI_Rev	GCTTGCGGCCGCTTAGGTGGCGACCG
pCA_HA-M1-BASP1-His	HINDIII_BASP1_FW	GCTAGCATAAGCTTATGGGAGGCAAGC
	BamHI_BASP1_Rev	GCGATTGGATCCCTCTTTGACGGCCACGCTTTG
pCA_HA-M1-BASP1 G3A_His	HINDIII_BASP1_G3A_FW	GCTAGCATAAGCTTATGGGAGCCAAGC
	BamHI_BASP1_Rev	GCGATTGGATCCCTCTTTGACGGCCACGCTTTG

Table 5. *Kinases, Phosphatases, Ligases and Proteases*

Name	Manufacturer	Reference number	Lot number	Target
Lambda Phosphatase	NEB	P0753L	-	Dephosphorylation of PLPPR3 ICD
PKA	NEB	P6000L	-	S/T phosphorylation
TEV protease	In-house made	-	-	ENLYFQ/G
3C precision protease	In-house made	-	-	LEVLFQ/GP
T4 DNA ligase	NEB	M0202L	10141840	Ligation
10x buffer for T4 DNA ligase	NEB	B0202A	10127256	-
Antarctic Phosphatase	NEB	M0289L	10034942	Dephosporylation of vector

Antarctic phosphatase reaction buffer	NEB	B0289S	10036011	-

Table 6. *Restriction enzymes*

Enzyme	Manufacturer	Reference number	Lot number	Restriction site 5' – 3'
FD BamHI	ThermoScientific	FD0054	00904911	G/GATCC
FD SalI	ThermoScientific	FD0644	00661713	G/TCGAC
FD NotI	ThermoScientific	FD0596	00908525	GC/GGCCGC
FD DpnI	ThermoScientific	FD1704	00643506	GA(CH$_3$)/TG
FD EcoRI	ThermoScientific	FD0274	00147813	G/AATTC
FD HindIII	ThermoScientific	FD0505	00658701	A/AGCTT
FD KpnI	ThermoScientific	FD0524	00914286	GGTAC/C
FD LguI	ThermoScientific	FD1934	01153577	GCTCTTC N$_1$
FD MfeI	ThermoScientific	FD0754	00156013	C/AATTG
FD MunI	ThermoScientific	FD0754	00668957	C/AATTG
FD NcoI	ThermoScientific	FD0574	00900685	C/CATGG
FD NdeI	ThermoScientific	FD0584	00121947	CA/TATG
FD NheI	ThermoScientific	FD0974	01245977	G/CTAGC
FD PaeI	ThermoScientific	FD0604	00245533	GCATG/C
FD SacI	ThermoScientific	FD1133	00133808	GAGCT/C
FD PstI	ThermoScientific	FD0614	00664430	CTGCA/G
FD XbaI	ThermoScientific	FD0684	00449305	T/CTAGA
FD XhoI	ThermoScientific	FD0694	00653868	C/TCGAG
10x FD buffer	ThermoScientific	-	01275830	-
BsrGI-HF	NEB	R3575		T/GTACA
10x CutSmart buffer	NEB	-	-	-

Table 7. *Beads*

Beads	Manufacturer	Reference number	Lot number	Target
Talon Metal Affinity Resin	TaKaRa	635502	2202797A	6x His
M1 Sepharose Resin	In-house made	/	/	M1 Flag
Ni Sepharose 6 Fast Flow	GE Healthcare	17-5318-02	10285765	6x His
Chitin Resin	NEB	S6651L	0171309	Intein-CBD
GFP-Trap A	Chromotek	gta-20	131101001A	GFP
Dynabeads Protein A	Invitrogen	10002D	00670968	IgG

Table 8. *Devices*

Device	Manufacturer
Centrifuge 5417R (rotor ID: F45-30-11)	Eppendorf (Hamburg)
Centrifuge 5430R (rotor ID: F35-6-30)	Eppendorf (Hamburg)
Heating Block RCT classic	IKA
Analytical weighing scale CPA64	Sartorius (Göttingen)
Weighing scale PCB	Kern
Varioskan Flash	ThermoScientific
Fusion SL	Vilber Lourmat (Eberhardzell)
Ministar silverline	VWR
Vortex Genie-2	Scientific Industires
Waterbath TW8 and TW12	Julabo (Seelbach)
VacuSafe	Integra (Biebertal)
Icemachine AF-10	Scotsman (Milan)
Centrifuge 5427R (rotor ID: FA-45-12-17)	Eppendorf (Hamburg)

(rotor ID: FA-45-24-11)	
Centrifuge 3K10 (rotor ID: 11133)	Sigma
Pipetboy accujet® pro	Brand
Concentrator 5301 (rotor ID: FA-45-48-11)	Eppendorf
Prometheus NT48 NanoDSF	Nanotemper Technologies
Optima™ Max Ultracentrifuge (rotor ID: TLA 110)	Beckman Coulter
PH Meter (SI analytics electrode)	Schott
Spektrophotometer CARY50 Bio	Vario
Ultra-Thin LED illuminator	biostep
Analytical weighing scale CP64	Sartorius (Göttingen)
Sonicator Sonoplus (sonicator staff MS73)	Bandeln
Cell counter TC20™	BioRad
Paula	Leica
LUNA fl	Logos
Shaking incubator Innova 42	New Brunswick
Centrifuge Avanti J-26 XP (rotor ID: JA-10)	Beckman Coulter
NanoDrop DS-11 Fx+	DeNovix
Sterile bench Safe2020	ThermoScientific
Shaking incubator Incu-shaker CO_2 mini	Benchmark
Centrifuge Heraeus Megafuge 16 (rotor ID: 75003629)	ThermoScientific
Incubator Heracell 150i	ThermoScientific
Rotator Rotamix RM1	Elmi
Äkta Pure with F9-T fractioner	Cytiva
Äkta Micro with Frac950 fractioner	GE
Äkta Prime Plus	GE
Monolith NT.115	Nanotemper technologies
Shaker MaxQ4450	ThermoScientific
Shaker DOS-10L	neoLab
Roller RM5-30V	CAT
PowerPac HC	BioRad
ScanJet G40I0	HP
Thermocycler PEQStar	Peqlab (VWR)
Shaker KS4000i control	IKA
Pipettes: Transferpette®S (100-1000 µl; 20 - 200 µl; 10 - 100 µl; 5 - 50 µl; 2 - 20 µl; 0.1 -2.5 µl)	Brand
Plasma-surface cleaner Zepto	Diener

Table 9. *Size exclusion columns*

Column	Manufacturer	Reference number	Lot number	Äkta
Analytical Superdex 200 increase 5/150 GL	Cytivia	28990949	10330768	Pure
Analytical Superdex 200 increase 5/150 GL	Cytivia	28990945	10315093	Mikro
Preparative HiLoad™ 16/60 Superdex™ 200 prep grade	GE	17-1069-01	10055421	Prime

Table 10. *Microscopes*

Microscope	Manufacturer	Purpose	Objectives
Eclipse Ts2 (Light microscope)	Nikon	Cell counting, Monitoring of cell vitality and morphology	10x air, 20x air
Eclipse Ts2-fl (Epi-fluorescence microscope)	Nikon	Monitor positive transfected cells	20x air, 40x air
Eclipse Ti2 (wide field)	Nikon	Observation of condensates *in vitro* and optogenetic live cell imaging	60x oil-immersion

SoRa CSU-W1 (spinning disc confocal)	Nikon	Observation of condensates *in vitro* and optogenetic live cell imaging	60x oil-immersion

Table 11. *Software*

Software	Manufacturer
Fusion-FX	Vilber Lourmat
ImageJ	NIH, USA
NIS-Elements	Nikon
Office Professional Plus 2016	Microsoft
Prism 5	Graphpad software, USA
BioRender	BioRender software

Table 12. *Kits*

Kit	Manufacturer	Reference number	Lot number
SulfoLink® Immobilization Kit for Peptides	ThermoScientific	44999	VK314677
NucleoSpin® Gel and PCR Clean Up	Macherey & Nagel	740609.250	2006/006
NucleoSpin plasmid	Macherey & Nagel	740588.250	1907/003
NucleoBond Xtra Maxi	Macherey & Nagel	740414/100	1606/004
Q5 Site directed mutagenesis	NEB	E0554S	10164452
Pierce BCA protein assay kit	ThermoScientific	23225	4G289332
Pierce silverstain kit	ThermoScientific	24612	VA293534
JBScreen Thermofluor Specific	Jena Bioscience	CS-333	JBS00016152
JBScreen Thermofluor Fundament	Jena Bioscience	CS-332	JBS00015823
Kod hot start DNA polymerase	Merck	70086-3	3809401
DyLight™ 488 NHS Ester	ThermoScientific	46403	-

Table 13. *Cell lines*

Cell line	Organism	Manufacturer	Reference
HEK293T	Human	ATCC	-
Expi293F	Human	ThermoFisher Scientific	A14527
Expi293F GNTI-	Human	ThermoFisher Scientific	A39250
HEK293S GNTI-	Human	ATCC	CRL-3022
High5	Insect	-	-
S*f*9	Insect	-	-
N1E-115	Insect	ATCC	CVCL_0451

Table 14. *Antibodies*
WB-western blot; IF- immunofluorescence; IP- immunoprecipitation

Antibody	Host	Manufacturer	Clonality	Reference number	Lot number	Purpose	Dilution
α-PLPPR3	rabbit	in-house made (EuroGentec)	poly	/	/	WB IP IF	1:1000 1:250 1:500
α-M1 Flag	mouse	In-house made	poly	/	/	WB	1:5000
α-His Tag	mouse	Qiagen	poly	34660	/	WB	1:2000
α-DRD2, clone 3D9	mouse	Merck Millipore	mono	MABN53	3728327	WB	1:1000
α-DRD2	rabbit	Merck Millipore	poly	AB5084P	3873403	WB	1:1000
α-DRD2	rabbit	Proteintech	poly	55084-1-AP	/	WB	1:1000
α-PTEN	rabbit	Cell Signalling Technologies	mono	9559L	17	WB	1:1000
α-GFP	rabbit	Invitrogen	poly	A11122	2481666	WB IF	1:1000 1:500
α-GFP	chicken	GTX	poly	13970	/	WB	1:1000
Goat Anti-Rabbit IgG (H+L), Peroxidase	goat	Vector laboratories inc.	poly	PI-1000	ZJ0211	WB 2nd	1:5000
Horse Anti-Mouse IgG (H+L), Peroxidase	horse	Vector laboratories inc.	poly	PI-2000	ZH1027	WB 2nd	1:5000
Peroxidase-conjugated Goat Anti chicken IgY++(IgG (H+L)	Goat	Jackson Immuno Research	poly	103-035-155	109940	WB 2nd	1:5000

3.2 Media, Buffer and Solution

3.2.1 Media

HEK cell medium

DMEM

1% (v/v) Penicillin/Streptavidin

10% (v/v) Fetal Calf serum

Expi cell medium

Expi Expressionmedium

0.1% (v/v) Penicillin/Streptavidin (possible, but mainly used w/o antibiotics)

3.2.2 Buffers and Solutions

Stripping buffer

0.2 M Glycine

0.1% SDS

1% Tween20

In 500 ml ddH$_2$O

pH 2.2

PhosTag Transfer 1x

200 ml Transfer buffer 10x

400 ml MeOH

10 ml SDS 20%

1390 ml ddH$_2$O

PhosTag stacking gel

0.6 ml Acrylamide 30% w/v

1 ml 1.4 M Bis/Tris pH 6.8

2.4 ml ddH2O

0.02 ml 10% APS w/v

0.004 ml TEMED

50µM PhosTag running gel

2.7 mL Acrylamide 30% w/v

2.5 ml 1.4 M Bis/Tris pH 6.8

4.6 ml ddH$_2$O

0.1 ml 5 mM PhosTag with 3% v/v MeOH

0.1 ml 10 mM ZnCl$_2$

0.05 ml 10% APS w/v

0.01 ml TEMED

PhosTag running buffer

300 ml 5x PhosTag running buffer

15 ml NaHSO$_3$ (0.5 mol/l)

1185 ml ddH$_2$O

5x PhosTag running buffer

0.5 mol/l Tris base

0.5 mol/l MOPS

0.5% SDS

in 1 L ddH$_2$O

pH 7.8

Store at 4°C in the dark

50x phosphatase inhibitor

200 mM Sodium orthovanadate

800 mM Sodium molybdate

800 mM Sodium fluoride

1.6 M β-Glycerophosphate

in 10 ml

LB medium

20 g LB Broth

in 1 L ddH$_2$O

autoclave

Kanamycin (30 mg/ml)

300 mg

In 10 ml ddH$_2$O

Goat serum 4%

4 ml Goat serum

96 ml PBS (pH 7.4)

Ammoniumperoxodisulfate 10%

1 g

10 ml ddH2O

Ampicillin (100 mg/ml)

1 g

in 10 ml ddH$_2$O

PBS

1 buffer tablet

in 500 ml ddH$_2$O

pH 7.4

5% Milk TBS-T

10 g milk powder

in 200 ml 1x TBS-T

5% BSA TBS-T

10 g BSA powder

in 200 ml 1x TBS-T

PHEM Buffer

18.14 g PIPES

6.5 g Hepes

3.8 g EGTA

0.99 g $MgSO_4$

pH 7.4 (10 M NaOH or KOH)

fill up to 1 L with ddH_2O

4% PFA/4% Sucrose

Heat 400 ml PBS

20 g PFA

2 drops NaOH

20 g Sucrose

pH 7.5 (HCl)

fill up to 500 ml with ddH_2O

Ponceau-S

0.1% Ponceau-S (w/v) in 5% acetic acid

or

2% Ponceau-S (w/v) in 30% TCA, 30% sulfosalicyclic acid

RIPA Buffer

50 mM Tris pH 7.5

150 mM NaCl

0.5% (w/v) Sodiumdeoxycholate

1% (v/v) NP 40

0.1% (w/v) SDS

pH 7.4

in ddH$_2$O

SDS-Polyacrylamid Gel

4x Proto Gel Run Buffer

1.5 M TRIS/HCl

0.4% (w/v) SDS

pH 8.8 (HCl)

in ddH$_2$O

4x Proto Gel Stacking Buffer

0.5 M TRIS/HCl

0.4% (w/v) SDS

pH 6.8 (NaOH)

in ddH$_2$O

Running gel (10%)

3.96 ml ddH$_2$O

2.5 ml 4x Proto Gel Run Buffer

3.33 ml Acrylamide (Rotiphorese® Gel 30 (37.5:1))

100 µl 10% (w/v) APS

10 µl TEMED

Stacking gel (4%)

2.325 ml ddH2O

937.5 µl 4x Proto Gel Stacking Buffer

487.5 µl Acrylamide (Rotiphorese® Gel 30 (37.5:1))

18.75 µl 10% (w/v) APS

3.75 µl TEMED

1x Running buffer

1800 ml ddH$_2$O

200 ml Rotiphorese 10x SDS-PAGE

10x Transfer buffer

19.3 mM TRIS/HCl

130 mM Glycine

pH 3.0-5.0 (HCl)

1x Transfer buffer

1400 ml ddH$_2$O

400 ml MeOH

200 ml 10x Transfer buffer

10x TBS-T buffer

50 mM TRIS/HCl

150 mM NaCl

0.05% Tween 20

pH 7.4 (NaOH)

1x TBS-T buffer

1800 ml ddH$_2$O

200 ml 10x TBS-T

1x TAE buffer

1800 ml ddH$_2$O

200 ml Rotiphorese 10x TAE

Coating solution 1:50 (for coverslips)

2950 µl PBS

50 µl Poly-L-Ornithine (1.5 mg/ml)

PLPPR3 ICD stock (buffer A)

20 mM Hepes

150 mM NaCl

Filter with 0.22 μm

pH 7.4 (NaOH)

PLPPR3 ICD lysis buffer (buffer B)

20 mM Hepes

150 mM NaCl

1 tablet/10 ml Protease inhibitor, mini (Roche)

2.5 mM $CaCl_2$

Filter with 0.22 μm

pH 7.4 (NaOH)

PLPPR3 ICD wash buffer (buffer C)

20 mM Hepes

150 mM NaCl

2.5 mM $CaCl_2$

Filter with 0.22 μm

pH 6.0 (HCl)

PLPPR3 ICD elution buffer (buffer D)

20 mM Hepes

150 mM NaCl

0.2 mM Flag peptide (DYKDDDDK)

5 mM EDTA

5 mM DTT (in elution tube, not in buffer directly)

Filter with 0.22 μm

pH 6.0 (HCl)

PLPPR3 ICD SEC buffer (buffer E)

20 mM Hepes

150 mM NaCl

5 mM DTT

Filter with 0.22 µm and degassed

pH 6.0 (HCl)

PTEN stock (buffer A.2)

50 mM Tris-HCl

500 mM NaCl

5% Glycerol (v/v)

5 mM β-Mercaptoethanol

1 mM PMSF

Filtered with 0.22 µm

pH 8.0

PTEN lysis and wash buffer (buffer B.2)

50 mM Tris-HCl

500 mM NaCl

5% Glycerol (v/v)

5 mM β-Mercaptoethanol

1 mM PMSF

20 mM Imidazole

Filtered with 0.22 µm

pH 8.0

PTEN elution buffer (buffer C.2)

50 mM Tris-HCl

500 mM NaCl

5% Glycerol (v/v)

5 mM β-Mercaptoethanol

1 mM PMSF

300 mM Imidazole

Filtered with 0.22 μm

pH 8.0

PTEN SEC buffer 1 (buffer D.2)

25 mM Tris-HCl

200 mM NaCl

2 mM TCEP

Filtered with 0.22 μm and degassed

pH 8.0

PTEN SEC buffer 2 (buffer E.2)

20 mM Tris-HCl

150 mM NaCl

5 mM DTT

Filtered with 0.22 μm and degassed

pH 7.5

1% PVA coating solution

1 g PVA

100 ml ddH$_2$O

Heat to 80°C

Stir until dissolved

Filter and store at -20°C

10x F-actin buffer

1 M KCl

20 mM MgCl$_2$

0.1 mM Imidazole

pH 7.4 (NaOH)

Filter and store at -20°C

Add 10 mM fresh ATP (pH 7.0)

10x G-actin buffer

20 mM Tris/HCl

1 mM $CaCl_2 \cdot 2H_2O$

10 mM DTT

pH 8.2 (NaOH)

Filter and store at -20°C

Add 4 mM fresh ATP (pH 7.0)

3.3 Methods

3.3.1 Molecular biology methods

3.3.1.1 Primer design

Primer design and vector card building was performed with the software Lasergene SeqBuider version 7.0.0 (DNAStar). Generally, primers were designed between 20 to 30 bp's length with the required restriction sites according to the construct and a short overlap of the gene of interest. The primers began and ended with a guanine (G) or cytosine (C) for enhanced stability and had a GC-content of around 50 to 60%. Five base pairs were added 5' of the restriction site for efficient restriction. Primers were ordered from Sigma at 0.025 µmol, desalted and dry shipped.

3.3.1.2 Cloning

Cloning was performed in collaboration with Katrin Büttner (AG Eickholt), Willem Bintig (AG Eickholt), Anja Koch and Brian Lally (AG Scheerer, Charite - Universitaetsmedizin Berlin).

In general, we performed a polymerase chain reaction (PCR) using KOD hot start DNA polymerase (Merck) according to protocol. We combined 10 µl 5x KOD buffer, 10 µl dNTPs (2 mM each), 6 µl MgSO$_4$ (25 mM), 3 µl 1:10 forward primer (10 µM), 3 µl 1:10 reverse primer (10 µM), 2 µl 1:100 DNA template (10-20 ng), 2 µl KOD polymerase (1 U/µl) and filled up to 100 µl with ddH$_2$O in a PCR reaction tube. The samples were mixed and distributed on 2 PCR tubes to makes a final of 50 µl per PCR reaction tube. 35 cycles were conducted in the thermocycler PEQStar (Peqlab, VWR) with the following protocol:

Table 15. Touchdown PCR protocol
Denaturation was performed at 95°C and annealing at 63°C temperature. The annealing temperature was lowered by 1°C each cycle for the first 12 cycles until 53°C. Elongation was performed at 70°C. Thereafter, 23 cycles were performed at 53°C annealing temperature. The PCR product was short-term stored at 8°C.

Denaturation	95°C	2:30 min	
Denaturation	95°C	30 s	
Annealing	63°C (-1°C/cycle)	30 s	12x
Elongation	70°C	1 min	
Denaturation	95°C	30 s	
Annealing	53°C	30 s	23x
Elongation	70°C	1 min	
End synthesis	70°C	5 min	
Store	8°C	forever	

PCR products were separated on a 1% agarose gel supplemented with GelRed (1:40.000) with help of the 1kb plus DNA marker (ThermoScientific). The gels were run for 25 min at 120 V in TAE buffer (Roth). Vilber Lourmat System® using UV visualized correct bands. Bands were cut out with a freshly disinfected scapula and DNA fragment purified using NucleoSpin® Gel and PCR Clean Up (Macherey&Nagel). The DNA fragment and DNA backbone were digested with restriction enzymes (ThermoScientific) for 1 hour at 37°C in a 1.5 ml MCT containing 20 µl DNA fragment or 1 µg DNA backbone, 5 µl FD 10x buffer, 1 µl FD enzyme 1, 1 µl FD enzyme 2 and filled up to 50 µl with ddH$_2$O. The reaction was quenched by 10 µl 6x DNA purple loading dye and digested DNA separated on a 1% agarose gel supplemented with GelRed (1:40.000) with help of the 1kb plus DNA marker (ThermoScientific). The gels were run for 25 min at 120 V in 1x TAE buffer (Roth). Vilber Lourmat System® using UV visualized correct band sizes, which were cut out and purified.

DNA insert and DNA backbone were combined in a 1:3 ratio (v/v) with 2 µl 10x T4 Ligation buffer and 2 µl T4 Ligase (NEB), filled up to 20 µl with ddH$_2$O and incubated

at 37°C for 1 hour or alternatively at RT for 5 hours. Entire 20 µl ligation mix was transformed in 100 µl chemically competent NEB stable bacteria. In brief, competent cell were thawed on ice for 15 min, ligation mix added and gently swirled and incubated for 25-30 min on ice. Thereafter, a heat shock was performed at 42°C for 45 s and cells cooled for 2 min on ice. 500 µl SOC medium (NEB) were added to the cell mix and incubated for 1 hour at 37°C, while shaking at 800 rpm. The ligation mix was gently spread on an antibiotic-resistant (Ampicillin or Kanamycin) agar plate under sterile conditions (Bunsen burner). The plate was incubated 16-18 hours at 37°C.

Positive colonies were inoculated in 5 ml LB medium with antibiotic (1 µg/µl). Mini preparations were incubated for 16-18 hours at 37°C, shaking at 180 rpm. The DNA was isolated using NucleoSpin plasmid kit (Macherey&Nagel). DNA was test digested like mentioned earlier, to ensure correct ligation of insert. Correct clones were sent for sequencing (see 3.3.1.3). Positively sequenced clones were re-transformed and spread on antibiotic-containing agar selection plates. A single colony was used to inoculate 300 ml LB medium, in a 1 L flask containing 1 µg/µl antibiotics. The maxi preparation was incubated for 16-18 hours at 37°C, shaking at 180 rpm and the DNA isolated with NucleoBond Xtra Maxi kit (Macherey&Nagel) and stored at -20°C.

Anja Koch and Brian Lally cloned expression constructs with help of Gibson Assembly® Master Mix (NEB) and self-designed building blocks.

3.3.1.3 Sequencing

For sequencing, 1 µg plasmid DNA was diluted in 12 µl ddH$_2$O and combined with 2 µl of a 1:10 sequencing primer dilution (10 µM) in a 1.5 ml MCT. Samples were sequenced by services of LGC Genomics (Berlin).

Results were downloaded as sequencing files (.ab) from the LGC website directly and analysis performed with the software Lasergene SeqMan 7.0.0 (DNAStar) using the build vector cards of the construct as comparison.

3.3.2 Biochemical methods

3.3.2.1 Cell culture

HEK293T and N1E-115 cells

Our technicians Kerstin Schlawe or Kristin Lehmann performed sub culturing twice a week. In brief, trypsin and DMEM containing 10% FBS and 1% P/S (DMEM++) was pre-warmed at 37°C in a water bath. Cell medium was aspirated and cells were washed once with RT PBS. PBS was aspirated and 2 ml trypsin added to the flask. Trypsin was incubated 2-3 min at RT and stopped by adding 8 ml of DMEM++. The cell suspension was transferred into a 15 ml Falcon tube and centrifuged 5 min at 800x g at RT. The supernatant was aspirated and cells resuspended with 5-10 ml of fresh DMEM++. The new passage was seeded 1:10 in a fresh 75cm^3 flask and incubated at 37°C, 5% CO_2 and 80% rH.

Expi293F cells

Sub culturing of Expi293F cells was done twice a week. Cells were counted using a BioRad cell counter. 20 µl of cell suspension was transferred into a 0.5 ml MCT. 10 µl cell suspension were mixed with 10 µl trypan blue and 10 µl of the mixture was pipetted into a BioRad counting slide. After determination of live cells and viability > 98%, cells were seeded with 0.5 x 10^6 cells/ml in 30 ml pre-warmed Expi293 expression medium in a sterile 200 ml glass Erlenmeyer flask and incubated at 37°C, 8% CO_2, 80% rH and 125 rpm shaking. Upscaling was performed linear up to 120 ml.

For protein overexpression, the cell density was determined as described previously. In general, 75 x 10^6 cells per 30 ml expression culture were seeded in a new 200 ml Erleyenmeyer flask. Cells were transfected with Expifectamine transfection kit (ThermoScientific) or PEI Max, linear (Gibco). For transfection, 30 µg DNA per 30 ml expression culture were diluted in 1.5 ml OptiMem, as well as 81 µl Expifectamine (1 mg/ml) or PEI Max (1 mg/ml) in 1.5 ml OptiMem. Both were incubated 5 min at RT and then added together. After 25 min of incubation at RT the transfection mix was pipetted into 30 ml cell suspension. For Expifectamine transfected cells, 1.5 ml enhancer 1 and 150 µl enhancer 2 per 30 ml culture were mixed together and added exactly 19.5 h post transfection. Cells were incubated 96 hours at 37°C, 8% CO2, 80% rH and 125 rpm

shaking. Cells or medium, depending on the transfected construct were harvested by centrifugation at 4000x g for 5 min at RT. The harvested samples were snap frozen in $N_{2(l.)}$.

Expi293F GNTI⁻ cells

Anja Koch (AG Scheerer, Charité - Universitaetsmedizin Berlin) performed routine sub-culturing of Expi293F GNTI⁻ cells, seeding, transfection and harvesting of expression constructs, however similar sub culturing routines were used to Expi293F cells.

3.3.2.2 Seeding and Transfection of adherent cells

Cells were seeded on poly-L-ornithine coated coverslips. For coating, Poly-L-ornithine (1.5 mg/ml) was diluted 1:50 in PBS to a final concentration of 30 µg/ml. A small cell culture dish was laid out with parafilm and single cover slips (Ø 18 mm or Ø 30 mm) were placed on top. 100 µl PLO solution was pipetted on each coverslip and covered with a coverslip of same size. The coverslips were allowed to incubate for minimum 1 hour at 37°C, 5% CO2 and 80% rH. After, the coverslips were placed into the respective cell culture well plates and washed three times with PBS. The plates were kept up to 1 week under sterile conditions at 4°C.

Cells were seeded with densities of 0.08×10^6 cells/well for live cell imaging in glass bottom four well IBIDI dishes, 0.3×10^6 cells/well for co-immunoprecipitation in 6 well plates and 0.15×10^6 cells/well in 12 well plates. The respective number of cells was diluted in DMEM medium supplemented with 10% FBS and 1% P/S. The cells were left to adhere for 24 hours at 37°C, 5% CO2 and 80% rH.

For transfection of adherent cells, we used Lipofectamin2000 (Invitrogen). In general, per well 1 µg DNA was diluted in 100 µl well OptiMem (Gibco) as well as 3 µl Lipofectamin2000 (1 mg/ml) in 100 µl OptiMem and separately incubated for 5 min at RT. DNA mixture was added to the Lipofectamin mixture and incubated for 10 min in a 37°C tempered water bath. The transfection mixture was added dropwise on the cells. After 5 hours, the medium was changed fully into DMEM medium supplemented with 10% FBS and 1% P/S.

3.3.2.3 Cell lysate

One day post-transfection, cell medium was aspirated and washed one time with ice cold PBS to remove any residual medium. RIPA buffer supplemented with 1:50 phosphatase inhibitor (in-house prepared), 1:100 protease inhibitor cocktail set III (Merck) and 1:100 cantharidin (Roth) was cooled on ice and 200 µl per well (6 well) added. Using a cell scraper, cells were detached and transferred into a fresh 1.5 ml MCT. Cell suspension was overhead rotated at 13 rpm, 4°C for 20 min and centrifuged at 21.000x g, 4°C for 20 min. The supernatant was transferred into a fresh 1.5 ml MCT, 4x Laemmli buffer added, boiled for 5 min at 95°C and stored at -20°C.

3.3.2.4 SDS-PAGE

Protein samples were thawed and mixed by vortexing. Separation was performed by 4% stacking and 10% running SDS gel (Laemmli, 1970). Gels were prepared in the Mini Trans-Blot® Cell from BioRad. 3 µl PageRuler™ Plus Prestained Protein ladder was pipetted into the first well and 15-30 µl sample in the following wells. Gels were run at 80 V constant for 20 min (in the stacking gel). Subsequently, the voltage was increased to 120 V for 1.5 hours until the running front was at the bottom. After the casket was dismantled, the gel was washed one time with ddH$_2$O and stained with coomassie (Serva) for 1-2 hours. Destaining was performed with ddH2O, until the background was transparent.

3.3.2.5 Western Blot

For western blots, SDS-Gels were washed with ddH$_2$O and equilibrated in 1x Transfer buffer. Blotting was performed on supported Nitrocellulose (BioRad) or where indicated on PVDF (ThermoFisher) with 30 seconds of 100% Methanol activation. The Mini Trans Blot® Cell from BioRad was used to perform wet transfer at 0.4 A for 2 hours in a box surrounded by ice to reduce heat. Positive transfer was monitored with Ponceau-S for 1 minute. The diazo dye was reversibly washed off with ddH$_2$O and 1x TBST.

3.3.2.6 PhosTag Gel

Zinc PhosTag™ Gels (50 µM) were used to identify the phosphorylation state of purified proteins and cell lysates. 8% PhosTag gel, were cast in the BioRad systems similar to an SDS-PAGE (see 3.3.2.4) with the following solutions:

Table 16. *50 µM PhosTag™ Gel with zinc chloride*

Running Gel (50 µM PhosTag)	Stacking Gel
2.7 mL Acrylamide 30% w/v	0.6 ml Acrylamide 30% w/v
2.5 ml 1.4 M Bis/Tris pH 6.8	1 ml 1.4 M Bis/Tris pH 6.8
4.6 ml ddH$_2$O	2.4 ml ddH2O
0.1 ml 5 mM PhosTag with 3% v/v MeOH	-
0.1 ml 10 mM ZnCl$_2$	-
0.05 ml 10% APS w/v	0.02 ml 10% APS w/v
0.01 ml TEMED	0.004 ml TEMED

Stacking and running gel were polymerised for 1 hour at RT. Gels were freshly used or stored for maximum 1 day in moist paper at 4°C. The gels were fixed into the Mini Trans-Blot® Cell from BioRad and PhosTag running buffer added. The samples were run at 0.03 A constant for 2.5 hours. The gel was washed with ddH$_2$O and three times 5 to 10 min with 1x transfer buffer containing 1 mM EDTA to eliminate zinc ions from the gel.

Proteins were blotted on PVDF membranes with wet electro blotting method. The membrane was activated with 100% MeOH for 15 s. The transfer chamber was filled with 1x PhosTag transfer buffer, put into an icebox and proteins were blotted for 2.5 hours at 0.35 A constant. The membrane was washed with ddH$_2$O. Ponceau-S was used to monitor positive transfer and washed off with ddH$_2$O and 1x TBST. Blocking was performed with 5% milk in TBST for 1 hour at RT under light agitation. The primary PLPPR3 antibody was added 1:1000 in 5 ml 5% milk TBST and incubated o.n. at 4°C on a roller. The following day, the membrane was washed four times 5 to 10 min with 1x TBST at RT. The secondary anti-rabbit[HRP] coupled antibody was added 1:5000 in 5% milk TBST for 1 hour at RT. The membrane was washed four times 5 to 10 min with 1x TBST at RT and the specific phosphorylation states detected via immune detection.

3.3.2.7 Immunodetection

The membrane was blocked with 5% skimmed milk in TBS-T for 1 hour. The milk was discarded and replaced by fresh milk i the primary antibody (for dilution see Table 14.).

The membrane was incubated overnight at + 4°C on a roller in a 50 ml Falcon tube. The following day the membrane was washed four times 5 minutes with 1x TBS-T. The secondary horseradish peroxidase (HRP) coupled antibody (Table 14.) was applied in 5% skimmed milk TBS-T for 1 hour at RT. After incubation, the milk was discarded and the membrane washed four times 5 minutes. The immunoreaction was started by ECL western blot substrate with luminol and H_2O_2 in a ratio 1:1. After application on the membrane, the solution was incubated 1 minute at RT before manual exposure and detection with Vilber Lourmat System® using chemiluminescence detection.

3.3.2.8 Immunochemistry

Cells were fixed one day post transfection with 500 µl 4% Paraformaldehyde/4% sucrose in PHEM buffer per well. The cell culture medium was aspirated, washed once with PBS at RT and PFA added to the cells. After 15-20 min of incubation at RT, PFA was aspirated and the cells washed four times 5 min with PHEM buffer. The cells were permeabilised with 0.01% Triton-X 100 in PHEM buffer for 1 hour at RT, washed three times for 5 min and blocked 1 hour with 0.1% goat-serum in PHEM at RT. A light-proof dish was coated with parafilm and primary antibodies applied to each coverslip in the required dilution in blocking buffer o.n. at 4°C.

The following day, the cells were washed four times 5 min with PHEM buffer. Secondary antibodies were centrifuged 15 min at 21.000x g at 4°C and applied in the required dilution (Table 14) in blocking buffer onto the cells and incubated for 1 hour at RT. Cells were washed four times 5 min with PHEM buffer. In the last washing step, HOECHST dye was applied 1:10.000 to stain the nuclei. Coverslips were mounted on glass slides with 15 µl Prolong™ Gold antifade reagent. Samples were stored in a sample holder at + 4°C.

3.3.2.9 Purification of PLPPR3 Intracellular domain from medium

Buffer A (20 mM Hepes, 150 mM NaCl pH 7.4) was prepared and filtered through a 0.22 µm membrane. Lysis buffer (buffer B) was prepared by adding 2.5 mM $CaCl_2$ and 1 tablet of Protease inhibitor (Roche) per 10 ml to buffer A. Buffer B was used to equilibrate M1 Flag sepharose beads. In brief, 700 µl beads slurry were transferred into a

fresh MCT and 1 ml of buffer B added. Beads were gently mixed by inverting and centrifuged at 500x g for 3 min at 4°C. Supernatant was removed and 1 ml fresh buffer B added, gently mixed and centrifuged again. The steps were repeated three times in total. For the last step, the supernatant was left on the beads until further use.

PLPPR3 ICD-containing medium was defrosted swiftly in a 37°C tempered water bath, until only some ice was left. The 50 ml Falcon tube was put on ice and 2.5 mM $CaCl_2$ added directly into the medium. Supernatant of beads was carefully removed and beads were added into medium. The tube lid was sealed with parafilm and overhead rotated at 14 rpm, 2h at 4°C in the cold room.

Buffer C was prepared by adding 2.5 mM $CaCl_2$ and re-titrating pH to 6.0 using buffer A as stock. In addition, buffer D was prepared from buffer A by adding 2 mM Flag peptide and 5 mM EDTA. Thereafter, a 2 ml gravity flow column was equilibrated with ddH_2O and buffer B, before the beads containing medium was applied. The flow through was collected and the beads washed three times 10 ml with buffer C. The protein was eluted with 3 ml buffer D for 30 min with top and bottom lid closed. Eluate was collected per gravity flow into a 5 ml MCT that contained 15 µl DTT (5 mM final) and mixed gently.

Eluted protein was filtered with 0.22 µm spin-filters at 14.000 rpm and 4°C for 3 min to remove aggregates. A 15 ml amicon concentrator (30 kDa MWCO) was equilibrated with 3 ml ddH_2O and 3 ml buffer D and centrifuged at 4000x g and 4°C for 3 min. The eluate was transferred into the concentrator and centrifuged at 5000x g and 4°C until 50 µl was reached.

Äkta pure was prepared by equilibration of superdex 200 increase 5/150 GL column into degassed buffer E (20 mM Hepes, 150 mM NaCl, 5 mM DTT pH 6.0) with a flow speed of 0.15 ml/min. The 50 µl sample loop was equilibrated with buffer E and the protein transferred. The size exclusion method "SEC test" was run using a flow speed of 0.15 ml/min in down flow with a pre-column pressure of 3.0 MPa and auto zero UV. Fractionation was done in a 96 well plate with 100 µl sample size. The fractions that contain PLPPR3 ICD were pooled and concentrated with a 0.5 ml concentrator (30 MWCO). After the concentration was determined with a nanodrop, the protein was aliquoted and flash frozen in $N_{2(L.)}$ and stored at -80°C.

3.3.2.10 *In vitro* protein labeling

PLPPR3 ICD was labelled fluorescently with DyLight® 488 NHS Ester Dye (ThermoScientific), as specified in the product instructions. 500 µl of freshly purified PLPPR3 ICD in a buffer of 20 mM Hepes, 150 mM NaCl pH 6.0 (1-2 mg/ml) was added to the vial containing the dye and incubated for 1 hour at RT. Excess dye was removed with a dialyzer tube (Merck), with a cut-off of 12-14 kDa in a buffer of 20 mM Hepes, 150 mM NaCl, 5 mM DTT pH 6.0 overnight at 4°C, with slow stirring. The first exchange of buffer was done after 1 hour. The next day, protein concentration and degree of labelling were determined using a nanodrop to measure absorption at A_{280} and A_{493}, as recommended by the manufacturer. PLPPR3 ICD 488 was aliquoted, snap frozen and stored at -80°C.

3.3.3.11 *In vitro* PLPPR3 ICD condensate formation

Condensates of PLPPR3 ICD were formed *in vitro* with purified protein and polyethylene glycol 8000 (PEG8000) as crowding reagent. In brief, buffer E (20 mM Hepes, 150 mM NaCl, 5 mM DTT pH 6.0) was combined with 1 µg/µl (20 µM) PLPPR3 ICD and PEG8000 (Merck) in a 0.5 ml micro centrifugal tube to 4 µl, mixed thoroughly and a 2.5 µl droplet pipetted on an imaging dish (Miltenyi Biotec) coated with 1% polyvinyl alcohol (Sigma). To prevent evaporation, the outer lining of the imaging dish was draped with a moist tissue and the lid closed. 5-6 drops were imaged on one imaging dish with a 60x oil-immersion objective on SoRa spinning disc confocal (Nikon).

3.3.2.12 SILAC

A fresh batch of HEK239T cells was thawed swiftly at 37°C, sterilized and added into 10 ml of DMEM with 10% FBS and 1% P/S. Cells were passaged and seeded into two separate 25 cm^3 flasks termed "light" and "heavy". The "light" flasks contained the normal isotopes of lysine and arginine, while the "heavy" flask contained the heavy ^{13}C and ^{15}N isotopes of ^{8}lysine (^{13}C$_6$H$_{14}$^{15}N$_2$O$_2$) and ^{10}arginine (^{13}C$_6$H$_{14}$^{15}N$_4$O$_2$) which shifts mass of 8 for lysine and 10 for arginine (Silantes, 282986444). The cells were passaged 6-8 times to ensure full incorporation of the "light" or "heavy" amino acids.

For expression, 4 x 75 cm^3 flasks were seeded with 10 x 10^6 cells and transfected after 24 hours with HA-M1-PLPPR3 ICD-His in a pCAX backbone. Thereby, DNA to PEI ratio was 1:3 per flask. 30 µg DNA in 1 ml OptiMem and 90 µl PEI (1 mg/ml) in 1 ml OptiMem were incubated separately a RT and mixed after 5 min. After 25 min incubation the transfection mix was added gently to the cells and the medium fully changed 5 h later. Cells were incubated at 37°C, 5% CO$_2$ and 80% rH. The medium was collected after 2-3 days post transfection and snap frozen at -80°C. Purification of SILAC samples was performed like mentioned previously in section 3.3.2.9.

3.3.2.13 Crosslinking of PLPPR3 ICD

Crosslinking of PLPPR3 ICD was performed using either DSS (ThermoScientific) or BS3 (ThermoScientific). In general, 20 µM PLPPR3 ICD were combined with or without 5% PEG and incubated 30 min at RT. Samples were crosslinked with 0.5 mM DSS final concentration for 30 min at RT and quenched with 50 mM Tris/HCl final concentration. The samples were reduced with 25 mM DTT (final concentration) for 30 min at 55°C and after cooling down, alkylated with 40 mM CAA final concentration 30 min in the dark. As final step samples were denatured with 4x Roti-Load, boiled 10 min at 95°C and stored at -20°C.

Crosslinked samples were run on a fresh 10% SDS-Gel at 80 V for 20 min in the stacking gel and 120 V in the running gel until the bromophenol band reached the bottom. The gel was stained with Coomassie (Serva) o.n. and destained with water for several hours. After documentation using a scanning device, crosslinked bands were cut out and stored at + 4°C in 0.5 ml MCTs with 200 µl fresh ddH$_2$O. The samples were processed and analyzed further by Heike Stephanowitz and Max Ruwolt from the Liu Lab (FMP Berlin).

3.3.2.14 Limited Proteolytic digest

For each reaction, 8.4 µM PLPPR3 ICD was combined with 16.8 µM trypsin (Gibco) (1:2) in a total volume of 25 µl. Samples were incubated at 22°C for 0, 2, 5, 10, 30 and 60 min. As setup control, 8.4 µM PLPPR3 ICD was united with PBS and likewise incubated for 60 min at 22°C, while 8.4 µl PLPPR3 ICD was used as positive control. Subsequently, 4x Roti-Load was added and all samples were boiled for 5 min at 95°C. A

volume of 20 µl from each sample was loaded onto a 10% SDS-gel. The gel was run at 80 V for 20 minutes and then increased to 120 V, until loading dye reached the bottom of the gel. The Gel was washed once with ddH_2O and stained with coomassie (Serva). Destaining was performed with ddH_2O.

3.3.2.15 Forming Giant Unilamellar Vesicles (GUVs)

Giant unilamellar vesicles (GUVs) were created using various lipid mixtures. GUVs had a composition of 90 mol% POPC, 10 mol% POPS and 0.4 mol% DilC18. Variation in POPS ranging from 5-20mol% and 5-20 mol% NTA moiety are indicated. Two methods were used to generate GUVs, of which electro formation was performed for sensitive experiments. Sucrose and glucose solutions were measured with an Osmometer (Osmomat 3000 basic/Gonotech) to determine Osmolality.

Polyvinyl alcohol (PVA) method

A silicon spacer was used to mark an area on a 24 mm x 32 mm coverslip. The coverslip was turned around and 1 µl of a 1% PVA stock evenly spread with a pipet tip. The coverslip was dried 15 min at 65°C on a heating block. A Hamilton syringe was washed with chloroform under a hood and 1 µl phospholipid mix evenly spread with the cannula of the syringe. The lipid film was dried several minutes at RT. A silicon spacer was placed 45° angled on the coverslip and gently pressed down with a pipet tip. The lipid film was monitored under a confocal microscope to observe the lipid layers. 150 µl sucrose (380 mOsmol/Kg) was added on to the lipid film. A smaller 21 mm x 26 mm coverslip was placed on the silicon spacer to seal off the chamber. After 20 min of incubation, GUVs were washed off the film and transferred into a fresh MCT. A 1:10 dilution with glucose (420 mOsmol/Kg) was used to sediment GUVs and observe their quality. PVA created GUVs were used for testing and *in vitro* assays.

Electro formation method

ITO plates were washed with 70% EtOH. Next, ITO plates as well as a Hamilton syringe and all glassware in contact with lipids were washed with Chloroform under a hood. The

Hamilton syringe was used to take up 5 µl of a phosphor-lipid stock solution (4 mM) and pipetted on the marked area on the plates. The cannula of the syringe was used to slowly and evenly spread the mixture. After drying of the lipid film, it was observed under a confocal microscope, to quality check the layers. Samples were heated to 30°C, a signal generator was set to 10 Hz, and 3.5 V. ITO plates were built together using spacers to generate a chamber in between and sealed off with clamps on the side. 1.8 ml of sucrose (380 mOsmol/Kg) was added into the chamber, an alligator clip added to each contact side and the generator started. GUVs were electroformed 1-2 hours and after washed off the ITO plates into a fresh MCT. To check GUV quality, GUVs were sedimented 1:10 (90 µl glucose with 10 µl GUV) using 420 mOsmol/Kg glucose solution and monitored under a confocal microscope. Subsequently, all electroformed GUVs were sedimented o.n. at RT, the excess liquid removed and used for in vitro assays up to several days.

3.3.2.16 *In vitro* actin assay

In vitro actin assays were performed with a mixture of rabbit skeletal muscle alpha-actin (Hypermol) with 5% atto647-actin (Hypermol). After rehydration according to the manufacturer's instructions, G-actin was centrifuged at 100.000x g for 1 h and 4°C to sediment all potential actin seeds. In general, 1.2 µM total actin was used in combination with 20 µM PLPPR3 ICD (3% labelled PLPPR3 ICD-488) and F-actin buffer (Hypermol) containing 1 mM ATP. For several actin assays, I utilized various actin concentrations ranging from 1.2 to 4.4 µM actin. Condensate formation was initiated by 5% PEG, the solution mixed thoroughly and 2.5 µl pipetted on a 1% PVA coated imaging dish (Miltenyi biotec). The dishes were plasma cleaned prior to PVA treatment for 5 min at 40% power. Imaging was performed with a 60x oil-immersion objective on SoRa spinning disc confocal (Nikon) with 488 nm and 647 nm lasers (both 5-10%) and 100-200 ms exposure.

3.3.3 Biophysical methods

3.3.3.1 Fluorescence recovery after photo bleaching

Fluorescence recovery after photo bleaching (FRAP) was performed to monitor the molecular dynamics of PLPPR3 ICD condensates. A mixture of 20 µM PLPPR3 ICD

with 3% labelled PLPPR3 ICD 488 was combined with 5% PEG8000 (w/v) and buffer E (20 mM Hepes, 150 mM NaCl, 5 mM DTT pH 6.0) to a total volume of 4 µl. The reaction was mixed thoroughly and 2.5 µl pipetted on a freshly PVA coated imaging dish (Miltenyi Biotec) with draped moist tissue. FRAP was done on a SoRa spinning disc (Nikon) with 60x oil immersion objective. A roi of the same size was defined for stimulation, background and reference. Stimulation was done at 2 min, 15 min, 30 min and 60 min with a FRAP loop of 2 s pre-bleach, 2 s stimulation with 488 laser at 70-100% and post-bleach imaging for 240-300s (1 frame/s). Bleaching was performed either of the entire condensate or a partial bleach in a defined area within the droplet.

Data processing was done with Fiji ImageJ (1.51n).

3.3.3.2 Thermostability

Thermostability measurements were performed with nanoDSF of Nanotemper. I used 20 µM PLPPR3 ICD diluted in buffer E (20 mM Hepes, 150 mM NaCl, 5 mM DTT pH 6.0) to monitor unfolding. As positive control, I used Bovine Serum Albumin (BSA) at 50 µM diluted in buffer E, while buffer E served as negative control. Before performing measurements, I generated pre-scans of PLPPR3 ICD (500 counts) and BSA (3500 counts) to observe fluorescence. For measurement I loaded standard capillaries with BSA (3x), buffer E (3x) and with PLPPR3 ICD (4x) and used three independently expressed and purified PLPPR3 ICD batches. The proteins were heated from 20°C to 90°C with an increase in 1°C per min. Melting curves were generated by observing the 330 nm to 350 nm (tryptophan and tyrosine absorbance) ratio in relation to increasing temperature. The integrated software by Nanotemper calculated the first derivative of the ratio, resulting in a peak that corresponds to the melting temperature Tm.

3.3.3.3 Circular Dichroism (CD)

CD Spectroscopy (Jasco 5-720) was conducted under guidance of Heike Nikolenko (AG Lange) at Leibnitz institute of Pharmacology (FMP) Berlin. PLPPR3 ICD was freshly purified in a buffer containing 20 mM phosphate buffer, 150 mM NaF and 1 mM DTT at pH 6.0. Additionally, I purified a sample with low NaF concentration (20 mM) to check for increased secondary structure elements due to condensate formation. The peak

fractions were combined and diluted to 5 µM in a volume of 500 µl. We performed a baseline scan of the device against air, then against air with the cuvette and thirdly with 150 mM NaF buffer.

Table 17. *CD spectra parameter*

Parameter	Instrument: Jasco J-720
Sensitivity [mdeg]	Standard [mdeg]
Start	260
End	180-195 (depending on sample)
Data Pitch	0.1
Scanning mode	Continuous
Scanning speed	100
Response	1.0
Band width [nm]	1.0
Cell length [cm]	0.1
Concentration [M]	5×10^{-6}
Accumulation	15

All measurements were performed at RT with 200 µl PLPPR3 ICD in a cuvette that was washed thoroughly with ddH$_2$O, flushed with MeOH and dried with N$_2$ gas. We used scanning parameters listed in table 17 and started at 260 nm until we reached 180 nm or until the high-tension measurements reached 800 V, to prevent damage to the photomultiplier.

Data analysis was performed in collaboration with Heike Nikolenko. We subtracted the baseline and calculated the molar ellipcity. To normalize the data, we used the number of residues (455) to calculate the molar ellipcity per residue. For spectra comparison, we introduced a data cut and reduced the spectra to 1 nm data points. Our spectra were compared, using the software CDNN (Applied Photophysics Ltd) to 35 standard spectra to estimate secondary structure elements. CDNN analyzes data to determine helix, anti and parallel β-structure, turns and coils.

3.3.3.4 Mass spectrometry

The following protocol was performed in collaborative effort with Manuela Staeber (MPI) and Kathrin Textoris-Taube from our high throughput mass spectrometry facility (HTMS) at Charité Universitaetsmedizin Berlin.

Following excision from the SDS-Gel, gel pieces were digested with trypsin for identification and relative quantification (Lehmann et al., 2010). The resulting peptides were analyzed by liquid-chromatography in combination with tandem mass spectrometry analysis (LC-MS/MS) with a Q Exactive Plus mass spectrometer (Thermo Fisher Scientific, Bremen, Germany). Fractionation was performed with a two-linear column system Ultimate 3000 RSLCnano (Thermo Fisher Scientific). A trapping guard column (PepMap C18, 5 mm x 300 μm x 5 μm, 100Å, Thermo Fisher Scientific) was utilized to concentrate digested peptides and elute with an analytical 75 μm i.d. × 250mm nano LC column (Acclaim PepMap C18, 2 μm; 100 Å; Thermo Fisher Scientific) by using a mobile phase from 0.1% formic acid (FA, Buffer msA) to 80% acetonitrile with 0.1% FA (Buffer msB). Additionally, a linear gradient from 8 to 28% of buffer msB was applied for 60 min at a flow rate of 300 nL /min. For automatic transition between full MS scan and MS/MS acquisition, the Q exactive instrument was run in data dependent mode. The Orbitrap utilized survey full scan MS spectra (m/z 350 – 1650) with a resolution of 70.000 resolution (m/z 200). The ions were accumulated for 50 ms to a target of $3 \cdot 10^6$ target value, while the dynamic exclusion was 10 s. Sequential, the highest ten abundant multiply charged ions ($z \geq 2$) were separated and fragmented further. This was performed using higher-energy collisional dissociation (HCD) with 100 ms injection time, 17.500 resolution and AGC of $5 \cdot 10^4$. The following conditions have been used during the run: no sheath and auxiliary gas flow; spray voltage, 2.1 kV; heated capillary temperature, 275 °C; normalized HCD collision energy 27%. The lock mass of the background ion was m/z 445.1200.

Relative label free protein identification was done by using the software MaxQuant version 1.6.0.1 with default Andromeda LFQ parameter (Cox et al., 2014). The spectra were compared to mouse (*mus musculus*) data base (17.040 entires - uniprot.org) as well as a decoy and contaminates data base. Several criteria were introduced for MS/MS spectra: A precursor mass tolerance of 10 ppm, fragment tolerance of 0.5 Da, trypsin specificity with a maximum of 2 missed cleavages, cysteine carbamidomethylation set as fixed and methionine oxidation as variable modification. Filtering of data was performed with a False Discovery Rate (FDR) of 1%

3.3.3.7 Phospho-masspectrometry and Interactome of PLPPR3 ICD

All following steps of our interactome study of PLPPR3 were done in collaboration with Marie-Luise Kirchner (AG Mertins, Berlin institute of health).

The eluates from M1 Flag pulldowns were firstly diluted 1:4 in a urea buffer (6 M urea, 2 M thiourea, 10 mM Hepes, and pH 8.0), secondly reduced with 12 mM DTT for 30 min at RT and thirdly alkylated with 40 mM CAA for 20 min at RT. Following a digest with 1 µg endopeptidase LysC (Wako) and 1 µg trypsin (Promega) overnight, the digest was quenched by adding 10% trifluoroacetic acid. Using a StageTip protocol, the peptides were extracted utilizing two packed disks of Empore 3M C18 material in 20 µl pipette tips (Rappsilber et al., 2003). The tips were equilibrated with 50 µl MeOH and washed with 100 µl buffer A (3% Acetonitrile (ACN), 0.1 % formic acid (FA)). After loading, the peptides were washed twice with 100 µl buffer A to remove any remaining salts.

60 µl of Buffer B (80% Acetonitrile and 0.1% formic acid) was used to elute peptides from StageTips. A speedvac (Eppendorf) was utilized to remove the organic solvent, the samples resolved in Buffer A and separated on a reversed-phase column (20 cm fritless silica microcolumns with an inner diameter of 75 µm, packed with ReproSil-Pur C18-AQ 1.9 µm resin (Dr. Maisch GmbH)). Separation was performed with help of a 90 min gradient with a 250 nl/min flow rate of increased Buffer B concentration (from 2% to 60%) on a High-Performance Liquid Chromatography (HPLC) system (ThermoScientific).

The samples were ionized with electrospray ionization (ESI) (ThermoScientific) and analyzed by an Orbitrap Q Exactive Plus instrument (ThermoScientific), with the spectrometer running in a data dependent mode. The Orbitrap full scan had the following parameter 70K resolution, $3 \cdot 10^6$ ion count target and maximum injection time 50 ms, followed by top 10 MS2 scans using higher-energy collision dissociation (17.500 resolution; $1 \cdot 10^5$ ion count target; 1.6 m/z isolation window; maximum injection time: 250 ms). Precursors for MS2 had minimum charge state of 2 up to 7, while the dynamic exclusion rate was fixed to 30 s with a tolerance of 10 ppm and respective isotopes. After each run, blank injections were performed to randomize the acquisition queue.

For data analysis, the raw data were analyzed utilizing MaxQuant software package (version 1.6.3.4; Max Planck Institute of Biochemistry, Martinsried, Germany), plus the human uniprot database (2020-06) as decoy, as well as mouse uniprot database (2019-06)

for variable modifications of oxidation (M), N-terminal acetylation, deamidation (N, Q), phosphorylation (STY) and fixed modification of carbamidomethyl cysteines. A FDR of 1% was used and unique and razor peptides were taking into account for quantification, while label-free quantification (LFQ) and "match between runs" were used. The MaxQuant score was set to 40, to identify confident phosphor-peptides and MS2 spectra exported with MaxQuant Viewer. Perseus software (version 1.6.2.1) was utilized to analyze data statistically. Each biological replicate was defined as group and filtered for a minimum intensity value of 3 in minimum one group. Missing values after log2 transformation were extrapolated with random noise simulating the detection limit of the mass spectrometer. The extrapolated values were log normal distributed with 0.3 x the standard deviation of the measured, logarithmic values, down-shifted by 1.8 standard deviations. Using a two-sample Student's t-test, discrepancies between groups were analyzed, while with help of permutation-based methods and significance cut-offs (0.05 or 0.01), p-values were modified.

4 Results

PLPPR3 is a transmembrane protein with six transmembrane and a long intracellular domain. Like the other four PLPPR family members, detailed structural information of PLPPR3 is currently not available. Structure information can have a major impact on understanding the function of a protein. At a basic level, function is governed by structure and, therefore unsurprisingly, structure aids the interaction of ligands to perform a certain task (Barber & Stark, 2014).

In order to gain understanding into the structure of PLPPR3, I collaborated with the groups of Dr. Patrick Scheerer and Prof. Christian Spahn (Institute of medical Biophysics (IMBP) – Charité - Universitaets-medizin Berlin). I used various expression cell lines and established purification pipelines that would allow me to investigate the PLPPR3 structure by Cryogenic Electron microscopy (Cryo-EM). Preliminary data in our laboratory has demonstrated, that PLPPR3 (74 kDa) can form homo-multimers of roughly 300 kDa size (Fatih Ipek, PhD Thesis 2022). Cryo-EM was the best fitting method for both, monomer PLPPR3 and PLPPR3 complex (Herzik et al., 2019). While the protein complex was too large for nuclear magnetic resonance (NMR) (H. Yu, 1999), PLPPR3 intracellular domain (ICD) was too flexible to crystallize for X-ray crystallography (Smyth & Martin, 2000). I aimed to purify PLPPR3, as well as the transmembrane domains and the intracellular domain. However, due to low expression and aggregation of PLPPR3 full-length and transmembrane domain fusion protein (Appendix), I first established a purification pipeline for PLPPR3 ICD (Chapter 1). During my studies, I identified the 'high disordered' state of PLPPR3 ICD (Chapter 2), which impacted structural characterization. Because intrinsically disordered regions (IDRs), often induce phase separation, I began by analyzing liquid-liquid-phase separation (LLPS) of PLPPR3 ICD in cells and *in vitro* (Chapter 3). Finally, I tested the potential involvement of LLPS in filopodia formation during neuronal morphogenesis by establishing an *in vitro* model (Chapter 4).

Chapter 1. Establishing a PLPPR3 ICD purification pipeline

4.1.1 PLPPR3 Intracellular domain from Expi293F cells and medium

The ICD of PLPPR3 is an interesting structural target that we hypothesized to act as a scaffold and signaling hub for effector proteins. With 432 amino acids (Figure 9), the ICD takes up two-thirds of the entire molecule. I created a construct without the transmembrane domains (aa 284-716), which I fused with an N-terminal hemagglutinin signaling peptide (HA), followed by an M1 Flag tag and a C-terminal His-Tag. I chose this tag system for purification, due the high specificity of M1 antibody to recognize M1 Flag tag, which was demonstrated during GPCR purification (Heyder et al., 2021). The M1 antibody only recognizes the "free" M1 Flag tag in a calcium dependent manner (Einhauer & Jungbauer, 2001; Prickett et al., 1989; Slootstra et al., 1996). Therefore, I added a cleavable sequence in front of M1 flag that was cleaved off following protein expression, leaving the "free" M1 flag tag for purification. I used a modified, cleavable Hemagglutinin signaling peptide (A0M7P7) from influenza A strain *A. Victoria/3/75* (Guan et al., 1992; Jou et al., 1980). The full construct HA-M1-PLPPR3 ICD-His was cloned into a pCAX backbone and expressed under a CAG promoter. The CAG promoter is a combination of a cytomegalovirus early enhancer and a chicken beta-actin promoter and achieved enhanced protein expression compared to other promoters (Alexopoulou et al., 2008; Dou et al., 2021). For expression, I established an Expi293F cell line in our laboratory. According to the manufacturer, Expi293F cells are engineered human embryonic kidney (HEK293T) cells that were adapted to grow in suspension. Therefore, cells can be grown in much higher density in comparison to adherent cells, offering a higher yield of the protein of interest. I overexpressed HA-M1-PLPPR3 ICD for several days and experimentally determined that 4 days after transfection, the cells reached the maximum expression level (data not shown). Consequently, I harvested HA-M1-PLPPR3 ICD-His after 96 h expression (4 days).
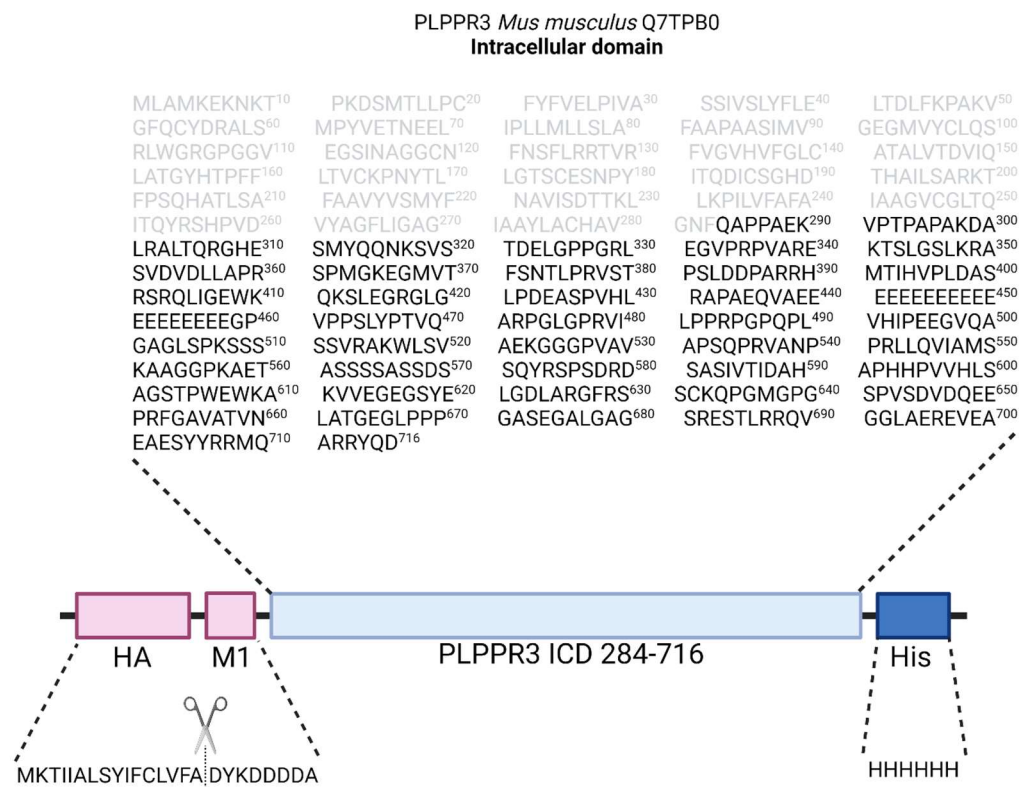
Figure 9. Design and Sequence of pCAX_PLPPR3 ICD
I used a cleavable hemagglutinin signal peptide –MKTIIALSYIFCLVFA- followed by a modified Flag peptide –DYKDDDDA- and PLPPR3 ICD aa 284-716 with a c-terminal 6x His-tag. PLPPR3 amino acid sequence (Uniprot: Q7TPB0) with the transmembrane domains indicated in light grey. The Intracellular domain begins at glutamine 284. The ICD was predicted to interact with several other proteins. I was interested in isolating the cytosolic ICD for biochemical and biophysical characterization.

A study in the 1990s demonstrated, that HA can enhance translocation of receptors into the endoplasmic reticulum (ER) membrane (Guan et al., 1992). We speculated that the protein is trafficked further in vesicles along the secretory pathway like GPCRs, until it reaches the plasma membrane (Jones et al., 2020; Shao & Hegde, 2011). As the fusion construct lacked the transmembrane domains, important for membrane insertion, we suspected the fusion construct could be targeted for secretion. Thus, I harvested cells and supernatant separately and purified PLPPR3 ICD from each sample.

First, I purified HA-M1-PLPPR3 ICD-His (Figure 10 A) by affinity chromatography and size exclusion chromatography (SEC) on a Superdex 200 increase 5/150 GL (Figure 10 B). The size exclusion chromatogram displayed an overlay of PLPPR3 ICD purified from the supernatant with PLPPR3 ICD purified from cells (Figure 10 C; compare red and black line). Both profiles show, that PLPPR3 ICD eluted at the same retention volume of 1.46 ml (fraction B3/B4), with the same homogenous peak, indicating a same sized protein species in each setup. However, when compared to protein, purified from cells,

PLPPR3 ICD purified from supernatant, was enriched nearly four times, as indicated by the absorption at 280 nm. Aromatic amino acid residues such as tryptophan and phenylalanine have an absorption maximum of 280 nm, which was utilized as measure of protein quantity.

Additionally, purified PLPPR3 ICD was analyzed by sodium dodecyl sulfate polyacrylamide gel electrophoresis (SDS-PAGE), which separated proteins based on molecular weight. All separated proteins were visualized by coomassie blue staining, a colloid dye which non-selectively bound all proteins (De Moreno et al., 1986). Each step of the purification indicated in Figure 10 B, was monitored by SDS-PAGE, to track PLPPR3 ICD during purification and finally, assess the amount and purity (Figure 10 D and E). Purified PLPPR3 ICD was observed above the 55 kDa marker band (Figure 10 D and E, arrows 1 – 4), while the calculated molecular weight was 48.7 kDa, which was consistent with overexpressed PLPPR3 ICD in N1E-115 cells (Kroon, 2023). We hypothesized that post-translational modifications and net negative charge of PLPPR3 ICD, may have altered migration within the polyacrylamide gel. Interestingly, in the same published work, full-length PLPPR3 was examined to separate at 100 kDa, however the calculated molecular weight was 76.7 kDa. Using a phostag SDS-PAGE to visualize the phosphorylation status (Kinoshita et al., 2009), I detected that PLPPR3 ICD, purified from the supernantant lacks several phosphorylation bands (data not shown). The bands in Figure 10 E (arrow 3 and 4), indicated a higher yield and purity of PLPPR3 ICD compared to the bands in Figure 10 D (arrow 1 and 2), represented by higher intensity of coomassie stain and less additional bands, respectively.
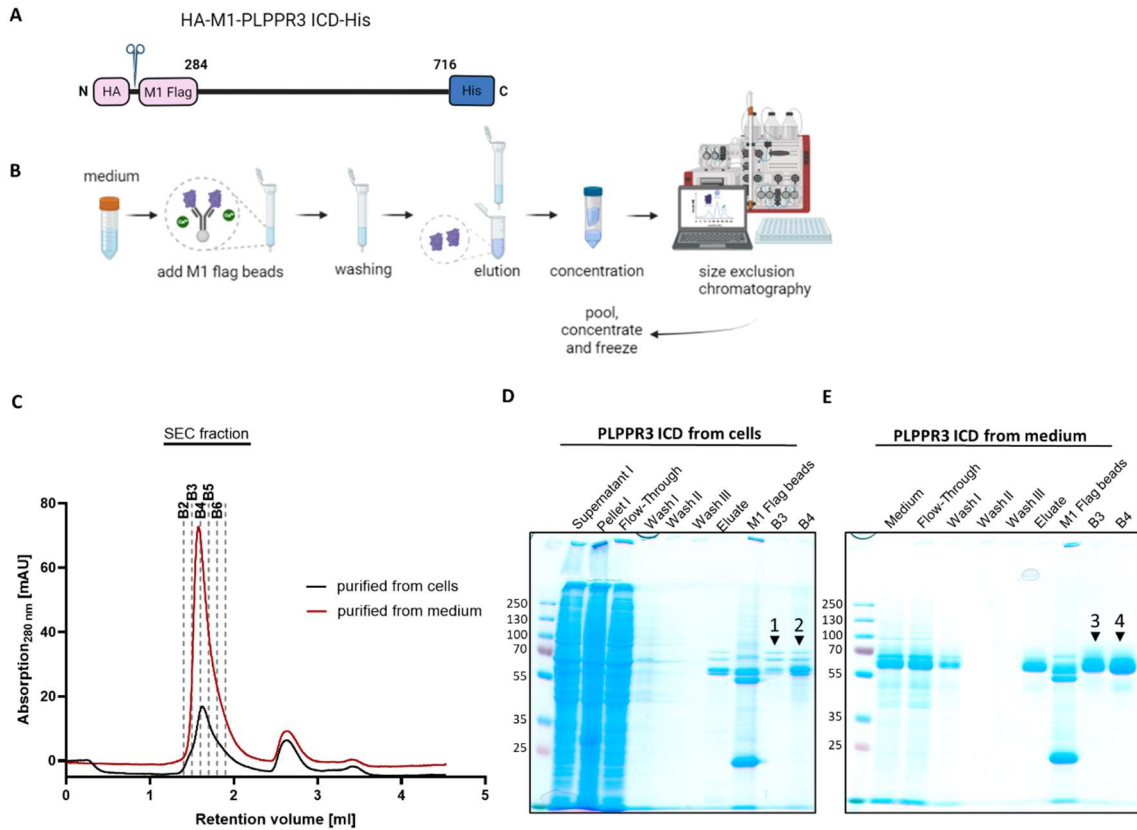
Figure 10. Purification of PLPPR3 ICD from medium and cells
*Establishment of a purification pipeline that enriched PLPPR3 ICD from supernatant in comparison to purification from cells. **A** The purification construct was designed with a cleavable HA signaling peptide, followed by the purification tag M1 flag, ICD aa residues 284-716 of PLPPR3 (PLPRR3 ICD) and a 6x His tag. **B** Scheme of established purification pipeline of PLPPR3 ICD from medium. Created with Biorender.com. **C** SEC profiles of PLPPR3 ICD purified from cells and medium. Both profiles were homogenous and showed a retention volume of 1.46 ml for PLPPR3 ICD. **D** SDS-PAGE of PLPPR3 ICD from cells showed a PLPPR3 ICD band above 55 kDa (arrow 1 and 2), which is unaltered in SDS-PAGE of PLPPR3 ICD from supernatant. **E** PLPPR3 ICD from medium was more enriched and less contaminated with other non-specific proteins (arrow 3 and 4).*

4.1.2 Verification of PLPPR3 ICD purified from supernatant

As I established a medium-purified PLPPR3 ICD in high quantity and purity, I decided to carry on with this strategy. To verify the purified protein as PLPPR3 ICD, I re-expressed, harvested and purified the construct from the supernatant. We switched to an Äkta pure system with an entire new superdex 200 increase 5/150 GL column, which made comparison of fractions between systems impossible, due to different tubing and void volume of the machine. Therefore, I performed SEC of purified PLPPR3 ICD with the new system and separated all peak fractions with a high 280 nm absorption on an SDS-gel. I discovered, that the peak fraction B2/B3 of the former system corresponded

to A9/A10 on the new system, indicated by high intensity band of fraction A9 and A10 (Figure 11 A).

To confirm, that bands in Figure 11 A (black arrow 1) were specific for PLPPR3 ICD, I performed a western blot. Purified protein was detected with a PLPPR3-specific antibody that was in-house purified and recognized an epitope at the C-terminus of the protein (Brosig et al., 2019). Therefore, bands in Figure 11 B above 55 kDa, indicated PLPPR3 ICD (arrow 2), while smaller bands likely were degraded fragments of PLPPR3 ICD. Furthermore, I cut out the band corresponding to fraction A10 (red box) for mass spectrometry (LC-MS/MS) and verified PLPPR3 ICD in collaboration with Dr. Kathrin Textoris-Taube and Manuela Staeber (HTMS facility Charité Berlin) as the top enriched protein with a protein score of 17140 (Figure 11 C). The protein score described the sum of the highest ions scores for each distinct sequence. Thereby, we could achieve a sequence coverage of 91% with 52 unique peptides found. Overall, the red sequence in Figure 11 D presented that we identified all major peptides with no great gaps in between.

Score	Molecular weight	Matches	Significant peptides	Significant and unique peptides	coverage
17140	48762	587	52	52	91%

D

```
  1   DYKDDDDAKL MQAPPAEKVP TPAPAKDALR ALTQRGHESM YQQNKSVSTD ELGPPGRLEG VPRPVAREKT SLGSLKRASV
 81   DVDLLAPRSP MGKEGMVTFS NTLPRVSTPS LDDPARRHMT IHVPLDASRS RQLIGEWKQK SLEGRGLGLP DEASPVHLRA
161   PAEQVAEEEE EEEEEEEEEE EEEEEEGPVP PSLYPTVQAR PGLGPRVILP PRPGPQPLVH IPEEGVQAGA GLSPKSSSSS
241   VRAKWLSMAE KGGGPVAVAP SQPRVANPPR LLQVIAMSKA AGGPKAETAS SSSASSDSSQ YRSPSDRDSA SIVTIDAHAP
321   HHPVVHLSAG STPWEWKAKV VEGEGSYELG DLARGFRSSC KQPGMGPGSP VSDVDQEEPR FGAVATVNLA TGEGLPPPGA
401   SEGALGAGSR ESTLRRQVGG LAEREVEAEA ESYYRRMQAR RYQDVDGRPH HHHHH
```

Figure 11. Western blot and mass spectrometry of PLPPR3 ICD
A Due to a switch from Äkta micro to an Äkta pure system with a novel superdex 200 increase 5/150 GL column, I confirmed that the peak fractions B2/B3 on the Äkta micro system corresponded to A9/A10 on the Äkta pure system for my purified protein. B I verified PLPPR3 ICD by western blotting using our specific PLPPR3 antibody and observed bands that correspond to PLPPR3 ICD (black arrow 2). C/D I cut out the band of fraction A10 (red box) and sent it for mass spectrometry, where, in collaboration with Dr.

Kathrin Textoris-Taube and Manuela Staeber, we could achieve a good sequence coverage of 91% (red). We found PLPPR3 ICD as the top enriched protein with protein score of 17140 and 52 unique peptides. The protein score described the sum of the highest ions scores for each distinct sequence.

4.1.3 Conclusion Chapter 1

In this chapter, I established a purification pipeline of PLPPR3 ICD by using the Expi293F system, together with a construct exploiting the hemagglutinin signaling peptide and the specificity of M1 Flag tag. This combination, allowed me to purify my protein in high quantity (Figure 10 C) and quality (Figure 11 A). I assessed the properties of PLPPR3 ICD, purified from cells in comparison to purified from medium and could detect no differences in protein species in size exclusion chromatography, nor in SDS-PAGE (Figure 11). In consideration of the HA signaling peptide, I hypothesized an enhanced translocation of PLPPR3 ICD to the ER membrane (Guan et al., 1992). PLPPR3 ICD however, is a cytosolic fusion protein, lacking insertable, hydrophobic transmembrane domains. Therefore, I reflected that PLPPR3 ICD could not be inserted into ER membranes. PLPPR3 ICD is likely transported in secretory vesicles to the membrane, where it is released into the medium by exocytosis.

As phosphorylation of proteins play an important regulatory function in signaling pathways and cellular processes (Ardito et al., 2017; P. Cohen, 2000; Garcia-Garcia et al., 2016; Johnson, 2009; Nishi et al., 2014), I carefully evaluated all downstream *in vitro* assays. In fact, medium-purified PLPPR3 ICD displayed identical characteristics to *E. coli* purified PLPPR3 ICD by our former PhD student Fatih Ipek (unpublished data) as well as PLPPR3 ICD purified from HEK293S cells (data not shown). Though not part of this thesis, the established PLPPR3 ICD protein gives us an opportunity to study phosphorylation selectively *in vitro* in the future.

Therefore, I continued all further *in vitro* assays with medium-purified PLPPR3 ICD. I generally combined several size exclusion fractions, containing high amounts of PLPPR3 ICD, concentrated and stored aliquots at -80°C. Overall, my established purification pipeline of PLPPR3 ICD was highly reproducible and resulted in a good quantity of purified proteins with a high purity. Of all the strategies I pursued, this setup was the most promising.

Chapter 2. PLPPR3 ICD is a highly disordered protein domain

As relatives of Phospholipid phosphatases (PLPPs), PLPPRs have six transmembrane helices and an intracellular domain. Transmembrane helices of PLPPR3 likely follow a structured state, similar to PLPPs (Fan et al., 2014), while the intracellular domain remains uncharacterized. However, many transmembrane proteins have intracellular domains (ICDs) that are intrinsically disordered and serve as scaffolds for proteins or control other key features of signaling pathways (Kassem et al., 2021; Sigalov et al., 2008; Verkest et al., 2022). To gain insight and to study the structural state of PLPPR3 ICD, I employed online prediction tools, as well as experimental approaches.

4.2.1 Disorder prediction of PLPPR3

To assess PLPPR3 properties for disorder, I used PONDR as common prediction tool in the field (http://www.pondr.com/). It predicted the likelihood of residues to be disordered. The input was mouse PLPPR3 sequence (uniprot: Q7TPB0) and output a prediction value score between 0 and 1 for each amino acid (aa) residue. Scores above 0.5 indicated potential disorder, scores below 0.5 possible order. Figure 12 graphically displayed predicted scores for each residue of PLPPR3. As expected, residues 30-280 showed rather high confidence order prediction, which represented the transmembrane domains. The intracellular N-terminus (aa 1-18), was predicted disordered as well as residues 281-716, which are part of the intracellular domain. Some observable stretches within the ICD are predicted stable e.g. aa 399-418, aa 590-610 and aa 640-650, the same stretches that correspond to the Alphafold 2 predicted confident loops (Appendix). Additionally, disorder was present in the transmembrane region for the intra- and extracellular loops. Furthermore, I used EMBOSS (https://www.bioinformatics.nl/cgi-bin/emboss/charge) to predict primary sequence charge distribution. In general, protein charge was demonstrated to be important for protein solubility, folding and ligand interaction (Xu et al., 2013; Zhou & Pang, 2018). I identified that overall charges are equally distributed, however three stretches show a noticeable inclination towards one charge direction. The residues 180-438 globally incline more towards a slightly positive charge, followed by a highly negative charge (polyE box). The residues 458-550, which follow the polyE box, are globally positively charged again.
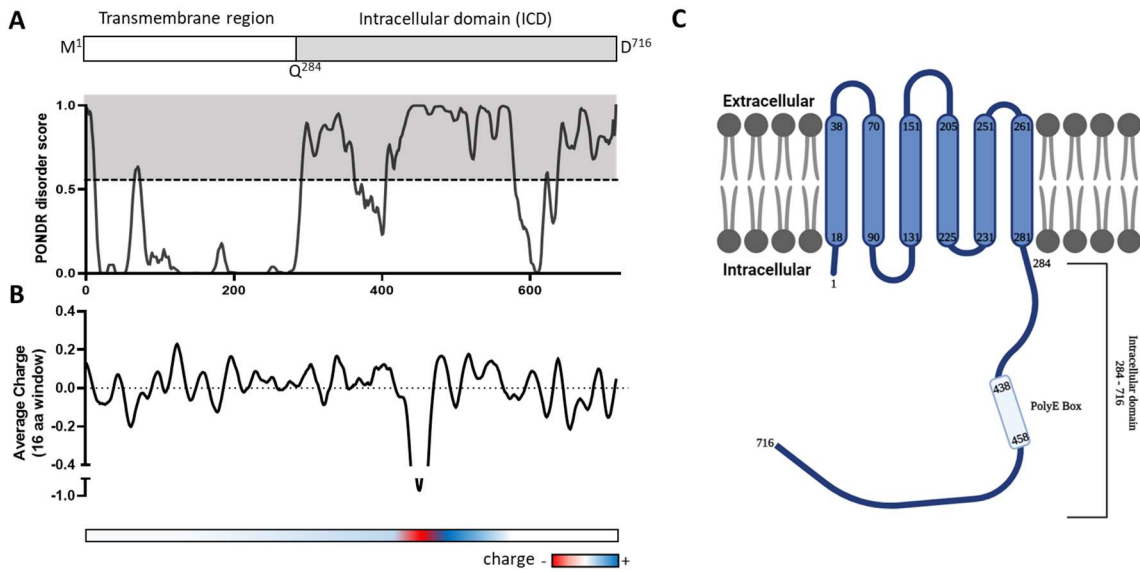
Figure 12. Disorder and charge prediction of PLPPR3
A Prediction of PLPPR3 (uniprot: Q7TPB0) with PONDR disorder predictor (http://www.pondr.com/).
Visually represented is the increase of disorder with begin of the intracellular domain (ICD) at residue
Q^{284}. B Charge distribution prediction of PLPPR3 with sliding window 16 aa. Overall PLPPR3 has equal
global charges, with exception of the highly negative polyE box (aa 438-458) and the flanking globally
positively charged residues. C Cartoon representation of PLPPR3 with indicated transmembrane domains,
loops, polyE box and intracellular domain.

4.2.2 Random coil makes up the majority of PLPPR3 ICD

The PONDR plot visualized potential disorder state in various regions of PLPPR3 ICD.

In order to verify this experimentally, I utilized Circular Dichroism (CD) spectroscopy in

collaboration with Heike Nikolenko from the Leibnitz institute of pharmacology (FMP)

to assess secondary structure elements. CD is a method that harvests the difference

between left and right circularly polarized light of chiral molecules such as proteins

(Greenfield, 2007). It yields information about structures that are responsible for chirality,

such as helices and beta sheets (Rodger et al., 2005). One drawback to the method is, that

buffers have to be as transparent as possible, with close to no materials that are optically

active.

Therefore, I modified my protein purification buffer from 20 mM Hepes, 150 mM NaCl

and 5 mM DTT at pH 6.0 to 20 mM Phosphate buffer with 150 mM sodium fluoride

(NaF) and 1 mM DTT at pH 6.0, to reduce optical activity and background noise.

Additionally, to 150 mM NaF, I used a second, low salt concentration sample (20 mM

NaF), to observe potential changes in structure. Low salt was observed to modulate

conformations of intrinsically disordered proteins (Maity et al., 2022). Phosphate buffer

has been utilized as a low background CD spectroscopy buffer for recording (Chakraborty & Lentz, 2012). Firstly, I checked that the modified protein purification buffer did not alter PLPPR3 ICD stability. All three chromatograms (Figure 13 A) showed the same homogenous peak at 1.46 ml retention volume, which indicated, the modified buffer did not affect protein stability.

After calibrating the CD spectroscope, we measured a baseline of phosphate buffer. This ensured that all effects by the buffer were cancelled out and further measurements displayed PLPPR3 ICD only. We measured 5 µM PLPPR3 ICD in a cuvette with 0.1 cm length at RT. The parameters used for each measurement are shown in table 17 methods section (3.3.3.3). Both samples were measured 15 times after each other, which reduced measurement fluctuations. The accumulated curves of molar ellipcity for PLPPR3 ICD with 20 mM NaF and 150 mM NaF were plotted against the wavelength (Figure 13 B).
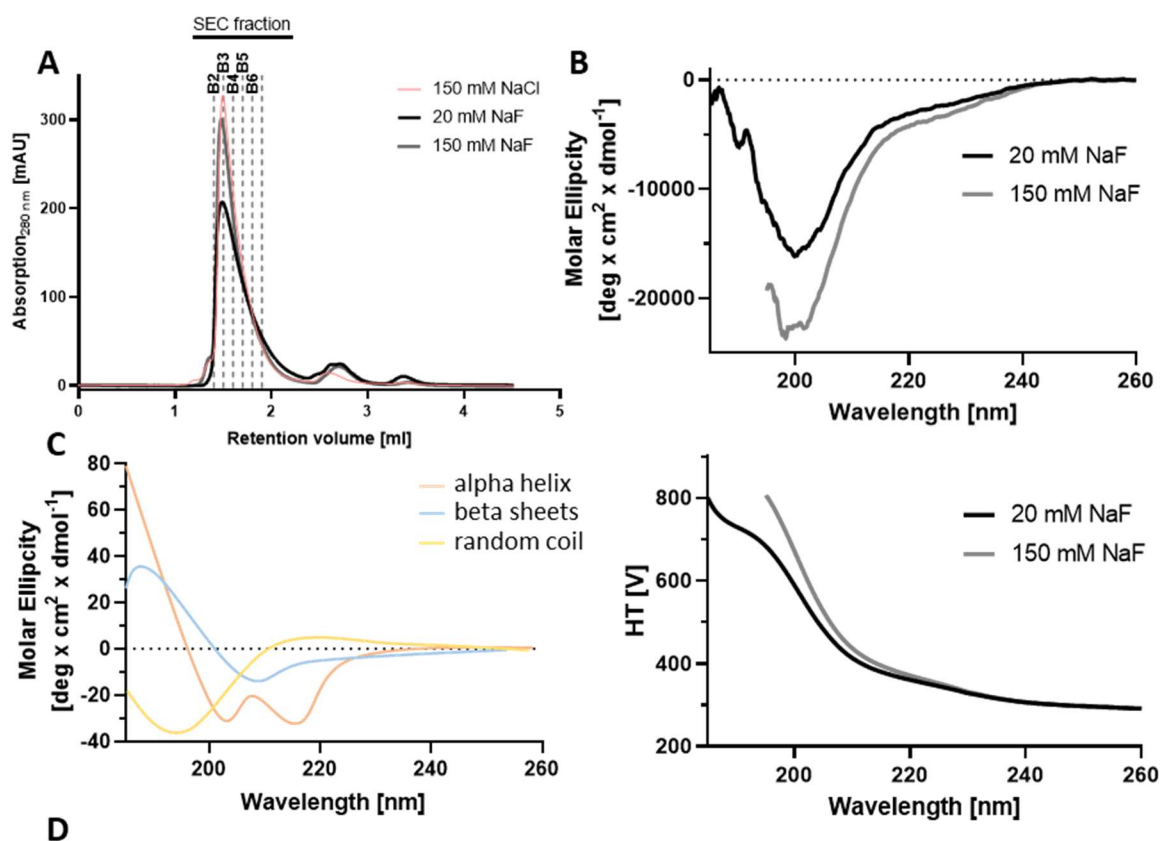
	20 mM NaF		150 mM NaF
Wavelength	190-260 nm	195-260 nm	195-260 nm
Helix	6.40%	7.60%	7.30%
Antiparallel	16.30%	23.40%	16.70%
Parallel	2.40%	3.50%	2.80%
Beta-Turn	30.40%	29.00%	35.20%
Random Coil	44.50%	39.00%	42.90%
Total Sum	100.00%	102.50%	104.90%

Figure 13. CD spectra of PLPPR3 ICD
A Size exclusion chromatogram comparing purified PLPPR3 ICD in 20 mM Hepes, 150 mM NaCl, 5 mM DTT at pH 6.0 (red) with PLPPR3 ICD in 20 mM Phosphat buffer, 20 mM NaF, 1 mM DTT (black) and 20 mM Phosphat buffer, 150 mM NaF, 1 mM DTT at pH 6.0 (grey). All three chromatograms show the same homogenous peak at 1.46 ml retention volume (fraction B3/B4) and indicate that phosphate buffer and sodium fluoride did not affect PLPPR3 ICD stability. B Top panel: CD spectra of PLPPR3 ICD in 20 mM Phosphatbuffer, 20 mM (150 mM) NaF, 1 mM DTT at pH 6.0 with 15 accumulations. Both CD spectra show a negative molar ellipticity at 200 nm indicating disorder of PLPPR3 ICD. Bottom panel: High tension (HT) Voltage indicating the quality of the CD spectra at each wavelength. C Example spectra of different secondary structure elements. Adapted from Greenfield, 2007. D CDNN prediction of secondary structure element content. 20 mM NaF spectra prediction is between 190 nm – 260 nm and 195 nm – 260 nm, showing that the majority of PLPPR3 ICD is random coil and beta turn. Similar prediction is calculated for 150 mM NaF.

The top Panel in Figure 13 B displayed both CD spectra with 20 mM and 150 mM NaF, the bottom panel the corresponding high tension (HT) voltage as a measurement of CD data quality. HT voltage is produced during data collection and is voltage applied to the detector to amplify the CD signal. With rising voltage, more noise is recorded, which indicates the quality of the spectra (Miles et al., 2021). Both spectra showed similar patterns that absorbed the polarized light at 200 nm. I compared both spectra to example spectra (Figure 13 C), when it became evident that the pattern of PLPPR3 ICD spectra resembled predominantly disordered protein spectra. The negative molar ellipticity at 200 nm is an indication for disorder (Chemes et al., 2012; Miles et al., 2021). In addition, we analyzed our spectra with the deconvolution software CDDN (v2.0.3.188), which compared our spectra to 35 standard spectra and predicted secondary structure elements (Figure 13 D). Interestingly, the 150 mM NaF spectrum showed over 40% random coil and 35% beta-turn elements which indicated a rather flexible disordered protein. However, several structural elements were detected, including close to 20% beta sheets and 7% helices. Similar values have been detected for 20 mM NaF spectrum. I could not detect any major differences between the two monitored concentrations with CD spectroscopy.

4.2.3 PLPPR3 ICD is fully digested during limited proteolysis

Proteases are a class of pivotal enzymes, which catalyze the cleavage of peptide bonds, thereby leading to complete degradation of proteins (Rao et al., 1998). Limited proteolysis is a simple method that uses low amounts of proteases to cut exposed and flexible peptide chains, while leaving stable three-dimensional structure elements untouched. Thus, proteases cleave accessible linear peptide motifs better, then folded, inaccessible proteins

(Fontana et al., 1997). I established a limited proteolytic digest (Hubbard, 1998; Quevillon-Cheruel et al., 2007) with trypsin to introduce further evidence that ICD is lacking major secondary structure elements, as seen by the CD spectroscopy (section 4.2.2). I combined 16.8 µM trypsin with 8.4 µM ICD at final concentration and digested at 22°C for 0, 2, 5 10, 30 and 60 minutes. The reaction was quenched with ¼ SDS buffer 4x, boiled at 95°C and separated by SDS-PAGE in two independent experiments. The resulting coomassie stained protein bands (Figure 14) presented a slow, but steady proteolytic digest, indicated by the black arrows (1), (2) and (3). The bands (1-3) increased over time, while the prominent protein band (*) decreased. Thereby, band (1) had a lower molecular weight and was the first to appear after 2 min, followed by bands (2 and 3) at 5 min with even lower molecular weights. This illustrated that PLPPR3 ICD was digested into intermediate fragments over time. To control for an effect by temperature, I incubated PLPPR3 ICD with PBS for 60 min at 22°C, instead of trypsin, which resulted in the same band pattern as compared to 0 min and the untreated PLPPR3 control. This demonstrated that temperature alone was not the reason for degradation. The proteolytic digest revealed that PLPPR3 ICD has many exposed regions that are accessible for tryptic digest. In addition, there is no apparent stabilized band as would be expected by a structured protein, where only part of the protein would be exposed and digested. Although I observed several increasing fragments, a comparison with literature suggested, that these were intermediate peptides, which were further digested over time (B. Li et al., 2014; Nouwen et al., 2000). Thus, I concluded that PLPPR3 ICD showed a band profile of a digested protein and underlined the evidence that it has many linear, exposed motifs.
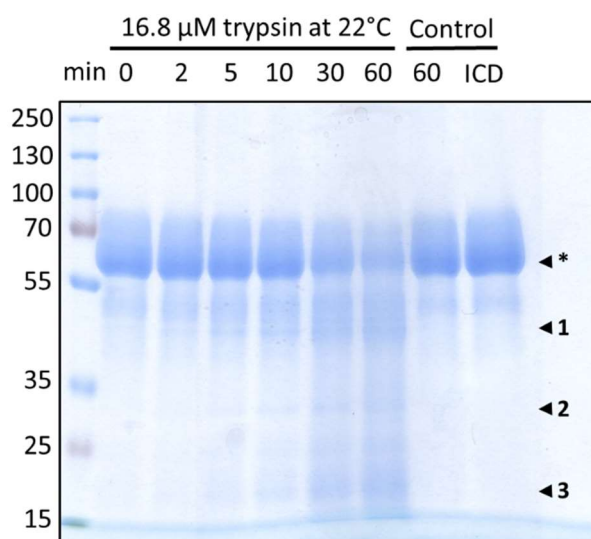
Figure 14. Limited proteolytic digest of PLPPR3 ICD with trypsin
*Combination of 8.4 μM and 16.8 μM trypsin in 1.5 ml Eppendorf tubes. The reaction was incubated either 0, 2, 5, 10, 30 and 60 min and quenched with 8.33 μl SDS 4x buffer. As setup control 10.5 μM ICD was diluted with 5 μl PBS and incubated 60 min at 22°C. As positive control I used 8.4 μM untreated ICD. All samples were boiled 5 min at 95°C and 20 μl loaded on a 10% SDS-Gel that was run 80 V for 20 min and 120 V until the loading dye reached the end of the gel. Bands were stained with coomassie and destained with ddH$_2$O. Two independnetl experiments were performed with individual purificated PLPPR3 ICD. **1, 2** and **3** show bands that are increasing over the reaction period of 60 min due to the proteolytic digest, while ***** shows that the prominent ICD band is getting less over time.*

4.2.4 PLPPR3 ICD is insensitive to unfolding by temperature

Lastly, to verify that PLPPR3 ICD is a disordered protein domain I used a thermostability assay. The assay utilized increased temperature to unfold ("melt") PLPPR3 ICD. Thereby, the intrinsic fluorescence of aromatic amino acids at 330 nm and 350 nm was measured, which differed between folded and unfolded state (Figure 15 A). The ratio of 330/350 nm was exploited to calculate the specific melting temperature Tm. I used a nano differential scanning fluormetry (nanoDSF) device and loaded 20 μM of ICD in each standard capillary. Protein "unfolding" was visualized from 20°C to 90°C with an increase of 1°C per minute. I measured three independent experiments with 4 replicates each. As a negative control, I used my assay buffer 20 mM Hepes, 150 mM NaCl, 5 mM DTT at pH 6.0, where I expected to observe no unfolding. In contrast, as a positive control, I diluted 50 μM bovine serum albumin (BSA) in assay buffer and expected to monitor unfolding of structured BSA. From the melting curves, I used the first derivative of 330 nm/350 nm ratio (Figure 15 B), to calculate the specific melting temperature Tm (Figure 15 C). The mean of all melting curves of PLPPR3 ICD demonstrated a similar pattern to the mean of the buffer control, which led to the assumption, that there was no unfolding and no folded structure. Calculating the melting temperature (Tm) for PLPPR3 ICD proved challenging. The assay, designed to measure unfolding with increased temperature, successfully demonstrated this for BSA, yielding a Tm of approximately 67°C for the control. In contrast, PLPPR3 ICD did not exhibit unfolding with rising temperature due to its unique behavior. This phenomenon can indicate a lack of secondary structure elements for the majority of the protein (Leuenberger et al., 2017; Ortega-Alarcon et al., 2021), however was also observed for several structured proteins. Therefore, this result was only taken as indication for potential disorder.
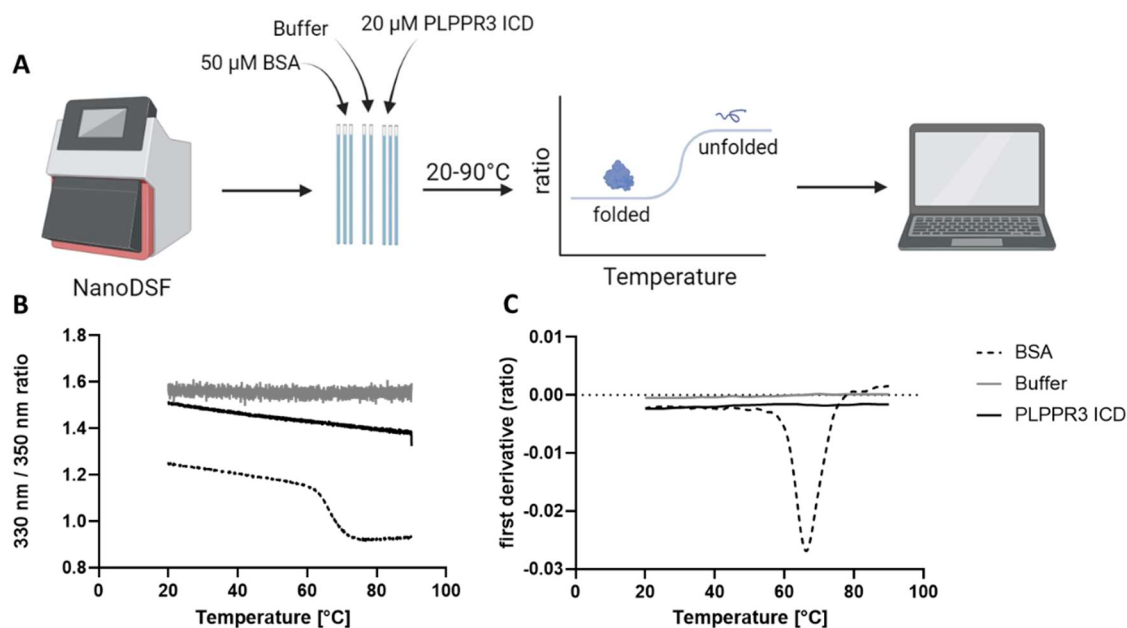
Figure 15. Thermostability (nanoDSF) assay of PLPPR3 ICD
*A Schematic representation of the experimental setup. Intrinsic fluorescence of aromatic residues at 330 nm and 350 nm was measured upon protein unfolding. From the 330/350 nm ratio, a specific melting temperature Tm was calculated. Created with Biorender.com **B** Thermic unfolding of 20 μM PLPPR3 ICD was monitored from 20°C to 90°C using nanoDSF. As positive control I used 50 μM bovine serum albumin (BSA) and as negative control, assay buffer containing 20 mM Hepes, 150 mM NaCl, 5 mM DTT pH 6.0. **C** First derivative of 330/350 nm ratio resulted in a defined peak for BSA, which indicated the specific melting temperature Tm. However, PLPPR3 ICD did not show any unfolding with increasing temperature and is comparable to the measured buffer, which indicated that PLPPR3 ICD is not folded.*

4.2.5 Conclusion Chapter 2

In this Chapter, I wanted to address the question, if PLPPR3 ICD is disordered. While the question remains if ICD is a single, unstructured domain, I could observe that PLPPR3 ICD has a high degree of disorder with several experiments presented in this Chapter. In Figure 12, the prediction showed that full length PLPPR3 has a high degree of order due to the transmembrane domains, while loops, N-terminus and ICD have a higher degree of disorder. Although I observed several secondary structure elements like helices and anti-parallel beta sheets in CD (Figure 13 A), the majority of the protein domain is random coil and beta turns. Finally, two biophysical experiments were conducted to verify folding and unfolding events. During my proteolytic digest assay, I was not able to see a clear stabilized protein band (Figure 14), which indicated a full tryptic digest. I concluded from this experiment, that PLPPR3 ICD lacked a tertiary structure and thus is an unfolded protein domain. In a further approach, I determined the thermostability of PLPPR3 ICD by thermal unfolding. The experiment indicated that there was no unfolding visible of PLPPR3 ICD (Figure 15). To add, in the Appendix, I present alphafold 2 prediction

models, which were used to understand PLPPR3. Alphafold 2 suggested a low confidence model, either due to missing structural data for similar structures or due to high flexibility (Appendix 6.1). In any case, combining all the experimental and predicted data, I came to the conclusion that PLPPR3 ICD is a highly flexible and disordered protein region.

Chapter 3. Liquid-Liquid phase separation of PLPPR3 ICD

Many intrinsically disordered protein domains (IDRs) can form liquid-like condensates (Brocca et al., 2020; Tesei et al., 2021). These condensates (cf. section 1.5), play a critical function in maintaining biochemical processes in confined spaces (Pezzotti et al., 2023; Zhu & Jiang, 2022). Previous work in our laboratory, showed, that PLPPR3 forms clusters along the axonal membrane in neurons (Brosig et al., 2019). To address the question, if disordered PLPPR3 ICD (Chapter 2) can form biomolecular condensates, I therefore looked at condensate formation in cells as well as *in vitro*, by employing my purification system established in Chapter 1.

4.3.1 Predicting PLPPR3 ICD phase separation

To understand if PLPPR3 ICD had the possibility to undergo biomolecular condensate formation, I used several prediction tools including PlaToLoCo for low complexity domains (LCDs) (Jarnot et al., 2020; https://platoloco.aei.polsl.pl/#!/query) and FuzDrop for prediction of spontaneous condensate formation, droplet and aggregation promoting regions (https://fuzdrop.bio.unipd.it/predictor). I used FuzDrop as a main prediction tool, to graphical visualize the probability to promote droplet formation (Figure 16). Full-length PLPPR3 (uniprot: Q7TPB0) was predicted with a probability of 0.9960 to phase separate. This probability predominantly stems from residues within the intracellular domain (ICD). These specific residues serve as the primary origin of regions that promote droplet formation. FuzDrop predicted that droplet promoting regions included the N-terminus (aa 1-17), a long stretch of 250 amino acids (aa 281-525), which involved the polyE box, as well as three shorter stretches (aa 548-585; aa 635-647; aa 664-685). On the other hand, several short residue motifs have been predicted to promote aggregation, a process by which proteins assemble into insoluble structures (Ye et al., 2022). One key difference between condensates and aggregates is reversibility, which aggregates lack (Shin et al., 2017; Venko & Žerovnik, 2023). This prediction gave me a first idea of the region that form condensates and was in accordance with my previous data suggesting that ICD is highly disordered.

Figure 16. PLPPR3 probability to undergo phase separation
*A FuzDrop (https://fuzdrop.bio.unipd.it/predictor) was used to predict PLPPR3 (Q7TPB0) phase separation probability. The overall LLPS probability of PLPPR3 was predicted with 0.9960. Interestingly, the majority of residues predicted to be involved in droplet-promoting regions are located in the ICD, with exception of the N-terminus (aa 1-17). These regions can lead to droplet formation (condensates). **B** Droplet-promoting regions indicated on a predicted cartoon structure of PLPPR3, which was generated by alphafold 2 and schematic representation of droplets. **C** Several regions were predicted to promote aggregation, indicated on a predicted cartoon structure of PLPPR3, which can lead to aggregated structures such as the schematic representation (modified after Hatos et al., 2022).*

4.3.2 Characterization of PLPPR3 ICD *in vitro* condensates

The logical next step was to test condensate formation of PLPPR3 ICD *in vitro*. Using my purification pipeline (Chapter 1), I purified PLPPR3 ICD from Expi293F medium via M1 Flag tag and by size-exclusion chromatography (SEC). In my initial experiments, I used PEG8000 (PEG) as molecular crowding reagent, to promote condensate formation. PEG mimics the crowding effect of the intracellular environment, which is a key factor of complex condensate formation (S. Park et al., 2020; Tyrrell et al., 2015). In general, I used 5% (w/v) PEG8000 with PLPPR3 ICD at a final concentration of 20 µM (1 mg/ml)

in a buffer of 20 mM Hepes, 150 mM NaCl, 5 mM DTT at pH 6.0. I pipetted a small drop (2.5 µl) on an imaging dish, which in general was coated with 1% (w/v) polyvinyl alcohol (PVA) and visualized condensates under a 60x oil immersion objective with a widefield microscope.

After crowding with PEG, I observed droplet formation (Figure 17 A). These condensates were circular and detected in various sizes. Smaller droplets thereby coalesced to larger ones with diameter of 10 µm or more. Noticeably, the convergence of two condensates was a gradual process, compared to the coalescing of two condensates, which was less than 1 s (Figure 17 B), indicating liquid-like condensates.
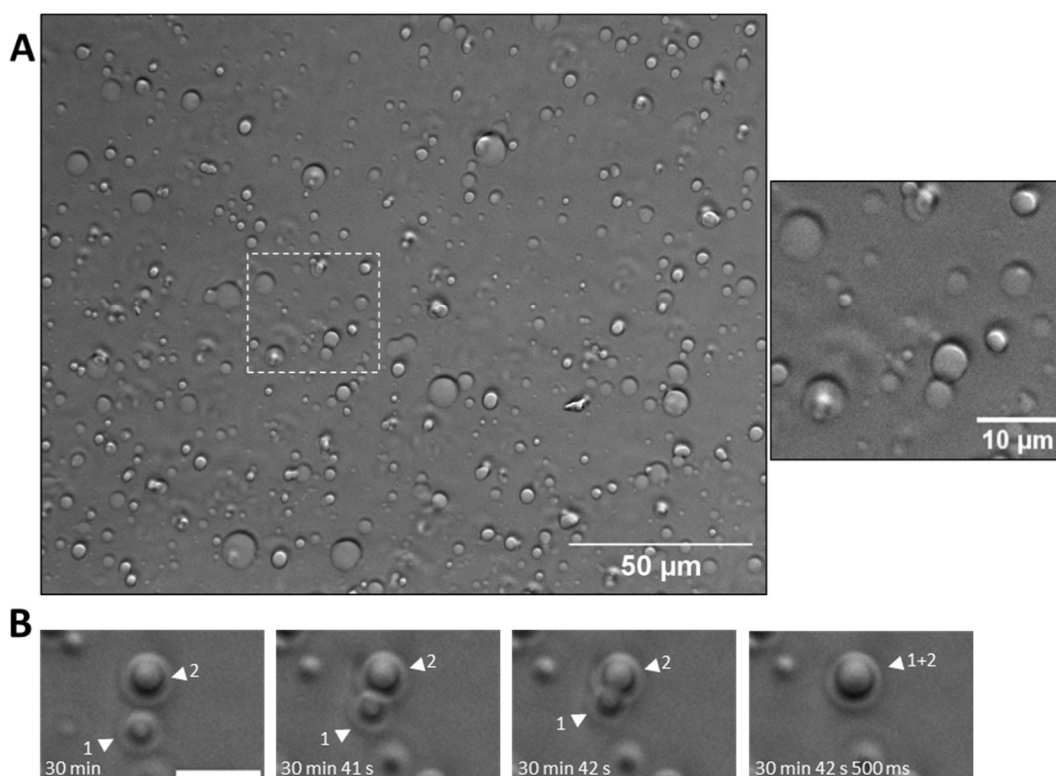
Figure 17. Condensate droplets of 20 µM PLPPR3 ICD with 5% PEG8000 (w/v)
*A PLPPR3 ICD forms condensates with the molecular crowding reagent PEG8000 in a buffer of 20 mM Hepes, 150 mM NaCl, 5 mM DTT at pH 6.0 on amine-treated imaging dishes. Imaging was performed with an 60x oil immersion objective. **B** Coalescing of two condensates (1) and (2) over time forming the larger condensate (1+2) on a 1% PVA coated dish. Coalescing was observed within 1 second or less. PVA coating prevented complete wetting of the droplet to the surface. Scalebar: B: 5 µm.*

Next, I characterized *in vitro* condensates of PLPPR3 ICD and thus established a phase diagram with three independent experiments, to analyze for dependence of PEG to PLPPR3 ICD concentration. I screened PEG ratios from 0-5% and PLPPR3 ICD

concentrations ranging from 0 - ca. 100 µM. With no PEG as crowding reagent I could not detect any condensates in this setup. However, I observed that condensates began to form at 5 µM with 1% PEG (Figure 18). The more PEG was introduced to the system, the lower concentration of PLPPR3 ICD was needed to detect condensates. Generally, phase transition from areas of no LLPS (red) to LLPS (green) was not always clear and resulted in "intermediate states", where I noticed condensates to form at the edge of the drop. I interpreted these as no LLPS states. Each "+" or "-" represented one experiment at a specific concentration. From the diagram, I chose a PEG and PLPPR3 ICD concentration, which I used in all following experiments. I thereby tried to stay as close to the phase transition as possible, with regard to the observable condensate size. Therefore, I chose 20 µM PLPPR3 ICD with 5 % PEG, which is in the range of other condensate forming proteins such as tau (Wegmann et al., 2018) and α-synuclein (Ray et al., 2020).
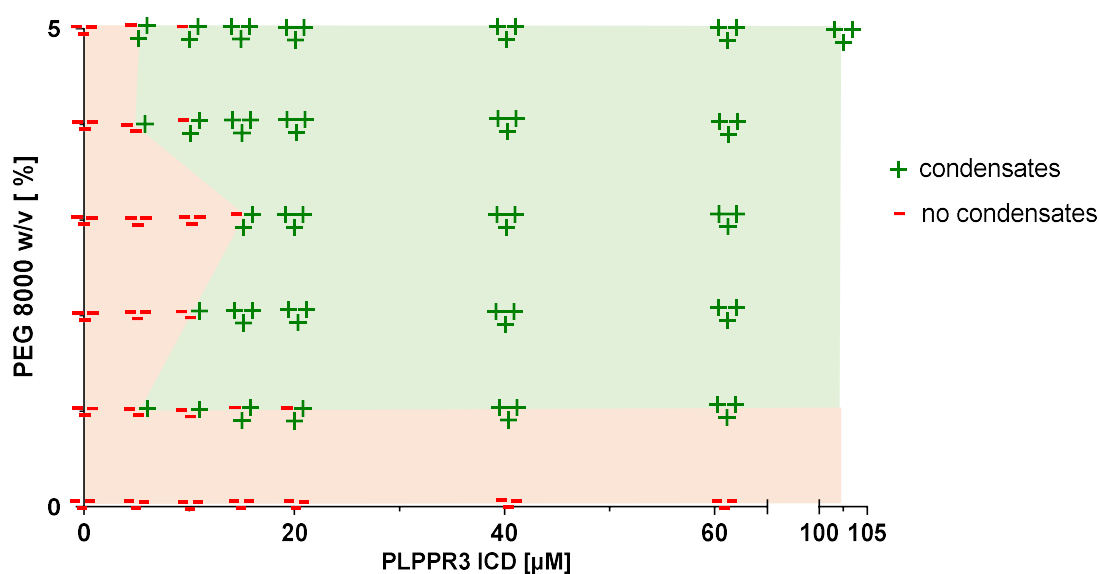
Figure 18. **Phase diagram of PLPPR3 ICD in dependence of PEG8000**
PLPPR3 ICD was screened at various concentration from 0 – ca. 100 µM for its ability to form condensates in vitro in the presence of various PEG8000 concentrations. I conducted three independent experiments at each concentration and established a transition between LLPS (green) and no LLPS (red). PLPPR3 ICD was observed at lowest 5 µM and 1% PEG to form circular, but small condensates. With increasing PEG, or PLPPR3 ICD concentration, droplet size increased. However, the transitions were not strict with tested concentrations. All "intermediate states", where LLPS was observed at the edge of the drop, were counted to "no condensates". For all downstream experiments I chose to use 20 µM PLPPR3 ICD and 5% PEG.

After determining the conditions that support PLPPR3 ICD condensate formation, my next approach was to determine if LLPS of PLPPR3 ICD was based on electrostatic interactions. Electrostatic interactions are one major type of intermolecular interaction

that drive LLPS (Krainer et al., 2021) and are affected by salts such as sodium chloride (NaCl) (Perez-Jimenez et al., 2004). To test this, I concentrated PLPPR3 ICD and diluted out 150 mM NaCl, by using low salt buffers. I investigated LLPS at 20 mM NaCl, 50 mM NaCl and 150 mM NaCl after 30 min of incubation at RT using phase contrast. For analysis, I defined a fixed region of interest (roi) and detected edges of all condensates within the roi. I applied the "measuring" tool of ImageJ and determined the mean pixel intensity. Interestingly, this experiment displayed that PLPPR3 ICD formed condensates without the addition of PEG at 20 mM NaCl (Figure 19 B). An increase of NaCl antagonized LLPS and lowered the amount of condensates (Figure 19 A), until at physiological 150 mM NaCl less condensates were detected (Figure 19 B). Therefore, I interpreted from these data, that PLPPR3 ICD condensate formation is driven by electrostatic interactions.

To further characterize PLPPR3 ICD condensate formation, I tested the role of hydrophobic interactions (Düster et al., 2021). I utilized several different concentrations of 1,6-Hexandiole (1,6-HD) to disrupt weak hydrophobic interactions (Krainer et al., 2021). I applied 0%, 3%, 5% and 10% (v/v) 1,6-HD to 20 µM PLPPR3 ICD in the presence of 5% (w/v) PEG8000 and imaged the condensates with phase contrast. I didn't observe any significant differences of condensate size and number with 0% and 3% or 5% 1,6-HD (Figure 19 C-D). However, between 0% and 10% 1,6-HD, there was a reduction in condensate size after 30 min of incubation. Interestingly, also the number of condensates was reduced (data not shown). Therefore, I concluded from this set of experiments that PLPPR3 ICD condensates in addition to electrostatic interactions, are also driven by weak hydrophobic interactions.
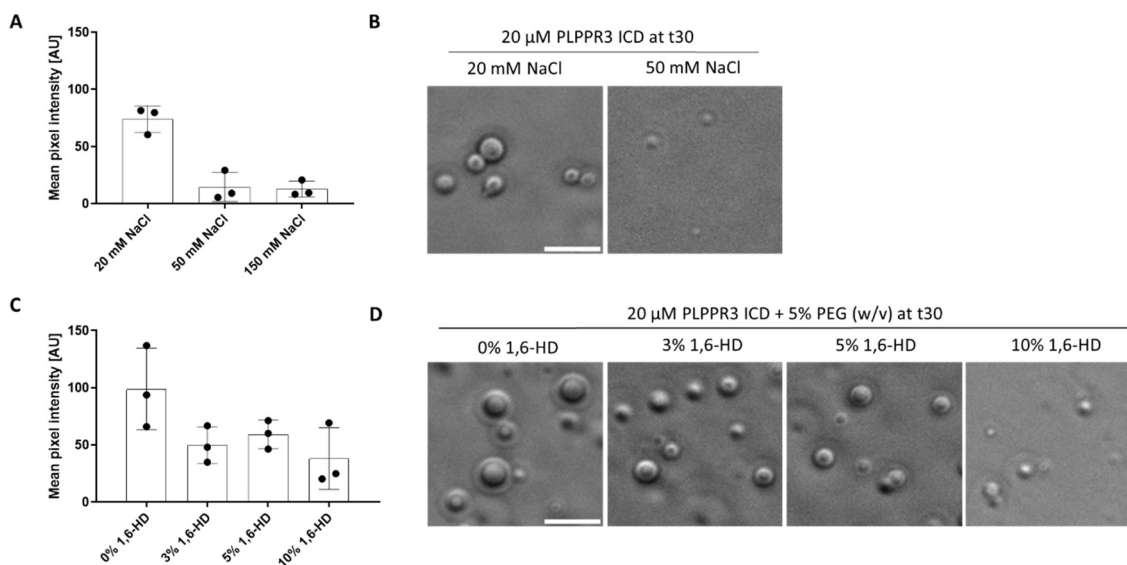
Figure 19. PLPPR3 ICD condensates depend on electrostatic and hydrophobic interactions
A Quantification of PLPPR3 ICD (20 μM) forming condensates in vitro without the presence of PEG under low salt (20 mM NaCl). With increasing NaCl concentration from 20 mM to 50 mM, as well as 150 mM, condensates were observed to decrease. Error bars indicate SD. N = 3. B Visual representation of PLPPR3 ICD condensates at 20 mM NaCl and 50 mM NaCl with phase contrast. PLPPR3 ICD condensate formation is based on electrostatic interactions. C Quantification of condensate formation of 20 μM PLPPR3 ICD in the presence of 5% (w/v) PEG and 1,6-Hexandiole (1,6-HD). 1,6-HD is an aliphatic alcohol which can disrupt weak hydrophobic interactions. 0% was used as control and 3%, 5% and 10% 1,6 HD to disrupt all hydrophobic interactions. There was no significant differences between 0%, 3% and 5% 1,6-HD, however a decrease of condensates with 10% 1,6 HD compared to control. Error bars indicate SD. N = 3. D Visual representations of condensates treated with no, 3%, 5% or 10% 1,6-HD. There were no differences of condensate, treated with 3% 1,6-HD and 5%-1,6 HD compared to 0% 1,6-HD control, however smaller condensates were observed with 10% 1,6-HD.

In order to validate liquid-like behavior of PLPPR3 ICD condensates, I utilized fluorescence recovery after photo bleaching (FRAP) experiments. FRAP uses high laser intensity to permanently inactive (bleach) fluorophores attached to proteins of interest. After bleaching, non-bleached fluorophores replace bleached ones, if there is an exchange with the external environment (Sprague & McNally, 2005). Thereby, faster recovery is proportional to higher rates of diffusion (McSwiggen et al., 2019), that can be translated to faster reorganization and therefore more liquid-like behavior.

To test this, I used 20 μM PLPPR3 ICD including 3% labelled PLPPR3 ICD-488, which I crowded with 5% PEG to initiate LLPS *in vitro*. I bleached the entire droplet at various time points (5, 15, 30 and 60 min), to observe exchange of PLPPR3 ICD molecules with the condensate surrounding over time. The recovery rates decreased from roughly 50% maximum recovery (5 min) to roughly 20% recovery after 60 min, indicating that the exchange with the surrounding decreased over time (Figure 20 A). However, I could not

exclude that the surrounding was depleted of freely diffusible PLPPR3 ICD molecules. Nonetheless, the FRAP data at 5 min displayed a recovery, which suggested an efficient exchange of condensate with the environment.

I used partial bleaching to observe liquid-like behavior of condensates. I utilized the laser beam to bleach a circular part of the condensate only, not the full condensate. This was important to test the efficiency of internal reorganization. I used the same PLPPR3 ICD setup as mentioned before and bleached at 30 min after condensate initiation, to be less effected by disturbing coalescence events. Figure 20 B displayed a fast recovery over 300 s to roughly 50%, indicating a successful reorganization of the fluorophore-tagged molecules within the droplet. The representative images in addition demonstrated, that the bleached region is fully restored, however the overall fluorescence intensity decreased. Therefore, I concluded from these experiments that PLPPR3 ICD condensates were able to exchange molecules with their surrounding and in addition displayed liquid-like behavior by internal reorganization.
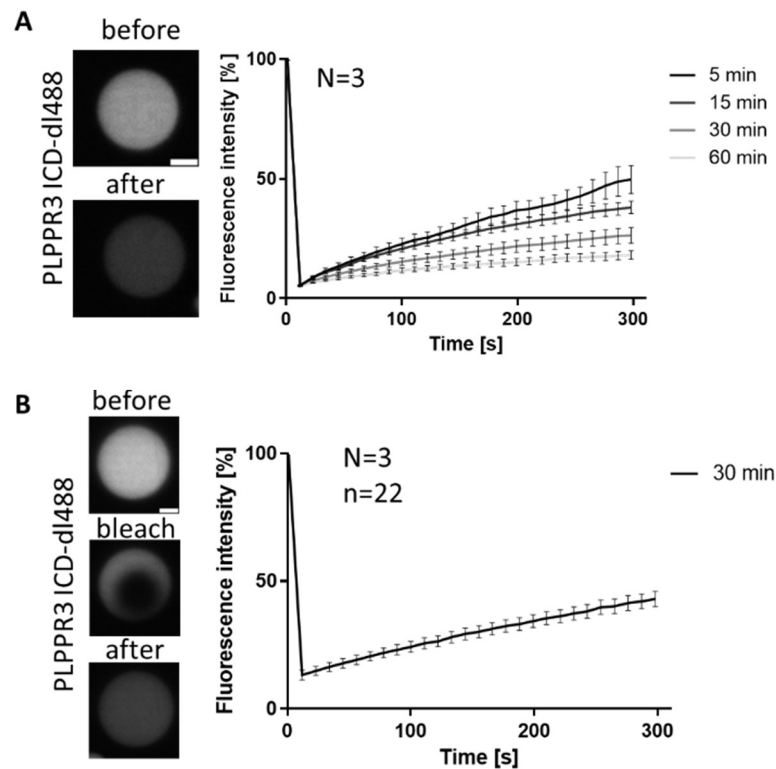
Figure 20. FRAP of PLPPR3 ICD condensates
*Imaging was performed with 1 frame per second for 5 s (baseline), followed by bleaching a defined region of interest (roi) for 2 s at 100% 488 laser-power and 6 min post-bleach acquisition on a SoRa spinning disc confocal. **A** Fluorescence recovery after Photo bleaching (FRAP) of entire PLPPR3 ICD condensates was performed at different time points after condensate initiation by PEG. Noticeably, the recovery rates decreased with increased time after condensate formation. The entire droplet FRAP revealed a decreased exchange of PLPPR3 ICD molecules with the surrounding. **B** Partial FRAP of PLPPR3 ICD condensates*

was performed after 30 min of condensate initiation by PEG. Partial bleaching detected an exchange of bleached PLPPR3 ICD molecules within the droplet. Scale bars 5 µm. Error bars indicate SD based on all replicates n.

4.3.3 Residues 582 – 716 after polyE box drive PLPPR3 phase separation

The ability to drive phase separation is encoded in the primary amino acid sequence (Martin & Mittag, 2018). Thereby, certain domains may act as drivers, initiating condensate formation (Hutin et al., 2023; Ramirez et al., 2023). Which residues drive condensate formation of PLPPR3 ICD? I examined the primary sequence of PLPPR3 ICD and hypothesized, that the polyE box could be a significant driver. This highly negative patch of 20 glutamic acid residues is unique and its function remains unknown. Therefore, I designed constructs of the membrane-proximal and distal ICD parts with and without polyE box, including HA-M1 tag system (Figure 21 A-D). All constructs were expressed in Expi293F cells for 4 days. After purification using the same strategy as for PLPPR3 ICD, I used the fragments to perform *in vitro* condensate assays. All experiments were performed with three times independently purified fragments.
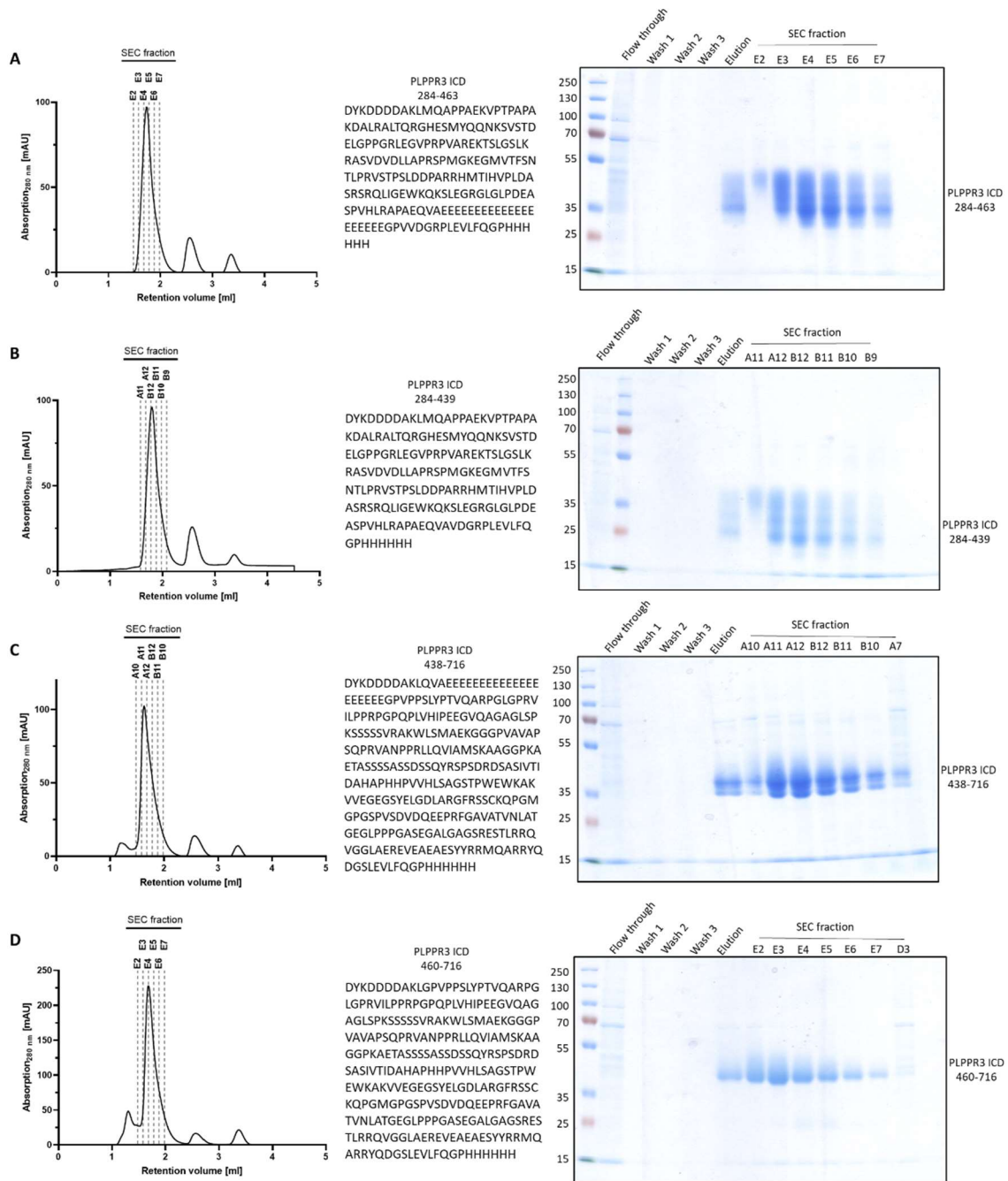
Figure 21. Purification gels of PLPPR3 ICD polyE fragments
Size exclusion chromatogram (SEC), primary amino acid sequence and purification gel of PLPPR3 ICD **A** 284 – 463, **B** 284 – 439, **C** 438 – 716 and **D** 438 – 716.

I diluted each protein to 1 µg/µl with hepes buffer (20 mM hepes, 150 mM NaCl, 5 mM DTT, pH 6.0) and initiated condensate formation with 5% PEG. After 30 min incubation at RT, I imaged condensates with a 60x oil-immersion objective on a widefield microscope. As control, I used 20 µM PLPPR3 ICD (aa 284 – 716), which displayed circular condensates (Figure 22 A). In contrast, PLPPR3 ICD which contained the polyE box (aa 284 – 463) (Figure 22 B), nor PLPPR3 ICD without the polyE box (aa 284 – 439)

(Figure 22 C) formed condensates. Despite the membrane proximal part of ICD forming no condensates, the distal PLPPR3 ICD including the polyE box (aa 438 – 716), exhibited circular condensates (Figure 22 D), however only a couple condensates were observed. PLPPR3 ICD however, in the absence of polyE (aa 460 – 716), formed more circular condensates (Figure 22 E). Interestingly, the condensates were sparser and smaller in size, compared to PLPPR3 ICD (284 – 716) condensates. With this assay, I demonstrated, that residues 460 – 716 are important for the initiation of condensates, however, since condensates decreased in overall size, I speculated that residues 284 – 439 may play a role in multivalent interactions. Consequently, the polyE box was not required for condensate initiation, however I could not exclude any importance for multivalent interactions with other PLPPR3 ICD molecules.
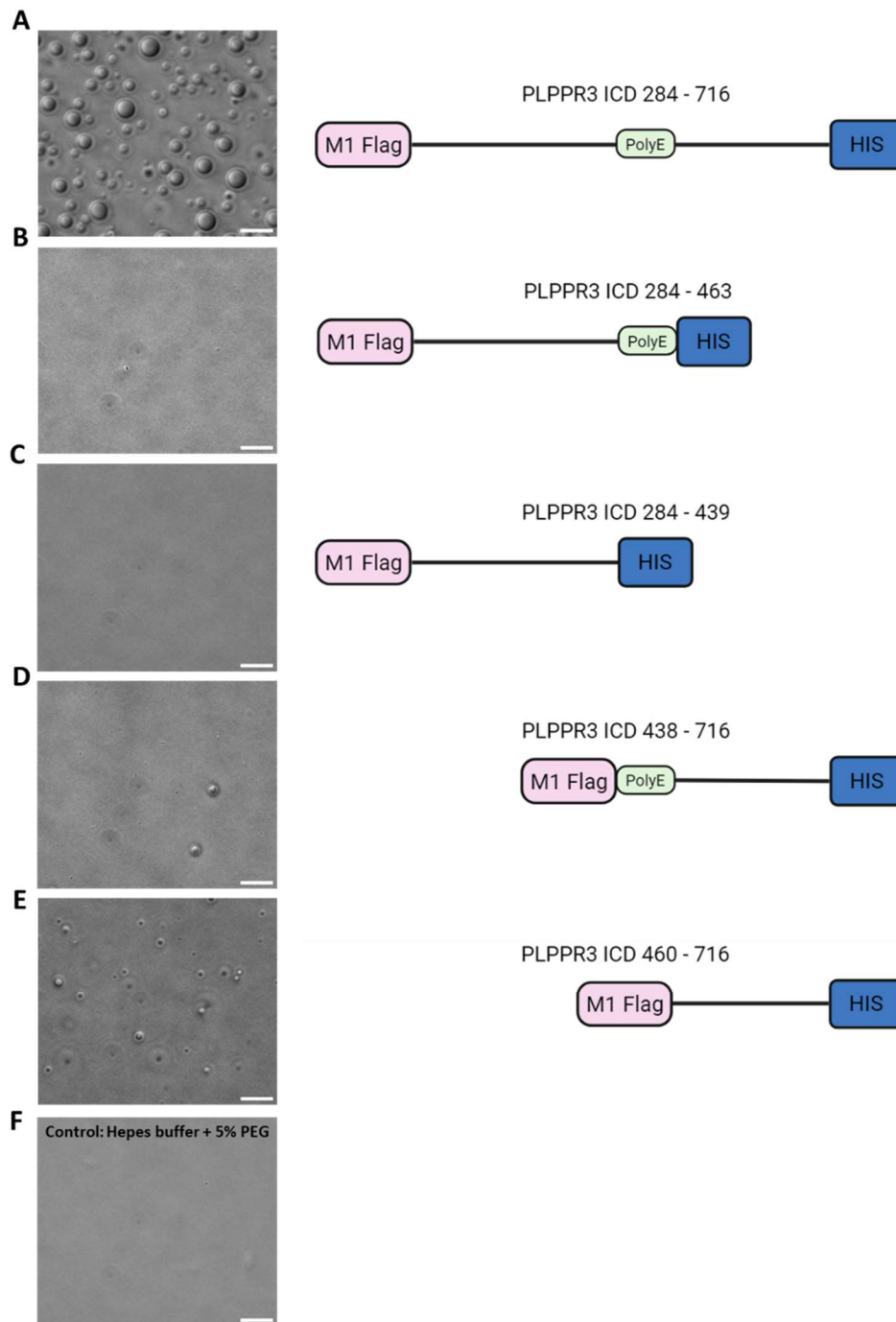
Figure 22. Condensate formation of PLPPR3 ICD polyE fragments
To identify possible driving motifs of PLPPR3 ICD (aa 284-716), I divided it into smaller fragments and checked for possible involvement of the polyE box. Purified proteins were diluted in hepes buffer (20 mM hepes, 150 mM NaCl, 5 mM DTT pH 6.0 to 1 µg/µl and LLPS initiated by adding 5% PEG. Condensates were imaged 30 min after initiation at RT using a 60x oil-immersion objective with a widefield. A 20 µM PLPPR3 ICD (aa 284-716) displayed condensates. B 49 µM PLPPR3 ICD (aa 284 – 463) including the polyE showed no condensate formation. C 43 µM PLPPR3 ICD (aa 284 – 439) lacks polyE and similarly does not form condensates. D 30 µM PLPPR3 ICD (aa 438 – 716) is the distal ICD with polyE box and exhibits a few condensates, however not many compared to entire ICD. E 33.5 µM PLPPR3 ICD (aa 460 – 716) demonstrates condensate formation, which seems to be increased without polyE in comparison. F buffer control with PEG displaying no condensate formation. Created with BioRender.com (Scale bar: 10 µm)

In a further attempt to narrow down the residues, necessary for condensate formation, I used the PLPPR3 ICD fragment (aa 460 – 716) for further investigations. I subdivided the fragment into smaller proteins and based my construct design on PONDR disorder prediction (http://www.pondr.com/). It predicted that PLPPR3 $ICD_{460 - 581}$ had a high probability p of disorder (p > 0.8), as did PLPPR3 $ICD_{638 - 716}$. In comparison, PLPPR3 $ICD_{582 - 637}$ was predicted more ordered (p < 0.5). All three constructs were expressed in Expi293F cells for 4 days. After purification (Figure 23 A-C), I performed *in vitro* assays with PEG to observe which construct undergoes condensate formation.
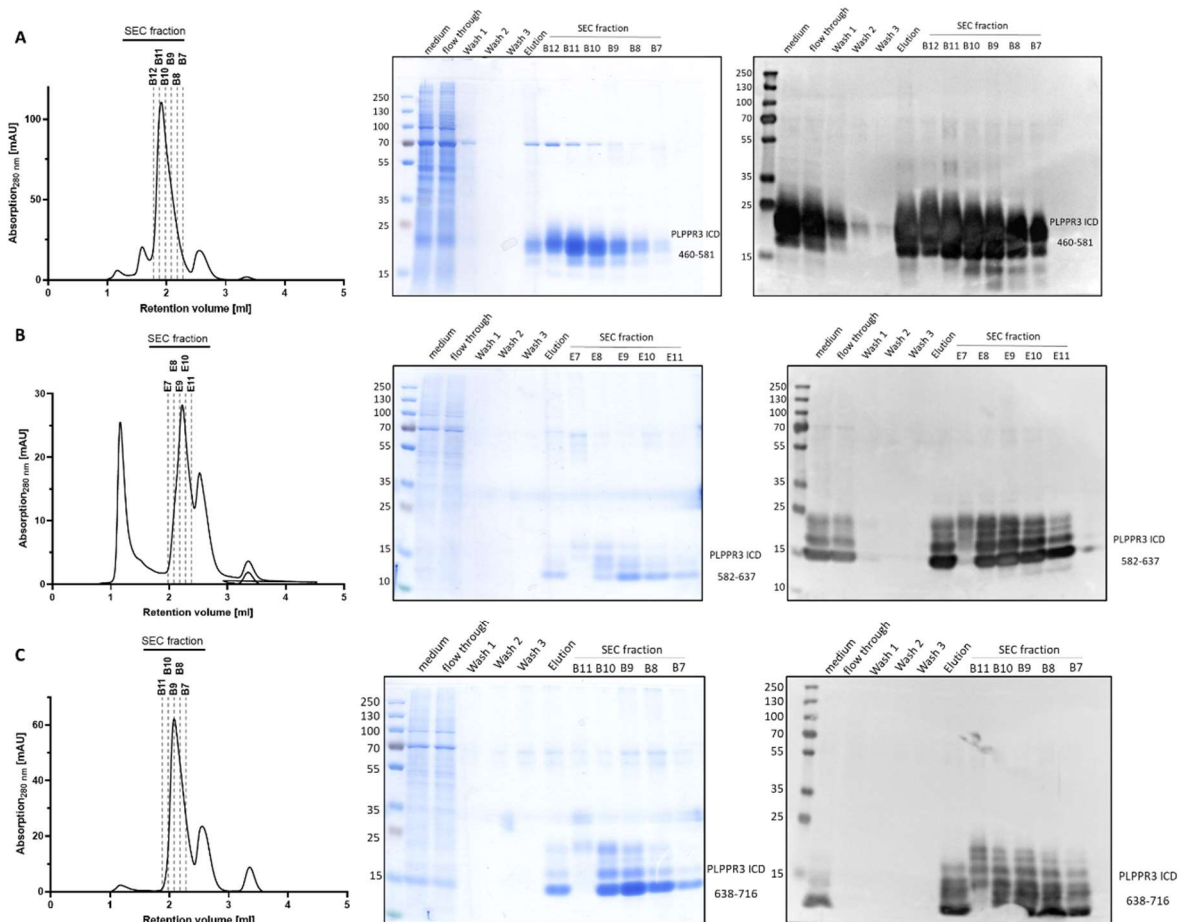
Figure 23. Purification gels of PLPPR3 ICD driver fragments
Size exclusion chromatogram, purification gel and respective western blot of PLPPR3 ICD 460 – 581 **A**, 582 – 637 **B** and 638 – 716 **C**. Western blot performed with M1-Flag antibody (in-house purified) 1:5000 and secondary mouse HRP- coupled antibody 1:5000.

For the assay, I used 65 µM PLPPR3 $ICD_{460 - 581}$, 61 µM PLPPR3 $ICD_{582 - 637}$ and 85 µM PLPPR3 $ICD_{638 - 716}$. Firstly, I investigated all constructs on their own, however I could not observe any condensates after 30 min at RT (Figure 24 A-C), while the positive control, 20 µM PLPPR3 ICD showed many condensates and the negative control, buffer

and PEG, showed none. Next, I began combining two purified constructs, realizing that perhaps PLPPR3 ICD needed two interacting stretches for condensates to form. Although I didn't observe condensate formation for the combinations of PLPPR3 $ICD_{460-581}$ with PLPPR3 $ICD_{582-637}$ and PLPPR3 $ICD_{460-581}$ with PLPPR3 $ICD_{638-716}$ (Figure 24 F-G), I recognized small, circular condensates for PLPPR3 $ICD_{582-637}$ with PLPPR3 $ICD_{638-716}$ (Figure 24 H, black arrow 1). In a simple control experiment, I combined all three ICD fragments and observed that indeed, much larger condensates formed (Figure 24 E I, black arrow 2), similar to my observation in Figure 22 E. Therefore, I concluded based on these findings, that PLPPR3 ICD condensate formation heavily depends on the stretches 582 – 637 and 638 – 716 to "initiate" condensate formation. With regards to my findings, I further speculated that other investigated stretches such as 460 – 581 and the longer 284 – 463, might serve as multivalent interaction sites, governing condensate interaction with itself.
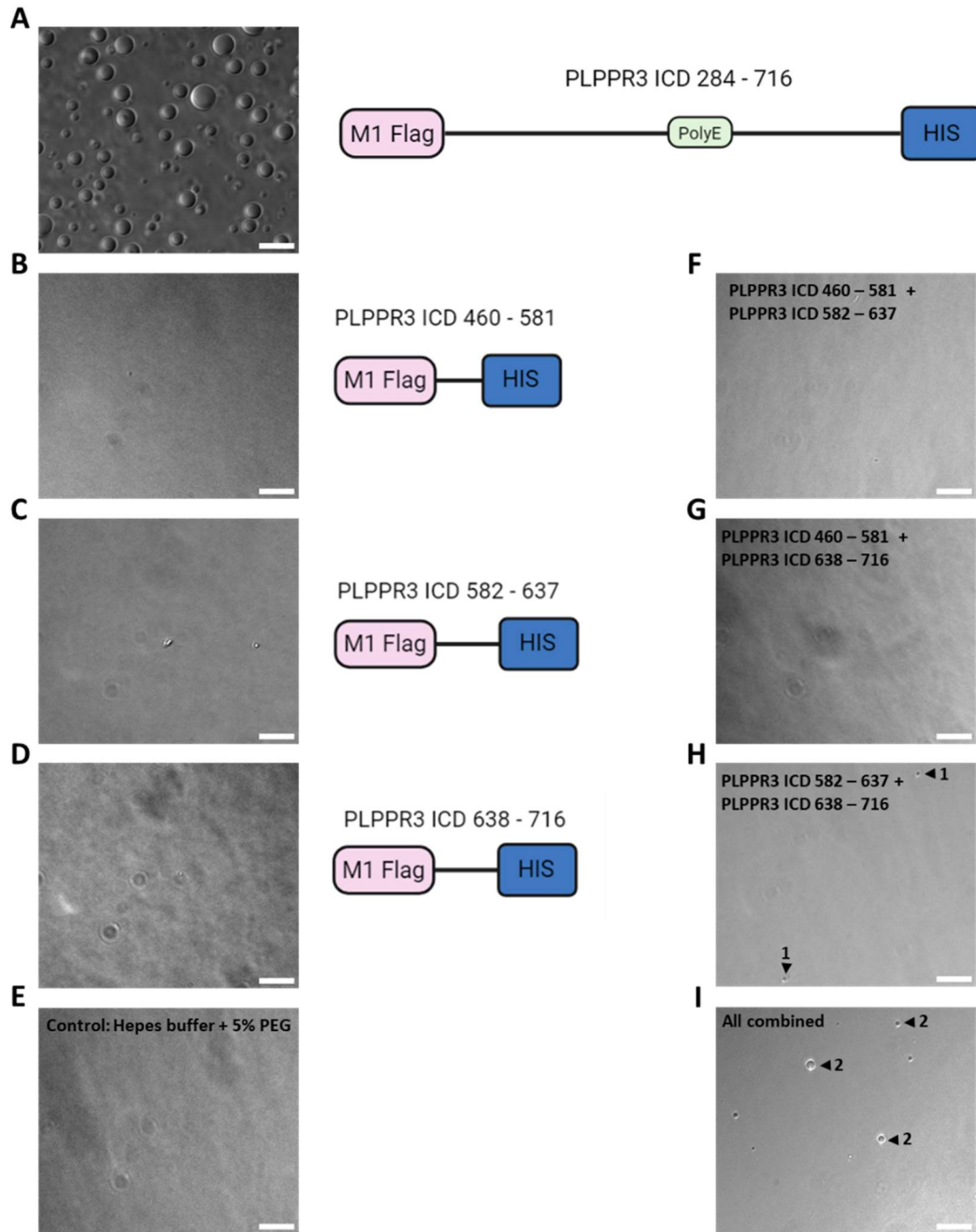
Figure 24. PLPPR3 ICD 460-716 fragments drive condensate formation

PLPPR3 ICD fragments were investigated in in vitro assays with 5% PEG8000 as crowding reagent. After 30 min incubation at RT on a 1% PVA-coated imaging chamber a 60x oil-immersion objective was utilized to visualize condensates with phase contrast. A 20 μM PLPPR3 ICD as control showed many circular condensates. B 65 μM PLPPR3 ICD$_{460-581}$, C 61 μM PLPPR3 ICD$_{582-637}$ and D 85 μM PLPPR3 ICD$_{638-716}$ showed no condensate formation as well as the buffer control in E. F Combination of 65 μM PLPPR3 ICD$_{460-581}$ with 35 μM PLPPR3 ICD$_{582-637}$ and G combination of 65 μM PLPPR3 ICD$_{460-581}$, with 85 μM PLPPR3 ICD$_{638-716}$ didn't result in any condensates, however H combining 40 μM PLPPR3 ICD$_{582-637}$, with 85 μM PLPPR3 ICD$_{638-716}$ showed small, but circular and mobile condensates (black arrow 1). I Unification of all three proteins (47 μM 460 – 581, 78 μM 582 – 637, 24 μM 638 – 716), resulted in several circular condensates (black arrow 2). Scale bar: 10 μm. Created with BioRender.com

4.3.4 Controlling PLPPR3 ICD condensate formation by CRY2 optogenetics

To test for LLPS in cells, I made use of cryptochrome 2 (CRY2) oligomerization domain from *Arabidopsis thaliana* (Park et al., 2017), which can be manipulated by blue-light (488 nm) to homo-oligomerize (Che et al., 2015). CRY2 is a wide-used optogenetic tool that is used to drive a local high concentration, thereby "seeding" condensates (Schneider et al., 2021; X. Wang et al., 2021) (Figure 25 A). By inducing homo-oligomerization, I created spatiotemporal control over CRY2 and subsequently over any protein attached to it (Duan et al., 2017; Trnka et al., 2021). Therefore, I generated a fusion construct of PLPPR3 ICD, followed by mscarlet (Bindels et al., 2016) and CRY2. The final construct pMT4-PLPPR3 ICD-mscarlet-CRY2 was expressed in HEK293T cells.

I induced oligomerization of CRY2 with initially 70% 488 nm laser power for 20 s, which was later reduced to 1% for 20 s. Clusters of PLPPR3 were observed right after blue-light activation (Figure 25 A). They were round, highly mobile and coalesced, thereby increasing their size (Figure 25 B). I monitored these clusters carefully and came to my first assessment, that I observed PLPPR3 ICD clusters with liquid-like properties. Due to CRY2 clustering after light induction, PLPPR3 ICD came into close proximity with other ICD molecules, thereby creating the necessary local concentration for phase separation.

This part of the project was handed-over to my doctoral colleague Domonkos Nagy-Herczeg, who continued work on condensate formation in cells. I created a control construct of mscarlet-CRY2 and subcloned it into a pMT4 backbone. In collaboration with Domonokos Nagy-Herczeg, we expressed and light-stimulated pMT4-mscarlet-CRY2 in HEK293T cells and observed clusters, which were not round, did not coalesce with each other and were not mobile (data not shown). With this key experiment, we concluded that PLPPR3 ICD clusters demonstrated liquid-like properties, while the control did not. This suggested that PLPPR3 ICD clusters may indeed be condensates.

With this spatiotemporal, controllable system, we have a tool to monitor condensate formation of PLPPR3 ICD in cells. We can observe coalescing events and measure fusion velocity, which gives understanding of physical parameters such as surface tension. Further, we can bleach condensates and track recovery rates by fluorescence recovery after photo bleaching (FRAP), which gives insight into molecule exchange rates of condensates with the surrounding. Taken together, I conceptualized that PLPPR3 ICD formed condensates in cells and successfully established an ontogenetic CRY2 assay.
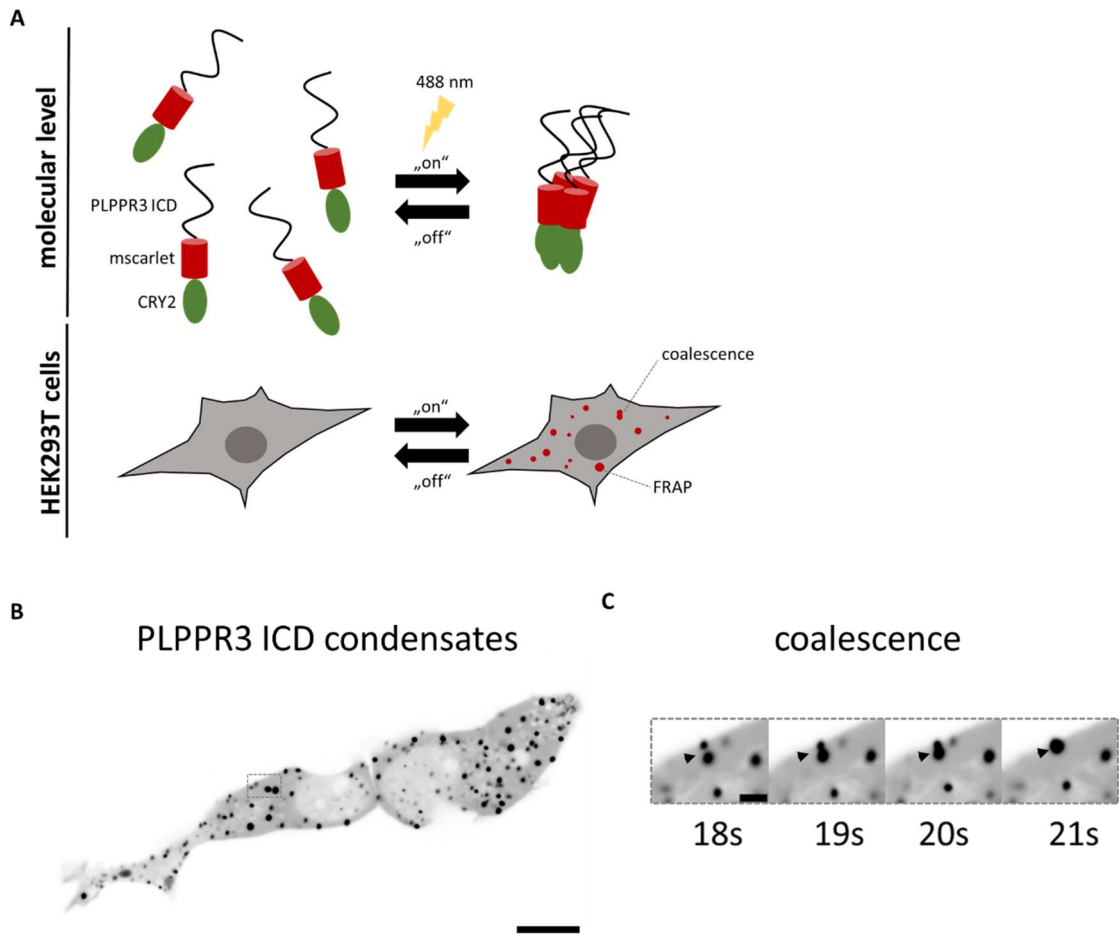
Figure 25. CRY2 optogenetic control of PLPPR3 ICD
*Transfection of PLPPR3 ICD-mscarlet-CRY2 into HEK293T cells and expression for 24 hours. Imaging was perfomed on SoRa spinning disc with 60x oil-immersion objective. Induction of PLPPR3 ICD liquid-liquid phase separation by spatiotemporal control of CRY2 clustering at 70% laser power 488 nm for 20 s. **A** Schematic representation of CRY2 clustering by light induction with blue light (488 nm). CRY2 domains homo-oligomerized, creating a "seed" that brought PLPPR3 ICD into close proximity to other PLPPR3 ICD molecules. On a cellular level, the clustering lead to condensate formation (modified after Park et al., 2017). **B** PLPPR3 ICD formed circular condensates after blue light induction (20 s; 70% 488 nm) that are highly mobile and **C** coalesced together. Scalebars: HEK293T cells: 10 μm and coalescing: 2 μm.*

4.3.5 Cross linking mass spectrometry of PLPPR3 ICD

In the previous sections, PLPPR3 ICD was introduced as an IDR that had the ability to form condensates. Many PLPPR3 ICD molecules come into close proximity and create a "demixed" condensate within a solution. The distal part of PLPPR3 ICD is important for condensatet formation, resulting in smaller condensates. To understand how efficient condensate formation functioned, I teamed up with our postdoc Dr. Willem Bintig and implemented cross linking mass spectrometry (CL-MS) in collaboration with the group of Prof. Fan Liu from Leibnitz institute of pharmacology (FMP) Berlin. In general, during protein crosslinking two amino acids are chemically linked by a covalent bond

(Jayachandran et al., 2022). This process involves a crosslinker, a molecule of defined length with reactive groups on either side for chemical linking (Lenz et al., 2021). CL-MS combines the power of crosslinking with mass spectrometry and is used to describe protein-protein interactions in multi-protein complexes and protein binding interfaces (F. Liu et al., 2015; O'Reilly & Rappsilber, 2018; Piersimoni et al., 2022). Therefore, we utilized this method to address the question which amino acid residues come into close proximity and interact during condensate formation.

We used a disuccinimidyl suberate (DSS) crosslinker with a distance of 11.4 Å to cross link PLPPR3 ICD during condensate formation, versus without condensates. Each end of the cross linker contained a reactive N-hydroxysuccinimide (NHS) ester group that reacted with primary amines such as lysine residues. We used 20 µM PLPPR3 ICD with and without 5% PEG8000 (w/v), checked for condensate formation under a light microscope with a 20x objective and added DSS (0.5 mM final concentration) after 30 min incubation. DSS was incubated for 30 min at RT and quenched with 1 M Tris/HCl pH 8.0 (50 mM final concentration). After reduction with dithiothreitol (DTT) and alkylation with chloroacetamide (CAA), we boiled samples in the presence of Laemmli buffer and separated samples by SDS-PAGE on a 10% Gel. Proteins bands were stained with Coomassie, cut-out and four independent CL-MS experiments analyzed by our collaborators at FMP Berlin. The analysis of the data was performed in collaboration with Dr. Willem Bintig (Figure 26).

We observed interesting differences in band patterns in the coomassie stained gel (Figure 26 C). The first and second lanes represented controls of PLPPR3 ICD with and without PEG with no apparent differences, due to the denatured environment and boiling of the samples. Lanes three and four on the other hand, showed crosslinked PLPPR3 ICD. Lane three displayed PLPPR3 ICD higher oligomer band patterns of 250 kDa and above (Figure 26 C; black arrows 1), which we expected due to crosslinking of several ICD molecules together. However, when we added PEG to PLPPR3 ICD, we initiated condensate formation *in vitro* and crosslinked molecules during that state. In lane four, we observed that PLPPR3 ICD shifted to even higher oligomer patterns (Figure 26 C, black arrow 2), which was visible by a coomassie blue stained gel pocket. On the other hand, monomer band intensity (Figure 26 C, black arrow 3) decreased, compared to monomer bands in all other lanes. Each cut-out band was analyzed by mass spectrometry and returned as "hits". Each "hit" represented a peptide with a lysine residue crosslinked

to another. We used the hits to quantify and visualize proximities of lysine residues before and after molecular crowding by PEG (Figure 26 D). Heat maps displayed all lysine residues of PLPPR3 ICD on x- and y-axis and correlated, which two residues were crosslinked due to close proximity.

We observed pattern-specific changes with and without PEG. Interestingly, without PEG, we detected several crosslinks such as lysine365 with lysine341 or lysine348, lysine551 with lysine 507 and lysine611 with lysine551. We carefully translated these results as close proximity of the first half of PLPPR3 ICD to the first half of other PLPPR3 ICD molecules. Identically, for the last half of PLPPR3 ICD. However, interpretation had their limits, as we were not able to distinguish between intra- and intercrosslinks (Figure 26 B) and did not have CL-MS data after lysine634, due to a lack in lysine residues. Despite this, we analyzed patterns of crosslinked PLPPR3 ICD with PEG, where we detected an increase in crosslinked residues. We interpreted this as increase of proximity due to crowding with PEG and interaction of PLPPR3 ICD molecules, due to condensate formation. Impressively, we detected several intercrosslinks such as lysine341, lysine365, lysine551, lysine557, lysine611 and lysine633. These interactions were unequivocally a result of two PLPPR3 ICD molecules, because crosslinkers were only able to bind one lysine residue. Therefore, a crosslink between lysine341 to lysine 341, was definitely an intracrosslink. All other crosslinks were more difficult to decipher, however the monomer bands were speculated to be intracrosslinks too. In an attempt to map areas of proximity we decided to map monomer against multimer bands, with and without PEG (Figure 26 E-F).

To highlight areas of differences, we subtracted hits with PEG from hits without. The heat map in Figure 26 D, visualized areas of differences in monomer and multimer bands by color. Hits that decreased were red and hits that increased green. Various intercrosslink hits increased such as lysine341 to lysine348, lysine365 or lysine551. On the other hand, several hits decreased in the monomer band, such as lysine341 to lysine365. In general, monomer hits decreased, while multimer hits increased as a result. However, various hits were detected uniquely after crowding with PEG that localized to the distal part of PLPPR3 ICD (Figure 26 D).

I interpreted from these findings, that PLPPR3 ICD had minimally two stretches that may play a role in condensate initiation. Both were located at the distal part of PLPPR3 ICD and cover residues lysine551 to 557 and lysine 611 to 633. Due to the fact, that we observed possible interaction around lysine341 to 365 before crowding with PEG, I excluded this stretch to be important for condensate initiation, however speculated on an important role in increasing multivalent interactions.
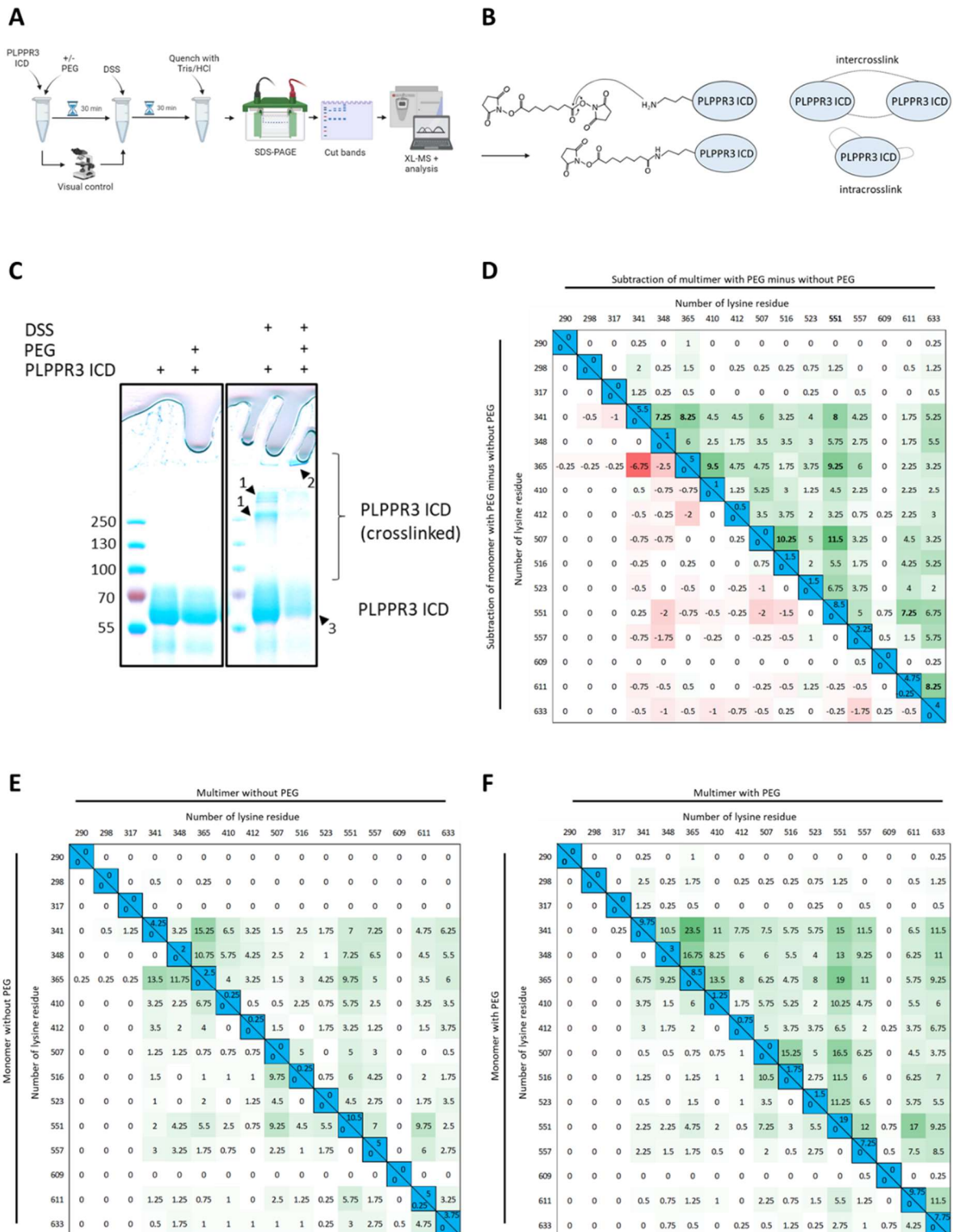
Figure 26. Pattern-specific differences of crosslinked PLPPR3 ICD with and without PEG
A Schematic representation of workflow of crosslinking PLPPR3 ICD with DSS crosslinker. Crosslinked samples were separated by SDS-PAGE on a 10% Gel and stained with coomassie. Gel bands were cut out and sent for cross-linking mass spectrometry (CL-MS). Created with BioRender.com B NHS ester reaction of DSS crosslinker with primary amine such as lysine. Both NHS groups can react and crosslink lysine residues covalently. Thereby, two types of crosslinks emerge, intercrosslinks between two proteins and intracrosslinks where one lysine is crosslinked to another of the same molecule. C Separated PLPPR3 ICD proteins in coomassie gel with and without crosslinker DSS. Lane 1 displays PLPPR3 ICD control, lane 2 PLPPR3 ICD control with PEG, while lane 3 presents PLPPR3 ICD crosslinked with DSS and lane 4 PLPPR3 ICD with PEG forming condensates crosslinked with DSS. D Heat map of subtracted multimer and monomer bands. The numbers displayed the increase (red) or decrease (green) of overall monomer band hits compared to multimer band hits. All blue numbers represented intercrosslinks. The monomer and multimer band hits before and after PEG are visualized in E and F. Observable was a decrease in monomer hits and an increase in multimer hits with PEG. Analysis and heatmaps of D, E and F kindly provided by Willem Bintig.

4.3.6 Conclusion Chapter 3

This Chapter was aimed at addressing if disordered PLPPR3 ICD was able to undergo liquid-liquid phase separation (LLPS). LLPS has emerged as a common key mechanism for orderly working cellular function (Babinchak & Surewicz, 2020). Condensates or membrane-less organelles can thereby have diverse features, ranging from reaction compartments to e.g. creating architecture in the synaptic zone (Feng et al., 2019; Peng et al., 2021).

In my first set of experiments, I investigated successfully, that PLPPR3 ICD was able to undergo LLPS in cells by optogenetic CRY2 control (Figure 25) and *in vitro* by crowding with PEG8000 (Figure 17 A). In the next set of experiments, I studied the main characteristics of liquid-like condensates. Coalescence of droplets was observed in many experiments (Figure 17 B) and is a classic property of liquids experiencing surface tension (Widom, 1988).

I employed Fluorescence Recovery after Photobleaching (FRAP) to further evaluate the liquidity of PLPPR3 ICD condensates. The FRAP analysis encompassed the entire condensate (Figure 20 A), as well as partial FRAP (Figure 20 B), revealing notable recovery of PLPPR3 ICD condensates and effective internal reorganization, which indicated liquid-like and dynamic structures (Gao et al., 2021; N. O. Taylor et al., 2019). To understand concentration dependency of PLPPR3 ICD condensates, I recapitulated a phase diagram using PEG8000 *in vitro* (Figure 18). I identified that PLPPR3 ICD can form condensates at 5 µM with 1% PEG, which speculated is not a high concentration considering the crowding effect of the cytoplasm itself (Mourão et al., 2014). However, currently the local concentration of PLPPR3 in neurons is not known.

In the last set of experiments, I explored the polyE box as the "LLPS driving domain" of PLPPR3 ICD. The polyE box as prominent stretch of 20 glutamic acid residues was not detected as LLPS initiator by *in vitro* experiments (Figure 22 A-C). However, I detected that residues 460 – 716 play a role in forming condensates (Figure 22 D). In an approach to examine this further, I fragmented PLPPR3 ICD 460 – 716 into shorter peptides, but could not monitor any condensates *in vitro*. Only the combination of peptides from residues 582 – 637 and 638 – 716 resulted in condensates (Figure 24 H). With regards to the performed crosslinking mass spectrometry (Figure 26 D), I propose that the "driver sequence" of PLPPR3 ICD condensate formation is between residues 582 to 716. Although, pinpointing single residues, involved in condensate formation was not possible yet, this is ongoing work. In addition, I propose that other fragments such as 460 – 481 and the first half of PLPPR3 ICD 284 – 459 might offer several contact sites, thereby increasing multivalence to form larger sized condensates (Figure 24 I) (C. Chen et al., 2022; Holehouse & Pappu, 2018).

Taking all experimental data together, I was able to certify the prediction (Figure 16 A) and demonstrated that PLPPR3 ICD could form liquid-like condensates *in vitro* and in cells. Although, I couldn't fully discover residues important for LLPS, I found out which sequence parts have a major impact. Given that PLPPR3 ICD is an isolated protein domain, in the next Chapter I will elucidate a potential mechanism involving also the transmembrane domains.

Chapter 4. Building an *in vitro* model of PLPPR3 ICD condensates as filopodia-facilitators

Branching is an essential mechanism in neurons to generate an extensive network of interconnecting neurites (Joachim Fuchs & Eickholt, 2021a). Branches emerge from precursors like filopodia, which are thin, actin-rich, finger-like protrusions that extend from the plasma membrane (Leondaritis & Eickholt, 2015). Our previous work, identified that PLPPR3 is able to promote filopodia at the axonal plasma membrane of neurons (Brosig et al., 2019). Further findings demonstrated, that PLPPR3 localized to clusters along the axon, which overlap which branching events.

We hypothesize that these clusters might be PLPPR3 condensates with two main purposes: aiding membrane deformation and promoting actin polymerization, by creating a high local concentration of actin monomers. In order to investigate and explore this mechanism, I began constituting an *in vitro* model. I tested membrane deformation by PLPPR3 ICD condensates, as well as G-actin recruitment into and F-actin polymerization out of PLPPR3 ICD condensates. Our model further hypothesizes, that PLPPR3 ICD condensates assists in filopodia formation. In collaboration with Domonkos Nagy-Herczeg, I investigated an optogenetic approach in parallel, to study this mechanism in cells, which will not be covered in this thesis.

4.4.1 PLPPR3 ICD condensates reshape lipid membranes

Membranes curvature creates the complex architecture of cells essential during different cellular physiological states and responses, including vesicle budding, endocytosis or filopodia formation (Jarsch et al., 2016). Due to PLPPR3s membrane association with six transmembrane domains, the next step was to investigate how PLPPR3 ICD phase separation may impact lipid membranes. Membrane localization of PLPPRs, either by transmembrane domains or by membrane-tagged fusion proteins were essential for PLPPR-induced filopodia formation (Fuchs et al., 2022). Hence, we hypothesized that the anchored, phase separating ICD of PLPPR3 may create substantial compressive stress at the lipid membrane, which results in membrane bending (Yuan et al., 2021).

Therefore, in collaboration with the laboratory of Dr. Roland Knorr (Humboldt University Berlin), I tested this concept using giant unilamellar vesicles (GUVs) as model

system. To mimic membrane proximity of PLPPR3 ICD condensates, I attracted PLPPR3 ICD by its c-terminal 6x his-tag to the GUV interface (Figure 27 A-B). GUVs have been extensively studied before and serve as ideal, yet simple, *in vitro* systems, mimicking physiological membranes (Bhatia et al., 2015; Carvalho et al., 2008). We incorporated nitrilotriacetic acid (NTA) tagged lipids into GUVs (Pramanik et al., 2022; Richmond et al., 2011; Schmid et al., 2015) to exploit Nickel-NTA (Ni-NTA) metal chelating affinity of histidine-tagged (his-tag) proteins (Porath et al., 1975). The aim was to visualize membrane reshaping as schematically depicted in Figure 27 C. I used several different lipid compositions such as neutral 1-palmitoyl-2-oleoyl-sn-glycero-3-phosphocholine (POPC) and POPC with 20% charged 1-palmitoyl-2-oleoyl-sn-glycero-3-phospho-L-serine (POPS). All lipid compositions included 0.4% 1,1'-Dioctadecyl-3,3,3',3'-Tetramethylindocarbocyanine Perchlorate (DiI_{C18}) dye and where specified 5% NTA doped lipids.

I observed that POPC with 20% POPS resulted in no attraction of PLPPR3 ICD condensates to the GUV interface (Figure 27 D, left panel). When I added 5% NTA moiety to the lipids, I observed many PLPPR3 ICD condensates at the GUV interface (Figure 27 D, right panel). In addition, several GUVs were reshaped as illustrated by the white arrow. In comparison, GUVs, electroformed from POPC lipids, already presented some condensate interaction and minimal reshaping (Figure 27 E, left panel). This time, adding 5% NTA moiety did not result in more attraction (Figure 27 E, right panel). However, the assay as presented here, was only conducted once. Several pilot studies conducted with PLPPR3 ICD condensates pointed towards the same trend of membrane bending.

In general, PLPPR3 ICD condensates were sufficient to reshape lipid membranes. An additional interaction of condensates with GUV interface by NTA moiety strongly depended on the lipid composition. Therefore, I hypothesized that PLPPR3 transmembrane domains could potentially act as condensate anchor, however more empirical data would be necessary to authenticate this hypothesis.
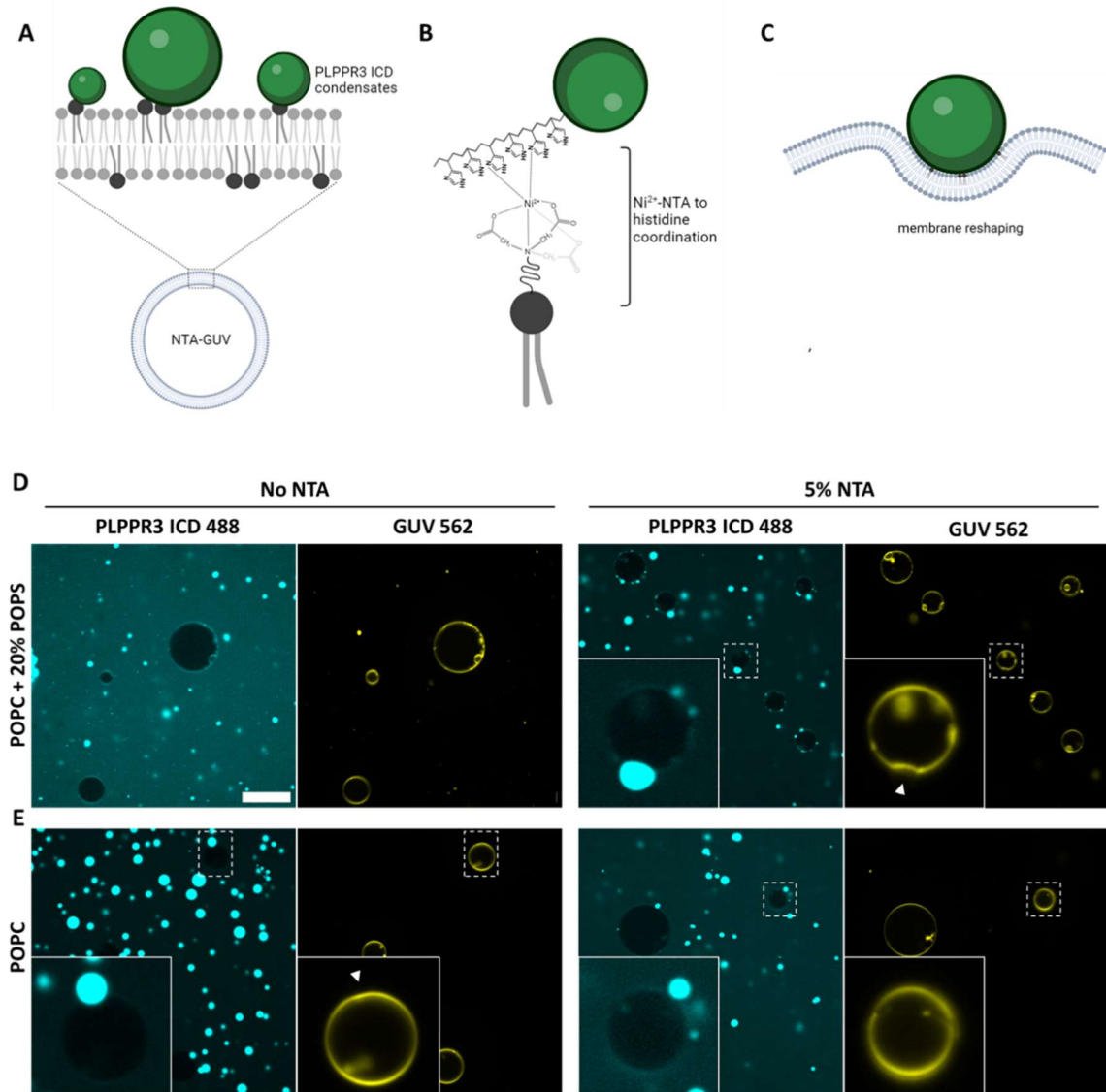
Figure 27. PLPPR3 ICD condensates induce membrane reshaping
A Scheme of condensate interaction with membrane. B Scheme of Ni^{2+}-NTA affinity interaction with histidine tagged protein. NTA binds to Ni^{2+} ions via four coordination sites, while the other two are coordinated from the histidine tag. C Scheme of membrane reshaping by PLPPR3 ICD condensates. The condensates are affinity attracted via Ni^{2+}-NTA. D Electroformed POPC + 20% POPS GUVs were analyzed with 20 µM PLPPR3 ICD and 5% PEG. Left panel: With no NTA moiety, condensates did not interact with GUVs. Right panel: Adding 5% NTA moiety affinity pulled PLPPR3 ICD condensates to GUV interfaces, which reshaped the lipid membrane (white arrow). E Electroformed POPC GUVs with 20 µM PLPPR3 ICD and 5% PEG. Left panel: Several condensates were observed to interact with and minimally reshape GUV in absence of NTA (white arrow). Right panel: In presence of 5% NTA interaction with GUV was detected, however no membrane reshaping. Scale bars: 20 µm. Created with BioRender.com

4.4.2 Recruitment of actin into PLPPR3 ICD condensates

Filopodia generation is a well-described mechanism of PLPPR3 that likely involves the actin cytoskeleton (Brosig et al., 2019; J. Fuchs et al., 2022; Joachim Fuchs & Eickholt, 2021a). Filamentous Actin (F-actin) is formed by polymerization of globular actin (G-actin) into dynamic filaments (Cooper, 2000). Under physiological conditions with Mg^{2+} or other divalent ions present, polymerization occurs spontaneously in dependence on the actin monomer concentration (Kang et al., 2013). Divalent ions have been observed to stabilize binding of adenosine 5'-triphosphate (ATP) to actin (Kabsch et al., 1990). As a dynamic filament, actin undergoes continuous association and dissociation, resulting in a balanced state referred to as treadmilling (Wegner, 1976). Subsequently to the polymerization of ATP-actin into filaments, ATP is hydrolyzed to adenosine 5'-diphosphate (ADP), leading to slow dissociation of inorganic phosphate (P_i) and accordingly to ADP-actin (Jégou et al., 2011; Pollard, 2016). Although, PLPPR3 has not been shown to bind actin directly, we hypothesized that PLPPR3 ICD condensates can interact with actin and serve as actin nucleation compartments, as previously shown for the actin binding protein VASP (Graham et al., 2023) and N-WASP (Case et al., 2019). Both VASP and N-WASP have been demonstrated to form condensates, recruit actin monomers into the condensate and to polymerize out of condensates.

To determine the optimal actin concentration, I conducted *in vitro* assays testing various concentrations. In order to prevent self-assembly, I used an actin concentration below the critical concentration of ~ 2 µM. Therefore, I utilized 1.2 µM actin in accordance with other published actin polymerization assays (Graham et al., 2023; McCall et al., 2018). In addition, in order to investigate the formation of an actin network, I used actin at 2.2 µM, 3.2 µM and 4.2 µM. Prior to the assay, actin unserwent centrifugation at 100.000x g for 1 h at 4°C to sediment potential nucleation seeds.

I combined unlabeled actin monomers with 5% monomers, labeled with atto-actin 647, to visualize actin under a SoRa spinning disc confocal with a 60x oil-immersion objective. To test potential crowding effects on actin, I tested all concentrations in presence and absence of 5% PEG. All experiments were performed with F-actin buffer, a buffer composition, that contained all components essential for actin polymerization, including working concentrations of 100 mM KCl, 1 mM ATP and 2 mM $MgCl_2$. Figure 28 A shows that at 1.2 µM actin, no actin filaments were observed in the absence of PEG. With 5% PEG however, a few filaments were observed, which indicated beginning of actin

filament polymerization. All tested concentrations above 2.2 µM (Figure 28 B – C), resulted in actin polymerization and the formation of an actin network. Notably, there was an increase in network formation, with increased actin concentration, regardless of presence or absence of PEG. Thus, I implemented 1.2 µM actin for all further downstream *in vitro* assays, which is in accordance to the concentration utilized by Graham et al., 2023 and McCall et al., 2018.
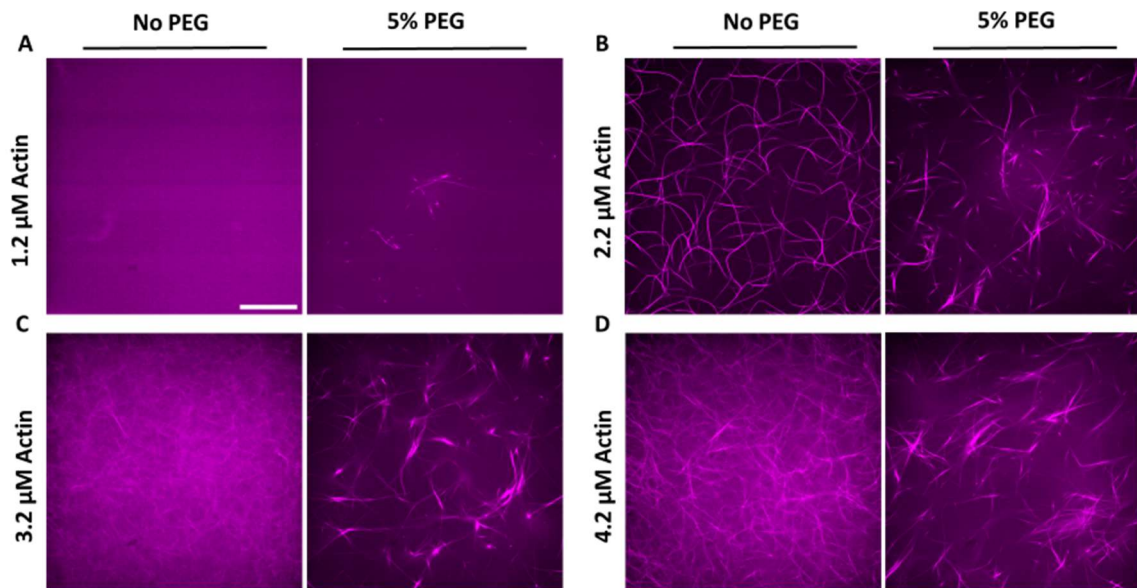
Figure 28. *In vitro* **actin polymerization at various concentrations**
Various actin concentrations ranging from 1.2 µM to 4.4 µM were tested in presence and absence of 5% PEG. A 1.2 µM actin was observed as a dispersed signal without any actin filaments, unlike in the presence of PEG. B 2.2 µM actin displayed a loosely polymerized actin network both, with and without PEG. C-D 3.2 µM and 4.2 µM actin respectively, in the presence and absence of PEG, exhibited a highly dense polymerized actin network. N=3. Scale bar 20 µm

Actin is an abundant and conserved protein that can transit from monomeric G-actin to filamentous F-actin (Dominguez & Holmes, 2011). F-actin plays a pivotal role in the formation and support of filopodia (Nemethova et al., 2008). In order to test for actin recruitment into PLPPR3 ICD condensates, I performed an *in vitro* assay with the mixture of monomeric 647-fluorophore labelled alpha-actin and 488-fluorophore labelled PLPPR3 ICD in the presence of 5 µM Latrunculin B (Lat B), which disrupts actin filaments. Lat B is a toxin isolated from Red Sea Sponge, which inhibits actin polymerization by forming a stoichiometric 1:1 complex with actin monomers (Spector et al., 1983, 1989), thereby preventing F-actin assembly. In collaboration with Dr. Thomas Böddeker (Knorr lab, Humboldt University Berlin), we determined the co-partioning efficiency of actin into PLPPR3 ICD condensates (Figure 25 B).

After PLPPR3 ICD condensate initiation with 5% PEG, I observed that actin noticeably changed properties. While actin signal was homogenously dispersed in the absence of PEG induced condensates (cf. Figure 28 A), actin signal shifted to round shapes, which was due to co-localization with PLPPR3 ICD condensate signal (Figure 29 A). This indicated, that actin had a high affinity towards the condensate. Compared to the dispersed actin signal in absence of PEG induced condensates, actin signal with PEG was high in the condensate and low in the surrounding.

We analyzed the co-partioning efficiency with help of a radial distribution function g(r) in dependence of the condensate radius (Figure 29 B). This mathematical model is widely used in molecular simulations, to describe the probability distribution of locating the center of one particle in close proximity to another (Aste & Di Matteo, 2006; Frenkel & Smit, 2002; Mason & Clark, 1966; Scott, 1962). To specify, we analyzed the fluorescence intensity outside of the condensate, in comparison to intensity within the condensate, in both laser channels. Due to a sequential image acquisition for each laser channel, the condensates visually do not overlap in the image. We solved this by tracking each condensate, in each channel, during data analysis. The radial distribution function (RDF) of actin (Figure 29 B, magenta), displayed a high probability to be in close proximity to PLPPR3 ICD. Therefore, I concluded from the experimental evidence, that actin co-partionend into PLPPR3 ICD condensates.
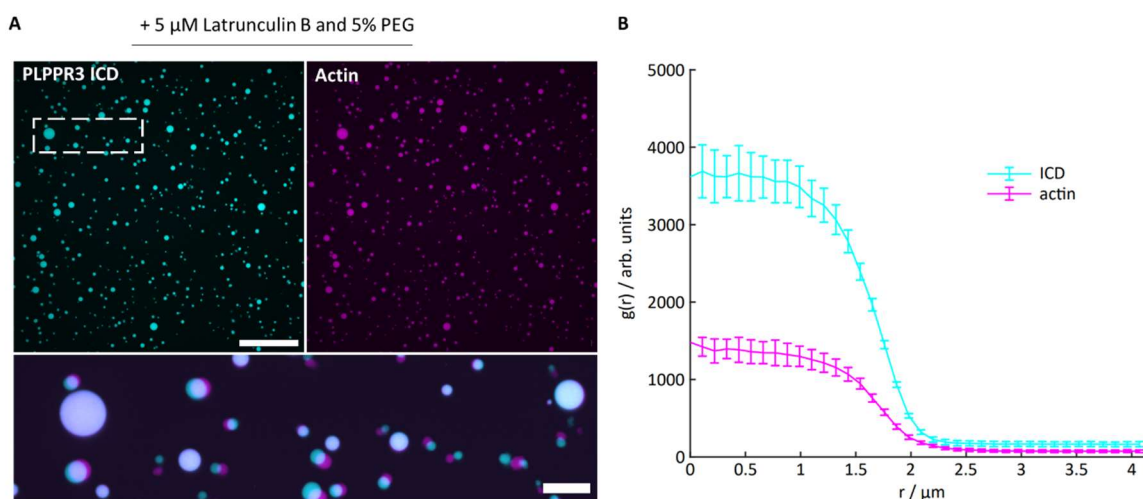
Figure 29. Actin co-partioning into PLPPR3 ICD condensates
*Condensates formed with 20 µM PLPPR3 ICD in the presence of 1.2 µM actin, 5% PEG and 5µM Latrunculin B to avoid actin polymerization. **A** Maximal projection of 64 slices (Δz 0.3 µM) of PLPPR3 ICD condensates (cyan) and actin (magenta). Actin co-partitions into PLPPR3 ICD condensates. Scale bars 50 µM and 10 µM respectively. **B** Analysis of actin co-partioning using a radial distribution function (RDF) in dependence of condensate radius in µm. The RDF showed a high probability of actin to be in close proximity to PLPPR3 ICD. Analysis and graph kindly provided by Dr. Thomas Böddeker. Error bars indicated SEM of all performed experiments.*

4.4.3 F-actin polymerization from PLPPR3 ICD condensates

To investigate, if actin filaments polymerize in PLPPR3 ICD condensates *in vitro*, I utilized 647-fluorophore labelled alpha-actin and 488-fluorophore labelled PLPPR3 ICD in the presence of F-actin buffer containing 1 mM ATP, 2 mM $MgCl_2$ and 0.1 mM KCl. I employed actin at 1.2 µM below the critical concentration of ~ 2 µM to avoid spontaneous polymerization. After addition of PEG as condensate initiator, I incubated the samples at RT for 30 min and imaged condensates with a 60x oil-immersion objective on a SoRa spinning disc confocal.

I observed that actin formed ring-shaped F-actin structures in PLPPR3 condensates. In absence of PEG (and therefore no PLPPR3 ICD condensates), ring-shaped F-actin structures did not form (Figure 30 A-C, left panels). In addition, I detected several filamentous structures erupting from condensates (Figure 30 A, right panel). Thereby, the filament wasn't exposed to the aqueous solution, but rather co-extended PLPPR3 ICD condensates.

I investigated the importance of chronological order of PLPPR3 ICD, actin and PEG addition. Therefore, I combined (i) PLPPR3 ICD, actin and PEG, (ii) actin and PEG, and added PLPPR3 ICD after 15 min and (iii) PLPPR3 ICD and PEG, and added actin after 15 min. Each setup was imaged after 30 min incubation.

Generally, I perceived less filamentous structures and more ring-shaped F-actin structures when I combined PLPPR3 ICD, actin and PEG at once (Figure 30 A and D). Interestingly, in two of three independent experiments, I observed that pre-incubation of actin and PEG, with PLPPR3 ICD added afterwards, resulted in more circular condensates that co-partioned actin, but lacked ring-shaped F-actin structures (Figure 30 B and E). Instead, I observed actin clustered on condensates, indicating that condensates might be necessary for actin accumulation and polymerization. In the last setup, I pre-incubated PLPPR3 ICD with PEG, which formed condensates and thereafter added actin. Impressively, actin formed ring-shaped F-actin structures and polymerized out of several condensates (Figure 30 C and F). In addition, numerous condensates became torus-shaped with no PLPPR3, nor actin density in the center. Distinctively, several condensates containing ring-shaped F-actin coalesced, however ring structures did not merge. As a result, plenty condensates were not circular, which indicated a constant struggle between surface tension and actin polymerization.

Taken together, these results demonstrated that G-actin co-partioned with PLPPR3 ICD condensates and induced the transition from monomer to F-actin polymer state. F-actin in condensates formed ring-shapes, which sporadically extended polymerized structures from condensates. Thereby, condensates co-extended with F-actin structures, which resulted in a deformed, non-circular condensate. I hypothesize that actin polymerization is enhanced, due to increased actin concentrations within the condensate. In addition, I investigated the possible dependence of actin polymerization from PLPPR3 ICD condensates. Notably, actin polymerization depended on PLPPR3 ICD condensates to form. Condensates that formed simultaneous with or before actin polymerization, formed ring-shaped F-actin structures and polymerized from condensates. In summary, it is likely that PLPPR3 ICD condensates, play a pivotal role as an intricate actin nucleation mechanism, facilitating actin polymerization.
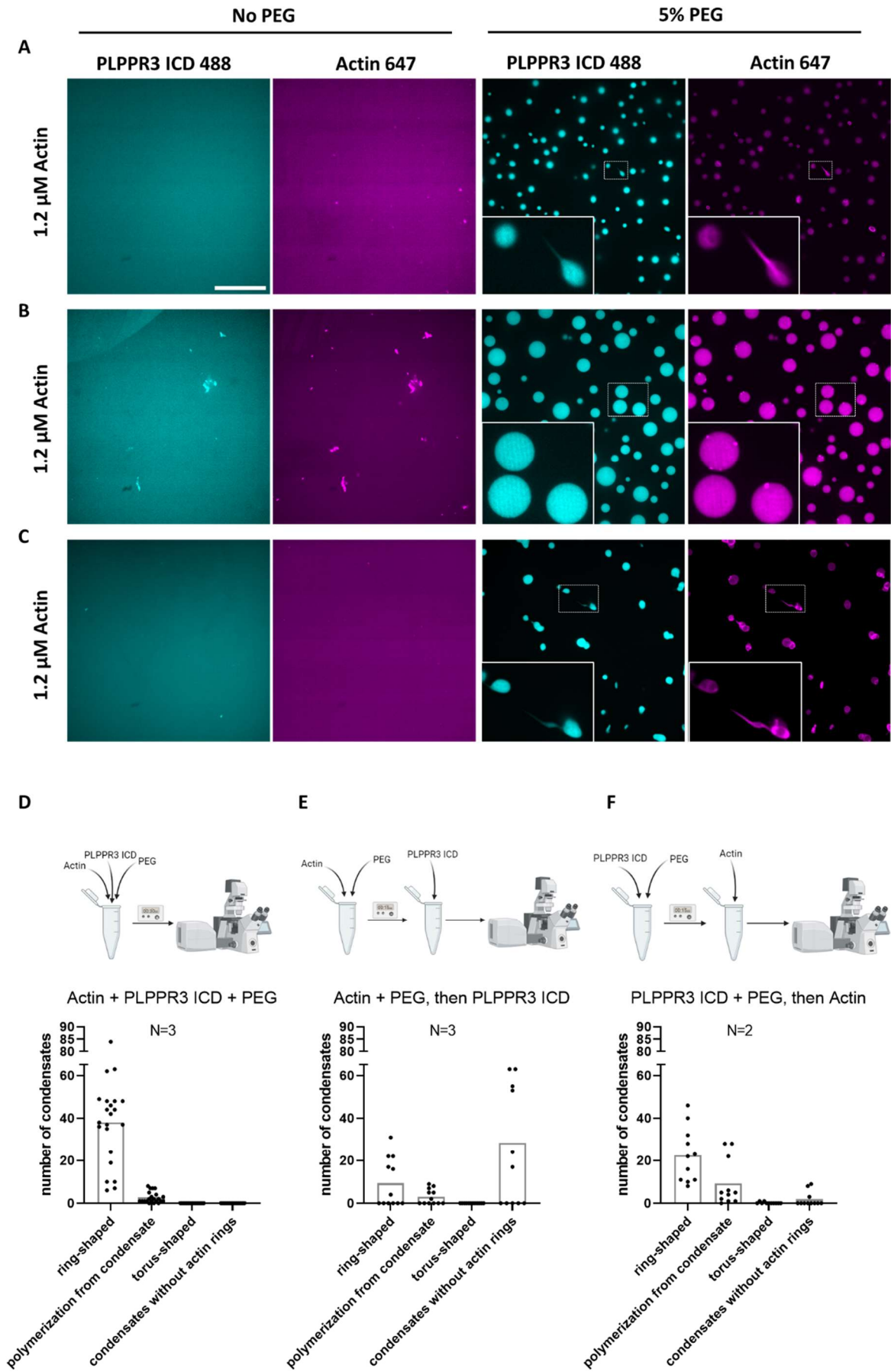
Figure 30. Actin polymerization from PLPPR3 condensates
Actin was observed as ring-shaped, torus-shaped, polymerized from condensates and co-partionend without rings, depending on the order of incubation. **A** 20 µM PLPPR3 ICD was incubated with 1.2 µM actin and 5% PEG for 30 min at RT, thereby forming condensates and polymerized actin simultaneously. **B** 1.2 µM actin was pre-incubated with 5% PEG. After 15 min, 20 µM PLPPR3 ICD was added and formed condensates, which resulted in no ring-shaped F-actin structures. **C** 20 µM PLPPR3 ICD was incubated with 5% PEG to form phases. After 15 min, 1.2 µM actin was added. Scale bars: 20 µm. **D-F** Incubation scheme and quantification of A-C, respectively. Created with Biorender.com.

4.4.4 Actin to PLPPR3 ICD ratio determines condensate deformation

To test the effect of condensate deformation through F-actin intermediate states, such as ring-shaped-, rod-shaped- and toroid-shaped F-actin structures, I used various ratios of actin and PLPPR3 ICD (Figure 31). Actin was observed to polymerize out of PLPPR3 ICD condensates through intermediate states, such as ring-shaped F-actin structures, thereby deforming the condensates. To control for interaction of actin and PLPPR3 ICD, I monitored samples without and with 5% PEG. After initiation of condensate formation, samples were incubated 30 min at RT, before imaging was performed with a 60x oil-immersion objective on a SoRa spinning disc confocal. At an actin to PLPPR3 ICD ratio of ~ 1:20, circular condensates, co-partioning actin were monitored with 5% PEG. Ring-shaped F-actin structures began forming, however not many polymerization events from the condensates were observed. In comparison without PEG, no interaction was detected.

Increasing the actin concentration to 5.2 µM (ratio ~ 1:4) resulted in a more clear deformation of circular condensates towards torus shapes. Actin was observed to polymerize out of many tori shaped "condensates" (Figure 31 A middle panel). As in previous experiments without PEG, a dispersed signal of PLPPR3 ICD was detected, while additionally actin monomers polymerized to F-actin, forming an actin network. Escalating the actin concentration further to 10.2 µM (ratio ~ 1:2), resulted in actin, polymerized from every PLPPR3 ICD condensate and the formation of a denser network, in which PLPPR3 ICD is enriched in the "condensates" and weakly in the filaments (Figure 31 A bottom panel).

Next, I tested the effect of PLPPR3 ICD condensates on actin polymerization. Thus, I decreased PLPPR3 ICD concentration to 10 µM, leaving actin at 1.2 µM (ratio ~ 1:10). Following the phase diagram (Figure 18), PLPPR3 ICD was still able to form condensates, however, the concentration approached a threshold that was close to a state, where no condensates formed. The few condensates that formed, co-partionend actin and formed ring-shaped F-actin structures that deformed the condensate (Figure 31 B upper

panel). Several were observed as torus-shaped structures, similar to Figure 31 A. I further decreased PLPPR3 ICD concentration to 7.5 µM (ratio ~ 1:7.5), which resulted in PLPPR3 ICD enrichment in "clusters" along the actin filament, however, no condensates were observed. Filaments however, were not comparable to filaments without PLPPR3 ICD and were hypothesized to pursue PLPPR3 ICD clusters. Therefore, I concluded from this experiment, that with increasing actin concentration, actin has the prospect of deforming a circular condensate and polymerize out. In addition, lacking an observable condensate, actin filaments co-localized with PLPPR3 ICD clusters. Together, the results of these experiments suggest that there may be a strong affinity between PLPPR3 ICD and actin.
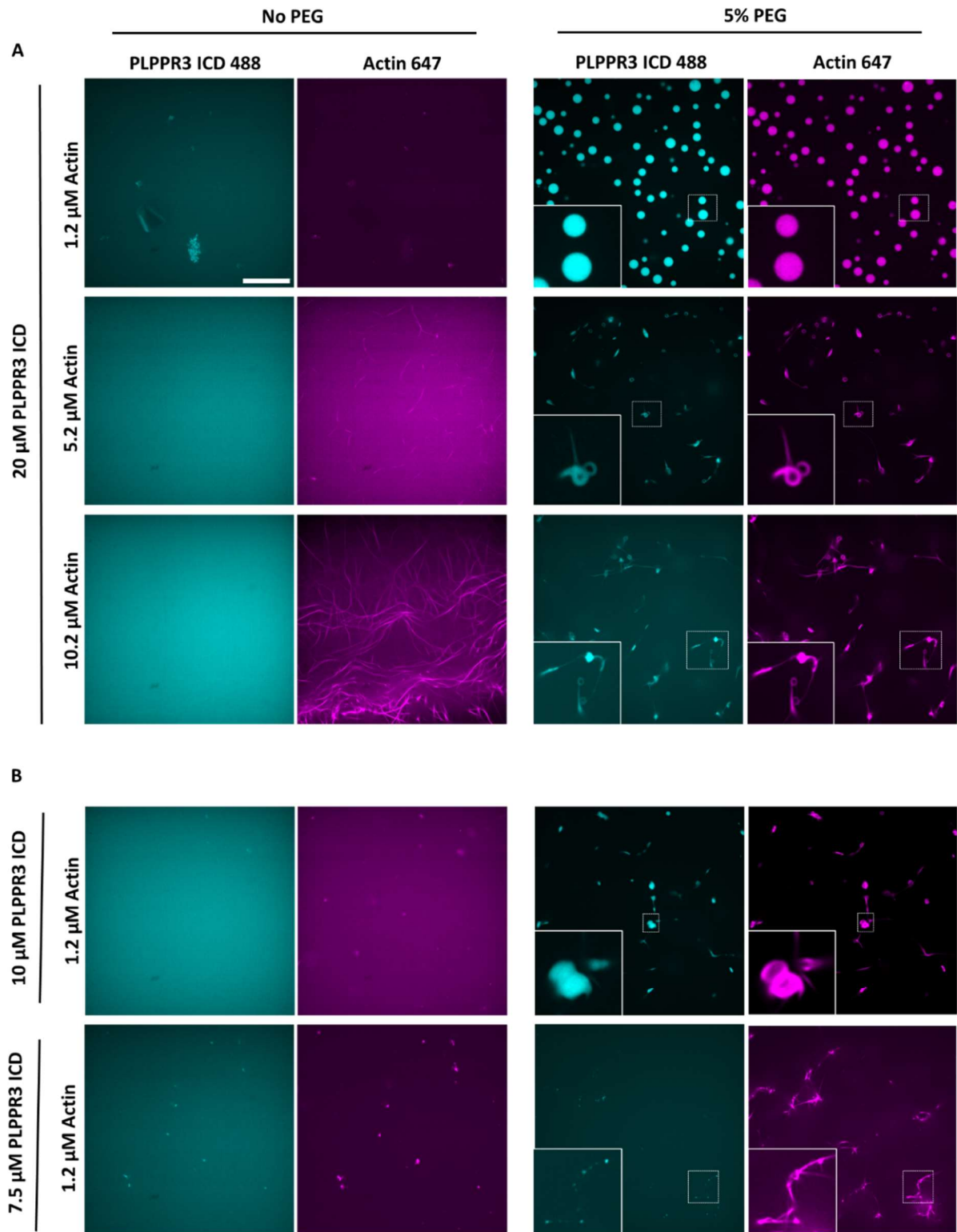
Figure 31. Actin to PLPPR3 ICD ratios

*Comparison of different ratios of PLPPR3 ICD 488 and actin 647 in presence and absence of 5% PEG. **A** Increasing actin concentration from 1.2 – 10.2 µM, while PLPPR3 ICD was constant at 20 µM. With increasing actin, circular PLPPR3 ICD condensates are deformed to torus-shaped condensates with actin polymerizing out. With a higher concentration of actin, networks form that intergrate PLPPR3 ICD condensates. **B** Decreasing PLPPR3 ICD concentration to 10 µM and 7.5 µM with constant 1.2 µM actin resulted in more actin network formation and integration of PLPPR3 ICD condensates. At 7.5 µM, however, no condensate formation was detected and only several "clusters" were observed to interact with actin filaments. Scale bar: 20 µm.*

4.4.5 Conclusion Chapter 4

In this chapter I exploited the simplicity of an *in vitro* model system to reconstitute phase separation-mediated formation of actin-based structures that could be relevant for filopodia formation. I utilized purified PLPPR3 ICD, purified actin and GUVs to build an *in vitro* model. Previous work in our laboratory highlighted the fact, that PLPPR3 induces filopodia formation in neuronal axons (Brosig et al., 2019).

I began building an *in vitro* model, by employing GUVs as a membrane mimicking model system. I observed that PLPPR3 ICD condensates were able to reshape lipid membranes, in dependence of the GUV lipid composition (Figure 27 D-E). By exploiting Ni-NTA affinity, I attracted condensates to GUV interfaces, which partially bent GUV membranes (Mangiarotti et al., 2023). Increasing the NTA moiety of GUVs to 20%, showed a higher affinity of condensates to GUV interface and displayed higher bending (data not shown). Therefore, I concluded that in a reconstituted *in vitro* model, PLPPR3 condensates can reshape lipid membranes.

To address the idea that condensates alter actin polymerization characteristics (cf. Graham et al., 2023), I investigated that actin co-partioned into PLPPR3 ICD condensates in presence of Latrunculin B (Figure 29 A-B). In absence of Latrunculin B, I observed that actin formed ring-shaped F-actin structures within PLPPR3 ICD condensates that occasionally polymerized out (Figure 30 A). In order to form ring-shaped F-actin structures in PLPPR3 ICD condensates, it was imperative that the condensates form first. In the absence of condensates, hardly any ring-shaped F-actin structures or outwards polymerized actin was observed (Figure 30 A-C). In accordance with other publications, actin polymerization from condensates likely depends on the increased actin concentration.

An increased actin concentration resulted in an enhanced polymerization from condensates (Figure 31 A). As a result, condensates more likely formed torus-shaped F-actin structures. I speculated that the potential, generated by ring-shaped F-actin structures, exceeded the potential energy of surface tension, consequently deforming the circular PLPPR3 ICD condensate to a more stable geometry (Stukan et al., 2006). Likely, this would lead to a toroid geometry, which presumably is the thermodynamically most

favorable form (Osada, 2019; Vengerov et al., 1985). I speculated that the transition to toroid-shaped F-actin structures in PLPPR3 ICD condensates involves intermediate states (Vilfan et al., 2006), possibly taking the form of rod-like F-actin structures as described for actin in VASP condensates (Graham et al., 2023).

Collectively, I began building an *in vitro* model of PLPPR3 ICD-facilitated filopodia formation. In the set of experiments, I characterized actin co-partioning into PLPPR3 condensates. Although I worked with a very simplistic model, I demonstrated basic biophysical principles that are relevant for filopodia formation in biological systems. PLPPR3 ICD condensates thereby served as nucleation hubs, co-partioning monomeric G-actin, to enhance formation of F-actin that polymerized inside the condensate, as well as protruding out of the condensate. The next step would involve combination of GUVs with actin polymerization in PLPPR3 ICD condensates to complement the model. However, the strength of exploring this *in vitro* model, rested in the potential for expanding it, which possibly could involve actin binding proteins (ABPs) for F-actin stabilization in the future.

5 Discussion

The work presented in this thesis identified PLPPR3 intracellular domain (ICD) as an intrinsically disordered protein region that undergoes liquid-liquid phase separation (LLPS). PLPPR3 is a transmembrane protein, primarily located in the axonal plasma membrane, which is upregulated during neuronal morphogenesis (Brosig et al., 2019). As member of the PLPPR family (Fuchs et al., 2022), PLPPR3's most well studied function is filopodia induction (Brosig et al., 2019; Joachim Fuchs & Eickholt, 2021a).

Protein molecules containing intrinsically disordered regions can undergo an interaction driven process, termed LLPS, to form protein condensates (H. Wang et al., 2021). Hereby, condensates serve as pivotal reaction chambers, readily accumulating and sequestering molecules, without the need of a physical lipid membrane (Mitrea & Kriwacki, 2016). In addition, condensates at the membrane may have diverse purposes such as curvature sensing (Anila et al., 2023) and ligand-induced receptor clustering (Jajaman & Ditlev, 2020).

My work demonstrated that PLPPR3 ICD undergoes LLPS *in vitro* and in cellular assays. These condensates have the ability to reshape giant unilamellar vesicle (GUV) membranes, recruit monomeric actin and facilitate polymerization to F-actin. Considering the well-studied filopodia induction of PLPPR3, the data presented in this thesis, provides a conclusive model mechanism of PLPPR3 ICD condensate-facilitated filopodia formation.

5.1 PLPPR3 ICD is a highly disordered, phase separating protein domain

My work presented PLPPR3 ICD as an intrinsically disordered protein domain *in vitro*. While PLPPR3 ICD showed no temperature sensitivity during thermal unfolding (Figure 15), the CD spectra solidified that the majority of PLPPR3 ICD is in a disordered state (Figure 13). Moreover, the proteolytic digest highlighted the susceptibility of PLPPR3 ICD to trypsin digestion, suggesting that the sequence lack well-defined secondary structure elements (Figure 14). This indicated that many parts of the PLPPR3 ICD sequence lack secondary structure elements. Therefore, in accordance with the predictions (Figure 12), PLPPR3 ICD is highly disordered. Due to their flexible nature, intrinsically disordered proteins are important cellular regulators. As a result of their

primary sequence being solvent exposed, intrinsically disordered regions are accessible to signaling molecules, kinases, phosphatases and other interaction partners (Trivedi & Nagarajaram, 2022; Wright & Dyson, 2015). However, PLPPR3 ICD is not only disordered. Considering Alphafold 2 predictions (Figure 37) and Circular Dichrosim spectra (Figure 13), several helices and anti-parallel beta sheets are present. These secondary structure elements lead to a minimal amount of stability in the designated domain area (Figure 12) and could be part of a protein interaction motif. Compared to intrinsically disordered regions that transition to secondary structures upon binding partner interaction, preformed structural elements speed up the binding process (Huang & Liu, 2009; Shammas et al., 2013) and therefore are of advantage considering binding kinetics. To test for binding partners of PLPPR3, crosslinking of overexpressed PLPPR3 in primary neuronal cells may aid. By utilizing crosslink-mass spectrometry, it may be possible to establish an interactome of PLPPR3 with the approximate binding locations of the interactors.

5.1.1 Intrinsically disordered domains drive LLPS of PLPPR3 ICD

Overall, the majority of PLPPR3 ICD is disordered. Figure 32 A illustrates all predicted secondary structure elements with surrounding IDRs. Interestingly, the structure elements evenly distributed throughout the ICD, without major hotspots. Considering their flexibility, solvent accessibility and sensitivity to their surrounding (Moses et al., 2023; R. Van Der Lee et al., 2014), IDRs may serve as interaction regions with other PLPPR3 ICD proteins during LLPS (Figure 32 B). LLPS leads to the formation of condensates, which were dependent on multivalent interaction sites as well as electrostatic and hydrophobic interactions (Feng et al., 2021; Mondal et al., 2022; Zumbro & Alexander-Katz, 2020). Multivalent interactions are reversible interactions between molecules, used for self-assembly (Huskens, 2006). Especially, interaction sites around aa residues 341 and 365 offered several multivalent sites during *in vitro* PLPPR3 ICD condensate formation (Figure 32 B; cf. Figure 26 D). Lysine341 and lysine365 were crosslinked to many other lysine residues of different PLPPR3 ICD proteins, in close proximity, during PLPPR3 ICD condensate formation. This suggested that this region might influence interaction with other PLPPR3 ICD during LLPS. The polyE fragments containing residues aa 341 and 365 (aa residue 284 – 463; aa residue 284 – 439) showed no condensate formation and were not responsible for driving LLPS (Figure 22 B-C). In

contrast, aa residue 438 – 716 and aa residue 460 – 716 showed condensate formation, however, appeared to form smaller condensates in absence of residues around aa 341 and 365 (Figure 22 D-E). Therefore, I suggest that these sequence regions must be important for multivalent interactions with other PLPPR3 ICD proteins.

The formation of condensates by LLPS are driven by multivalent interactions between protein-protein or protein-RNA complexes (Alberti et al., 2019) and by interaction of binding partners (Milovanovic et al., 2018; Su et al., 2016). In the case of PLPPR3 ICD, aa 582-637, in combination with aa 638-716 emerged as essential region of PLPPR3 ICD, driving phase separation (Figure 24). However, I was not able to pin point the exact amino acid residues. By sequentially deleting or mutating various residues of the respective peptide regions in PLPPR3 ICD, it might be possible to narrow down the responsible residues further. An alternative approach would be the synthesis of various PLPPR3 ICD peptides in length of 10-15 aa to localize the residues and locate the region.

By utilizing the PLAAC prediction tool (http://plaac.wi.mit.edu/), I discovered that PLPPR3, in contrast to other membrane less organelles, lacked prion-like domains (PrLDs). PrLDs are low complexity domains enriched in polar amino acids and glycine residues, which promote phase separation in many proteins such as FUS and TDP-43 (Hennig et al., 2015; Maharana et al., 2018). Instead, the sequence of PLPPR3 contained disproportionate amounts of glycine and proline residues, as well as glutamine and tyrosine and several combinations of glutamine-serine (GS), aspartic acid-serine (DS) and arginine-serine (RS), which are important for low complexity sequences (Orti et al., 2021). These residues could play a major role in PLPPR3 ICD phase separation. To test this, it would be essential to substitute glycine and proline residues to alanine in the regions that came into close proximity during our crosslinking assay (Figure 32).

Posttranslational modifications (PTMs) such as phosphorylation and acylation play an important role in regulation of condensate forming proteins (Ferreon et al., 2018; Jingxian Li et al., 2022; Wegmann et al., 2018). Due to secretion of PLPPR3 ICD, my variant was unphosphorylated, however, phosphorylation is likely to impact endogenous PLPPR3. In total, 26 phosphorylation sites were discovered in membrane-tagged PLPPR3 ICD (Kroon, 2023) that mainly clustered into two hotspots (Figure 32 A). The first hot spot comprised the aa residues 311-380, where 13 phosphorylation sites were unraveled, while the second one from aa 560-575 comprised six. With regard to the crosslinking data (Figure 26 D-F), proximities of several peptides were close to phosphorylation hot spots,

suggesting a potential influence of phosphorylation during multivalent interaction of endogenous PLPPR3 ICD phase separation. It would be interesting to test this directly by overexpressing a PLPPR3 ICD variant utilizing CRY2 oligomerization domain with all 26 phosphorylation sites substituted to alanine. Thereby, negative charges could induce changes in repulsion and attraction of oppositely charged neighboring residues and ultimately with residues of other PLPPR3 ICDs. Similarly, posttranslational modifications, such as phosphorylation, were elevated in arginine-rich RNA binding proteins (RBPs) (Kundinger et al., 2020) and found to regulate solubility and aggregation (Kundinger et al., 2021). PLPPR3 has 41 arginine residues, of which 33 distribute throughout the ICD as single or twin arginine residues (R, RR). However, one third localized between aa residues 311-380, which was identified as one hot-spot for phosphorylation (Figure 32 A). To test an influence of arginine, it would be interesting to substitute arginine by lysine and alanine, to account for similar and neutrally charged residues, respectively. A second arginine-rich sequence involved the aa residues 682-716, which was not in the identified cluster of phospho-modifications. Instead, this aa stretch shows several twin arginine residues, followed by glutamine (^{687}RRQ), methionine (^{707}RRM) and tyrosine (^{712}RRY). Accordingly, the prediction of this stretch suggests folding into a helix and thus may support interaction of binding partners (Figure 32 A).
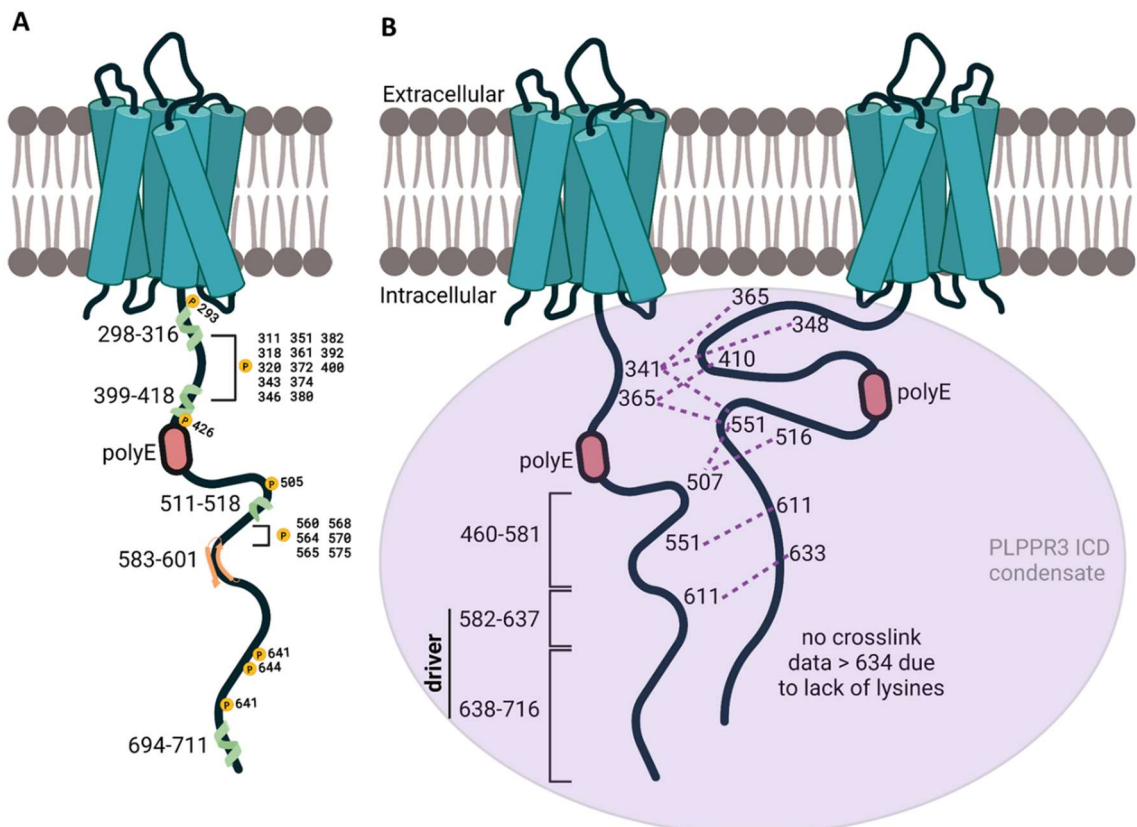
Figure 32. Model of PLPPR3 ICD phase separation
A Schematic PLPPR3 ICD intracellular domain with predicted secondary structure elements (helices in green, beta sheets in orange) by alphafold 2 and validated phosphorylation-modified residues (Kroon, 2023). B Schematic representation of two PLPPR3 ICD molecules that come into close proximity at peptide residues, discovered by crosslinking mass spectrometry. Potential driving areas of PLPPR3 ICD condensate formation indicated at 582-716. No crosslinking data available > 634, due to a lack of lysine residues. Created with BioRender.com.

5.1.2 PLPPR3 ICD shows liquid-like properties

Phase separation of PLPPR3 ICD into a condensed phase showed a number of characteristics, including liquid-like material properties and circularity (Alberti et al., 2019). Condensates, as liquid-like structures, share features of liquids, like fusion and, coalescing, and are governed by surface tension, which results in a spherical architecture (Widom, 1988). These features, observed for PLPPR3 ICD *in vitro*, include spherical architecture (Figure 17 A), fusion and coalescence of condensates (Figure 17 B) and fulfilled requirements for liquid-like assemblies. The same liquid-like properties were observed for cellular-based PLPPR3 ICD assays using CRY2 optogenetic tools for inducing condensate formation (Figure 25 B-C).

The combination of liquid-like properties with a lack of physical barrier, propagated a highly dynamic exchange of molecules with the surrounding (Clifford P. Brangwynne et al., 2009; Feng et al., 2019; Shin & Brangwynne, 2017). To assess the material properties of condensates, such as dynamic molecular exchange rate with its surrounding, as well as with itself, recovery rates of bleached condensates and partially bleached condensates were obtained using FRAP (Alberti et al., 2019; Taylor et al., 2019). *In vitro* studied PLPPR3 ICD condensates displayed a recovery of fully bleached condensates (Figure 20 A), along with partially bleached condensates (Figure 20 B), which grounded a dynamic exchange of molecules from the surrounding and within condensates. However, a recent publication suggested that condensate bleaching alone may not proof liquid-like properties, due to similar recovery rates of non-phase separating proteins (McSwiggen et al., 2019). However, bleaching one-half of the condensate, while leaving the other half unbleached, was suggested to distinguish recovery rates from non-phase separating proteins (Muzzopappa et al., 2022). As partial FRAP has been the common practice in the field, it would be essential to perform the "half-bleaching assay" *in vitro* as well as performing all FRAP measurements in cell culture assays. Taken together, with the earlier mentioned characteristics for liquid-like properties, PLPPR3 ICD formed liquid-like condensates *in vitro*. Other properties such as electrostatic (Boyko et al., 2019) and

hydrophobic interactions (Hong et al., 2022; Krainer et al., 2021) presented in Figure 19 A and Figure 19 B, respectively, demonstrated that condensate formation of PLPPR3 ICD relied on both. To ultimately test if cells displaying PLPPR3 ICD puncta are indeed condensates, one could treat with 1,6-hexanediole and low salt, to correlate this observation in cell culture.

5.2 Possible role of PLPPR3 ICD condensates during filopodia formation

PLPPR3 is best studied for its ability to induce filopodia formation (Brosig et al., 2019; Joachim Fuchs et al., 2020; Joachim Fuchs & Eickholt, 2021a), however how this is accomplished remains unknown. Brosig et al., 2019a observed clusters of endogenous antibody-stained PLPPR3 at the axonal plasma membrane of hippocampal neurons. In the same work, filopodia emergence from PLPPR3-enriched clusters was visualized by F-actin using utrophin-GFP (Burkel et al., 2007). As F-actin and the actin cytoskeleton ultimately are important for filopodia, we hypothesized that PLPPR3 clusters are involved in their formation. It is intriguing to speculate that these clusters were PLPPR3 condensates from which actin filaments emerged.

Condensates were identified as membrane less compartments that play significant roles in many processes and reactions, such as membrane bending (Yuan et al., 2021) and internal concentration of molecules (Banani et al., 2017). In relation to the reported data, our hypothesis centers on a proposed model incorporating the following assumptions: (i) formation of PLPPR3 condensates via LLPS, (ii) deformation of the membrane by PLPPR3 condensates, (iii) actin recruitment by PLPPR3 condensates and (iv) polymerization of actin out of condensates to form filopodia. The condensates thereby play a pivotal role as compartments facilitating membrane reshaping and concentrating actin to form filopodia (Figure 33).
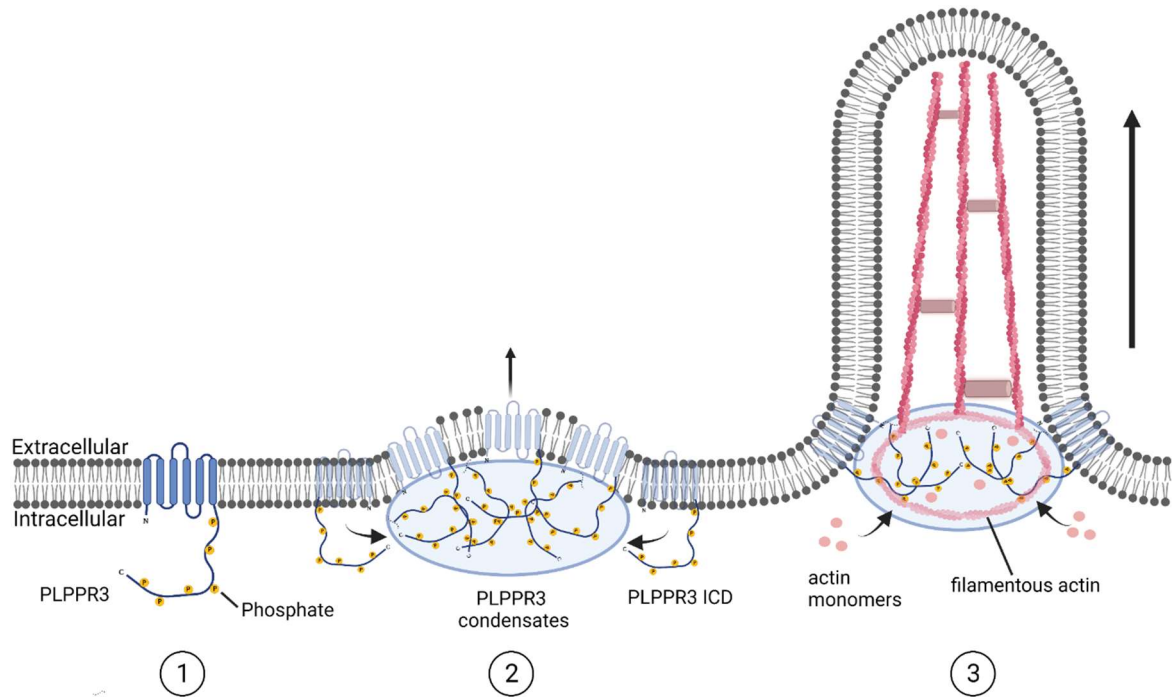
Figure 33. Working model of PLPPR3-facilitated filopodia initiation
[1] PLPPR3 is upregulated during neuronal morphogenesis at the plasma membrane, corresponding to DIV5 to DIV9. [2] The local high concentration of PLPPR3 leads to a clustering of intracellular c-termini, via a mix of electrostatic and hydrophobic interactions, as well as multivalent interactions (discussed in section 5.1) to form a membrane-anchored condensate. The condensate applies pressure on the membrane, which anchoring and interaction of c-termini magnify further, until the membrane reshapes outwards. [3] Monomeric actin co-partions into PLPPR3 ICD condensate and is concentrated several fold times. This concentration results in actin nucleation and subsequent polymerization from the condensate to extend the membrane to initialize filopodia formation. Created with BioRender.com.

(i) Formation of condensates via LLPS

The first step in our model (Figure 33 [1]) involves the upregulation of PLPPR3 during neuronal growth, which we showed corresponded to the period of 5 - 9 days *in vitro* (DIV5- DIV9) (Brosig et al., 2019; Kroon, 2023). This timeframe, correlated with generation of axon branches in *in vitro* model systems (Polleux & Snider, 2010). During this period, PLPPR3 may reach high concentrations in expression locally, which manifested as clusters at axonal membranes (Brosig et al., 2019). The exact concentration remains unknown, however studies suggest that for postsynaptic density proteins, local concentration can reach up to 100 µM, while for some mitochondrial LLPS proteins it is around 1 µM (Farahi et al., 2021).

I propose that these previously labeled PLPPR3 clusters along the neurons axons were indeed PLPPR3 condensate, supported by the following key observations. First, preliminary data generated in the laboratory, displayed a dispersion of axonal PLPPR3 clusters upon 1,6-hexandiole (1,6-HD) treatment in fixed samples that reappeared after 1,6-HD was washed out (unpublished data). 1,6-HD is an alcohol, that dispersed condensates by disrupting hydrophobic interactions (Düster et al., 2021; Ulianov et al., 2021). Second, the model suggested that driving regions of PLPPR3 ICD initialize phase separation, upon local high concentration, which ultimately resulted in a condensate, anchored to the membrane, comparable to the findings in the study by Case et al., 2019 (Figure 33 [2]). It remains uncertain if receptor clustering at the membrane facilitates condensate formation, or if condensate formation induces and locally confines receptor clustering and the subsequent signal propagation (Banjade & Rosen, 2014; Xiaolei Su et al., 2016).

(ii) Deformation of the membrane by PLPPR3 condensates

Filopodia are narrow membrane protrusions that contain bundled actin (Gallop, 2020). Protruding from the membrane implicates membrane reshaping, either by a protrusion itself or by assistance of proteins. One form of assisting proteins involves bin-amphiphysin-rvs (BAR) domains, a class of curved protein domains, centrally involved in membrane remodeling (Kessels & Qualmann, 2020; Simunovic et al., 2015). In a cellular context, BAR domains and PLPPR3 ICD condensate might work in synergy to reshape the membrane. BAR domain proteins have been additionally implicated during actin cytoskeletal remodeling (Carman & Dominguez, 2018; Stanishneva-Konovalova et al., 2016), as well as CDC42-dependent filopodia formation (Millard et al., 2005). Especially, the F-BAR domain is observed to be essential for the formation of filopodia (Taylor et al., 2019), as exemplified by the slit-robo GTPase activating protein (srGAP2) (Guerrier et al., 2009). However, I propose that PLPPR3 condensate formation is sufficient to reshape the membrane, without the aid of BAR domains (Figure 33 [2]). My preliminary *in vitro* data demonstrated that anchored PLPPR3 ICD condensates at a membrane model system e.g. GUVs, were sufficient to reshape membranes (Figure 27). Anchoring of PLPPR3 ICD condensates into GUV membranes by his-tag to Ni-NTA affinity, imitated the function of the transmembrane domains of PLPPR3. Currently, our aim is to utilize supported lipid-bilayers (SLBs) (C Huang et al., 2019), to measure contact

angles of PLPPR3 ICD condensates to reinforce my data. Contact angles can give information about material properties and determine the behavior of condensates on different surfaces, such as GUVs or even the plasma membrane (Figure 34 B) (Kusumaatmaja et al., 2021). Although the presented data was preliminary, recent work determined membrane-reshaping events *in vitro* (Figure 34 A) (Mangiarotti et al., 2023; Stachowiak et al., 2012), of which some even described tubulation of GUV membranes by condensates (Figure 34 C) (Yuan et al., 2021). Membranes reshape by compression (Mondal & Baumgart, 2023)and by attraction/repulsion of intrinsically disordered domains, which lead to concave/convex bending respectively (Yuan et al., 2023). One could also surmise that the negative charged PLPPR3 polyE box, the stretch of 20 glutamic acid residues residing in the cytosol, may repulse the negative charged inner leaflet of the plasma membrane, leading to a convex, outwards bending effect.
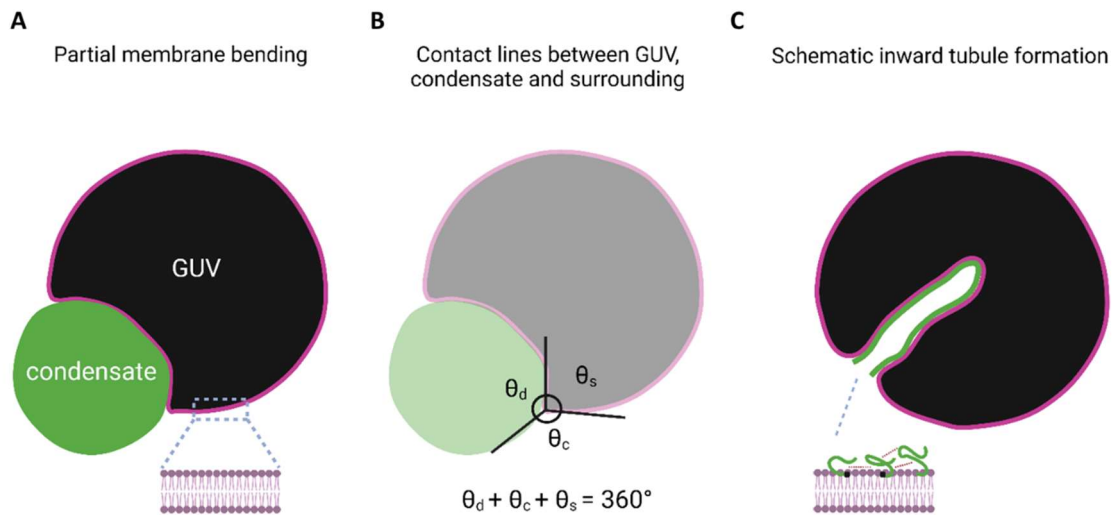
Figure 34. Schematic representation of condensate membrane bending
A Representation of condensate induced partial membrane reshaping. Membrane deformation of the condensate depends on the strength of interaction (modified after Mangiarotti et al., 2023). B Partial membrane reshaping leads to the formation of contact lines between condensate and GUV (θ_d), GUV and surrounding (θ_s) and surrounding and condensate (θ_c). The contact angles θ determine the character of the droplet–membrane deformation and have a sum of 360° (modified after (Kusumaatmaja et al., 2021; Mangiarotti et al., 2023). C Schematic representation of inward tubule formation by LLPS. The proteins attract membranes and creating a compressive stress, which creates protein-lined membrane tubules (modified after Yuan et al., 2021). Created with BioRender.com

(iii) Actin recruitment by PLPPR3 condensates

Membrane protrusions such as filopodia require actin filaments to elongate from beneath the membrane (Aramaki et al., 2016). The classic "convergent elongation model" described reorganization of the actin network by Arp2/3 activity, while the "tip nucleation model" defined formin clusters on the plasma membrane as nucleation source for actin

filaments (C. Yang & Svitkina, 2011). It is currently unknown, how PLPPRs make filopodia (Fuchs et al., 2022). Our model however, elucidates that PLPPR3 ICD condensates serve as actin nucleation compartments with filamentous actin polymerization as consequence, independent of Arp2/3 or formins (Figure 33 [3]). Testing this, by overexpression of PLPPR3 in presence of Arp2/3 and formin inhibitors in cells and observing filopodia, would illustrate independence of both. However, first I tested the idea of actin accumulation in a minimal *in vitro* system, using monomeric actin and PLPPR3 ICD. I observed that actin co-partioned into PLPPR3 ICD condensates, in presence of the actin-destabilizing drug Latrunculin B to prevent polymerization (Figure 29). When no Latrunculin B was present, monomeric actin accumulated inside of PLPPR3 ICD condensates and formed ring-shaped F-actin structures (Figure 30).

How actin is recruited into condensates is currently unknown, however we suggested that PLPPR3 ICD might have a weak actin-binding domain. In this case, condensate formation may aid binding of a low affinity PLPPR3-actin interaction, by local increases in the actin monomer concentration. To test this hypothesis, one could crosslink purified PLPPR3 ICD in presence and absence of PEG to actin. This could give rise to an approximate interaction site of actin in PLPPR3 ICD by crosslinking mass spectrometry analysis. By deleting the cognate binding motif, several outcomes are possible. One possibility involves less actin monomers that enter the condensate and form no F-actin structures as a result, while the other speculates on monomer actin entering the condensate, but a perturbation of the interaction with PLPPR3 ICD. Interestingly, PLPPR3 ICD condensates can polymerize actin without any actin regulatory proteins, similar to the observation made by Chen et al., 2023 for the reconstituted post-synaptic density. By implementing an actin co-sedimentation assay (Srivastava & Barber, 2008), it is possible to test, if PLPPR3 ICD co-sediments with F-actin or monomeric actin, which would indicate a preferential binding. Ultimately, repeating the co-sedimentation assay with PLPPR3 ICD condensates, would underline preferentially interaction with actin monomers, however could also show interaction to actin filaments. Speculating on whether PLPPR3 ICD condensates have the potential to rearrange actin filaments and potentially guide polymerization is an intriguing consideration.

(iv) Polymerization of F-actin out of PLPPR3 condensates to form filopodia

The earlier described ring-shaped F-actin structures occasionally polymerized out of the condensate, which probably results from an actin polymerization force being greater than the condensates surface tension (Simon et al., 2018). Effects of actin polymerization on membrane dynamics has been intensively studied before (Carlsson, 2018; Gov & Gopinathan, 2006) and highlighted forces generated by F-actin polymerization, which demonstrated capability to extend membranes. Generally, by increased actin concentration *in vitro*, I observed that close to all condensates experienced actin polymerization (Figure 31 A), an indication that this potential mechanism is dependent on actin concentration. Similarly, a recent study reported co-partioning and concentration-dependent actin polymerization from Vasodilator-stimulated phosphoprotein (VASP) condensates *in vitro* (Graham et al., 2023). VASP is a known actin-binding protein that is involved in filopodia formation (Lebrand et al., 2004). Several other works described analog findings, including actin in N-WASP condensates (Yan et al., 2022), actin in model polypeptide condensates as proof of concept (McCall et al., 2018) and polymerization as actin bundles from *in vitro* generated postsynaptic density proteins, including PSD-95, SynGap and Homer1 (Chen et al., 2023). My own work illustrated that filamentous actin, polymerizing from condensates are rather bundle-like, considering their size of approximately 0.5-1 μm (Figure 30 A and Figure 31 A) in comparison to single actin filaments of 7-8 nm (Grazi, 1997).

There is evidence that cytoskeletal protein polymerization from condensates such as actin, is a general mechanism of membrane remodeling by phase separating proteins (Ganar et al., 2021; Mohapatra & Wegmann, 2023; K. Zhang et al., 2023), especially those involved in filopodia generation. What my current data did not fully present was membrane extension by polymerized actin (Figure 33 [3]). My preliminary data, suggested that combining PLPPR3 condensates with actin and GUVs to mimic a simplistic membrane model of filopodia initiation is sufficient (data not shown). However, due to a lack of a rigid cytoskeleton during *in vitro* assays, polymerization of actin filaments generally followed a "path of least resistance", which meant that in my setup, actin did not polymerize into GUV membranes. Although condensates were recently reviewed as cytoskeletal interactors (Mohapatra & Wegmann, 2023), I can only speculate that there might be a supportive function of the cytoskeleton towards PLPPR3 ICD condensates, but no direct interaction or anchoring to the cytoskeleton. Testing if PLPPR3 ICD

condensates have the ability to nucleate microtubules through co-partioning of tubulin (Hernández-Vega et al., 2017), would contribute a more comprehensive understanding of PLPPR3 ICD condensates and microtubule network within the cellular environment. Despite, we are currently working on a solution, which aims to engulf PLPPR3 ICD condensates by GUV membranes, to obtain proof of principle (Mangiarotti et al., 2023) of this idea. To test my model of PLPPR3 ICD condensate-facilitated filopodia, abolishing condensate formation, by deleting driver regions, would be a proof of principle, which would result in less filopodia in cells. By replacing the driver region with a known IDR e.g. of FUS, this effect could be rescued, similar to the assay performed by McDonald et al., 2020. Employing this assay, could reinforce my *in vitro* model assumptions.

5.3 Is PLPPR3 phase separation dependent on PI3K/PTEN pathway?

Many works have demonstrated that phase separation of proteins such as the microtubule associated protein tau or the intracellular signaling integrator LAT can be induced by binding partners (P. Li et al., 2023; Xiaolei Su et al., 2016), while others require PTMs such as phosphorylation, RNA or molecular chaperones (Luo et al., 2021). PLPPR3 is upregulated during neuronal morphogenesis around DIV5 to DIV9, however how condensate formation is regulated remains an open question. Previous work generated in our laboratory, determined PLPPR3-induced axonal filopodia as a PI3K/PTEN-dependent mechanism (Brosig et al., 2019) (Figure 35). By locally inhibiting PTEN, PLPPR3 contributed to PI(3,4,5)P3-rich membranes, which recruited F-actin into patches. These specialized structures showed emergence of filopodia in previously published works (Kalil & Dent, 2014; Ketschek & Gallo, 2010). Therefore, in this section, I would like to address whether PLPPR3 phase separation is PI3K/PTEN-dependent or if LLPS is an additional way PLPPR3 can facilitate axonal filopodia.
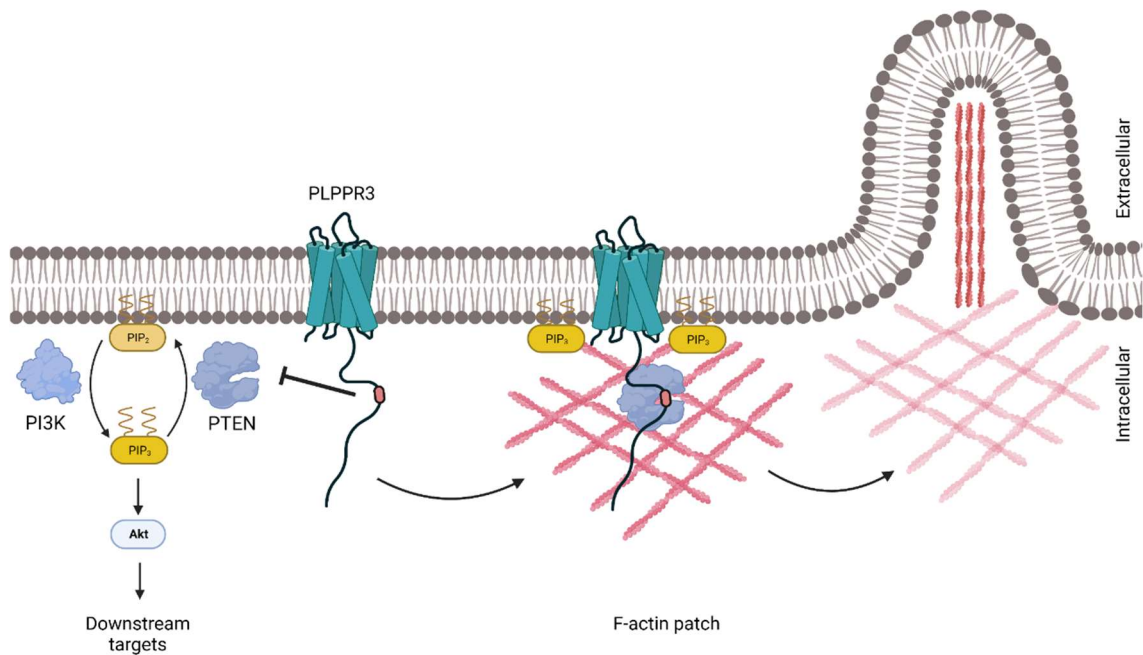
Figure 35. PLPPR3 locally inhibits PTEN at the axonal plasma membrane
PI3K/PTEN dependence of PLPPR3 induced filopodia. Phosphoinositol-3-kinase (PI3K) phosphorylates PI(3,4)P2 to PI(3,4,5)P3 at the axonal plasma membrane, while PTEN antagonizes this pathway. PI3K/AKT can act on many downstream targets, which control growth, neural development and the cell cycle. PLPPR3 was shown to locally inhibit PTEN, thus inducing PI(3,4,5)P3-rich membranes, which recruit F-actin into F-actin patches. These patches are sufficient to create protrusions such as filoipodia. Modified after Brosig et al., 2019. Created with BioRender.com.

My model proposition (Figure 33) allowed two possible scenarios: PI3K/PTEN-dependency and PI3K/PTEN-independency (Figure 36). A PI3K/PTEN dependency could result in a PTEN-PLPPR3 complex that sequesters PTEN, before phase separation. Although PTMs such as phosphorylation can initiate LLPS, I would argue against the fact that they drive PLPPR3 condensates. One argument is that all *in vitro* assays were performed with unphosphorylated PLPPR3 ICD as result of secretion; however, the optogenetic assays were performed in HEK293T cells. In cells, by the sheer amount of overexpressed protein, the likelihood to observe condensates would be high, if PTMs would initiate PLPPR3 condensates (Ray et al., 2020; Vistrup-Parry et al., 2021; Wegmann et al., 2018). Taking into account other binding partner-induced phase separating proteins such as LAT (Su et al., 2016) and synapsin 1 (Milovanovic et al., 2018), the most probable is that PLPPR3 phase separation is initiated by an unknown extracellular signal (Figure 36 A [1]) or binding partner. It is arguable whether PTEN could initiate phase separation; however, with a dependency on PI3K/PTEN, it would be likely that PTEN co-partions into PLPPR3 condensates (Figure 36 A [2]). What would

PTEN's function be there? One suggestion would be that it could mask and neutralize the negative charge of the polyE box, to allow a better interaction with the negatively charged inner leaflet of the plasma membrane. However, the likelihood is rather small considering that PTEN is not necessary to form PLPPR3 ICD condensates *in vitro* and the negative charge of the polyE box was suggested to be an intentional spacer of the ICD. To test this, one could titrate purified PTEN into PLPPR3 ICD condensates and observe if PTEN co-partions *in vitro*. In addition, one could monitor co-localization of PLPPR3 clusters with PTEN signal in primary cells or cell lines. In a PI3K/PTEN-dependent scenario, filopodia would be generated by condensate membrane-reshaping and PI(3,4,5)P3 recruited F-actin patches, which enter condensates, reform and polymerize out (Figure 36 A [3]). Using my *in vitro* model system, one could include PI(3,4,5)P3 in GUV membranes and test this idea. Since PI(3,4,5)P3 recruited F-actin patches are sufficient to induce axonal filopodia (Kakumoto & Nakata, 2013; Ketschek & Gallo, 2010), a dependency on PI3K/PTEN is rather unlikely.

More probable is the scenario that PLPPR3 condensates facilitate axonal filopodia independent of PI3K/PTEN. What primarily supports this idea is the fact that my *in vitro* model displayed all the necessary steps for the support of filopodia formation. From membrane reshaping (Figure 36 B [2]), to actin nucleation and outwards polymerization (Figure 36 B [3]), PLPPR3 ICD condensates are capable to accomplish this independent of PI3K/PTEN *in vitro*. Cells however, are more complex and studying this mechanism in cell lines or primary cultures can be more demanding. With help of an optogenetic PLPPR3 variant, that forms clusters with blue-light activation, one can investigate filopodia in cells, similar to the PLPPR3 ICD-mscarlet-CRY2 work, described in section 4.3.4.

To add, filopodia-induction is a major trait of PLPPR family members (Fuchs et al., 2022). PLPPR1 and PLPPR5 were observed to induce filopodia *in vivo* (Broggini et al., 2016), in neuroblastoma cell lines (Broggini et al., 2010; Yu et al., 2015) and primary cortical as well as hippocampal neurons (Coiro et al., 2014; Velmans et al., 2013). Although PLPPR4 is not studied well with regard to filopodia induction, the available data suggests that expression of PLPPR4 increases filopodia density in HEK293T cells (X. Liu et al., 2016). PLPPR4 is also the only other PLPPR with a long IDR that can potentially undergo LLPS. Other PLPPRs regulate filopodia differently or could potentially utilize multimerization with one of the phase separating PLPPRs to induce

filopodia (Yu et al., 2015). To current knowledge, no other PLPPR family member has been associated with PTEN. The polyE box, suggested to be part of the interaction motif (Brosig et al., 2019), is not conserved among the family (Fuchs et al., 2022). Therefore, it is more likely that PLPPR3-facilitated filopodia via condensates, is a mechanism independent of PI3K/PTEN. Testing this with an optogenetic PLPPR3 variant, to induce clustering in presence of a PI3K inhibitor in cell lines or primary neurons (similar to Brosig et al., 2019), could give rise to a more clear statement. By inhibiting PI3K, less PI(3,4,5)P3 is expected and therefore less filopodia. If light-activation of overexpressed optogenetic PLPPR3 would rescue this phenotype, by forming condensates and facilitating filopodia formation, then PLPPR3 would induce filopodia independent of PI3K/PTEN. It is intriguing to understand how PLPPR3 could potentially transition between a condensate PI3K/PTEN independent filopodia induction and a PI3K/PTEN dependent induction involving binding to PTEN.
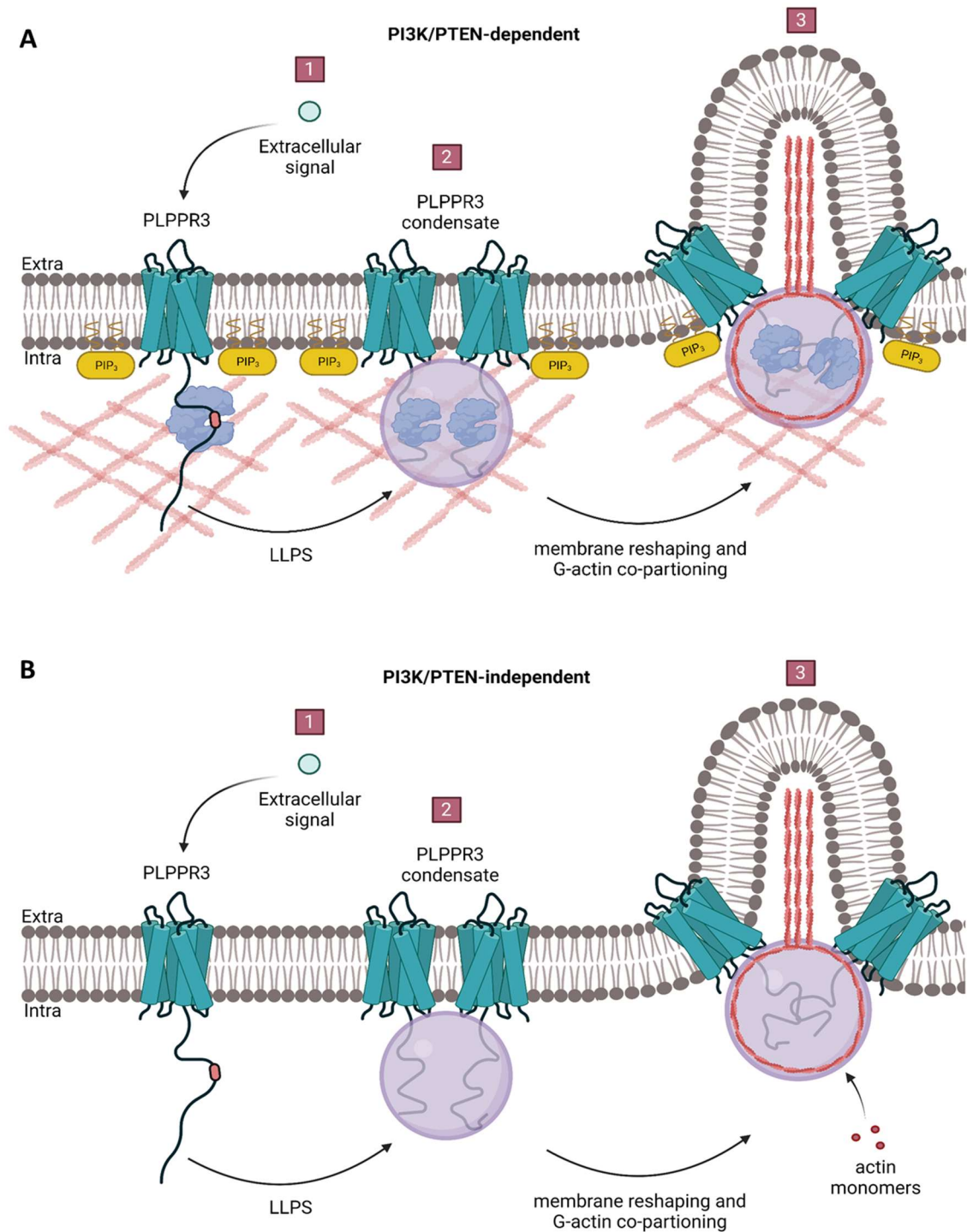
Figure 36. PI3K/PTEN dependent and independent models of PLPPR3
A In a PI3K/PTEN dependent scenario, PTEN is suggested to interact with PLPPR3 ICD before LLPS. This would result in local elevated levels of local PI(3,4,5)P3, which recruit F-actin to the plasma membrane. After binding of an extracellular signal [1], the intracellular regions of PLPPR3 undergo LLPS to form a condensate, in which PTEN co-partions [2]. The condensate can reshape the membrane and attract monomeric actin by restructuring F-actin patches. Actin accumulates in the condensate and polymerizes out to form a new filopodium [3]. B A PI3K/PTEN independent scenario, is much simpler and involves an extracellular signal [1] that binds PLPPR3 and thus induces condensates via LLPS [2]. Similarly, the condensates can restructure the membrane and attract monomeric actin, which nucleates in the condensate, forms ring-shaped F-actin structures and polymerizes out to form a new filopodium [3]. Created with BioRender.com

5.4 Conclusion

In this work, I demonstrated that the intracellular C-terminus of PLPPR3 is highly disordered. I presented that PLPPR3 ICD can undergo liquid-liquid phase separation to form condensates *in vitro*, as well as in cells using optogenetics. Further, I validated that PLPPR3 ICD condensates were able to reshape lipid GUV membranes. My experiments visualized that actin can enter PLPPR3 ICD condensates and form ring-shaped F-actin structures. These filamentous structures sporadically polymerized from PLPPR3 ICD condensates. Therefore, I utilized my data to hypothesize a working model for PLPPR3-facilitated filopodia initiation. This model describes PLPPR3 condensates as Arp2/3/formin-independent filopodia initiation pathway that harbors the accumulation and nucleation properties of condensates. It remains inconclusive if PLPPR3 ICD condensates are independent of PI3K/PTEN, however several facts speak for an independent mechanism. How PLPPR3 condensates are regulated in the plasma membrane remains to be elucidated. In summary, I have developed a new model mechanism for PLPPR3, through which neuronal cells can initiate the formation of axonal filopodia

6 Appendix

6.1 Alphafold 2 prediction of PLPPR3 ICD

Understanding protein structures can facilitate the understanding of protein function and purpose. In 2021, Google DeepMind developed the protein prediction algorithm - alphafold 2 -, which uses neural-network based modeling to predict a protein structure with high accuracy (Jumper et al., 2021). Thereby, the input is a primary amino acid sequence, which is aligned in a multiple sequence alignment (MSA) as well as a checked for published sequence structure similarities. The combined data is used to calculate a prediction of the protein which is iterated several times. Alphafold 2 was made more accessible by implementing it into Google colaboratory (Mirdita et al., 2022). I used ColabFold v1.5.1 (https://colab.research.google.com/github/sokrypton/ColabFold/blob/main/AlphaFold2.ipynb) to predict PLPPR3, PLPPR3 ICD and my purification construct M1-PLPPR3 ICD-His (Table 18).

Interestingly, Alphafold 2 predicted the transmembrane domains with high confidence (red), while the intracellular domain, apart from a couple of mid helical structures was predicted as flexible low confident (blue) peptide chain (Figure 37 A-C). The algorithm confidently modelled helices from residues 399-418 (**H1**-ASRSRQLIGEWKQKS LEGRG), 693-716 (**H2** - LAEREVEAEAESYYRRMQA RRYQD) and an antiparallel beta sheet from 584-599 (**B1** – IVTIDAHAPHHPVVHL) which were colored in red. Potentially, all green and yellow predicted helices could be present, but would need further characterization. Low confidence predicted structural elements and other domains of ICD could either be result of flexibility or by limited structural data of PLPPRs and distant relatives. However, all experimental and predicted results pointed towards a disordered flexible protein domain that is difficult to characterize structurally.
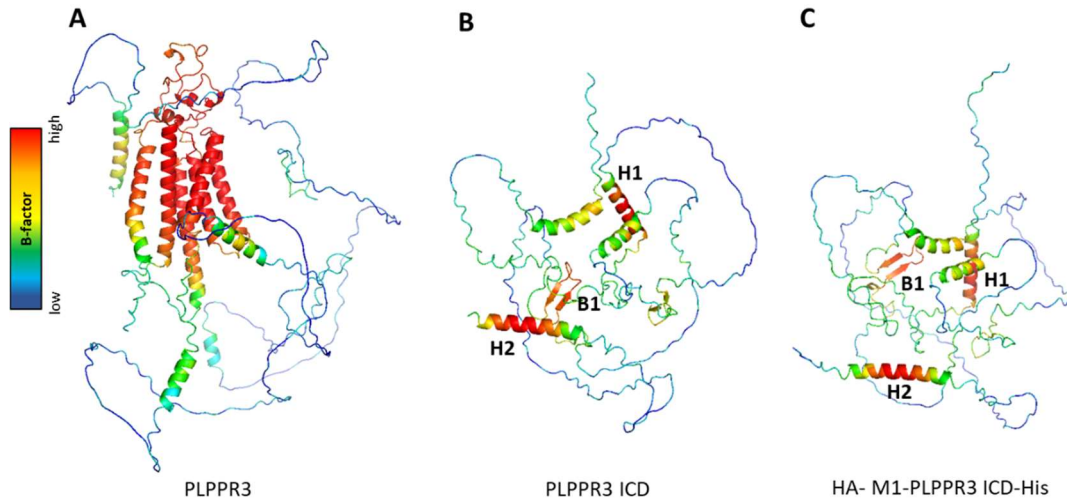
Figure 37. ColabFold prediction with Alphafold 2 algorithm of PLPPR3 variants
*ColabFold prediction of **A** PLPPR3 (uniport: Q7TBP0), **B** PLPPR3 ICD (aa 283 – 716) and **C** M1-PLPPR3 ICD-His variant. While the TM regions of PLPPR3 were modelled with high confidence, the intracellular domain, apart from two small helices and potentially two beta-sheets, was predicted with low confidence. Helices H1 (aa 399-418), H2 (aa 693 – 716) and anti-parallel sheet B1 (aa 584 – 599) were predicted with higher confidence. Coloring by B-factor.*

Table 18. *Primary amino acid sequences*
Sequences of PLPPR3, PLPPR3 ICD and M1-PLPPR3 ICD-His for alphafold 2 predictions.

Protein	Alphafold 2 predicted sequence
PLPPR3 (uniprot: Q7TPB0)	MLAMKEKNKTPKDSMTLLPCFYFVELPIVASSIVSLYFLELTDLFKPAKVGFQCYDRALSMPYVETNEEL IPLLMLLSLAFAAPAASIMVGEGMVYCLQSRLWGRGPGGVEGSINAGGCNFNSFLRRTVRFVGVHVF GLCATALVTDVIQLATGYHTPFFLTVCKPNYTLLGTSCESNPYITQDICSGHDTHAILSARKTFPSQHATL SAFAAVYVSMYFNAVISDTTKLLKPILVFAFAIAAGVCGLTQITQYRSHPVDVYAGFLIGAGIAAYLACH AVGNFQAPPAEKVPTPAPAKDALRALTQRGHESMYQQNKSVSTDELGPPGRLEGVPRPVAREKTSLG SLKRASVDVDLLAPRSPMGKEGMVTFSNTLPRVSTPSLDDPARRHMTIHVPLDASRSRQLIGEWKQK SLEGRGLGLPDEASPVHLRAPAEQVAEEEEEEEEEEEEEEEEEEEEEGPVPPSLYPTVQARPGLGPRVILP PRPGPQPLVHIPEEGVQAGAGLSPKSSSSSVRAKWLSVAEKGGGPVAVAPSQPRVANPPRLLQVIAM SKAAGGPKAETASSSSASSDSSQYRSPSDRDSASIVTIDAHAPHHPVVHLSAGSTPWEWKAKVVEGEG SYELGDLARGFRSSCKQPGMGPGSPVSDVDQEEPRFGAVATVNLATGEGLPPPGASEGALGAGSRES TLRRQVGGLAEREVEAEAESYYRRMQARRYQD
PLPPR3 ICD (aa 283 – 716) (uniprot: Q7TPB0)	QAPPAEKVPTPAPAKDALRALTQRGHESMYQQNKSVSTDELGPPGRLEGVPRPVAREKTSLGSLKRA SVDVDLLAPRSPMGKEGMVTFSNTLPRVSTPSLDDPARRHMTIHVPLDASRSRQLIGEWKQKSLEGR GLGLPDEASPVHLRAPAEQVAEEEEEEEEEEEEEEEEEEEEEGPVPPSLYPTVQARPGLGPRVILPPRPGP QPLVHIPEEGVQAGAGLSPKSSSSSVRAKWLSVAEKGGGPVAVAPSQPRVANPPRLLQVIAMSKAAG GPKAETASSSSASSDSSQYRSPSDRDSASIVTIDAHAPHHPVVHLSAGSTPWEWKAKVVEGEGSYELG DLARGFRSSCKQPGMGPGSPVSDVDQEEPRFGAVATVNLATGEGLPPPGASEGALGAGSRESTLRRQ VGGLAEREVEAEAESYYRRMQARRYQD
M1-PLPPR3 ICD-His (aa 283-716)	DYKDDDDAKLMQAPPAEKVPTPAPAKDALRALTQRGHESMYQQNKSVSTDELGPPGRLEGVPRPVA REKTSLGSLKRASVDVDLLAPRSPMGKEGMVTFSNTLPRVSTPSLDDPARRHMTIHVPLDASRSRQLI GEWKQKSLEGRGLGLPDEASPVHLRAPAEQVAEEEEEEEEEEEEEEEEEEEEEGPVPPSLYPTVQARPGL GPRVILPPRPGPQPLVHIPEEGVQAGAGLSPKSSSSSVRAKWLSVAEKGGGPVAVAPSQPRVANPPRL LQVIAMSKAAGGPKAETASSSSASSDSSQYRSPSDRDSASIVTIDAHAPHHPVVHLSAGSTPWEWKAK VVEGEGSYELGDLARGFRSSCKQPGMGPGSPVSDVDQEEPRFGAVATVNLATGEGLPPPGASEGALG AGSRESTLRRQVGGLAEREVEAEAESYYRRMQARRYQDVDGRPHHHHHH

6.2. Interactome of PLPPR3 ICD

To screen for interaction partners of PLPPR3 ICD I used my well-established purification pipeline (Chapter 1) and coupled PLPPR3 ICD to M1 Flag beads via M1 Flag tag. I used the brain of P1 C57BL/6 (C57BL/6NCrl; Jackson Laboratories) mice that were sacrificed under the ethical standards of LaGeSo (T034 7/11). The brain was homogenized and proteins were extracted using RIPA buffer and incubated with PLPPR3 ICD coupled to beads. After washing off non-specific interactors, all proteins were eluted from the beads, snap frozen and stored at -80°C. For visualizing interactors, samples were run on an SDS-PAGE and stained with coomassie as well as silver staining for higher sensitivity. As control, I used pure M1 flag beads and Expi293F cell medium, to check if nonspecific proteins would bind to either one, once incubated with and without brain lysate. I observed in both gels, that beads and cell medium showed no unspecific binding. PLPPR3 ICD without brain lysate displayed a strong band at ~ 55 kDa that corresponded to the positive PLPPR3 ICD control protein. The samples incubated with P1 brain lysate presented additional bands appearing below 55 kDa, at 15 kDa and in the higher molecular range of > 70 kDa (Figure 38 A-B). Interestingly, these bands were observed in the coomassie stained gel, but more clearly in the silver stained gel (black arrows). The eluates were analyzed in three independent experiments, in collaboration with Dr. Marie-Luise Kirchner (BIH Berlin) by LC-MS/MS.

We evaluated 20 most prominent proteins, by combining significant hits from relevant pairwise t-test comparisons, of which PLPPR3 ICD was the most enriched. (Figure 33 C). Previous studies and unpublished data from our own laboratory demonstrated that PLPPR3 was able to bind to itself and form higher oligomers. All other interactions were categorized into the groups COP1 vesicle subunits, calcium modifiers and others (Figure 38 D). Although, we found several interesting targets, for instance Trim67, which was published to interact with PLPPR3 and PLPPR4 (Menon et al., 2021; Yaguchi et al., 2012), none was further investigated. Given that PLPRR3 ICD exported via secretion into the medium, COPI vesicle subunits need more attention to be verified. The category comprising calcium modifiers was interesting, due to the fact that PLPPR4 was shown to bind Calmodulin, while PLPPR3 contained a similar binding motif (Fuchs et al., 2022; Tokumitsu et al., 2010). However, also these potential interaction partners would need to be verified independently, by co-immunoprecipitation, microscopy and co-localization studies.
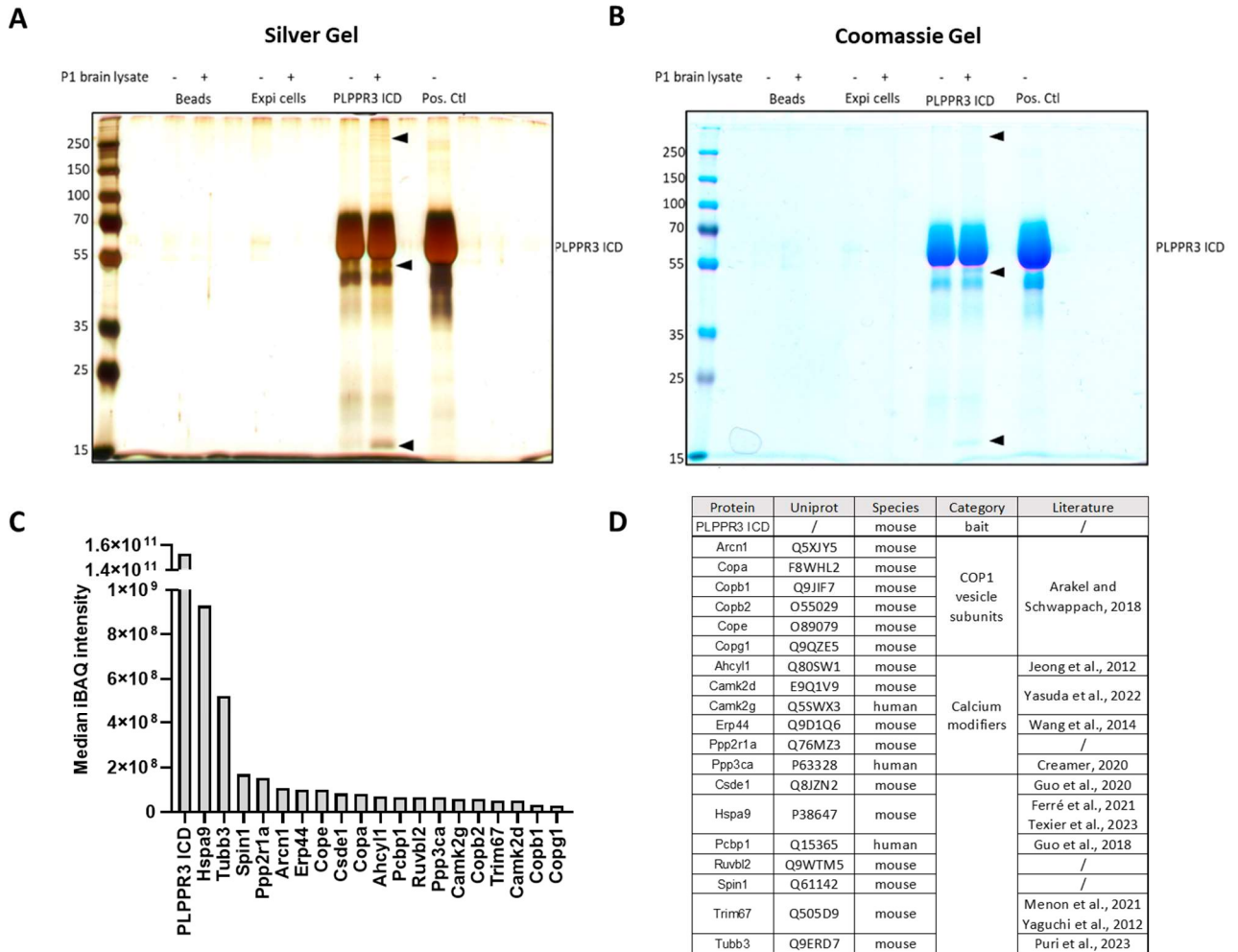
Figure 38. Interactome study of PLPPR3 ICD
*PLPPR3 ICD, expressed by Expi293F cells, were coupled to M1 Flag beads and incubated with homogenized P1 mouse brain lysate (C57BL/6). After washing off non-specific interactors, PLPPR3 ICD was eluted with 5 mM EDTA and 0.2 mM Flag peptide. The samples were analyzed by Dr. Marie-Luise Kirchner (BIH Berlin). Beads, Expi cells and PLPPR3 ICD were incubated +/- P1 brain lysate. As positive control, I used non-treated purified PLPPR3 from a different batch. Black arrows indicated potential interaction proteins, visualized by **A** silver staining and **B** coomassie staining in an SDS-PAGE. **C** By combining significant hits from relevant pairwise t-test comparison, we discovered many proteins, of which the displayed 20 were the most enriched, according to mean iBAQ intensity (He et al., 2019). **D** Compiling of the potential interactors and grouping into categories, according to their general function. We analyzed both mouse and human protein species, due to the fact that I expressed PLPPR3 ICD in human Expi293F cells, which were incubated with mouse brain lysate.*

6.3 Purification pipeline of PLPPR3 transmembrane domain

Additionally to PLPPR3 ICD, I aimed to purify PLPPR3 transmembrane (TM) domains without ICD. The TM domains are predicted to be the most stable structures in PLPPR3, due to their six helical membrane spanning domains. Our ulterior motive was to generate a purification pipeline that resulted in enough isolated protein to perform Cryo-EM. Due to multimerization of PLPPR3, we expected the 32 kDa large PLPPR3 TM construct to form stable higher multimers that would overcome lower Cryo-EM imaging resolution of 50 kDa (Y. Liu et al., 2019).
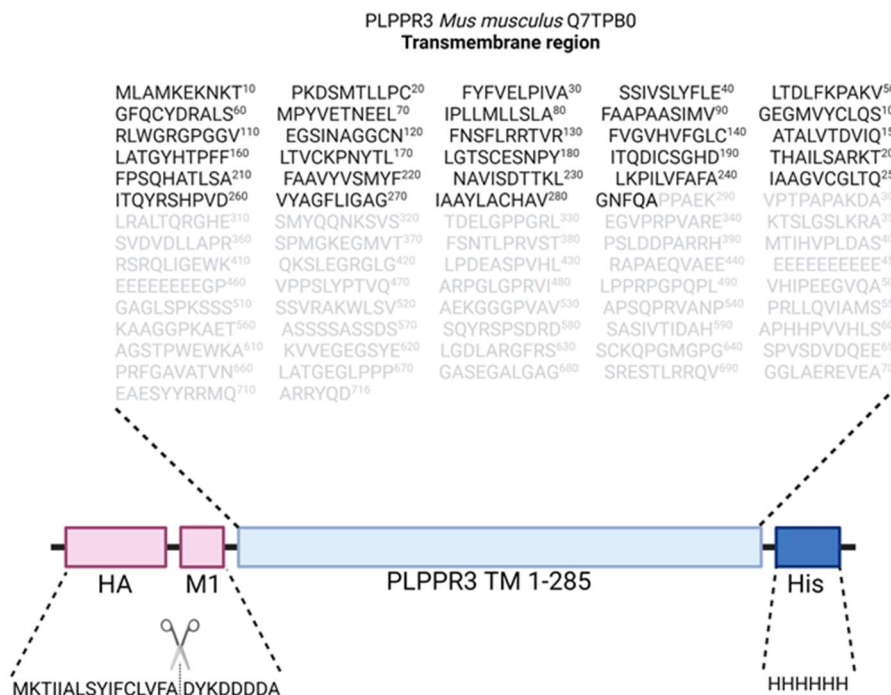
Figure 39. Sequence of PLPPR3 TM
*A PLPPR3 (uniprot: Q7TPB0) amino acid sequence with the transmembrane domains indicated in red. **B** The residues 1-285 were fused with an N-terminal HA-M1 tag system and a C-terminal 6x his-tag. The construct HA-M1-PLPPR3 TM was expressed in Expi293 GNTI- cells for 4 days.*

I applied the HA-M1 strategy (Chapter 1), which resulted in the fusion construct HA-M1-PLPPR3 TM (aa 1-285) (Figure 39) and was cloned into a pMT4 backbone. The construct was expressed in Expi293F GNTI- cells for 4 days. GNTI- deficient Expi293F cells lacked N-Acetylglusaminyltransferase, which therefore could not post translationally modify fusion constructs with complex N-glycan, leading to a better expression of the protein (Reeves et al., 2002).

This fusion construct was not shuttled into the Expi293F GNTI⁻ medium, due to the transmembrane domains (data not shown). Therefore, I screened for the solubility of the

fusion construct with two detergents that were most promising for PLPPR3 full-length purification: n-dodecyl-β-D-maltoside (DDM/CHS) and Octyl Glucose Neopentyl Glycol (NG311). Figure 40 A displayed the coomassie stained SDS gel for the detergent screen. While many bands were visible and purification was not pure, arrows 1-4 indicated solubilized M1-Flag-PLPPR3 TM. This was additional verified by western blot (Figure 40 B), which indicated a double band (3 and 4). However, to address the question, which detergent to continue further purification with, I aimed for NG311. In Figure 40 A, arrow 2 indicated a stronger band compared to 2, which meant that I was able to solubilize and capture more fusion protein with NG311 than DDM/CHS. Therefore, I carried out further experiments with NG311.
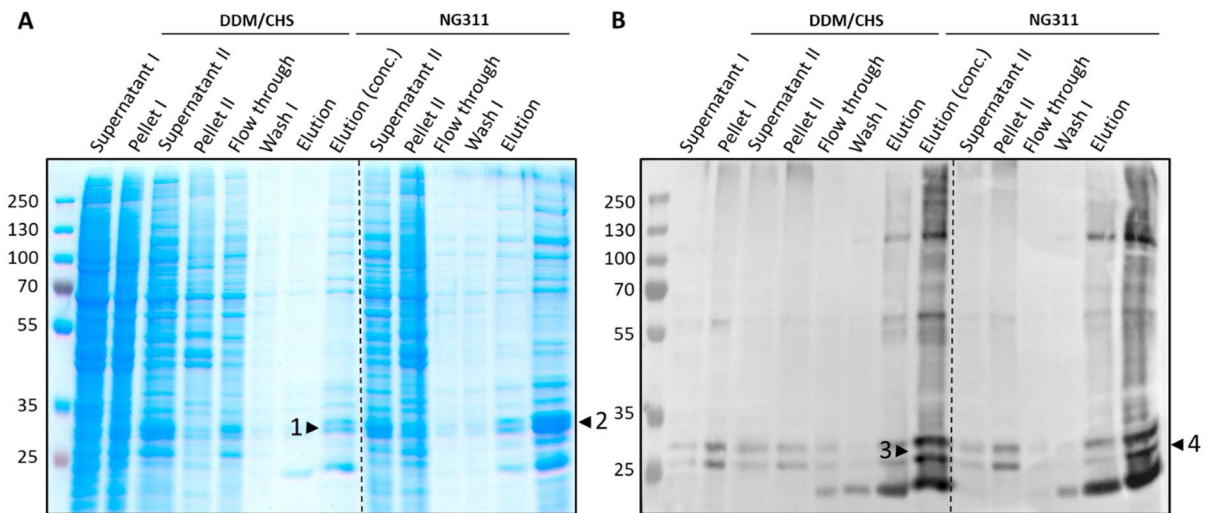
Figure 40. Detergent testing for HA-M1-PLPPR3 TM
M1-PLPPR3 TM was solubilized with 2% DDM/CHS or 2% NG311 for 1.5h at 4°C. After centrifugation, the supernatant II was incubated with M1 flag beads for 2 hours. The beads were washed and the captured M1-PLPPR3 TM fusion construct eluted. All collected samples were separated on a 10% SDS Gel and one gel was western blotted on nitrocellulose and incubated with a primary M1-flag antibody (1:5000) in 5% BSA TBS-T with 2.5 mM CaCl$_2$, while the other gel was stained with Coomassie. After incubation of secondary mouse coupled HRP antibody for 1h at RT in 5% BSA TBS-T, chemiluminescence was detected for 1 min. Arrow 1 and 3 represent NG311 solubilized M1-PLPPR3 TM in coomassie gel and western blot. Arrow 2 and 4 represent DDM/CHS solubilized M1-PLPPR3 TM in coomassie gel and western blot.

I established a full-scale purification of 30 ml expression volume (Figure 41 A), in which I solubilized some HA-M1-PLPPR3 TM. The SEC chromatogram displayed a low yield peak of ~ 4 mAU at fraction B4/B5 (2.55 ml) (Figure 41 C), which was separated by an SDS-PAGE (Figure 41 B), however, detected no coomassie stained bands. In western blot (Figure 41 D), with help of an M1-Flag antibody, I visualized two distinctive bands, one at ~ 30 kDa (arrow 1) which would relate to the TM construct, while the second band appeared at ~ 120 kDa (arrow 2). I speculated that this band might be aggregated HA-

M1-PLPPR3 TM or a higher oligomer, that wasn't denatured by boiling and SDS. Therefore, I was able purify low amounts of PLPPR3 TM, however the next steps included obtaining a better yield. This could be achieved by using a higher amount of HA-M1-PLPPR3 TM transfected Expi293F GNTI- cells and by using concentrators with smaller molecular weight cut off < 30 kDa. The first strategies looked promising and can be followed-up in future, however, I did not continue this part of the project and refocused on PLPPR3 ICD purification.
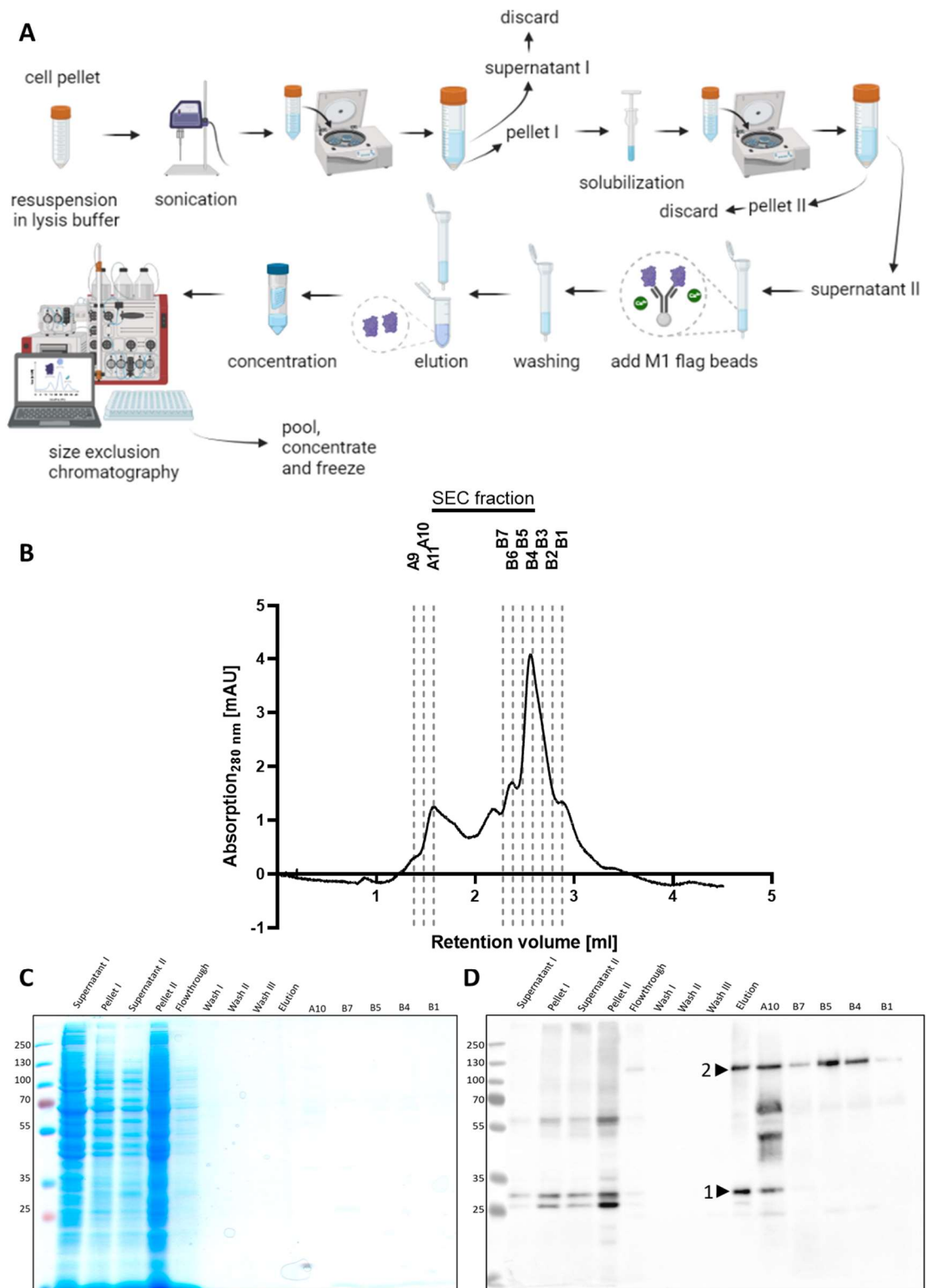
Figure 41. Full-scale purification of HA-M1-PLPPR3 TM
*A Purification scheme of HA-M1-PLPPR3 TM. Cells were defrosted and lysed by sonication, solubilized with 2% NG311 and fusion protein captured by M1 flag antibody affinity chromatography. The eluted protein was further purified by size exclusion chromatography. **B** Coomassie stained SDS-PAGE **C** Size exclusion chromatogram with peak fractions A10 (1.57 ml) and B4/B5 (2.55 ml). **D** Western blot of purification gel with M1 antibody 1:5000.*

6.4 PTEN purification from insect cells

Firstly isolated at the end of the 1990s, Phosphatase and Tensin homolog (PTEN) was found mutated in various human cancers (Li et al., 1997). Located at the plasma membrane, PTEN antagonizes Phosphatidylinositol 3-kinase (PI3K), which synthesizes the second messenger phosphoinositol (3,4,5) triphosphate (PI(3,4,5)P_3). PTEN hydrolyzes PI(3,4,5)P_3 back to phosphoinositol (4,5) bisphosphate (PI(4,5)P_2) (Cully et al., 2006). In our previous work, we could show that PLPPR3 can negatively influence PTEN and redirect growth to axon branches as a result of local PIP3 stabilization (Brosig et al., 2019). Thus, I had the idea to purify PTEN for various assays, including stabilization of PLPPR3 structure, inhibitory assays (data not shown) and *in vitro* liquid-liquid phase separation assays.

I used the protocol of Lee et al., 2015 and overexpressed human PTEN (uniprot: P60484) in *High Five* insect cells in collaboration with my colleague David Speck from AG Scheerer (Charite - Universitaetsmedizin Berlin). For testing, we generated two P1 viruses A and B and subsequently, a P2 virus for each in *Sf*9 cells. 125 ml medium were inoculated with 1:25, 1:75, 1:225 (v/v) P2 virus. PTEN was overexpressed in High-Five insect cells for 48 hours at 27°C, harvested by centrifugation at 4000x g and snap frozen in $N_{2\ (l.)}$.

Purification was done similar to Lee et al., 2015, with the small changes that sonication was performed with a sonicator staff 3 times 30 s, 6 cycles with 60% power, cell debris was removed at 20.000x g for 1 hour and the sample was purified with a Superdex 200 increase 5/150 GL column. In brief, I performed a his-Tag affinity purification with subsequent removal of the N-terminal His-Tag with TEV protease and size exclusion chromatography. The chromatogram (Figure 42 A), showed one peak in the Mock A and B virus, while two peaks were observed for 1:25, 1:75 or 1:225 of the viral test expression. The second peak represents our purified PTEN protein, while the first is likely to be aggregated protein of higher molecular weight.

I compared virus A with B and saw that virus A infection yields higher amounts of PTEN. In addition, I could see shoulders in the PTEN peak of dilutions 1:25 and 1:75 of virus B, which indicated inhomogeneity. Therefore, I chose virus A as our infection virus for all subsequent expressions. I further compared virus A dilutions, where I could see the most homogenous peak with a high yield of PTEN at 1:25. Due to experimental reasons, all further expressions were done with a dilution of 1:50 with virus A.

Score	Molecular weight	Matches	Significant peptides	Significant and unique peptides	Coverage
20370	47763	711	49	2	95%

E

GMTAIIKEIVSRNKRRYQEDGFDLDLTYIYPNIIAM
GFPAERLEGVYRNNIDDVVRFLDSKHKNHYKIYNL
CAERHYDTAKFNCRVAQYPFEDHNPPQLELIKPFC
EDLDQWLSEDDNHVAAIHCKAGKGRTGVMICAYL
LHRGKFLKAQEALDFYGEVRTRDKKGVTIPSQRRY
VYYYSYLLKNHLDYRPVALLFHKMMFETIPMFSGG
TCNPQFVVCQLKVKIYSSNSGPTRREDKFMYFEFP
QPLPVCGDIKVEFFHKQNKMLKKDKMFHFWVNT
FFIPGPEETSEKVENGSLCDQEIDSICSIERADNDKE
YLVLTLTKNDLDKANKDKANRYFSPNFKVKLYFTKT
VEEPSNPEASSSTSVTPDVSDNEPDHYRYSDTTDS
DPENEPFDEDQHTQITKV

Figure 42. PTEN purification
Phosphatase and Tensin homolog (PTEN) is an interaction partner of PLPPR3 (Brosig et al., 2019) that was used for stabilizing PLPPR3 structure. In collaboration with David Speck (AG Scheerer), we established two viruses "A" and "B" to overexpress the fusion construct pOET3-His-TEV-PTEN. Both P1 and P2 viruses were generated in Sf9 insect cells and test-expressed in 125 ml High-Five insect cells. Purification was performed similar to the protocol of Lee et al., 2015. A Size exclusion chromatograms of virus "A" and "B". The first peak represented aggregates and higher molecular proteins (Mock), while the second peak represented PTEN. B Fraction E6 and E7 at ~ 2 ml retention volume was separated on a 10% SDS-gel, as well as a western blot with a PTEN-specific antibody. C Both show a strong band at 55 kDa size, exemplifying PTEN. D The 55 kDa band at E6 was cut out and sent for mass spectrometry, which verified PTEN as the most abundant protein, with a sequence coverage of 95% E. F PTEN activity was monitored with malachite green assay and its substrate PI(3,4,5)P3. PTEN was observed to be active with a PI(3,4,5)P3 conversion rate of 10.67%, releasing 320.09 pmol of inorganic phosphate (P_i).

For evaluation, I took the two peak fractions E6 and E7 of virus A 1:25 and additionally fraction A7 of the aggregate peak. I analyzed these fractions by SDS-PAGE and western blot (Figure 42 B-C). I used a primary PTEN antibody (1:1000) to label PTEN. Western blot showed labelling of PTEN at 55 kDa, however it also indicated degradation products of PTEN. In addition, I cut out band 1 and 2 from the coomassie gel and verified PTEN via LC-MS/MS in collaboration with Dr. Kathrin Textoris-Taube and Manuela Staeber of the HT-MS facility at Charité - Berlin. We detected a sequence coverage of 95%, with all major unique peptides found (Figure 42 D-E).

To evaluate the activity of PTEN, I made use of its enzymatic hydrolysis of PI(3,4,5)P3 to PI(4,5)P2 and P_i. I used the malachite green assay to measure the activity of PTEN, via a complex forming between malachite green and inorganic phosphate that can be measured at 620 nm. The increase of complex is directly proportional to the activity of PTEN. After measuring the absorbance of standards, controls and reaction, I calculated 320.09 pmol free P_i and converted the value into a PI(3,4,5)P3 conversion rate of 10.67% (Figure 42 F). Although active, PTEN activity was not high for several reason. One main reason was the buffer I purified in, which did not contain DTT for reduction, which is essential for *in vitro* activity. A deprotonated cysteine is part of the catalytic residues in the p-loop. Once oxidized the catalytic activity will be reduced (Lee et al., 2015; Zhang et al., 2012). I purified PTEN mainly for complexation experiments with PLPPR3, for which reason, the activity was second important. This part of the project was handed over to Vasiliki Syropoulou.

6.5 BASP1 purification

Brain Acid Soluble Protein 1 (Basp1) also known as Cap23 and Nap22 is a highly conserved protein that was identified in the 1990s as a substrate for Protein Kinase C (PKC) (Widmer & Caroni, 1990). Numerous studies have shown that BASP1 plays a crucial role in neurodevelopment, where it is upregulated during neuronal differentiation and neurite outgrowth (Goodfellow et al., 2011; Korshunova et al., 2008). BASP1 is a 23 kDa large cytosolic protein that can be membrane inserted, when the second glycine residue is acetylated with myristic acid (Hartl & Schneider, 2019). BASP1 has been shown to interact with various molecules and proteins including phosphatidylinositol-4,5-bisphosphate (PI(4,5)P2) and Calmodulin (CaM) (Maekawa et al., 1993; Tong et al., 2008). Recently, Kroon, 2023 could identify BASP1 as an interactor of PLPPR3, which was validated by co-immunoprecipitation. Phosphorylation at serine 351 was shown to recruit BASP1 to the ICD of PLPPR3.

Therefore, I was interested in purifying human BASP1 (uniprot: P80723) as a validated interaction partner. I used the same HA-M1 tag strategy as described in Chapter 1 and purified BASP1 from Expi293F medium. Due to BASP1's membrane association, I wanted to mutate the second glycine residue to make it soluble, however by mistake, mutated the third glycine residue. The construct HA-M1-BASP1 G3A was overexpressed in Expi293F cells for four days and the protein containing medium harvested. I affinity purified BASP1 G3A via M1 flag tag and purified the protein with size exclusion chromatography (SEC) (Figure 43 A). In the coomassie stained SDS gel (Figure 43 C), a band of roughly 55 kDa was observed for the elution fraction and in addition for fractions E2, E3, E4 and E5, which corresponded to BASP1 G3A. BASP1 ran higher than its theoretical molecular weight of 23 kDa, due to its unique GC-rich amino acid composition (Maekawa et al., 1993; Widmer & Caroni, 1990). Fractions E2 to E5 were pooled, concentrated and stored at -80°C. To verify BASP1 G3A I performed a western blot with an M1 antibody, which also indicated bands at roughly 55 kDa size in various fractions (Figures 43 D). Using a purification gel, I observed the enrichment of BASP1 G3A throughout the purification steps. Medium and flow through displayed less strong bands then elution and SEC fractions. Furthermore, in collaboration with Dr. Kathrin Textoris-Taube and Manuela Staeber, we performed mass spectrometry of several protein bands using LC-MS/MS. Analysis of the bands of fraction E4 verified the presence of unique BASP1 G3A peptides and was overall detected with a cleavage coverage of 97% (Figure

43 B and E). Therefore, I concluded, that BASP1 G3A purification was successful, employing the purification procedure described in Chapter 1. I utilized BASP1 for downstream biochemical as well as condensate *in vitro* assays.
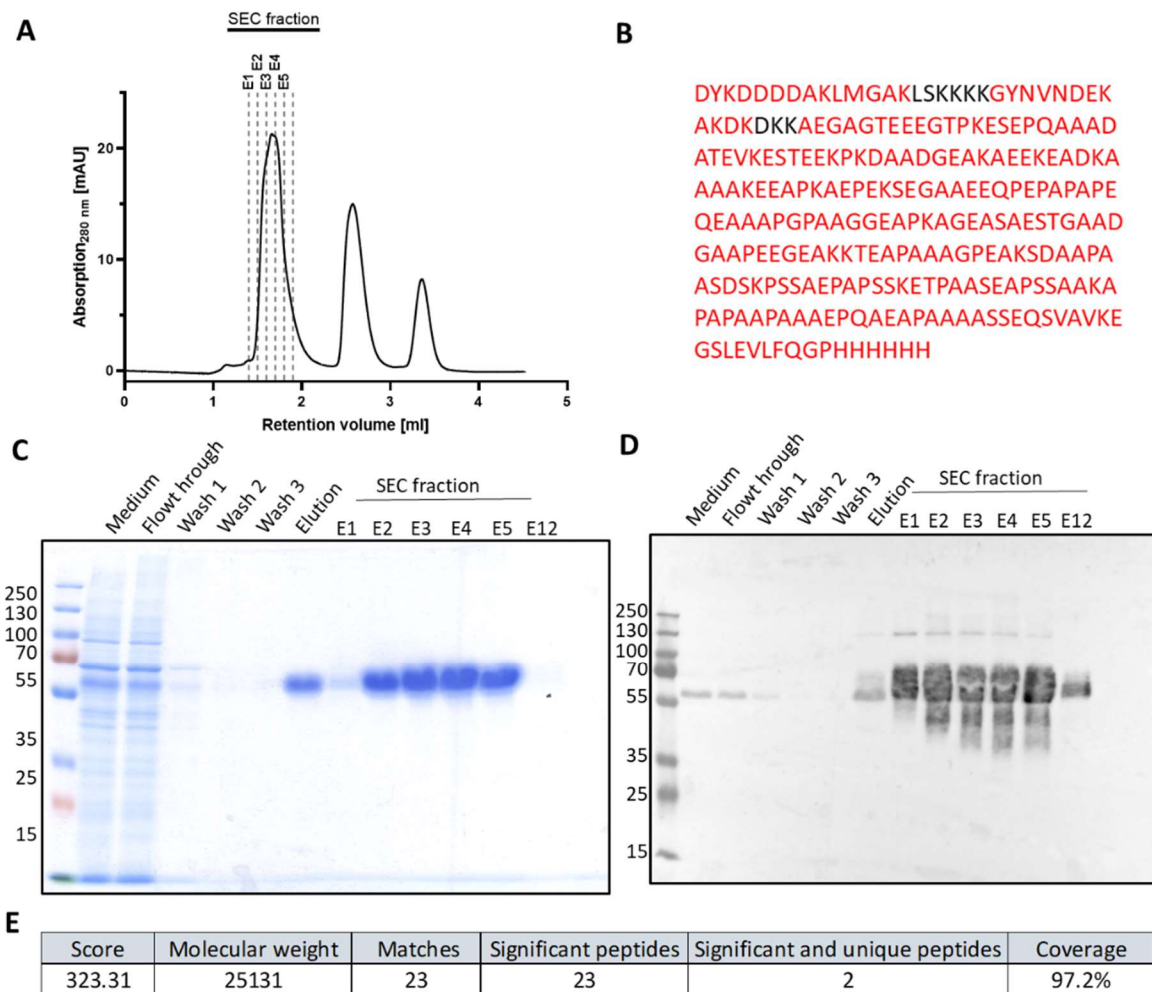
Figure 43. BASP1 G3A purification
*A Size exclusion chromatogram with peak fraction E3/E4 at ~ 1.74 ml. **B** Amino acid sequence of fusion construct. Red amino acids were covered and found during mass spectrometry. **C** Purification gel with BASP1 G3A at 55 kDa. **D** Western blot of purification gel with anti-M1 antibody 1:5000 in 5% BSA TBS-T and secondary anti-mouse HRP coupled antibody 1:5000. Visible is the specific band at 55 kDA. **E** Mass spectrometry analysis of cut out BASP1 G3A band E4 at 55kDa. 23 peptides were found of which 2 were significant for BASP1 G3A.*

6.6 CD Spectroscopy parameters

Table 19. *CD spectroscopy parameters for PLPPR3 ICD*

sample	Baseline air	Baseline buffer 150 mM NaF	PLPPR3 ICD 150 mM NaF	Baseline buffer 20 mM NaF	PLPPR3 ICD 150 mM NaF
Sensitivity (mdeg)	Standard [100mdeg]	Standard [100mdeg]	Standard [100mdeg]	Standard [100mdeg]	Standard [100mdeg]
Start [nm]	260	260	260	260	260
End [nm]	180	181	195	180	185
Data Pitch [nm]	0.1	0.1	0.1	0.1	0.1
Scanning mode	continous	continous	continous	continous	continous
Scanning speed [nm/min]	100	100	100	100	100
Response [s]	1.0	1.0	1.0	1.0	1.0
Band width [nm]	1.0	1.0	1.0	1.0	1.0
Cell length [cm]	/	0.1	0.1	0.1	0.1
Concentration [M]	/	/	$5 \cdot 10^{6}$	/	$5 \cdot 10^{6}$
Accumulation	15	15	15	15	15

7 References

Ahmed, M. B., Alghamdi, A. A. A., Islam, S. U., Lee, J. S., & Lee, Y. S. (2022). cAMP Signaling in Cancer: A PKA-CREB and EPAC-Centric Approach. In *Cells* (Vol. 11, Issue 13). MDPI. https://doi.org/10.3390/cells11132020

Alberti, S., Gladfelter, A., & Mittag, T. (2019). Considerations and Challenges in Studying Liquid-Liquid Phase Separation and Biomolecular Condensates. *Cell*, *176*(3), 419–434. https://doi.org/10.1016/j.cell.2018.12.035

Alberts, B., Alexander, J., Julian, L., Martin, R., Keith, R., & Peter, W. (2002). *Molecular Biology of the Cell* (4th editio).

Alexopoulou, A. N., Couchman, J. R., & Whiteford, J. R. (2008). The CMV early enhancer/chicken β actin (CAG) promoter can be used to drive transgene expression during the differentiation of murine embryonic stem cells into vascular progenitors. *BMC Cell Biology*, *9*. https://doi.org/10.1186/1471-2121-9-2

Allen, N. J., & Barres, B. A. (2009). Glia — more than just brain glue. *Nature*, *457*, 675–677. https://doi.org/https://doi.org/10.1038/457675a

Anila, M. M., Ghosh, R., & Różycki, B. (2023). Membrane curvature sensing by model biomolecular condensates. *Soft Matter*, *19*(20), 3723–3732. https://doi.org/10.1039/d3sm00131h

Arakel, E. C., & Schwappach, B. (2018). Formation of COPI-coated vesicles at a glance. *Journal of Cell Science*, *131*(5). https://doi.org/10.1242/jcs.209890

Aramaki, S., Mayanagi, K., Jin, M., Aoyama, K., & Yasunaga, T. (2016). Filopodia formation by crosslinking of F-actin with fascin in two different binding manners. *Cytoskeleton*, *73*(7), 365–374. https://doi.org/10.1002/cm.21309

Ardito, F., Giuliani, M., Perrone, D., Troiano, G., & Muzio, L. Lo. (2017). The crucial role of protein phosphorylation in cell signalingand its use as targeted therapy (Review). In *International Journal of Molecular Medicine* (Vol. 40, Issue 2, pp. 271–280). Spandidos Publications. https://doi.org/10.3892/ijmm.2017.3036

Aste, N., & Di Matteo, T. (2006). Nanometric architectures: emergence of efficient non-crystalline atomic organization in nanostructures. In R. H. J. Hannink & A. J. Hill (Eds.), *Nanostructure Control of Materials* (pp. 32–56). Woodhead Publishing. https://doi.org/https://doi.org/10.1533/9781845691189.32.

Attwood, M. M., & Schiöth, H. B. (2021). Characterization of Five Transmembrane Proteins: With Focus on the Tweety, Sideroflexin, and YIP1 Domain Families. *Frontiers in Cell and Developmental Biology*, *9*(July), 1–15. https://doi.org/10.3389/fcell.2021.708754

Azari, H., & Reynolds, B. A. (2016). In vitro models for neurogenesis. *Cold Spring Harbor Perspectives in Biology*, *8*(6). https://doi.org/10.1101/cshperspect.a021279

Babinchak, W. M., & Surewicz, W. K. (2020). Liquid–Liquid Phase Separation and Its Mechanistic Role in Pathological Protein Aggregation. *Journal of Molecular Biology*, *432*(7), 1910–1925. https://doi.org/10.1016/j.jmb.2020.03.004

Banani, S. F., Lee, H. O., Hyman, A. A., & Rosen, M. K. (2017). Biomolecular condensates: Organizers of cellular biochemistry. *Nat Rev Mol Cell Biol*, *18*(5), 285–298.

Banjade, S., & Rosen, M. K. (2014). Phase transitions of multivalent proteins can promote clustering of membrane receptors. *eLife*, *3*. https://doi.org/10.7554/eLife.04123

Barber, N. C., & Stark, L. A. (2014). Engaging with molecular form to understand function. *CBE Life Sciences Education*, *13*(1), 21–24. https://doi.org/10.1187/cbe.13-12-0247

Bashaw, G. J., & Goodman, C. S. (1999). Chimeric axon guidance receptors: The cytoplasmic domains of slit and netrin receptors specify attraction versus repulsion. *Cell*, *97*(7), 917–926. https://doi.org/10.1016/S0092-8674(00)80803-X

Beristain, A. G., Molyneux, S. D., Joshi, P. A., Pomroy, N. C., Di Grappa, M. A., Chang, M. C., Kirschner, L. S., Privé, G. G., Pujana, M. A., & Khokha, R. (2015). PKA signaling drives mammary tumorigenesis through Src. *Oncogene*, *34*(9), 1160–1173. https://doi.org/10.1038/onc.2014.41

Bhatia, T., Husen, P., Brewer, J., Bagatolli, L. A., Hansen, P. L., Ipsen, J. H., & Mouritsen, O. G. (2015). Preparing giant unilamellar vesicles (GUVs) of complex lipid mixtures on demand: Mixing small unilamellar vesicles of compositionally heterogeneous mixtures. *Biochimica et Biophysica Acta - Biomembranes*, *1848*(12), 3175–3180. https://doi.org/10.1016/j.bbamem.2015.09.020

Bindels, D. S., Haarbosch, L., Van Weeren, L., Postma, M., Wiese, K. E., Mastop, M., Aumonier, S., Gotthard, G., Royant, A., Hink, M. A., & Gadella, T. W. J. (2016). MScarlet: A bright monomeric red fluorescent protein for cellular imaging. *Nature Methods*, *14*(1), 53–56. https://doi.org/10.1038/nmeth.4074

Boeynaems, S., Chong, S., Gsponer, J., Holt, L., Milovanovic, D., Mitrea, D. M., Mueller-Cajar, O., Portz, B., Reilly, J. F., Reinkemeier, C. D., Sabari, B. R., Sanulli, S., Shorter, J., Sontag, E., Strader, L., Stachowiak, J., Weber, S. C., White, M., Zhang, H., … Elbaum-Garfinkle, S. R. K. (2023). Phase Separation in Biology and Disease; Current Perspectives and Open Questions. *J Mol Biol.*, *435*(1). https://doi.org/10.1016/j.jmb.2023.167971.

Bogaert, E., Boeynaems, S., Kato, M., Guo, L., Caulfield, T. R., Steyaert, J., Scheveneels, W., Wilmans, N., Haeck, W., Hersmus, N., Schymkowitz, J., Rousseau, F., Shorter, J., Callaerts, P., Robberecht, W., Van Damme, P., & Van Den Bosch, L. (2018). Molecular Dissection of FUS Points at Synergistic Effect of Low-Complexity Domains in Toxicity. *Cell Reports*, *24*(3), 529–537.e4. https://doi.org/10.1016/j.celrep.2018.06.070

Boija, A., Klein, I. A., Sabari, B. R., Dall'Agnese, A., Coffey, E. L., Zamudio, A. V., Li, C. H., Shrinivas, K., Manteiga, J. C., Hannett, N. M., Abraham, B. J., Afeyan, L. K., Guo, Y. E., Rimel, J. K., Fant, C. B., Schuijers, J., Lee, T. I., Taatjes, D. J., & Young, R. A. (2018). Transcription Factors Activate Genes through the Phase-Separation Capacity of Their Activation Domains. *Cell*, *175*(7), 1842–1855.e16. https://doi.org/10.1016/j.cell.2018.10.042

Boyko, S., Qi, X., Chen, T. H., Surewicz, K., & Surewicz, W. K. (2019). Liquid-liquid phase separation of tau protein: The crucial role of electrostatic interactions. *Journal of Biological Chemistry*, *294*(29), 11054–11059. https://doi.org/10.1074/jbc.AC119.009198

Bradke, F., & Dotti, C. G. (1999). The Role of Local Actin Instability in Axon Formation. *Science*, *283*(5409), 1931–1934. https://doi.org/10.1126/science.283.5409.1931

Brangwynne, C. P., Tompa, P., & Pappu, R. V. (2015). Polymer physics of intracellular phase transitions. *Nature Physics*, *11*(11), 899–904. https://doi.org/10.1038/nphys3532

Bräuer, A. U., & Nitsch, R. (2008). Plasticity-related genes (PRGs/LRPs): A brain-specific class of lysophospholipid-modifying proteins. *Biochimica et Biophysica Acta - Molecular and Cell Biology of Lipids*, *1781*(9), 595–600. https://doi.org/10.1016/j.bbalip.2008.04.004

Bräuer, A. U., Savaskan, N. E., Kühn, H., Prehn, S., Ninnemann, O., & Nitsch, R. (2003). A new phospholipid phosphatase, PRG-1, is involved in axon growth and regenerative sprouting. *Nature Neuroscience*, *6*(6), 572–578. https://doi.org/10.1038/nn1052

Brazil, D. P., & Hemmings, B. A. (2001). Ten years of protein kinase Bsignalling: a hard Akt to follow. *TRENDS in Biochemical Sciences*, *26*(11), 657–664. https://doi.org/https://doi.org/10.1016/S0968-0004(01)01958-2

Brindley, D. N., & Pilquil, C. (2009). Lipid phosphate phosphatases and signaling. *Journal of Lipid Research*, *50*(SUPPL.). https://doi.org/10.1194/jlr.R800055-JLR200

Brindley, D. N., & Waggoner, D. W. (1996). Phosphatidate phosphohydrolase and signal transduction. In *Chemistry and Physics of Chemistry and Physics of Lipids LIPIDS* (Vol. 80). ELSEVIER.

Brindley, D. N., & Waggoner, D. W. (1998). Mammalian Lipid Phosphate Phosphohydrolases*. *The Journal of Biological Chemistry*, *273*(38), 24281–24284. https://doi.org/https://doi.org/10.1074/jbc.273.38.24281

Brocca, S., Grandori, R., Longhi, S., & Uversky, V. (2020). Liquid–liquid phase separation by intrinsically disordered protein regions of viruses: Roles in viral life cycle and control of virus–host interactions. *International Journal of Molecular Sciences*, *21*(23), 1–31. https://doi.org/10.3390/ijms21239045

Broggini, T., Nitsch, R., & Savaskan, N. E. (2010). Plasticity-related Gene 5 (PRG5) Induces Filopodia and Neurite Growth and Impedes Lysophosphatidic Acid-and Nogo-A-mediated Axonal Retraction. *Molecular Biology of the Cell*, *21*, 521–537. https://doi.org/10.1091/mbc.E09

Broggini, T., Nitsch, R., & Savaskan, N. E. (2010). Plasticity-related Gene 5 (PRG5) Induces Filopodia and Neurite Growth and Impedes Lysophosphatidic Acid- and Nogo-A-mediated Axonal Retraction. *Molecular Biology of the Cell*, *21*(4), 521–537. https://doi.org/10.1091/mbc.E09-06-0506

Broggini, T., Schnell, L., Ghoochani, A., Mateos, J. M., Buchfelder, M., Wiendieck, K., Schäfer, M. K., Eyupoglu, I. Y., & Savaskan, N. E. (2016a). Plasticity Related Gene 3 (PRG3) overcomes myelin-associated growth inhibition and promotes functional recovery after spinal cord injury. *Aging*, *8*(10), 2463–2487. https://doi.org/10.18632/aging.101066

Broggini, T., Schnell, L., Ghoochani, A., Mateos, M. J., Buchfelder, M., Wiendieck, K., Schäfer, M. K., Eyupoglu, I. Y., & Savaskan, N. E. (2016b). Plasticity Related Gene 3 (PRG3) overcomes myelin-associated growthinhibition and promotes functional recovery after spinal cord injury. *Aging (Albany NY)*, *8*(10), 2463–2487. https://doi.org/10.18632/aging.101066.

Brosig, A., Fuchs, J., Ipek, F., Kroon, C., Schrötter, S., Vadhvani, M., Polyzou, A., Ledderose, J., van Diepen, M., Holzhütter, H. G., Trimbuch, T., Gimber, N.,

Schmoranzer, J., Lieberam, I., Rosenmund, C., Spahn, C., Scheerer, P., Szczepek, M., Leondaritis, G., & Eickholt, B. J. (2019a). The Axonal Membrane Protein PRG2 Inhibits PTEN and Directs Growth to Branches. *Cell Reports*, *29*(7), 2028–2040.e8. https://doi.org/10.1016/j.celrep.2019.10.039

Brosig, A., Fuchs, J., Ipek, F., Kroon, C., Schrötter, S., Vadhvani, M., Polyzou, A., Ledderose, J., van Diepen, M., Holzhütter, H. G., Trimbuch, T., Gimber, N., Schmoranzer, J., Lieberam, I., Rosenmund, C., Spahn, C., Scheerer, P., Szczepek, M., Leondaritis, G., & Eickholt, B. J. (2019b). The Axonal Membrane Protein PRG2 Inhibits PTEN and Directs Growth to Branches. *Cell Reports*, *29*(7), 2028–2040.e8. https://doi.org/10.1016/j.celrep.2019.10.039

Burkel, B. M., Von Dassow, G., & Bement, W. M. (2007). Versatile fluorescent probes for actin filaments based on the actin-binding domain of utrophin. *Cell Motility and the Cytoskeleton*, *64*(11), 822–832. https://doi.org/10.1002/cm.20226

Busnelli, M., Manzini, S., Parolini, C., Escalante-Alcalde, D., & Chiesa, G. (2018). Lipid phosphate phosphatase 3 in vascular pathophysiology. In *Atherosclerosis* (Vol. 271, pp. 156–165). Elsevier Ireland Ltd. https://doi.org/10.1016/j.atherosclerosis.2018.02.025

C Huang, W. Y., Alvarez, S., Kondo, Y., Kwang Lee, Y., Chung, J. K., Yue Monatrice Lam, H., Biswas, K. H., Kuriyan, J., & Groves, J. T. (2019). A molecular assembly phase transition and kinetic proofreading modulate Ras activation by SOS. *Science*, *363*(6431), 1098–1103. https://doi.org/10.1126/science.aau572

Cajal, S. R. (1989). *Recollections of My Life*. Cambridge: MIT. https://books.google.de/books?id=IbAoAAAAYAAJ

Calabresi, P., Mechelli, A., Natale, G., Volpicelli-Daley, L., Di Lazzaro, G., & Ghiglieri, V. (2023). Alpha-synuclein in Parkinson's disease and other synucleinopathies: from overt neurodegeneration back to early synaptic dysfunction. In *Cell Death and Disease* (Vol. 14, Issue 3). Springer Nature. https://doi.org/10.1038/s41419-023-05672-9

Carlsson, A. E. (2018). Membrane bending by actin polymerization. *Current Opinion in Cell Biology*, *50*, 1–7. https://doi.org/10.1016/j.ceb.2017.11.007

Carman, P. J., & Dominguez, R. (2018). BAR domain proteins—a linkage between cellular membranes, signaling pathways, and the actin cytoskeleton. In *Biophysical Reviews* (Vol. 10, Issue 6, pp. 1587–1604). Springer Verlag. https://doi.org/10.1007/s12551-018-0467-7

Carnero, A., & Paramio, J. M. (2014). The PTEN/PI3K/AKT Pathway in vivo, cancer mouse models. *Frontiers in Oncology*, *4*(SEP). https://doi.org/10.3389/fonc.2014.00252

Carvalho, K., Ramos, L., Roy, C., & Picart, C. (2008). Giant unilamellar vesicles containing phosphatidylinositol(4,5) bisphosphate: Characterization and functionality. *Biophysical Journal*, *95*(9), 4348–4360. https://doi.org/10.1529/biophysj.107.126912

Case, L. B., Zhang, X., Ditlev, J. A., & Rosen, M. K. (2019a). *Stoichiometry controls activity of phase-separated clusters of actin signaling proteins*. https://www.science.org

Case, L. B., Zhang, X., Ditlev, J. A., & Rosen, M. K. (2019b). Stoichiometry controls activity of phase-separated clusters of actin signaling proteins. *Science*, *363*(6431), 1093–1097. https://doi.org/10.1126/science.aau6313

Chakraborty, H., & Lentz, B. R. (2012). A simple method for correction of circular dichroism spectra obtained from membrane-containing samples. *Biochemistry*, *51*(5), 1005–1008. https://doi.org/10.1021/bi300025c

Che, D. L., Duan, L., Zhang, K., & Cui, B. (2015). The Dual Characteristics of Light-Induced Cryptochrome 2, Homo-oligomerization and Heterodimerization, for Optogenetic Manipulation in Mammalian Cells. *ACS Synth Biol*, *4*(10), 1124–1135. https://doi.org/10.1021/acssynbio.5b00048

Chemes, L. B., Alonso, L. G., Noval, M. G., & de Prat-Gay, G. (2012). Circular Dichroism Techniques for the Analysis of Intrinsically Disordered Proteins and Domains. In V. N. Uversky & A. K. Dunker (Eds.), *Methods in Molecular Biology* (Vol. 895, pp. 387–404). Springer Science+Business Media. https://doi.org/10.1007/978-1-61779-927-3_16

Chen, C., Jia, H., Nakamura, Y., Kanekura, K., & Hayamizu, Y. (2022). Effect of Multivalency on Phase-Separated Droplets Consisting of Poly(PR) Dipeptide Repeats and RNA at the Solid/Liquid Interface. *ACS Omega*, *7*(23), 19280–19287. https://doi.org/10.1021/acsomega.2c00811

Chen, X., Jia, B., Zhu, S., & Zhang, M. (2023). Phase separation-mediated actin bundling by the postsynaptic density condensates. *eLife*, *12*. https://doi.org/10.7554/eLife.84446

Cheng, J., Sahani, S., Hausrat, T. J., Yang, J. W., Ji, H., Schmarowski, N., Endle, H., Liu, X., Li, Y., Böttche, R., Radyushkin, K., Maric, H. M., Hoerder-Suabedissen, A., Molnár, Z., Prouvot, P. H., Trimbuch, T., Ninnemann, O., Huai, J., Fan, W., … Vogt, J. (2016). Precise Somatotopic Thalamocortical Axon Guidance Depends on LPA-Mediated PRG-2/Radixin Signaling. *Neuron*, *92*(1), 126–142. https://doi.org/10.1016/j.neuron.2016.08.035

Choi, J.-M., Holehouse, A. S., & Pappu, R. V. (2020). *Physical Principles Underlying the Complex Biology of Intracellular Phase Transitions*. https://doi.org/10.1146/annurev-biophys-121219

Clifford P. Brangwynne, Christian R. Eckmann, David S. Courson, Agata Rybarska, Carsten Hoege, Jöbin Gharakhani, Frank Jülicher, & Anthony A. Hyman. (2009). Germline P Granules Are LiquidDroplets That Localize by ControlledDissolution/Condensation. *Science*, *324*(5935), 1729–1732. https://doi.org/10.1126/science.1171716

Cohen, P. (2000). The regulation of proteinfunction by multisitephosphorylation – a 25 yearupdate. *Trends Biochem. Sci.*, *25*(12), 596–601. https://doi.org/10.1016/s0968-0004(00)01712-6

Cohen, S., Valm, A. M., & Lippincott-Schwartz, J. (2018). Interacting organelles. *Current Opinion in Cell Biology*, *53*, 84–91. https://doi.org/10.1016/j.ceb.2018.06.003

Coiro, P., Stoenica, L., Strauss, U., & Braüer, A. U. (2014a). Plasticity-related gene 5 promotes spine formation in murine hippocampal neurons. *Journal of Biological Chemistry*, *289*(36), 24956–24970. https://doi.org/10.1074/jbc.M114.597880

Coiro, P., Stoenica, L., Strauss, U., & Braüer, A. U. (2014b). Plasticity-related gene 5 promotes spine formation in murine hippocampal neurons. *Journal of Biological Chemistry*, *289*(36), 24956–24970. https://doi.org/10.1074/jbc.M114.597880

Cooper, G. (2000). *The Cell: A Molecular Approach* (2nd ed.). Sinauer Associates 2000. http://lib.ugent.be/catalog/ebk01:3450000000002155

Cosens, D. J., & Manning, A. (1969). Abnormal electroretinogram from drosophila Mutant. *Nature*, *224*, 285–287. https://doi.org/https://doi.org/10.1038/224285a0

Cox, J., Hein, M. Y., Luber, C. A., Paron, I., Nagaraj, N., & Mann, M. (2014). Accurate proteome-wide label-free quantification by delayed normalization and maximal peptide ratio extraction, termed MaxLFQ. *Molecular and Cellular Proteomics*, *13*(9), 2513–2526. https://doi.org/10.1074/mcp.M113.031591

Craig, A. M., & Banker, G. (1994). Neuronal polarity. *Annu. Rev. Neurosci.*, *17*, 267–310. https://doi.org/10.1146/annurev.ne.17.030194.001411.

Creamer, T. P. (2020). Calcineurin. *Cell Communication and Signaling*, *18*(1). https://doi.org/10.1186/s12964-020-00636-4

Cully, M., You, H., Levine, A. J., & Mak, T. W. (2006). Beyond PTEN mutations: The PI3K pathway as an integrator of multiple inputs during tumorigenesis. *Nature Reviews Cancer*, *6*(3), 184–192. https://doi.org/10.1038/nrc1819

Dailey, M. E., & Smith, S. J. (1996). The Dynamics of Dendritic Structure in Developing Hippocampal Slices. *The Journal of Neuroscience*, *16*(9), 2983–2994.

De Moreno, M. R., Smith, J. F., & Smith, R. V. (1986). Mechanism Studies of Coomassie Blue and Silver Staining of Proteins. In *American Pharmaceutical Association Journal of Pharmaceutical Sciences* (Vol. 907, Issue 9).

Dehmelt, L., & Halpain, S. (2004). Actin and Microtubules in Neurite Initiation: Are MAPs the Missing Link? In *Journal of Neurobiology* (Vol. 58, Issue 1, pp. 18–33). https://doi.org/10.1002/neu.10284

Dent, E. W., & Kalil, K. (2001). Axon Branching Requires Interactions between Dynamic Microtubules and Actin Filaments. *J. Neurosci.*, *21*(24), 9757–9769. http://kalil.anatomy.wisc.edu.

Dent, E. W., Kwiatkowski, A. V., Mebane, L. M., Philippar, U., Barzik, M., Rubinson, D. A., Gupton, S., Van Veen, J. E., Furman, C., Zhang, J., Alberts, A. S., Mori, S., & Gertler, F. B. (2007). Filopodia are required for cortical neurite initiation. *Nature Cell Biology*, *9*(12), 1347–1359. https://doi.org/10.1038/ncb1654

Dill, K. A., & Bromberg, S. (2003). Molecular driving forces : statistical thermodynamics in chemistry and biology / Ken A. Dill ; Sarina Bromberg. In *Molecular driving forces : statistical thermodynamics in chemistry and biology*. Garland Science.

Dobramysl, U., Jarsch, I. K., Inoue, Y., Shimo, H., Richier, B., Gadsby, J. R., Mason, J., Szałapak, A., Ioannou, P. S., Correia, G. P., Walrant, A., Butler, R., Hannezo, E., Simons, B. D., & Gallop, J. L. (2021). Stochastic combinations of actin regulatory proteins are sufficient to drive filopodia formation. *Journal of Cell Biology*, *220*(4). https://doi.org/10.1083/jcb.202003052

Dominguez, R., & Holmes, K. C. (2011). Actin structure and function. *Annual Review of Biophysics*, *40*(1), 169–186. https://doi.org/10.1146/annurev-biophys-042910-155359

Dotti, C. G., Sullivan, C. A., & Banker, G. A. (1988). The Establishment of Polarity by Hippocampal Neurons in Culture. In *The Journal of Neuroscience: Vol. I* (Issue 4).

Dou, Y., Lin, Y., Wang, T. yun, Wang, X. Y., Jia, Y. long, & Zhao, C. peng. (2021). The CAG promoter maintains high-level transgene expression in HEK293 cells.

FEBS Open Bio, *11*(1), 95–104. https://doi.org/10.1002/2211-5463.13029

Duan, L., Hope, J., Ong, Q., Lou, H. Y., Kim, N., McCarthy, C., Acero, V., Lin, M. Z., & Cui, B. (2017). Understanding CRY2 interactions for optical control of intracellular signaling. *Nature Communications*, *8*(1), 4–13. https://doi.org/10.1038/s41467-017-00648-8

Dunker, A. K., Lawson, J. D., Brown, C. J., Williams, R. M., Romero, P., Oh, J. S., Oldfield, C. J., Campen, A. M., Ratliff, C. M., Hipps, K. W., Ausio, J., Nissen, M. S., Reeves, R., Kang, C., Kissinger, C. R., Bailey, R. W., Griswold, M. D., Chiu, W., Garner, E. C., & Obradovic, Z. (2001). *Intrinsically disordered protein*.

Düster, R., Kaltheuner, I. H., Schmitz, M., & Geyer, M. (2021). 1,6-Hexanediol, commonly used to dissolve liquid-liquid phase separated condensates, directly impairs kinase and phosphatase activities. *Journal of Biological Chemistry*, *296*. https://doi.org/10.1016/J.JBC.2021.100260

Dyson, H. J., & Wright, P. E. (2005). Intrinsically unstructured proteins and their functions. *Nature Reviews Molecular Cell Biology*, *6*(3), 197–208. https://doi.org/10.1038/nrm1589

Einhauer, A., & Jungbauer, A. (2001). The FLAG^{TM} peptide, a versatile fusion tag for the purification of recombinant proteins. *Journal of Biochemical and Biophysical Methods*, *49*(1–3), 455–465. https://doi.org/10.1016/S0165-022X(01)00213-5

Ellis, S., & Mellor, H. (2000). The novel Rho-family GTPase Rif regulates coordinatedactin-based membrane rearrangements. *Current Biology*, *10*(21), 1387–1390.

Fan, J., Jiang, D., Zhao, Y., Liu, J., & Zhang, X. C. (2014). Crystal structure of lipid phosphatase Escherichia coli phosphatidylglycerophosphate phosphatase B. *Proceedings of the National Academy of Sciences of the United States of America*, *111*(21), 7636–7640. https://doi.org/10.1073/pnas.1403097111

Farahi, N., Lazar, T., Wodak, S. J., Tompa, P., Pancsa, R., & Uversky, N. (2021). Integration of Data from Liquid-Liquid Phase Separation Databases Highlights Concentration and Dosage Sensitivity of LLPS Drivers Integration of Data from Liquid-Liquid Phase Separation Databases Highlights Concentration and Dosage Sensitivity of LLPS. *International Journal of Molecular Sciences Article Int. J. Mol. Sci*. https://doi.org/10.3390/ijms

Feng, Z., Chen, X., Wu, X., & Zhang, M. (2019). Formation of biological condensates via phase separation: Characteristics, analytical methods, and physiological implications. *Journal of Biological Chemistry*, *294*(40), 14823–14835. https://doi.org/10.1074/jbc.REV119.007895

Feng, Z., Jia, B., & Zhang, M. (2021). Liquid-Liquid Phase Separation in Biology: Specific Stoichiometric Molecular Interactions vs Promiscuous Interactions Mediated by Disordered Sequences. *Biochemistry*, *60*(31), 2397–2406. https://doi.org/10.1021/acs.biochem.1c00376

Feric, M., Vaidya, N., Harmon, T. S., Mitrea, D. M., Zhu, L., Richardson, T. M., Kriwacki, R. W., Pappu, R. V., & Brangwynne, C. P. (2016). Coexisting Liquid Phases Underlie Nucleolar Subcompartments. *Cell*, *165*(7), 1686–1697. https://doi.org/10.1016/j.cell.2016.04.047

Ferré, C. A., Thouard, A., Bétourné, A., Le Dorze, A. L., Belenguer, P., Miquel, M. C., Peyrin, J. M., Gonzalez-Dunia, D., & Szelechowski, M. (2021). HSPA9/Mortalin

mediates axo-protection and modulates mitochondrial dynamics in neurons. *Scientific Reports*, *11*(1). https://doi.org/10.1038/s41598-021-97162-1

Ferreon, J. C., Jain, A., Choi, K. J., Tsoi, P. S., Mackenzie, K. R., Jung, S. Y., & Ferreon, A. C. (2018). Acetylation disfavors tau phase separation. *International Journal of Molecular Sciences*, *19*(5). https://doi.org/10.3390/ijms19051360

Flory, P. J. (1942). Themodynamics of high polymer solutions. *The Journal of Chemical Physics*, *10*(1), 51–61. https://doi.org/10.1063/1.1723621

Flynn, K. C. (2013). The cytoskeleton and neurite initiation. In *Bioarchitecture* (Vol. 3, Issue 4, pp. 86–109). https://doi.org/10.4161/bioa.26259

Fontana, A., Polverino De Laureto, P., De Filippis, V., Scaramella, E., & Zambonin, M. (1997). Probing the partly folded states of proteins by limited proteolysis. *Folding and Design*, *2*(2), R17–R26.

Forman-Kay, J. D., & Mittag, T. (2013). From sequence and forces to structure, function, and evolution of intrinsically disordered proteins. In *Structure* (Vol. 21, Issue 9, pp. 1492–1499). https://doi.org/10.1016/j.str.2013.08.001

Franzmann, T. M., Jahnel, M., Pozniakovsky, A., Mahamid, J., Holehouse, A. S., Nüske, E., Richter, D., Baumeister, W., Grill, S. W., Pappu, R. V., Hyman, A. A., & Alberti, S. (2018). Phase separation of a yeast prion protein promotes cellular fitness. *Science*, *359*(6371). https://doi.org/10.1126/science.aao5654

Frenkel, D., & Smit, B. (2002). *Understanding molecular simulation: From Algorithms to Applications* (Second Edition). Academic Press. https://doi.org/10.1016/B978-0-12-267351-1.X5000-7

Fuchs, J., Bareesel, S., Kroon, C., Polyzou, A., Eickholt, B. J., & Leondaritis, G. (2022). Plasma membrane phospholipid phosphatase-related proteins as pleiotropic regulators of neuron growth and excitability. *Frontiers in Molecular Neuroscience*, *15*. https://doi.org/10.3389/fnmol.2022.984655

Fuchs, J., Bareesel, S., Kroon, C., Polyzou, A., Eickholt, B. J., & Leondaritis, G. (2022). Plasma membrane phospholipid phosphatase-related proteins as pleiotropic regulators of neuron growth and excitability. In *Frontiers in Molecular Neuroscience* (Vol. 15). Frontiers Media S.A. https://doi.org/10.3389/fnmol.2022.984655

Fuchs, J., & Eickholt, B. J. (2021a). Precursor types predict the stability of neuronal branches. *Journal of Cell Science*, *134*(23), 1–16. https://doi.org/10.1242/jcs.258983

Fuchs, J., & Eickholt, B. J. (2021b). Precursor types predict the stability of neuronal branches. *Journal of Cell Science*, *134*(23). https://doi.org/10.1242/jcs.258983

Fuchs, J., Eickholt, B. J., & Leondaritis, G. (2020). Harnessing PTEN's Growth Potential in Neuronal Development and Disease. *Neuroscience Insights*, *15*, 0–3. https://doi.org/10.1177/2633105520959056

Gallo, G. (2013). Mechanisms Underlying the Initiation and Dynamics of Neuronal Filopodia. From Neurite Formation to Synaptogenesis. In *International Review of Cell and Molecular Biology* (Vol. 301, pp. 95–156). Elsevier Inc. https://doi.org/10.1016/B978-0-12-407704-1.00003-8

Gallop, J. L. (2020). Filopodia and their links with membrane traffic and cell adhesion.

In *Seminars in Cell and Developmental Biology* (Vol. 102, pp. 81–89). Elsevier Ltd. https://doi.org/10.1016/j.semcdb.2019.11.017

Ganar, K. A., Honaker, L. W., & Deshpande, S. (2021). Shaping synthetic cells through cytoskeleton-condensate-membrane interactions. *Current Opinion in Colloid and Interface Science*, *54*. https://doi.org/10.1016/j.cocis.2021.101459

Gao, Z., Zhang, W., Chang, R., Zhang, S., Yang, G., & Zhao, G. (2021). Liquid-Liquid Phase Separation: Unraveling the Enigma of Biomolecular Condensates in Microbial Cells. *Frontiers in Microbiology*, *12*. https://doi.org/10.3389/fmicb.2021.751880

Garcia-Garcia, T., Poncet, S., Derouiche, A., Shi, L., Mijakovic, I., & Noirot-Gros, M. F. (2016). Role of protein phosphorylation in the regulation of cell cycle and DNA-related processes in bacteria. In *Frontiers in Microbiology* (Vol. 7, Issue FEB). Frontiers Media S.A. https://doi.org/10.3389/fmicb.2016.00184

Gaub, B. M., Chaitanya Kasuba, K., Mace, E., Strittmatter, T., Laskowski, P. R., Geissler, S. A., Hierlemann, A., Fussenegger, M., Roska, B., & Müller, D. J. (2020). Neurons differentiate magnitude and location of mechanical stimuli. *PNAS*, *117*(2), 848–856. https://doi.org/10.1073/pnas.1909933117/-/DCSupplemental

Georges, P. C., Hadzimichalis, N. M., Sweet, E. S., & Firestein, B. L. (2008). The yin-yang of dendrite morphology: Unity of actin and microtubules. In *Molecular Neurobiology* (Vol. 38, Issue 3, pp. 270–284). Humana Press Inc. https://doi.org/10.1007/s12035-008-8046-8

Geraldo, S., Khanzada, U. K., Parsons, M., Chilton, J. K., & Gordon-Weeks, P. R. (2008). Targeting of the F-actin-binding protein drebrin by the microtubule plus-tip protein EB3 is required for neuritogenesis. *Nature Cell Biology*, *10*(10), 1181–1189. https://doi.org/10.1038/ncb1778

Ginell Garrett M.and Holehouse, A. S. (2023). An Introduction to the Stickers-and-Spacers Framework as Applied to Biomolecular Condensates. In J.-H. and B. P. R. Zhou Huan-Xiangand Spille (Ed.), *Phase-Separated Biomolecular Condensates: Methods and Protocols* (pp. 95–116). Springer US. https://doi.org/10.1007/978-1-0716-2663-4_4

Gomes, E., & Shorter, J. (2019). The molecular language of membraneless organelles. *Journal of Biological Chemistry*, *294*(18), 7115–7127. https://doi.org/10.1074/jbc.TM118.001192

Gong, C.-X., & Iqbal, K. (2008). Hyperphosphorylation of Microtubule-Associated Protein Tau: A Promising Therapeutic Target for Alzheimer Disease. *Curr Med Chem*, *15*(23), 2321–2328. https://doi.org/10.2174/092986708785909111

Goodfellow, S. J., Rebello, M. R., Toska, E., Zeef, L. A. H., Rudd, S. G., Medler, K. F., & Roberts, S. G. E. (2011). WT1 and its transcriptional cofactor BASP1 redirect the differentiation pathway of an established blood cell line. *Biochemical Journal*, *435*(1), 113–125. https://doi.org/10.1042/BJ20101734

Gov, N. S., & Gopinathan, A. (2006). Dynamics of membranes driven by actin polymerization. *Biophysical Journal*, *90*(2), 454–469. https://doi.org/10.1529/biophysj.105.062224

Govek, E. E., Newey, S. E., & Van Aelst, L. (2005). The role of the Rho GTPases in neuronal development. In *Genes and Development* (Vol. 19, Issue 1, pp. 1–49). https://doi.org/10.1101/gad.1256405

Graham, K., Chandrasekaran, A., Wang, L., Ladak, A., Lafer, E. M., Rangamani, P., & Stachowiak, J. C. (2023). Liquid-like VASP condensates drive actin polymerization and dynamic bundling Authors. *Nature Physics*, *19*, 574–585. https://doi.org/10.1038/s41567-022-01924-1

Grazi, E. (1997). What is the diameter of the actin filament? *FEBS Letters*, *405*(3), 249–252. https://doi.org/10.1016/S0014-5793(97)00214-7

Greenfield, N. J. (2007). Using circular dichroism spectra to estimate protein secondary structure. *Nature Protocols*, *1*(6), 2876–2890. https://doi.org/10.1038/nprot.2006.202

Gross, I., Brandt, N., Vonk, D., Köper, F., Wöhlbrand, L., Rabus, R., Witt, M., Heep, A., Plösch, T., Hipp, M. S., & Bräuer, A. U. (2022). Plasticity-Related Gene 5 Is Expressed in a Late Phase of Neurodifferentiation After Neuronal Cell-Fate Determination. *Frontiers in Cellular Neuroscience*, *16*(April), 1–17. https://doi.org/10.3389/fncel.2022.797588

Guan, X.-M., Sun Kobilka, T., & KobilkaS, B. K. (1992). Enhancement of MembraneInsertion and Function in a TypeIIIb Membrane Protein followingIntroduction of a Cleavable SignalPeptide. *The Journal of Biological Chemistry*, *267*(31), 21995–21998.

Guerrier, S., Coutinho-Budd, J., Sassa, T., Gresset, A., Jordan, N. V., Chen, K., Jin, W. L., Frost, A., & Polleux, F. (2009). The F-BAR Domain of srGAP2 Induces Membrane Protrusions Required for Neuronal Migration and Morphogenesis. *Cell*, *138*(5), 990–1004. https://doi.org/10.1016/j.cell.2009.06.047

Guna, A., & Hegde, R. S. (2018). Transmembrane Domain Recognition during Membrane Protein Biogenesis and Quality Control. *Current Biology*, *28*(8), R498–R511. https://doi.org/10.1016/j.cub.2018.02.004

Guo, A. X., Cui, J. J., Wang, L. Y., & Yin, J. Y. (2020). The role of CSDE1 in translational reprogramming and human diseases. *Cell Communication and Signaling*, *18*(1). https://doi.org/10.1186/s12964-019-0496-2

Guo, J., & Jia, R. (2018). Splicing factor poly(rC)-binding protein 1 is a novel and distinctive tumor suppressor. *Journal of Cellular Physiology*, *234*(1), 33–41. https://doi.org/10.1002/jcp.26873

Handwerger, K. E., Cordero, J. A., & Gall, J. G. (2005). Cajal Bodies, Nucleoli, and Speckles in the Xenopus Oocyte Nucleus Have a Low-Density, Sponge-like Structure. *Molecular Biology of the Cell*, *16*, 202–211. https://doi.org/10.1091/mbc.E04

Hanlon, C. D., & Andrew, D. J. (2015). Outside-in signaling - A brief review of GPCR signaling with a focus on the Drosophila GPCR family. *Journal of Cell Science*, *128*(19), 3533–3542. https://doi.org/10.1242/jcs.175158

Harmon, T. S., Holehouse, A. S., Rosen, M. K., & Pappu, R. V. (2017). *Intrinsically disordered linkers determine the interplay between phase separation and gelation in multivalent proteins*. https://doi.org/10.7554/eLife.30294.001

Harrison, R. G. (1910). The outgrowth of the nerve fiber as a mode of protoplasmic movement. *Journal of Experimental Zoology*, *9*(4), 787–846. https://doi.org/10.1002/jez.1400090405

Hartl, M., & Schneider, R. (2019). A unique family of neuronal signaling proteins implicated in oncogenesis and tumor suppression. *Frontiers in Oncology*, *9*(MAR), 1–13. https://doi.org/10.3389/fonc.2019.00289

Hatos, A., Tosatto, S. C. E., Vendruscolo, M., & Fuxreiter, M. (2022). FuzDrop on AlphaFold: visualizing the sequence-dependent propensity of liquid-liquid phase separation and aggregation of proteins. *Nucleic Acids Research*, *50*(W1), W337–W344. https://doi.org/10.1093/nar/gkac386

He, B., Shi, J., Wang, X., Jiang, H., & Zhu, H. J. (2019). Label-free absolute protein quantification with data-independent acquisition. *Journal of Proteomics*, *200*, 51–59. https://doi.org/10.1016/j.jprot.2019.03.005

Heckman, C. A., & Plummer, H. K. (2013). Filopodia as sensors. In *Cellular Signalling* (Vol. 25, Issue 11, pp. 2298–2311). https://doi.org/10.1016/j.cellsig.2013.07.006

Heiman, M. G., & Shaham, S. (2010). Twigs into branches: how a filopodium becomes a dendrite. In *Current Opinion in Neurobiology* (Vol. 20, Issue 1, pp. 86–91). https://doi.org/10.1016/j.conb.2009.10.016

Hemmings, B. A., & Restuccia, D. F. (2012). PI3K-PKB/Akt pathway. *Cold Spring Harbor Perspectives in Biology*, *4*(9). https://doi.org/10.1101/cshperspect.a011189

Hennig, S., Kong, G., Mannen, T., Sadowska, A., Kobelke, S., Blythe, A., Knott, G. J., Iyer, S. S., Ho, D., Newcombe, E. A., Hosoki, K., Goshima, N., Kawaguchi, T., Hatters, D., Trinkle-Mulcahy, L., Hirose, T., Bond, C. S., & Fox, A. H. (2015). Prion-like domains in RNA binding proteins are essential for building subnuclear paraspeckles. *Journal of Cell Biology*, *210*(4), 529–539. https://doi.org/10.1083/jcb.201504117

Herculano-Houzel, S. (2009). The human brain in numbers: A linearly scaled-up primate brain. *Frontiers in Human Neuroscience*, *3*(31), 1–11. https://doi.org/10.3389/neuro.09.031.2009

Hernández-Vega, A., Braun, M., Scharrel, L., Jahnel, M., Wegmann, S., Hyman, B. T., Alberti, S., Diez, S., & Hyman, A. A. (2017). Local Nucleation of Microtubule Bundles through Tubulin Concentration into a Condensed Tau Phase. *Cell Reports*, *20*(10), 2304–2312. https://doi.org/10.1016/j.celrep.2017.08.042

Herzik, M. A., Wu, M., & Lander, G. C. (2019). High-resolution structure determination of sub-100 kDa complexes using conventional cryo-EM. *Nature Communications*, *10*(1). https://doi.org/10.1038/s41467-019-08991-8

Heyder, N. A., Kleinau, G., Speck, D., Schmidt, A., Paisdzior, S., Szczepek, M., Bauer, B., Koch, A., Gallandi, M., Kwiatkowski, D., Bürger, J., Mielke, T., Beck-Sickinger, A. G., Hildebrand, P. W., Spahn, C. M. T., Hilger, D., Schacherl, M., Biebermann, H., Hilal, T., … Scheerer, P. (2021). Structures of active melanocortin-4 receptor–Gs-protein complexes with NDP-α-MSH and setmelanotide. *Cell Research*, *31*(11), 1176–1189. https://doi.org/10.1038/s41422-021-00569-8

Higgs, V. E., & Das, R. M. (2022). Establishing neuronal polarity: microtubule regulation during neurite initiation. *Oxford Open Neuroscience*, *1*. https://doi.org/10.1093/oons/kvac007

Hivert, B., Liu, Z., Chuang, C. Y., Doherty, P., & Sundaresan, V. (2002). Robo1 and Robo2 are homophilic binding molecules that promote axonal growth. *Molecular and Cellular Neuroscience*, *21*(4), 534–545. https://doi.org/10.1006/mcne.2002.1193

Holehouse, A. S., & Pappu, R. V. (2018). Functional Implications of Intracellular Phase Transitions. *Biochemistry*, *57*(17), 2415–2423. https://doi.org/10.1021/acs.biochem.7b01136

Hong, Y., Najafi, S., Casey, T., Shea, J. E., Han, S. I., & Hwang, D. S. (2022). Hydrophobicity of arginine leads to reentrant liquid-liquid phase separation behaviors of arginine-rich proteins. *Nature Communications*, *13*(1). https://doi.org/10.1038/s41467-022-35001-1

Hooke, R., Allestry, J., & Martyn, J. (1665). *Micrographia, or, Some physiological descriptions of minute bodies made by magnifying glasses :with observations and inquiries thereupon* . Printed by Jo. Martyn and Ja. Allestry, printers to the Royal Society. https://www.biodiversitylibrary.org/item/15485

Horiguchi, K., Hanada, T., Fukui, Y., & Chishti, A. H. (2006). Transport of PIP3 by GAKIN, a kinesin-3 family protein, regulates neuronal cell polarity. *Journal of Cell Biology*, *174*(3), 425–436. https://doi.org/10.1083/jcb.200604031

Horton, A. C., & Ehlers, M. D. (2003). Review Neuronal Polarity and Trafficking How are membrane constituents trafficked through such The establishment of subcellular domains with distinct 2 Department of Cell Biology molecular components and functional properties is a fun. *Neuron*, *40*, 277–295.

Huang, Y., & Liu, Z. (2009). Kinetic Advantage of Intrinsically Disordered Proteins in Coupled Folding-Binding Process: A Critical Assessment of the "Fly-Casting" Mechanism. *Journal of Molecular Biology*, *393*(5), 1143–1159. https://doi.org/10.1016/j.jmb.2009.09.010

Hubbard, S. J. (1998). The structural aspects of limited proteolysis of native proteins. *Biochimica et Biophysica Acta - Protein Structure and Molecular Enzymology*, *1382*(2), 191–206. https://doi.org/10.1016/S0167-4838(97)00175-1

Huggins, M. L. (1942). SOME PROPERTIES OF SOLUTIONS OF LONG-CHAIN COMPOUNDS"*. *J. Phys. Chem.*, *46*(1), 151–158. https://doi.org/https://doi.org/10.1021/j150415a018

Huskens, J. (2006). Multivalent interactions at interfaces. *Current Opinion in Chemical Biology*, *10*(6), 537–543. https://doi.org/10.1016/j.cbpa.2006.09.007

Hutin, S., Kumita, J. R., Strotmann, V. I., Dolata, A., Ling, W. L., Louafi, N., Popov, A., Milhiet, P. E., Blackledge, M., Nanao, M. H., Wigge, P. A., Stahl, Y., Costa, L., Tully, M. D., & Zubieta, C. (2023). Phase separation and molecular ordering of the prion-like domain of the Arabidopsis thermosensory protein EARLY FLOWERING 3. *Proceedings of the National Academy of Sciences of the United States of America*, *120*(28). https://doi.org/10.1073/pnas.2304714120

Hyman, A. A., Weber, C. A., & Jülicher, F. (2014a). Liquid-liquid phase separation in biology. In *Annual review of cell and developmental biology* (Vol. 30, pp. 39–58). https://doi.org/10.1146/annurev-cellbio-100913-013325

Hyman, A. A., Weber, C. A., & Jülicher, F. (2014b). Liquid-Liquid Phase Separation in Biology. *Annual Review of Cell and Developmental Biology*, *30*(1), 39–58. https://doi.org/10.1146/annurev-cellbio-100913-013325

Ideses, Y., Brill-Karniely, Y., Haviv, L., Ben-Shaul, A., & Bernheim-Groswasser, A. (2008). Arp2/3 branched actin network mediates filopodia-like bundles formation in vitro. *PLoS ONE*, *3*(9). https://doi.org/10.1371/journal.pone.0003297

Jajaman, K., & Ditlev, J. A. (2020). Biomolecular condensates in membrane receptor

signaling. *Curr Opin Cell Biol.*, *69*, 48–54.
https://doi.org/10.1016/j.ceb.2020.12.006

Jarnot, P., Ziemska-Legiecka, J., Dobson, L., Merski, M., Mier, P., Andrade-Navarro, M. A., Hancock, J. M., Dosztányi, Z., Paladin, L., Necci, M., Piovesan, D., Tosatto, S. C. E., Promponas, V. J., Grynberg, M., & Gruca, A. (2020). PlaToLoCo: The first web meta-server for visualization and annotation of low complexity regions in proteins. *Nucleic Acids Research*, *48*(W1), W77–W84. https://doi.org/10.1093/NAR/GKAA339

Jarsch, I. K., Daste, F., & Gallop, J. L. (2016). Membrane curvature in cell biology: An integration of molecular mechanisms. In *Journal of Cell Biology* (Vol. 214, Issue 4, pp. 375–387). Rockefeller University Press. https://doi.org/10.1083/jcb.201604003

Jasinska, R., Zhang, Q.-X., Pilquil, C., Singh, I., Xu, J., Dewald, J., Dillon, D. A., Berthiaume, L. G., Carman, G. M., Waggoner, D. W., & Brindley, D. N. (1999). Lipid phosphate phosphohydrolase-1 degrades exogenous glycerolipid and sphingolipid phosphate esters. In *Biochem. J* (Vol. 340).

Jayachandran, B., Parvin, T. N., Alam, M. M., Chanda, K., & MM, B. (2022). Insights on Chemical Crosslinking Strategies for Proteins. In *Molecules* (Vol. 27, Issue 23). MDPI. https://doi.org/10.3390/molecules27238124

Jégou, A., Niedermayer, T., Orbán, J., Didry, D., Lipowsky, R., Carlier, M. F., & Romet-Lemonne, G. (2011). Individual actin filaments in a microfluidic flow reveal the mechanism of ATP hydrolysis and give insight into the properties of profilin. *PLoS Biology*, *9*(9). https://doi.org/10.1371/journal.pbio.1001161

Jeong, W., Kim, J., Ahn, S. E., Lee, S. I., Bazer, F. W., Han, J. Y., & Song, G. (2012). AHCYL1 Is Mediated by Estrogen-Induced ERK1/2 MAPK Cell Signaling and MicroRNA Regulation to Effect Functional Aspects of the Avian Oviduct. *PLoS ONE*, *7*(11). https://doi.org/10.1371/journal.pone.0049204

Johnson, L. N. (2009). The regulation of protein phosphorylation. *Biochemical Society Transactions*, *37*(4), 627–641. https://doi.org/10.1042/BST0370627

Jones, A. J. Y., Gabriel, F., Tandale, A., & Nietlispach, D. (2020). Structure and dynamics of GPCRs in lipid membranes: physical principles and experimental approaches. *Molecules*, *25*(20), 1–39. https://doi.org/10.3390/molecules25204729

Jou, W. M., Verhoeyen, M., Devos, R., Saman, E., Fang, R., Huylebroeck, D., Fiers, W., Threlfall, G., Barber, C., Carey, N., & Emtage, S. (1980). Complete structure of the hemagglutinin gene from the human influenza A/Victoria/3/75 (H3N2) strain as determined from cloned DNA. *Cell*, *19*(3), 683–696. https://doi.org/10.1016/S0092-8674(80)80045-6

Jumper, J., Evans, R., Pritzel, A., Green, T., Figurnov, M., Ronneberger, O., Tunyasuvunakool, K., Bates, R., Žídek, A., Potapenko, A., Bridgland, A., Meyer, C., Kohl, S. A. A., Ballard, A. J., Cowie, A., Romera-Paredes, B., Nikolov, S., Jain, R., Adler, J., … Hassabis, D. (2021). Highly accurate protein structure prediction with AlphaFold. *Nature*, *596*(7873), 583–589. https://doi.org/10.1038/s41586-021-03819-2

Kabsch, W., Mannherz, H. G., Suckt, D., Pai, E. F., & Holmes, K. C. (1990). Atomic structure of the actin: DNase I complex. *Nature*, *347*, 37–44. https://doi.org/10.1038/347037a0

Kakumoto, T., & Nakata, T. (2013). Optogenetic Control of PIP3: PIP3 Is Sufficient to Induce the Actin-Based Active Part of Growth Cones and Is Regulated via Endocytosis. *PLoS ONE*, *8*(8). https://doi.org/10.1371/journal.pone.0070861

Kalil, K., & Dent, E. W. (2014). Branch management: Mechanisms of axon branching in the developing vertebrate CNS. In *Nature Reviews Neuroscience* (Vol. 15, Issue 1, pp. 7–18). https://doi.org/10.1038/nrn3650

Kanaan, N. M., Hamel, C., Grabinski, T., & Combs, B. (2020). Liquid-liquid phase separation induces pathogenic tau conformations in vitro. *Nature Communications*, *11*(1). https://doi.org/10.1038/s41467-020-16580-3

Kang, H., Bradley, M. J., Elam, W. A., & De La Cruz, E. M. (2013). Regulation of actin by ion-linked equilibria. *Biophysical Journal*, *105*(12), 2621–2628. https://doi.org/10.1016/j.bpj.2013.10.032

Kassem, N., Araya-Secchi, R., Bugge, K., Barclay, A., Steinocher, H., Khondker, A., Wang, Y., Lenard, A. J., Bürck, J., Sahin, C., Ulrich, A. S., Landreh, M., Cramer Pedersen, M., Rheinstädter, M. C., Amstrup Pedersen, P., Lindorff-Larsen, K., Arleth, L., & Kragelund, B. B. (2021). Order and disorder - An integrative structure of the full-length human growth hormone receptor. *Sci. Adv*, *7*(27), 1–19. https://doi.org/10.1126/sciadv.abh3805

Katherine, K., & Dent W., E. (2014). developing vertebrate CNS. *Nature Reviews. Neuroscience*, *15*(1), 7–18. https://doi.org/10.1038/nrn3650.Branch

Kato, M., Han, T. W., Xie, S., Shi, K., Du, X., Wu, L. C., Mirzaei, H., Goldsmith, E. J., Longgood, J., Pei, J., Grishin, N. V., Frantz, D. E., Schneider, J. W., Chen, S., Li, L., Sawaya, M. R., Eisenberg, D., Tycko, R., & McKnight, S. L. (2012). Cell-free formation of RNA granules: Low complexity sequence domains form dynamic fibers within hydrogels. *Cell*, *149*(4), 753–767. https://doi.org/10.1016/j.cell.2012.04.017

Kessels, M. M., & Qualmann, B. (2020). The role of membrane-shaping BAR domain proteins in caveolar invagination: From mechanistic insights to pathophysiological consequences. In *Biochemical Society Transactions* (Vol. 48, Issue 1, pp. 137–146). Portland Press Ltd. https://doi.org/10.1042/BST20190377

Ketschek, A., & Gallo, G. (2010). Nerve Growth Factor Induces Axonal Filopodia through Localized Microdomains of Phosphoinositide 3-Kinase Activity That Drive the Formation of Cytoskeletal Precursors to Filopodia. *Journal of Neuroscience*, *30*(36), 12185–12197. https://doi.org/10.1523/JNEUROSCI.1740-10.2010

Khurana, S., & George, S. P. (2011). The role of actin bundling proteins in the assembly of filopodia in epithelial cells. In *Cell Adhesion and Migration* (Vol. 5, Issue 5). Taylor and Francis Inc. https://doi.org/10.4161/cam.5.5.17644

Kinoshita, E., Kinoshita-Kikuta, E., & Koike, T. (2009). Separation and detection of large phosphoproteins using phos-tag sds-page. *Nature Protocols*, *4*(10), 1513–1521. https://doi.org/10.1038/nprot.2009.154

Koivisto, A. P., Belvisi, M. G., Gaudet, R., & Szallasi, A. (2022). Advances in TRP channel drug discovery: from target validation to clinical studies. In *Nature Reviews Drug Discovery* (Vol. 21, Issue 1, pp. 41–59). Nature Research. https://doi.org/10.1038/s41573-021-00268-4

Korshunova, I., Caroni, P., Kolkova, K., Berezin, V., Bock, E., & Walmod, P. S. (2008). Characterization of BASP1-mediated neurite outgrowth. *Journal of*

Neuroscience Research, *86*(10), 2201–2213. https://doi.org/10.1002/jnr.21678

Krainer, G., Welsh, T. J., Joseph, J. A., Espinosa, J. R., Wittmann, S., de Csilléry, E., Sridhar, A., Toprakcioglu, Z., Gudiškytė, G., Czekalska, M. A., Arter, W. E., Guillén-Boixet, J., Franzmann, T. M., Qamar, S., George-Hyslop, P. S., Hyman, A. A., Collepardo-Guevara, R., Alberti, S., & Knowles, T. P. J. (2021). Reentrant liquid condensate phase of proteins is stabilized by hydrophobic and non-ionic interactions. *Nature Communications*, *12*(1). https://doi.org/10.1038/s41467-021-21181-9

Kroon, C. (2023). *Phosphorylation of PLPPR3 membrane proteins as signaling integrator at neuronal synapses*. Charité - Universitätsmedizin Berlin.

Krugmann, S., Jordens, I., Gevaert, K., Driessens, M., Vandekerckhove, J., & Hall, A. (2001). Cdc42 induces filopodia by promoting the formation of anIRSp53:Mena complex. *Current Biology*, *11*(21), 1645–1655. https://doi.org/https://doi.org/10.1016/S0960-9822(01)00506-1

Krüppel, S., & Tetzlaff, C. (2020). The self-organized learning of noisy environmental stimuli requires distinct phases of plasticity. *Network Neuroscience*, *4*(1), 174–199. https://doi.org/10.1162/netn_a_00118

Kundinger, S. R., Bishof, I., Dammer, E. B., Duong, D. M., & Seyfried, N. T. (2020). Middle-Down Proteomics Reveals Dense Sites of Methylation and Phosphorylation in Arginine-Rich RNA-Binding Proteins. *Journal of Proteome Research*, *19*(4), 1574–1591. https://doi.org/10.1021/acs.jproteome.9b00633

Kundinger, S. R., Dammer, E. B., Yin, L., Hurst, C., Shapley, S., Ping, L., Khoshnevis, S., Ghalei, H., Duong, D. M., & Seyfried, N. T. (2021). Phosphorylation regulates arginine-rich RNA-binding protein solubility and oligomerization. *Journal of Biological Chemistry*, *297*(5). https://doi.org/10.1016/j.jbc.2021.101306

Kusumaatmaja, H., May, A. I., & Knorr, R. L. (2021). Intracellular wetting mediates contacts between liquid compartments and membrane-bound organelles. *Journal of Cell Biology*, *220*(10). https://doi.org/10.1083/jcb.202103175

Kwon, D. H., Zhang, F., Suo, Y., Bouvette, J., Borgnia, M. J., & Lee, S. Y. (2021). Heat-dependent opening of TRPV1 in the presence of capsaicin. *Nature Structural and Molecular Biology*, *28*(7), 554–563. https://doi.org/10.1038/s41594-021-00616-3

Lebrand, C., Dent, E. W., Strasser, G. A., Lanier, L. M., Krause, M., Svitkina, T. M., Borisy, G. G., & Gertler, F. B. (2004). Critical Role of Ena/VASP Proteins for Filopodia Formation in Neurons and in Function Downstream of Netrin-1. *Neuron*, *42*(1), 37–49. https://doi.org/10.1016/S0896-6273(04)00108-4

Lee, C. U., Hahne, G., Hanske, J., Bange, T., Bier, D., Rademacher, C., Hennig, S., & Grossmann, T. N. (2015). Redox Modulation of PTEN Phosphatase Activity by Hydrogen Peroxide and Bisperoxidovanadium Complexes. *Angewandte Chemie - International Edition*, *54*(46), 13796–13800. https://doi.org/10.1002/anie.201506338

Lehmann, A., Niewienda, A., Jechow, K., Janek, K., & Enenkel, C. (2010). Ecm29 Fulfils Quality Control Functions in Proteasome Assembly. *Molecular Cell*, *38*(6), 879–888. https://doi.org/10.1016/j.molcel.2010.06.016

Lenz, S., Sinn, L. R., O'Reilly, F. J., Fischer, L., Wegner, F., & Rappsilber, J. (2021). Reliable identification of protein-protein interactions by crosslinking mass spectrometry. *Nature Communications*, *12*(1). https://doi.org/10.1038/s41467-021-

23666-z

Leondaritis, G., & Eickholt, B. J. (2015). Short Lives with Long-Lasting Effects: Filopodia Protrusions in Neuronal Branching Morphogenesis. *PLoS Biology*, *13*(9). https://doi.org/10.1371/journal.pbio.1002241

Leuenberger, P., Ganscha, S., Kahraman, A., Cappelletti, V., Boersema, P. J., Von Mering, C., Claassen, M., & Picotti, P. (2017). Cell-wide analysis of protein thermal unfolding reveals determinants of thermostability. *Science*, *355*(6327). https://doi.org/10.1126/science.aai7825

Li, B., Chen, D., Wang, J., Yan, Z., Jiang, L., Duan, D., He, J., Luo, Z., Zhang, J., & Yuan, F. (2014). MOFzyme: Intrinsic protease-like activity of Cu-MOF. *Scientific Reports*, *4*. https://doi.org/10.1038/srep06759

Li, J., Yen, C., Liaw, D., Podsypanina, K., Bose, S., Wang, S. I., Puc, J., Miliaresis, C., Rodgers, L., McCombie, R., Bigner, S. H., Giovanella, B. C., Ittmann, M., Tycko, B., Hibshoosh, H., Wigler, M. H., & Parsons, R. (1997). PTEN, a putative protein tyrosine phosphatase gene mutated in human brain, breast, and prostate cancer. *Science*, *275*(5308), 1943–1947. https://doi.org/10.1126/science.275.5308.1943

Li, J., Zhang, M., Ma, W., Yang, B., Lu, H., Zhou, F., & Zhang, L. (2022). Post-translational modifications in liquid-liquid phase separation: a comprehensive review. *Molecular Biomedicine*, *3*(1). https://doi.org/10.1186/s43556-022-00075-2

Li, P., Chen, J., Wang, X., Su, Z., Gao, M., & Huang, Y. (2023). Liquid − liquid phase separation of tau: Driving forces, regulation, and biological implications. *Neurobiology of Disease*, *183*. https://doi.org/10.1016/j.nbd.2023.106167

Li, Y. R., King, O. D., Shorter, J., & Gitler, A. D. (2013). Stress granules as crucibles of ALS pathogenesis. *Journal of Cell Biology*, *201*(3), 361–372. https://doi.org/10.1083/jcb.201302044

Liao, Y. C., Fernandopulle, M. S., Wang, G., Choi, H., Hao, L., Drerup, C. M., Patel, R., Qamar, S., Nixon-Abell, J., Shen, Y., Meadows, W., Vendruscolo, M., Knowles, T. P. J., Nelson, M., Czekalska, M. A., Musteikyte, G., Gachechiladze, M. A., Stephens, C. A., Pasolli, H. A., … Ward, M. E. (2019). RNA Granules Hitchhike on Lysosomes for Long-Distance Transport, Using Annexin A11 as a Molecular Tether. *Cell*, *179*(1), 147–164.e20. https://doi.org/10.1016/j.cell.2019.08.050

Lishko, P. V., Procko, E., Jin, X., Phelps, C. B., & Gaudet, R. (2007). The Ankyrin Repeats of TRPV1 Bind Multiple Ligands and Modulate Channel Sensitivity. *Neuron*, *54*(6), 905–918. https://doi.org/10.1016/j.neuron.2007.05.027

Liu, F., Rijkers, D. T. S., Post, H., & Heck, A. J. R. (2015). Proteome-wide profiling of protein assemblies by cross-linking mass spectrometry. *Nature Methods*, *12*(12), 1179–1184. https://doi.org/10.1038/nmeth.3603

Liu, X., Huai, J., Endle, H., Schlüter, L., Fan, W., Li, Y., Richers, S., Yurugi, H., Rajalingam, K., Ji, H., Cheng, H., Rister, B., Horta, G., Baumgart, J., Berger, H., Laube, G., Schmitt, U., Schmeisser, M. J., Boeckers, T. M., … Vogt, J. (2016a). PRG-1 Regulates Synaptic Plasticity via Intracellular PP2A/β1-Integrin Signaling. *Developmental Cell*, *38*(3), 275–290. https://doi.org/10.1016/j.devcel.2016.06.019

Liu, X., Huai, J., Endle, H., Schlüter, L., Fan, W., Li, Y., Richers, S., Yurugi, H., Rajalingam, K., Ji, H., Cheng, H., Rister, B., Horta, G., Baumgart, J., Berger, H., Laube, G., Schmitt, U., Schmeisser, M. J., Boeckers, T. M., … Vogt, J. (2016b). PRG-1 Regulates Synaptic Plasticity via Intracellular PP2A/β1-Integrin Signaling.

Developmental Cell, *38*(3), 275–290. https://doi.org/10.1016/j.devcel.2016.06.019

Liu, Y., Huynh, D. T., & Yeates, T. O. (2019). A 3.8 Å resolution cryo-EM structure of a small protein bound to an imaging scaffold. *Nature Communications*, *10*(1), 1–7. https://doi.org/10.1038/s41467-019-09836-0

Lovinger, D. M. (2008). Communication Networks in the Brain Neurons, Receptors, Neurotransmitters, and Alcohol. *Alcohol Research & Health*, *31*(3), 196–214.

Lowery, L. A., & Vactor, D. Van. (2009). The trip of the tip: Understanding the growth cone machinery. In *Nature Reviews Molecular Cell Biology* (Vol. 10, Issue 5, pp. 332–343). https://doi.org/10.1038/nrm2679

Luo, Y., Wu, J., & Li, Y. (2021). Regulation of liquid-liquid phase separation with focus on post-translational modifications. *Chem. Commun. (Camb.)*, *57*(98), 13275–13287. https://doi.org/10.1039/d1cc05266g

Lyon, A. S., Peeples, W. B., & Rosen, M. K. (2021). A framework for understanding the functions of biomolecular condensates across scales. In *Nature Reviews Molecular Cell Biology* (Vol. 22, Issue 3, pp. 215–235). Nature Research. https://doi.org/10.1038/s41580-020-00303-z

Maekawa, S., Maekawaq, M., Hattoriq, S., & Nakamuraq, S. (1993). Purification and Molecular Cloning of a Novel Acidic Calmodulin-binding Protein from Rat Brain*. *THE JOURNAL OF BIOLOGICAL CHEMISTRY*, *268*(18), 13703–13709.

Maharana, S., Wang, J., Papadopoulos, D. K., Richter, D., Pozniakovsky, A., Poser, I., Bickle, M., Rizk, S., Guillén-Boixet, J., Franzmann, T. M., Jahnel, M., Marrone, L., Chang, Y.-T., Sterneckert, J., Tomancak, P., Hyman, A. A., & Alberti, † Simon. (2018). RNA buffers the phase separation behavior of prion-like RNA binding proteins. *Science*, *360*(6391), 918–921. https://doi.org/DOI: 10.1126/science.aar736

Maity, H., Baidya, L., & Reddy, G. (2022). Salt-Induced Transitions in the Conformational Ensembles of Intrinsically Disordered Proteins. *Journal of Physical Chemistry B*, *126*(32), 5959–5971. https://doi.org/10.1021/acs.jpcb.2c03476

Mamais, A., Raja, M., Manzoni, C., Dihanich, S., Lees, A., Moore, D., Lewis, P. A., & Bandopadhyay, R. (2013). Divergent α-synuclein solubility and aggregation properties in G2019S LRRK2 Parkinson's disease brains with Lewy Body pathology compared to idiopathic cases. *Neurobiology of Disease*, *58*, 183–190. https://doi.org/10.1016/j.nbd.2013.05.017

Mangiarotti, A., Chen, N., Zhao, Z., Lipowsky, R., & Dimova, R. (2023). Wetting and complex remodeling of membranes by biomolecular condensates. *Nature Communications*, *14*(1). https://doi.org/10.1038/s41467-023-37955-2

Martin, E. W., & Mittag, T. (2018). Relationship of Sequence and Phase Separation in Protein Low-Complexity Regions. *Biochemistry*, *57*(17), 2478–2487. https://doi.org/10.1021/acs.biochem.8b00008

Mason, G., & Clark, W. (1966). Fine Structure in the Radial Distribution Function from a Random Packing of Spheres. *Nature*, *211*(1), 957. https://doi.org/https://doi.org/10.1038/211957a0

Matenia, D., & Mandelkow, E. M. (2009). The tau of MARK: a polarized view of the cytoskeleton. In *Trends in Biochemical Sciences* (Vol. 34, Issue 7, pp. 332–342). https://doi.org/10.1016/j.tibs.2009.03.008

Mattila, P. K., & Lappalainen, P. (2008). Filopodia: Molecular architecture and cellular functions. *Nature Reviews Molecular Cell Biology*, *9*(6), 446–454. https://doi.org/10.1038/nrm2406

McCall, P. M., Srivastava, S., Perry, S. L., Kovar, D. R., Gardel, M. L., & Tirrell, M. V. (2018). Partitioning and Enhanced Self-Assembly of Actin in Polypeptide Coacervates. *Biophysical Journal*, *114*(7), 1636–1645. https://doi.org/10.1016/j.bpj.2018.02.020

McCoy Vernon, R., Andrew Chong, P., Tsang, B., Hun Kim, T., Bah, A., Farber, P., Lin, H., & Deborah Forman-Kay, J. (2018). Pi-Pi contacts are an overlooked protein feature relevant to phase separation. *eLIFE*, *7*(e31486), 1–48. https://doi.org/10.7554/eLife.31486.001

McDonald, N. A., Fetter, R. D., & Shen, K. (2020). Assembly of synaptic active zones requires phase separation of scaffold molecules. *Nature*, *588*(7838), 454–458. https://doi.org/10.1038/s41586-020-2942-0

McSwiggen, D. T., Mir, M., Darzacq, X., & Tjian, R. (2019). Evaluating phase separation in live cells: diagnosis, caveats, and functional consequences. *Genes and Development*, *33*(23–24), 1619–1634. https://doi.org/10.1101/gad.331520.119

Medalia, O., Beck, M., Ecke, M., Weber, I., Neujahr, R., Baumeister, W., & Gerisch, G. (2007). Organization of Actin Networks in Intact Filopodia. *Current Biology*, *17*(1), 79–84. https://doi.org/10.1016/j.cub.2006.11.022

Mehta, S., & Zhang, J. (2022). Liquid–liquid phase separation drives cellular function and dysfunction in cancer. In *Nature Reviews Cancer* (Vol. 22, Issue 4, pp. 239–252). Nature Research. https://doi.org/10.1038/s41568-022-00444-7

Ménager, C., Arimura, N., Fukata, Y., & Kaibuchi, K. (2004). PIP3 is involved in neuronal polarization and axon formation. *Journal of Neurochemistry*, *89*(1), 109–118. https://doi.org/10.1046/j.1471-4159.2004.02302.x

Menon, S., Goldfarb, D., Ho, C. T., Cloer, E. W., Boyer, N. P., Hardie, C., Bock, A. J., Johnson, E. C., Anil, J., Major, M. Ben, & Gupton, S. L. (2021). The TRIM9/TRIM67 neuronal interactome reveals novel activators of morphogenesis. *Molecular Biology of the Cell*, *32*(4), 314–330. https://doi.org/10.1091/mbc.E20-10-0622

Miki, H., Sasaki, T., Takai, Y., & Takenawa, T. (1998). Induction of filopodium formation by a WASP-related actin-depolymerizing protein N-WASP. *Nature*, *391*, 93–96. https://doi.org/https://doi.org/10.1038/34208

Miles, A. J., Janes, R. W., & Wallace, B. A. (2021). Tools and methods for circular dichroism spectroscopy of proteins: A tutorial review. *Chemical Society Reviews*, *50*(15), 8400–8413. https://doi.org/10.1039/d0cs00558d

Millard, T. H., Bompard, G., Heung, M. Y., Dafforn, T. R., Scott, D. J., Machesky, L. M., & Fütterer, K. (2005). Structural basis of filopodia formation induced by the IRSp53/MIM homology domain of human IRSp53. *EMBO Journal*, *24*(2), 240–250. https://doi.org/10.1038/sj.emboj.7600535

Millet, L. J., & Gillette, M. U. (2012). FOCUS: NEUROSCIENCE over a century of neuron culture: From the Hanging drop to Microfluidic devices. *YALE JoURNAL oF BIoLoGY AND MEDICINE*, *85*, 501–521.

Milovanovic, D., Wu, Y., Bian, X., & De Camilli, P. (2018). A liquid phase of synapsin and lipid vesicles. *Science*, *361*(6402), 604–607.

https://doi.org/10.1126/science.aat5671

Mirdita, M., Schütze, K., Moriwaki, Y., Heo, L., Ovchinnikov, S., & Steinegger, M. (2022). ColabFold - Making protein folding accessible to all. *bioRxiv*, 2021.08.15.456425. https://doi.org/10.1038/s41592-022-01488-1

Mitrea, D. M., & Kriwacki, R. W. (2016). Phase separation in biology; Functional organization of a higher order Short linear motifs - The unexplored frontier of the eukaryotic proteome. *Cell Communication and Signaling*, *14*(1). https://doi.org/10.1186/s12964-015-0125-7

Mohanty, P., Kapoor, U., Sundaravadivelu Devarajan, D., Phan, T. M., Rizuan, A., & Mittal, J. (2022). Principles Governing the Phase Separation of Multidomain Proteins. *Biochemistry*, *61*(22), 2443–2455. https://doi.org/10.1021/acs.biochem.2c00210

Mohapatra, S., & Wegmann, S. (2023). Biomolecular condensation involving the cytoskeleton. *Brain Research Bulletin*, *194*, 105–117. https://doi.org/10.1016/j.brainresbull.2023.01.009

Molliex, A., Temirov, J., Lee, J., Coughlin, M., Kanagaraj, A. P., Kim, H. J., Mittag, T., & Taylor, J. P. (2015). Phase Separation by Low Complexity Domains Promotes Stress Granule Assembly and Drives Pathological Fibrillization. *Cell*, *163*(1), 123–133. https://doi.org/10.1016/j.cell.2015.09.015

Mondal, S., & Baumgart, T. (2023). Membrane reshaping by protein condensates. *Biochimica et Biophysica Acta (BBA) - Biomembranes*, *1865*(3), 184121. https://doi.org/https://doi.org/10.1016/j.bbamem.2023.184121

Mondal, S., Narayan, K., Botterbusch, S., Powers, I., Zheng, J., James, H. P., Jin, R., & Baumgart, T. (2022). Multivalent interactions between molecular components involved in fast endophilin mediated endocytosis drive protein phase separation. *Nature Communications*, *13*(1). https://doi.org/10.1038/s41467-022-32529-0

Morita, K., Furuse, M., Fujimoto, K., & Tsukita, S. (1999). Claudin multigene family encoding four-transmembrane domain protein components of tight junction strands. *Proceedings of the National Academy of Sciences of the United States of America*, *96*(2), 511–516. https://doi.org/10.1073/pnas.96.2.511

Moses, D., Ginell, G. M., Holehouse, A. S., & Sukenik, S. (2023). Intrinsically disordered regions are poised to act as sensors of cellular chemistry. In *Trends in Biochemical Sciences* (Vol. 48, Issue 12, pp. 1019–1034). Elsevier Ltd. https://doi.org/10.1016/j.tibs.2023.08.001

Mourão, M. A., Hakim, J. B., & Schnell, S. (2014). Connecting the dots: The effects of macromolecular crowding on cell physiology. *Biophysical Journal*, *107*(12), 2761–2766. https://doi.org/10.1016/j.bpj.2014.10.051

Müller, D. J., Wu, N., & Palczewski, K. (2008). Vertebrate Membrane Proteins: Structure, Function, and Insights from Biophysical Approaches. *Pharmacological Reviews*, *60*(1), 43–78. https://doi.org/doi:10.1124/pr.107.07111.

Muzzopappa, F., Hummert, J., Anfossi, M., Tashev, S. A., Herten, D. P., & Erdel, F. (2022). Detecting and quantifying liquid–liquid phase separation in living cells by model-free calibrated half-bleaching. *Nature Communications*, *13*(1). https://doi.org/10.1038/s41467-022-35430-y

Nemethova, M., Auinger, S., & Small, J. V. (2008). Building the actin cytoskeleton: Filopodia contribute to the construction of contractile bundles in the lamella.

Journal of Cell Biology, *180*(6), 1233–1244.
https://doi.org/10.1083/jcb.200709134

Nilius, B., & Owsianik, G. (2011). The transient receptor potential family of ion channels. *Genome Biology*, *12*(218). https://doi.org/https://doi.org/10.1186/gb-2011-12-3-218

Nishi, H., Shaytan, A., & Panchenko, A. R. (2014). Physicochemical mechanisms of protein regulation by phosphorylation. *Frontiers in Genetics*, *5*(AUG), 1–10. https://doi.org/10.3389/fgene.2014.00270

Nobes, C. D., & Hall, A. (1995). Rho, Rac, and Cdc42 GTPases Regulate the Assembly of Multimolecular Focal Complexes Associated with Actin Stress Fibers, Lamellipodia, and Filopodia. In *Cell* (Vol. 81).

Noctor, S. C., Verónica Martínez-Cerdeñ, ;, & Kriegstein, A. R. (2007). Contribution of Intermediate Progenitor Cells to Cortical Histogenesis. *Arch Neurol*, *64*, 639–642. https://doi.org/10.1001/archneur.64.5.639

Nott, T. J., Petsalaki, E., Farber, P., Jervis, D., Fussner, E., Plochowietz, A., Craggs, T. D., Bazett-Jones, D. P., Pawson, T., Forman-Kay, J. D., & Baldwin, A. J. (2015). Phase Transition of a Disordered Nuage Protein Generates Environmentally Responsive Membraneless Organelles. *Molecular Cell*, *57*(5), 936–947. https://doi.org/10.1016/j.molcel.2015.01.013

Nouwen, N., Stahlberg, H., Pugsley, A. P., & Engel, A. (2000). Domain structure of secretin PulD revealed by limited proteolysis and electron microscopy. *EMBO Journal*, *19*(10), 2229–2236. https://doi.org/10.1093/emboj/19.10.2229

O'Reilly, F. J., & Rappsilber, J. (2018). Cross-linking mass spectrometry: methods and applications in structural, molecular and systems biology. In *Nature Structural and Molecular Biology* (Vol. 25, Issue 11, pp. 1000–1008). Nature Publishing Group. https://doi.org/10.1038/s41594-018-0147-0

Okabe, S., & Hirokawa, N. (1988). Microtubule Dynamics in Nerve Cells: Analysis Using Microinjection of Biotinylated Tubulin into PCI2 Cells. *The Journal of Cell Biology*, *107*, 651–664.

Ortega-Alarcon, D., Claveria-Gimeno, R., Vega, S., Jorge-Torres, O. C., Esteller, M., Abian, O., & Velazquez-Campoy, A. (2021). Stabilization effect of intrinsically disordered regions on multidomain proteins: The case of the methyl-cpg protein 2, mecp2. *Biomolecules*, *11*(8). https://doi.org/10.3390/biom11081216

Orti, F., Navarro, A. M., Rabinovich, A., Wodak, S. J., & Marino-Buslje, C. (2021). Insight into membraneless organelles and their associated proteins: Drivers, Clients and Regulators. *Computational and Structural Biotechnology Journal*, *19*, 3964–3977. https://doi.org/10.1016/j.csbj.2021.06.042

Osada, K. (2019). Versatile DNA folding structures organized by cationic block copolymers. In *Polymer Journal* (Vol. 51, Issue 4, pp. 381–387). Nature Publishing Group. https://doi.org/10.1038/s41428-018-0157-0

Pak, C. W., Kosno, M., Holehouse, A. S., Padrick, S. B., Mittal, A., Ali, R., Yunus, A. A., Liu, D. R., Pappu, R. V., & Rosen, M. K. (2016). Sequence Determinants of Intracellular Phase Separation by Complex Coacervation of a Disordered Protein. *Molecular Cell*, *63*(1), 72–85. https://doi.org/10.1016/j.molcel.2016.05.042

Park, H., Kim, N. Y., Lee, S., Kim, N., Kim, J., & Heo, W. Do. (2017). Optogenetic protein clustering through fluorescent protein tagging and extension of CRY2.

Nature Communications, *8*(1), 1–7. https://doi.org/10.1038/s41467-017-00060-2

Park, S., Barnes, R., Lin, Y., Jeon, B. jin, Najafi, S., Delaney, K. T., Fredrickson, G. H., Shea, J. E., Hwang, D. S., & Han, S. (2020). Dehydration entropy drives liquid-liquid phase separation by molecular crowding. *Communications Chemistry*, *3*(1). https://doi.org/10.1038/s42004-020-0328-8

Patel, A., Lee, H. O., Jawerth, L., Maharana, S., Jahnel, M., Hein, M. Y., Stoynov, S., Mahamid, J., Saha, S., Franzmann, T. M., Pozniakovski, A., Poser, I., Maghelli, N., Royer, L. A., Weigert, M., Myers, E. W., Grill, S., Drechsel, D., Hyman, A. A., & Alberti, S. (2015). A Liquid-to-Solid Phase Transition of the ALS Protein FUS Accelerated by Disease Mutation. *Cell*, *162*(5), 1066–1077. https://doi.org/10.1016/j.cell.2015.07.047

Pellegrin, S., & Mellor, H. (2005). The Rho Family GTPase RifInduces Filopodia through mDia2. *Current Biology*, *15*, 129–133. https://doi.org/DOI 10.1016/j.cub.2005.01.011

Peng, P.-H., Hsu, K.-W., & Wu, K.-J. (2021). Liquid-liquid phase separation (LLPS) in cellular physiology and tumor biology. *Am J Cancer Res*, *11*(8), 3766–3776. www.ajcr.us/

Perez-Jimenez, R., Godoy-Ruiz, R., Ibarra-Molero, B., & Sanchez-Ruiz, J. M. (2004). The Efficiency of Different Salts to Screen Charge Interactions in Proteins: A Hofmeister Effect? *Biophysical Journal*, *84*(4), 2414–2429. https://doi.org/10.1016%2FS0006-3495(04)74298-8

Pezzotti, S., König, B., Ramos, S., Schwaab, G., & Havenith, M. (2023). Liquid–Liquid Phase Separation? Ask the Water! *The Journal of Physical Chemistry Letters*, *14*(6), 1556–1563. https://doi.org/10.1021/acs.jpclett.2c02697

Piersimoni, L., Kastritis, P. L., Arlt, C., & Sinz, A. (2022). Cross-Linking Mass Spectrometry for Investigating Protein Conformations and Protein-Protein Interactions-A Method for All Seasons. In *Chemical Reviews* (Vol. 122, Issue 8, pp. 7500–7531). American Chemical Society. https://doi.org/10.1021/acs.chemrev.1c00786

Pizzagalli, M. D., Bensimon, A., & Superti-Furga, G. (2021). A guide to plasma membrane solute carrier proteins. *FEBS Journal*, *288*(9), 2784–2835. https://doi.org/10.1111/febs.15531

Pollard, T. D. (2007). Regulation of actin filament assembly by Arp2/3 complex and formins. In *Annual Review of Biophysics and Biomolecular Structure* (Vol. 36, pp. 451–477). https://doi.org/10.1146/annurev.biophys.35.040405.101936

Pollard, T. D. (2016). Actin and actin-binding proteins. *Cold Spring Harbor Perspectives in Biology*, *8*(8). https://doi.org/10.1101/cshperspect.a018226

Pollard, T. D., & Cooper, J. A. (2009). Actin, a Central Player in Cell Shape and Movement. *Science*, 1208–1213. https://doi.org/DOI: 10.1126/science.1175862

Polleux, F., & Snider, W. (2010). Initiating and growing an axon. In *Cold Spring Harbor perspectives in biology* (Vol. 2, Issue 4). https://doi.org/10.1101/cshperspect.a001925

Porath, J., Carlsson, J., Olsson, I., & Belfrage, G. (1975). Metal chelate affinity chromatography, a new approach to protein fractionation. *Nature*, *258*(5536), 598–599. https://doi.org/10.1038/258598a0

Powers, S. K., Holehouse, A. S., Korasick, D. A., Schreiber, K. H., Clark, N. M., Jing,

H., Emenecker, R., Han, S., Tycksen, E., Hwang, I., Sozzani, R., Jez, J. M., Pappu, R. V., & Strader, L. C. (2019). Nucleo-cytoplasmic Partitioning of ARF Proteins Controls Auxin Responses in Arabidopsis thaliana. *Molecular Cell*, *76*(1), 177–190.e5. https://doi.org/10.1016/j.molcel.2019.06.044

Pramanik, S., Steinkühler, J., Dimova, R., Spatz, J., & Lipowsky, R. (2022). Binding of His-tagged fluorophores to lipid bilayers and giant vesicles. *Soft Matter*, *18*(34), 6372–6383. https://doi.org/10.1039/D2SM00915C

Prehoda, K. E., Scott, J. A., Mullins, D., & Lim, W. A. (2000). Integration of Multiple SignalsThrough Cooperative Regulationof the N-WASP–Arp2/3Complex. *Science*, *290*, 801–806. https://doi.org/DOI: 10.1126/science.290.5492.801

Prickett, K. S., Amberg, D. C., & Hopp, T. P. (1989). A Calcium-Dependent Antibody for Identification and Purification of Recombinant Proteins. *BioTechniques*, *7*(6), 580–589.

Puri, D., Barry, B. J., & Engle, E. C. (2023). TUBB3 and KIF21A in neurodevelopment and disease. *Frontiers in Neuroscience*, *17*, 1–27. https://doi.org/10.3389/fnins.2023.1226181

Qamar, S., Wang, G. Z., Randle, S. J., Ruggeri, F. S., Varela, J. A., Lin, J. Q., Phillips, E. C., Miyashita, A., Williams, D., Ströhl, F., Meadows, W., Ferry, R., Dardov, V. J., Tartaglia, G. G., Farrer, L. A., Kaminski Schierle, G. S., Kaminski, C. F., Holt, C. E., Fraser, P. E., … St George-Hyslop, P. (2018). FUS Phase Separation Is Modulated by a Molecular Chaperone and Methylation of Arginine Cation-π Interactions. *Cell*, *173*(3), 720–734.e15. https://doi.org/10.1016/j.cell.2018.03.056

Quevillon-Cheruel, Sophie Collinet, B., Trésaugues, L., Minard, P., Henckes, G., Aufrère, R., Blondeau, K., Zhou, C.-Z., Liger, D., Bettache, N., Poupon, A., Aboulfath, I., Leulliot, N., Janin, J., & Tilbeurgh van, H. (2007). Cloning, Production, and Purification of Proteins for a Medium-Scale Structural Genomics Project. In S. Doublié (Ed.), *Macromolecular Crystallography Protocols* (1st ed., pp. 21–37). Humana Press.

Ramirez, D. A., Hough, L. E., & Shirts, M. R. (2023). Coiled-coil domains are sufficient to drive liquid-liquid phase separation of proteins in molecular models. *BioRxiv*. https://doi.org/10.1101/2023.05.31.543124

Rao, M. B., Tanksale, A. M., Ghatge, M. S., & Deshpande, V. V. (1998). Molecular and Biotechnological Aspects of Microbial Proteases †. *MICROBIOLOGY AND MOLECULAR BIOLOGY REVIEWS*, *62*(3), 597–635.

Rappsilber, J., Ishihama, Y., & Mann, M. (2003). Stop And Go Extraction tips for matrix-assisted laser desorption/ionization, nanoelectrospray, and LC/MS sample pretreatment in proteomics. *Analytical Chemistry*, *75*(3), 663–670. https://doi.org/10.1021/ac026117i

Ray, S., Singh, N., Kumar, R., Patel, K., Pandey, S., Datta, D., Mahato, J., Panigrahi, R., Navalkar, A., Mehra, S., Gadhe, L., Chatterjee, D., Sawner, A. S., Maiti, S., Bhatia, S., Gerez, J. A., Chowdhury, A., Kumar, A., Padinhateeri, R., … Maji, S. K. (2020). α-Synuclein aggregation nucleates through liquid–liquid phase separation. *Nature Chemistry*, *12*(8), 705–716. https://doi.org/10.1038/s41557-020-0465-9

Reeves, P. J., Callewaert, N., Contreras, R., & Gobind Khorana, H. (2002). Structure and function in rhodopsin: High-level expression of rhodopsin with restricted and homogeneous N-glycosylation by a tetracycline-inducible N-

acetylglucosaminyltransferase I-negative HEK293S stable mammalian cell line. *PNAS*, *99*(21), 13419–13424. https://doi.org/10.1073_pnas.212519299

Riback, J. A., Katanski, C. D., Kear-Scott, J. L., Pilipenko, E. V., Rojek, A. E., Sosnick, T. R., & Drummond, D. A. (2017). Stress-Triggered Phase Separation Is an Adaptive, Evolutionarily Tuned Response. *Cell*, *168*(6), 1028–1040.e19. https://doi.org/10.1016/j.cell.2017.02.027

Richmond, D. L., Schmid, E. M., Martens, S., Stachowiak, J. C., Liska, N., & Fletcher, D. A. (2011). Forming giant vesicles with controlled membrane composition, asymmetry, and contents. *PNAS*, *108*(23), 9431–9436. https://doi.org/10.1073/pnas.1016410108/-/DCSupplemental

Rodger, A., Marrington, R., Roper, D., & Windsor, S. (2005). Circular dichroism spectroscopy for the study of protein-ligand interactions. In *Methods Mol Biol.* (Vol. 305, pp. 343–364). https://doi.org/10.1385/1-59259-912-5:343

Rohatgi, R., Ma, L., Miki, H., Lopez, M., Kirchhausen, T., Takenawa, T., & Kirschner, M. W. (1999). The Interaction between N-WASP and the Arp2/3 Complex Links Cdc42-Dependent Signals to Actin Assembly. *Cell*, *97*(2), 221–231.

Rosenbaum, D. M., Rasmussen, S. G. F., & Kobilka, B. K. (2009). The structure and function of G-protein-coupled receptors. *Nature*, *459*(7245), 356–363. https://doi.org/doi:10.1038/nature08144. The

Rubinstein, M., & Colby, R. H. (2003). *Polymer Physics (Chemistry) (2003)*. Oxford University Press .

Samanta, A., Hughes, T. E. T., & Moiseenkova-Bell, V. Y. (2018). Transient receptor potential (TRP) channels. In *Subcellular Biochemistry* (Vol. 87, pp. 141–165). Springer New York. https://doi.org/10.1007/978-981-10-7757-9_6

Schaefer, A. W., Kabir, N., & Forscher, P. (2002). Filopodia and actin arcs guide the assembly and transport of two populations of microtubules with unique dynamic parameters in neuronal growth cones. *Journal of Cell Biology*, *158*(1), 139–152. https://doi.org/10.1083/jcb.200203038

Schiöth, H. B., & Lagerström, M. C. (2008). Structural diversity of g proteincoupled receptors and significance for drug discovery. *Nature Reviews Drug Discovery*, *7*(4), 339–357. https://doi.org/10.1038/nrd2518

Schlessinger, A., Yee, S. W., Sali, A., & Giacomini, K. M. (2013). SLC classification: An update. *Clinical Pharmacology and Therapeutics*, *94*(1), 19–23. https://doi.org/10.1038/clpt.2013.73

Schmid, E. M., Richmond, D. L., & Fletcher, D. A. (2015). Reconstitution of proteins on electroformed giant unilamellar vesicles. *Methods in Cell Biology*, *128*, 319–338. https://doi.org/10.1016/bs.mcb.2015.02.004

Schneider, N., Wieland, F.-G., Kong, D., M Fischer, A. A., Hörner, M., Timmer, J., Ye, H., & Weber, W. (2021). Liquid-liquid phase separation of light-inducible transcription factors increases transcription activation in mammalian cells and mice. In *Sci. Adv* (Vol. 7, Issue 1). https://www.science.org

Scita, G., Confalonieri, S., Lappalainen, P., & Suetsugu, S. (2008). IRSp53: crossing the road of membrane and actin dynamics in the formation of membrane protrusions. In *Trends in Cell Biology* (Vol. 18, Issue 2, pp. 52–60). https://doi.org/10.1016/j.tcb.2007.12.002

Scott, G. D. (1962). Radial Distribution of the Random Close Packing of Equal Spheres.

Nature, *194*(4832), 8956–8957. https://doi.org/https://doi.org/10.1038/194956a0

Shammas, S. L., Travis, A. J., & Clarke, J. (2013). Remarkably fast coupled folding and binding of the intrinsically disordered transactivation domain of cMyb to CBP KIX. *Journal of Physical Chemistry B*, *117*(42), 13346–13356. https://doi.org/10.1021/jp404267e

Shao, S., & Hegde, R. S. (2011). Membrane protein insertion at the endoplasmic reticulum. *Annual Review of Cell and Developmental Biology*, *27*, 25–56. https://doi.org/10.1146/annurev-cellbio-092910-154125

Sherrill, C. D. (2013). Energy component analysis of π interactions. *Accounts of Chemical Research*, *46*(4), 1020–1028. https://doi.org/10.1021/ar3001124

Shin, Y., Berry, J., Pannucci, N., Haataja, M. P., Toettcher, J. E., & Brangwynne, C. P. (2017). Spatiotemporal Control of Intracellular Phase Transitions Using Light-Activated optoDroplets. *Cell*, *168*(1–2), 159–171.e14. https://doi.org/10.1016/j.cell.2016.11.054

Shin, Y., & Brangwynne, C. P. (2017). Liquid phase condensation in cell physiology and disease. *Science*, *357*(6357). https://doi.org/10.1126/science.aaf4382

Sigal, Y. J., McDermott, M. I., & Morris, A. J. (2005). Integral membrane lipid phosphatases/phosphotransferases: Common structure and diverse functions. *Biochemical Journal*, *387*(2), 281–293. https://doi.org/10.1042/BJ20041771

Sigal, Y. J., Quintero, O. a, Cheney, R. E., & Morris, A. J. (2007). Cdc42 and ARP2/3-independent regulation of filopodia by an integral membrane lipid-phosphatase-related protein. *Journal of Cell Science*, *120*(Pt 2), 340–352. https://doi.org/10.1242/jcs.03335

Sigalov, A. B., Kim, W. M., Saline, M., & Stern, L. J. (2008). The intrinsically disordered cytoplasmic domain of the T cell receptor ζ chain binds to the Nef protein of simian immunodeficiency virus without a disorder-to-order transition. *Biochemistry*, *47*(49), 12942–12944. https://doi.org/10.1021/bi801602p

Simon, C., Caorsi, V., Campillo, C., & Sykes, C. (2018). Interplay between membrane tension and the actin cytoskeleton determines shape changes. *Physical Biology*, *15*(6). https://doi.org/10.1088/1478-3975/aad1ab

Simunovic, M., Voth, G. A., Callan-Jones, A., & Bassereau, P. (2015). When Physics Takes Over: BAR Proteins and Membrane Curvature. In *Trends in Cell Biology* (Vol. 25, Issue 12, pp. 780–792). Elsevier Ltd. https://doi.org/10.1016/j.tcb.2015.09.005

Singatulina, A. S., Hamon, L., Sukhanova, M. V., Desforges, B., Joshi, V., Bouhss, A., Lavrik, O. I., & Pastré, D. (2019). PARP-1 Activation Directs FUS to DNA Damage Sites to Form PARG-Reversible Compartments Enriched in Damaged DNA. *Cell Reports*, *27*(6), 1809–1821.e5. https://doi.org/10.1016/j.celrep.2019.04.031

Slootstra, J. W., Kuperus, D., Plückthun, A., & Meloen, R. H. (1996). Identification of new tag sequences with differential and selective recognition properties for the anti-FLAG monoclonal antibodies Ml, M2 and M5. *Molecular Diversity*, *2*(3), 156–164. https://doi.org/10.1007/BF01682203

Smith, C. L. (1994). The Initiation of Neurite Outgrowth by Sympathetic Neurons Grown In Vitro Does Not Depend on Assembly of Microtubules. *The Journal of Cell Biology*, *127*(5), 1407–1418.

Smyth, M. S., & Martin, J. H. J. (2000). Review x Ray crystallography. *J Clin Pathol: Mol Pathol*, *53*, 8–14.

Spector, I., Shochet, N. R., Kashman, Y., & Groweiss, A. (1983). Latrunculins: novel marine toxins that disrupt microfilament organization in cultured cells. *Science*, *219*(4584), 493–495. https://doi.org/10.1126/science.6681676

Spector, I., Shorlet, N. R., Blasberger, D., & Kashman, Y. (1989). Latrunculins - novel marine macrolides that disrupt microfilament organization and affert cell growth: I. Comparison with cytochalasin D. *Cell Motility and the Cytoskeleton*, *13*(3), 127–144. https://doi.org/10.1002/cm.970130302

Sprague, B. L., & McNally, J. G. (2005). FRAP analysis of binding: Proper and fitting. *Trends in Cell Biology*, *15*(2), 84–91. https://doi.org/10.1016/j.tcb.2004.12.001

Srivastava, J., & Barber, D. (2008). Actin co-sedimentation assay; for the analysis of protein binding to F-Actin. *Journal of Visualized Experiments*, *13*. https://doi.org/10.3791/690

Stachowiak, J. C., Schmid, E. M., Ryan, C. J., Ann, H. S., Sasaki, D. Y., Sherman, M. B., Geissler, P. L., Fletcher, D. A., & Hayden, C. C. (2012). Membrane bending by protein-protein crowding. *Nature Cell Biology*, *14*(9), 944–949. https://doi.org/10.1038/ncb2561

Stalder, D., & Gershlick, D. C. (2020). Direct trafficking pathways from the Golgi apparatus to the plasma membrane. *Seminars in Cell and Developmental Biology*, *107*, 112–125. https://doi.org/10.1016/j.semcdb.2020.04.001

Stanishneva-Konovalova, T. B., Derkacheva, N. I., Polevova, S. V., & Sokolova, O. S. (2016). The Role of BAR Domain Proteins in the Regulation of Membrane Dynamics. *Acta Naturae*, *8*(4), 60–69.

Stukan, M. R., An, E. A., Ivanov, V. A., & Vinogradova, O. I. (2006). Stability of toroid and rodlike globular structures of a single stiff-chain macromolecule for different bending potentials. *Physical Review E - Statistical, Nonlinear, and Soft Matter Physics*, *73*(5). https://doi.org/10.1103/PhysRevE.73.051804

Su, X., Ditlev, J. A., Hui, E., Xing, W., Banjade, S., Okrut, J., King, D. S., Taunton, J., Rosen, M. K., & Vale, R. D. (2016). Phase separation of signaling molecules promotes T cell receptor signal transduction. *Science*, *352*(6285), 595–599. https://doi.org/10.1126/science.aad9964

Svitkina, T. M., Bulanova, E. A., Chaga, O. Y., Vignjevic, D. M., Kojima, S. ichiro, Vasiliev, J. M., & Borisy, G. G. (2003). Mechanism of filopodia initiation by reorganization of a dendritic network. *Journal of Cell Biology*, *160*(3), 409–421. https://doi.org/10.1083/jcb.200210174

Tabata, K. ichi, Baba, K., Shiraishi, A., Ito, M., & Fujita, N. (2007). The orphan GPCR GPR87 was deorphanized and shown to be a lysophosphatidic acid receptor. *Biochemical and Biophysical Research Communications*, *363*(3), 861–866. https://doi.org/10.1016/j.bbrc.2007.09.063

Tang, X., & Brindley, D. N. (2020). Lipid phosphate phosphatases and cancer. In *Biomolecules* (Vol. 10, Issue 9, pp. 1–24). MDPI AG. https://doi.org/10.3390/biom10091263

Tang, X., McMullen, T. P. W., & Brindley, D. N. (2019). Increasing the low lipid phosphate phosphatase 1 activity in breast cancer cells decreases transcription by AP-1 and expressions of matrix metalloproteinases and cyclin D1/D3.

Theranostics, *9*(21), 6129–6142. https://doi.org/10.7150/thno.37094

Taniue, K., & Akimitsu, N. (2022). Aberrant phase separation and cancer. *FEBS Journal*, *289*(1), 17–39. https://doi.org/10.1111/febs.15765

Tariq, K., & Luikart, B. W. (2021). Striking a balance: PIP2 and PIP3 signaling in neuronal health and disease. *Exploration of Neuroprotective Therapy*, *1*(2). https://doi.org/10.37349/ent.2021.00008

Taylor, K. L., Taylor, R. J., Richters, K. E., Huynh, B., Carrington, J., McDermott, M. E., Wilson, R. L., & Dent, E. W. (2019). Opposing functions of F-BAR proteins in neuronal membrane protrusion, tubule formation, and neurite outgrowth. *Life Science Alliance*, *2*(3). https://doi.org/10.26508/lsa.201800288

Taylor, N. O., Wei, M. T., Stone, H. A., & Brangwynne, C. P. (2019). Quantifying Dynamics in Phase-Separated Condensates Using Fluorescence Recovery after Photobleaching. *Biophysical Journal*, *117*(7), 1285–1300. https://doi.org/10.1016/j.bpj.2019.08.030

Terenzio, M., Schiavo, G., & Fainzilber, M. (2017). Compartmentalized Signaling in Neurons: From Cell Biology to Neuroscience. *Neuron*, *96*(3), 667–679. https://doi.org/10.1016/j.neuron.2017.10.015

Tesei, G., Schulze, T. K., Crehuet, R., & Lindorff-Larsen, K. (2021). Accurate model of liquid-liquid phase behavior of intrinsically disordered proteins from optimization of single-chain properties. *BIOPHYSICS AND COMPUTATIONAL BIOLOGY*. https://doi.org/10.1073/pnas.2111696118/-/DCSupplemental

Texier, B., Prime, M., Atamena, D., Belenguer, P., & Szelechowski, M. (2023). Mortalin/Hspa9 involvement and therapeutic perspective in Parkinson's disease. *Neural Regeneration Research*, *18*(2), 293–298. https://doi.org/10.4103/1673-5374.346487

Tokumitsu, H., Hatano, N., Tsuchiya, M., Yurimoto, S., Fujimoto, T., Ohara, N., Kobayashi, R., & Sakagami, H. (2010). Identification and characterization of PRG-1 as a neuronal calmodulin-binding protein. *Biochemical Journal*, *431*(1), 81–91. https://doi.org/10.1042/BJ20100637

Tong, J., Nguyen, L., Vidal, A., Simon, S. A., Skene, J. H. P., & McIntosh, T. J. (2008). Role of GAP-43 in sequestering phosphatidylinositol 4,5-bisphosphate to raft bilayers. *Biophysical Journal*, *94*(1), 125–133. https://doi.org/10.1529/biophysj.107.110536

Trivedi, R., & Nagarajaram, H. A. (2022). Intrinsically Disordered Proteins: An Overview. *International Journal of Molecular Sciences*, *23*(22). https://doi.org/10.3390/ijms232214050

Trnka, F., Hoffmann, C., Wang, H., Sansevrino, R., Rankovic, B., Rost, B. R., Schmitz, D., Schmidt, H. B., & Milovanovic, D. (2021). Aberrant Phase Separation of FUS Leads to Lysosome Sequestering and Acidification. *Frontiers in Cell and Developmental Biology*, *9*(October), 1–13. https://doi.org/10.3389/fcell.2021.716919

Tuteja, N. (2009). Signaling through G protein coupled receptors. *Plant Signaling and Behavior*, *4*(10), 942–947. https://doi.org/10.4161/psb.4.10.9530

Tyrrell, J., Weeks, K. M., & Pielak, G. J. (2015). Challenge of Mimicking the Influences of the Cellular Environment on RNA Structure by PEG-Induced Macromolecular Crowding. *Biochemistry*, *54*(42), 6447–6453.

https://doi.org/10.1021/acs.biochem.5b00767

Ulianov, S. V., Velichko, A. K., Magnitov, M. D., Luzhin, A. V., Golov, A. K., Ovsyannikova, N., Kireev, I. I., Gavrikov, A. S., Mishin, A. S., Garaev, A. K., Tyakht, A. V., Gavrilov, A. A., Kantidze, O. L., & Razin, S. V. (2021). Suppression of liquid–liquid phase separation by 1,6-hexanediol partially compromises the 3D genome organization in living cells. *Nucleic Acids Research*, *49*(18), 10524–10541. https://doi.org/10.1093/nar/gkab249

Uversky, V. N., Gillespie, J. R., & Fink, A. L. (2000). Why are "natively unfolded" proteins unstructured under physiologic conditions? *Proteins*, *41*(3), 415–427. https://doi.org/DOI: 10.1002/1097-0134(20001115)41:3<415::aid-prot130>3.0.co;2-7

Van Der Lee, R., Buljan, M., Lang, B., Weatheritt, R. J., Daughdrill, G. W., Dunker, A. K., Fuxreiter, M., Gough, J., Gsponer, J., Jones, D. T., Kim, P. M., Kriwacki, R. W., Oldfield, C. J., Pappu, R. V., Tompa, P., Uversky, V. N., Wright, P. E., & Babu, M. M. (2014). Classification of intrinsically disordered regions and proteins. In *Chemical Reviews* (Vol. 114, Issue 13, pp. 6589–6631). American Chemical Society. https://doi.org/10.1021/cr400525m

Velmans, T., Battefeld, A., Geist, B., Farrés, A. S., Strauss, U., & Bräuer, A. U. (2013a). Plasticity-related gene 3 promotes neurite shaft protrusion. *BMC Neuroscience*, *14*. https://doi.org/10.1186/1471-2202-14-36

Velmans, T., Battefeld, A., Geist, B., Farrés, A. S., Strauss, U., & Bräuer, A. U. (2013b). Plasticity-related gene 3 promotes neurite shaft protrusion. *BMC Neuroscience*, *14*. https://doi.org/10.1186/1471-2202-14-36

Vengerov, Y. Y., Semenov, T. E., Streltsov, S. A., Makarov, V. L., Khorlin, A. A., & Gursky, G. V. (1985). Triple rings: A new type of compact structure of circular DNA. *Journal of Molecular Biology*, *184*(2), 251–255. https://doi.org/10.1016/0022-2836(85)90378-X

Venko, K., & Žerovnik, E. (2023). Protein Condensates and Protein Aggregates: In Vitro, in the Cell, and In Silico. In *Frontiers in Bioscience - Landmark* (Vol. 28, Issue 8). IMR Press Limited. https://doi.org/10.31083/j.fbl2808183

Verkest, C., Schaefer, I., Nees, T. A., Wang, N., Jegelka, J. M., Taberner, F. J., & Lechner, S. G. (2022). Intrinsically disordered intracellular domains control key features of the mechanically-gated ion channel PIEZO2. *Nature Communications*, *13*(1). https://doi.org/10.1038/s41467-022-28974-6

Vilfan, I. D., Conwell, C. C., Sarkar, T., & Hud, N. V. (2006). Time study of DNA condensate morphology: Implications regarding the nucleation, growth, and equilibrium populations of toroids and rods. *Biochemistry*, *45*(26), 8174–8183. https://doi.org/10.1021/bi060396c

Vistrup-Parry, M., Chen, X., Johansen, T. L., Bach, S., Buch-Larsen, S. C., Bartling, C. R. O., Ma, C., Clemmensen, L. S., Nielsen, M. L., Zhang, M., & Strømgaard, K. (2021). Site-specific phosphorylation of PSD-95 dynamically regulates the postsynaptic density as observed by phase separation. *iScience*, *24*(11), 103268. https://doi.org/10.1016/j.isci.2021.103268

Vodnala, M., Choi, E. B., & Fong, Y. W. (2021). Low Complexity Domains, Condensates, and Stem Cell Pluripotency. *World Journal of Stem Cells*, *13*(5), 416–438. https://doi.org/10.4252/wjsc.v13.i5.416

Waggoner, D. W., Gó Mez-Muñ Oz, A., Dewald, J., & Brindley, D. N. (1996).

Phosphatidate Phosphohydrolase Catalyzes the Hydrolysis of Ceramide 1-Phosphate, Lysophosphatidate, and Sphingosine 1-Phosphate*. *Journal of Biological Chemistry*, *271*(28), 16506–16509. https://doi.org/https://doi.org/10.1074/jbc.271.28.16506

Waggoner, D. W., Xu, J., Singh, I., Jasinska, R., Zhang, Q. X., & Brindley, D. N. (1999). Structural organization of mammalian lipid phosphate phosphatases: Implications for signal transduction. *Biochimica et Biophysica Acta - Molecular and Cell Biology of Lipids*, *1439*(2), 299–316. https://doi.org/10.1016/S1388-1981(99)00102-X

Wang, D. Y., Abbasi, C., El-Rass, S., Li, J. Y., Dawood, F., Naito, K., Sharma, P., Bousette, N., Singh, S., Backx, P. H., Cox, B., Wen, X. Y., Liu, P. P., & Gramolini, A. O. (2014). Endoplasmic reticulum resident protein 44 (ERp44) deficiency in mice and zebrafish leads to cardiac developmental and functional defects. *Journal of the American Heart Association*, *3*(5). https://doi.org/10.1161/JAHA.114.001018

Wang, H., Yang, Y., Liu, J., & Qian, L. (2021). Direct cell reprogramming: approaches, mechanisms and progress. *Nature Reviews Molecular Cell Biology*, *22*(6), 410–424. https://doi.org/10.1038/s41580-021-00335-z

Wang, X., Jiang, B., Gu, L., Chen, Y., Mora, M., Zhu, M., Noory, E., Wang, Q., & Lin, C. (2021). A photoregulatory mechanism of the circadian clock in Arabidopsis. *Nature Plants*, *7*(10), 1397–1408. https://doi.org/10.1038/s41477-021-01002-z

Webb, F. B. (1885). The Second Law of Thermodynamics. *Science*, *ns-6*(136), 212–214. https://doi.org/10.1126/science.ns-6.136.212

Weber, S. C., & Brangwynne, C. P. (2012). Getting RNA and protein in phase. *Cell*, *149*(6), 1188–1191. https://doi.org/10.1016/j.cell.2012.05.022

Wegmann, S., Eftekharzadeh, B., Tepper, K., Zoltowska, K. M., Bennett, R. E., Dujardin, S., Laskowski, P. R., MacKenzie, D., Kamath, T., Commins, C., Vanderburg, C., Roe, A. D., Fan, Z., Molliex, A. M., Hernandez-Vega, A., Muller, D., Hyman, A. A., Mandelkow, E., Taylor, J. P., & Hyman, B. T. (2018). Tau protein liquid–liquid phase separation can initiate tau aggregation. *The EMBO Journal*, *37*(7), 1–21. https://doi.org/10.15252/embj.201798049

Wegner, A. (1976). Head to Tail Polymerization of Actin. *J. Mol. Biol*, *108*, 139–150.

Wegner, A., & Isenbergt, G. (1983). 2-Fold difference between the critical monomer concentrations of the two ends of actin filaments in physiological salt conditions (actin/capping protein/fluorescence). *Proc. Nati Acad. Sci. USA*, *80*, 4922–4925.

Widmer, F., & Caroni, P. (1990). Identification, localization, and primary structure of CAP-23, a particle-bound cytosolic protein of early development. *Journal of Cell Biology*, *111*(6 PART 2), 3035–3047. https://doi.org/10.1083/jcb.111.6.3035

Widom, B. (1988). Note on the Interfaeial Tension of Phase-Separated Polymer Solutions. *Journal of Statistical Physics*, *52*(5). https://doi.org/10.1007/BF01011651

Wit, C. B., & Hiesinger, P. R. (2023). Neuronal filopodia: From stochastic dynamics to robustness of brain morphogenesis. *Seminars in Cell and Developmental Biology*, *133*, 10–19. https://doi.org/10.1016/j.semcdb.2022.03.038

Woodruff, J. B., Ferreira Gomes, B., Widlund, P. O., Mahamid, J., Honigmann, A., & Hyman, A. A. (2017). The Centrosome Is a Selective Condensate that Nucleates

Microtubules by Concentrating Tubulin. *Cell*, *169*(6), 1066–1077.e10. https://doi.org/10.1016/j.cell.2017.05.028

Wright, P. E., & Dyson, H. J. (2015). Intrinsically disordered proteins in cellular signalling and regulation. *Nature Reviews Molecular Cell Biology*, *16*(1), 18–29. https://doi.org/10.1038/nrm3920

Wu, X., Cai, Q., Feng, Z., & Zhang, M. (2020). Liquid-Liquid Phase Separation in Neuronal Development and Synaptic Signaling. *Developmental Cell*, *55*(1), 18–29. https://doi.org/10.1016/j.devcel.2020.06.012

Wu, X., Cai, Q., Shen, Z., Chen, X., Zeng, M., Du, S., & Zhang, M. (2019). RIM and RIM-BP Form Presynaptic Active-Zone-like Condensates via Phase Separation. *Molecular Cell*, *73*(5), 971–984.e5. https://doi.org/10.1016/j.molcel.2018.12.007

Xiaolei Su, Jonathon A. Ditlev, Enfu Hui, Wenmin Xing, Sudeep Banjade, Julia Okrut, David S. King, Jack Taunton, Michael K. Rosen, & Ronald D. Vale. (2016). Phase separation of signalingmolecules promotes T cell receptorsignal transduction. *Science*, *352*(6285), 595–599. https://doi.org/10.1126/science.aad9964

Xu, Y., Wang, H., Nussinov, R., & Ma, B. (2013). Protein charge and mass contribute to the spatio-temporal dynamics of protein-protein interactions in a minimal proteome. *Proteomics*, *13*(8), 1339–1351. https://doi.org/10.1002/pmic.201100540

Xue, S., Gong, R., He, F., Li, Y., Wang, Y., Tan, T., & Luo, S.-Z. (2019). Low-complexity domain of U1-70K modulates phase separation and aggregation through distinctive basic-acidic motifs. *Science Advances*, *5*, 1–9. https://www.science.org

Yaguchi, H., Okumura, F., Takahashi, H., Kano, T., Kameda, H., Uchigashima, M., Tanaka, S., Watanabe, M., Sasaki, H., & Hatakeyama, S. (2012). TRIM67 protein negatively regulates Ras activity through degradation of 80K-H and induces neuritogenesis. *Journal of Biological Chemistry*, *287*(15), 12050–12059. https://doi.org/10.1074/jbc.M111.307678

Yamagishi, A., Masuda, M., Ohki, T., Onishi, H., & Mochizuki, N. (2004). A Novel Actin Bundling/Filopodium-forming Domain Conserved in Insulin Receptor Tyrosine Kinase Substrate p53 and Missing in Metastasis Protein. *Journal of Biological Chemistry*, *279*(15), 14929–14936. https://doi.org/10.1074/jbc.M309408200

Yan, V. T., Narayanan, A., Wiegand, T., Jülicher, F., & Grill, S. W. (2022). A condensate dynamic instability orchestrates actomyosin cortex activation. *Nature*, *609*(7927), 597–604. https://doi.org/10.1038/s41586-022-05084-3

Yang, C., & Svitkina, T. (2011). Filopodia initiation. *Cell Adhesion & Migration*, *5*(5), 402–408. https://doi.org/10.4161/cam.5.5.16971

Yang, D., Zhou, Q., Labroska, V., Qin, S., Darbalaei, S., Wu, Y., Yuliantie, E., Xie, L., Tao, H., Cheng, J., Liu, Q., Zhao, S., Shui, W., Jiang, Y., & Wang, M. W. (2021). G protein-coupled receptors: structure- and function-based drug discovery. *Signal Transduction and Targeted Therapy*, *6*(1). https://doi.org/10.1038/s41392-020-00435-w

Yasuda, R., Hayashi, Y., & Hell, J. W. (2022). CaMKII: a central molecular organizer of synaptic plasticity, learning and memory. *Nature Reviews Neuroscience*, *23*(11), 666–682. https://doi.org/10.1038/s41583-022-00624-2

Yavin, E., & Yavin, Z. (1974). Attachment and culture of dissociated cells from rat embryo cerebral hemispheres on polylysine-coated surface. *J. Cell Biol.*, *62*, 540–546. https://doi.org/10.1083/jcb.62.2.540

Ye, S., Hsiung, C.-H., Tang, Y., & Zhang, X. (2022). Visualizing the multi-step process of protein aggregation in live cells. *Acc Chem Res*, *55*(3), 381–390. https://doi.org/10.1021/acs.accounts.1c00648

Yu, H. (1999). Commentary Extending the size limit of protein nuclear magnetic resonance. *PNAS*, *96*(2), 332–334. www.pnas.org.

Yu, P., Agbaegbu, C., Malide, D. A., Wu, X., Katagiri, Y., Hammer, J. A., & Geller, H. M. (2015a). Cooperative interactions of LPPR family members in membrane localization and alteration of cellular morphology. *Journal of Cell Science*, *128*(17), 3210–3222. https://doi.org/10.1242/jcs.169789

Yu, P., Agbaegbu, C., Malide, D. A., Wu, X., Katagiri, Y., Hammer, J. A., & Geller, H. M. (2015b). Cooperative interactions of LPPR family members in membrane localization and alteration of cellular morphology. *Journal of Cell Science*, *128*(17), 3210–3222. https://doi.org/10.1242/jcs.169789

Yu, P., Agbaegbu, C., Malide, D. A., Wu, X., Katagiri, Y., Hammer, J. A., & Geller, H. M. (2015). Cooperative interactions of LPPR family members in membrane localization and alteration of cellular morphology. *J Cell Sci*, *128*(17), 3210–3222. https://doi.org/10.1242/jcs.169789

Yuan, F., Alimohamadi, H., Bakka, B., Trementozzi, A. N., Daya, K. J., Fawzi, N. L., Rangamani, P., & Stachowiak, J. C. (2021). Membrane bending by protein phase separation. *PNAS*, *118*(11), 1–11. https://doi.org/10.1073/pnas.2017435118/-/DCSupplemental

Yuan, F., Lee, C. T., Sangani, A., Houser, J. R., Wang, L., Lafer, E. M., Rangamani, P., & Stachowiak, J. C. (2023). The ins and outs of membrane bending by intrinsically disordered proteins. *Science Advances1*, *9*(27), 12. https://doi.org/10.1126/sciadv.adg3485

Zaccolo, M. (2011). Spatial control of cAMP signalling in health and disease. In *Current Opinion in Pharmacology* (Vol. 11, Issue 6, pp. 649–655). Elsevier Ltd. https://doi.org/10.1016/j.coph.2011.09.014

Zaccolo, M., Zerio, A., & Lobo, M. J. (2021). Subcellular organization of the camp signaling pathway. *Pharmacological Reviews*, *73*(1), 278–309. https://doi.org/10.1124/pharmrev.120.000086

Zbinden, A., Pérez-Berlanga, M., De Rossi, P., & Polymenidou, M. (2020). Phase Separation and Neurodegenerative Diseases: A Disturbance in the Force. In *Developmental Cell* (Vol. 55, Issue 1, pp. 45–68). Cell Press. https://doi.org/10.1016/j.devcel.2020.09.014

Zeng, M., Chen, X., Guan, D., Xu, J., Wu, H., Tong, P., & Zhang, M. (2018). Reconstituted Postsynaptic Density as a Molecular Platform for Understanding Synapse Formation and Plasticity. *Cell*, *174*(5), 1172–1187.e16. https://doi.org/10.1016/j.cell.2018.06.047

Zeng, M., Shang, Y., Araki, Y., Guo, T., Huganir, R. L., & Zhang, M. (2016). Phase Transition in Postsynaptic Densities Underlies Formation of Synaptic Complexes and Synaptic Plasticity. *Cell*, *166*(5), 1163–1175.e12. https://doi.org/10.1016/j.cell.2016.07.008

Zhang, J. Z., Lu, T. W., Stolerman, L. M., Tenner, B., Yang, J. R., Zhang, J. F., Falcke, M., Rangamani, P., Taylor, S. S., Mehta, S., & Zhang, J. (2020). Phase Separation of a PKA Regulatory Subunit Controls cAMP Compartmentation and Oncogenic Signaling. *Cell*, *182*(6), 1531–1544.e15. https://doi.org/10.1016/j.cell.2020.07.043

Zhang, K., Huang, M., Li, A., Wen, J., Yan, L., Li, Y., Guo, L., Senthil, K. S., Zhou, Y., Chen, G., Liu, Y., Zhang, X., Yao, X., Qin, D., & Su, H. (2023). DIAPH3 condensates formed by liquid-liquid phase separation act as a regulatory hub for stress-induced actin cytoskeleton remodeling. *Cell Reports*, *42*(1). https://doi.org/10.1016/j.celrep.2022.111986

Zhang, X. C., Piccini, A., Myers, M. P., Van Aelst, L., & Tonks, N. K. (2012). Functional analysis of the protein phosphatase activity of PTEN. *Biochemical Journal*, *444*(3), 457–464. https://doi.org/10.1042/BJ20120098

Zhou, H. X., & Pang, X. (2018). Electrostatic Interactions in Protein Structure, Folding, Binding, and Condensation. *Chemical Reviews*, *118*(4), 1691–1741. https://doi.org/10.1021/acs.chemrev.7b00305

Zhu, J., & Jiang, L. (2022). Liquid–Liquid Phase Separation Bridges Physics, Chemistry, and Biology. *Langmuir*, *38*(30), 9043–9049. https://doi.org/10.1021/acs.langmuir.2c01358

Ziv, N. E., & Smith, S. J. (1996). Evidence for a Role of Dendritic Filopodia in Synaptogenesis and Spine Formation. *Neuron*, *17*, 91–102.

Zumbro, E., & Alexander-Katz, A. (2020). Influence of Binding Site Affinity Patterns on Binding of Multivalent Polymers. *ACS Omega*, *5*(19), 10774–10781. https://doi.org/10.1021/acsomega.0c00334

Zuo, X., Zhou, J., Li, Y., Wu, K., Chen, Z., Luo, Z., Zhang, X., Liang, Y., Esteban, M. A., Zhou, Y., & Fu, X. D. (2021). TDP-43 aggregation induced by oxidative stress causes global mitochondrial imbalance in ALS. *Nature Structural and Molecular Biology*, *28*(2), 132–142. https://doi.org/10.1038/s41594-020-00537-7

8 List of publications related to this thesis

Fuchs[*], J., **Bareesel[*], S.**, Kroon[*], C., Polyzou[*], A., Eickholt, B. J., & Leondaritis, G. (2022). Plasma membrane phospholipid phosphatase-related proteins as pleiotropic regulators of neuron growth and excitability. *Frontiers in Molecular Neuroscience*, *15*. https://doi.org/10.3389/fnmol.2022.984655

Kroon, C., **Bareesel, S.**, Kirchner, M., Gimber, N., Ranti, D., Brosig, A., Textoris-Taube, K., Zolnik, T. A., Mertins, P., Schmoranzer, J., Leondaritis, G., and Eickholt, B. J. (2024). Phosphorylation of PLPPR3 membrane proteins as signaling integrator at neuronal synapses. *BioRxiv*, 1-32. https://doi.org/10.1101/2024.03.11.584206

Bareesel et al., 2024 (*in preparation)*